Functionally Graded Lattice Infill and Cooling Channel Design Optimization for Additive Manufacturing

by

Lin Cheng

B.S., Xi'an Jiao Tong University, 2011

M.S., Shanghai Jiao Tong University, 2014

Submitted to the Graduate Faculty of

Swanson School of Engineering in partial fulfillment

of the requirements for the degree of

Doctor of Philosophy

University of Pittsburgh

2019

UNIVERSITY OF PITTSBURGH

SWANSON SCHOOL OF ENGINEERING

This dissertation was presented

by

Lin Cheng

It was defended on

June 11, 2019

and approved by

Hessam Babaee, Ph.D., Assistant Professor, Department of Mechanical Engineering and Materials Science

William S. Slaughter, Ph.D., Associate Professor, Department of Mechanical Engineering and Materials Science

Jeen-Shang Lin, Ph.D., Associate Professor, Department of Civil and Environmental Engineering

Dissertation Director: Albert C. To, Ph.D., Associate Professor, Department of Mechanical Engineering and Materials Science

Functionally Graded Lattice Infill and Cooling Channel Design Optimization for Additive Manufacturing

Lin Cheng, PhD

University of Pittsburgh, 2019

To realize the full potential of additive manufacturing (AM) techniques, a lattice structure design optimization methodology is proposed to design functionally graded lattice structures, in order to achieve optimal performance while satisfying manufacturing constraints.

A lattice structure topology optimization (LSTO) method is first proposed and the framework includes three key steps: (1) Asymptotic homogenization (AH) is developed to calculate effective properties of 3D printed lattice materials, such as elastic modulus, yield strength, thermal conductivity and forced convection heat transfer coefficient; (2) Density-based topology optimization methodology is employed to compute the density distribution of lattice structures by using the material interpolation from AH procedure; (3) A reconstruction method is developed to transform an optimal density profile into variable-density lattice structure for practical fabrications. The proposed LSTO method is extensively studied for various problems ranging from, structural (minimum compliance problem and constraint stress problem), dynamic (natural frequency maximization), and heat and mass transfer. Validation of the LSTO method conducted on practical components is able to significantly improve the physical performance of the component with lightweight design.

On the other hand, the LSTO method cannot handle functionally movable features optimization, e.g. cooling channels and bolt holes in components, which are non-designable and remains solid during optimization. To explore the potential benefits, the LSTO method is extended

to the concurrent optimization of lattice infill and movable features optimization. A unified scheme for the combination of density-based topology optimization with level set topology optimization is thus proposed and derived.

In addition to theory development, the LSTO method is further developed to solve a critical issue regarding build failures induced by residual stress inherent in the metal AM process. Specifically, a voxel-based methodology is proposed to efficiently generate Cartesian mesh for a solid part and its support structure. A build orientation optimization method and a LSTO-based support structure optimization method is developed to minimize the volume of sacrificial support structure under allowable stress constraint. Experiments have proved that the proposed framework can significantly reduce the residual stress, guarantee the manufacturability of the designs, and make it easy for trapped powder removal.

Table of Contents

List of Tables

List of Figures

Preface

I firmly believe that the inexhaustible power of human beings' evolution comes from the gradually increasing knowledge of the natural world. This strong belief motivates me to pursue my Ph.D. study in mechanical engineering. At this moment, when I recall the life at the University of Pittsburgh in the past five years, I would like to thank many people who have supported me from different aspects for the completion of this dissertation.

First, I am forever grateful to my advisor, Prof. Albert To for his advice, guidance and full support for the completion of my dissertation. I would like to thank him for giving me the freedom and flexibility on the selection of research topics, which allow me to work on the directions that I am really interested in. Furthermore, Prof. To encouraged me to attend many academic conferences to practice my presentations, helped polish my writings and communication skills, as well as guided me to address tough problems in my research. These are extremely valuable for my career and life.

I would like to express my gratitude to the committee members, Prof. Jeen-Shang Lin, Prof. William S. Slaughter, and Prof. Babaee Hessam for their insightful comments. These valuable suggestions have greatly improved the quality of the dissertation.

I am also grateful to the colleagues in the computational mechanics lab for their year-round collaborations and great foods. I would like to thank those past and current members: Pu Zhang, Qingcheng Yang, Xue Wang, Xuan Liang, Kevin Laux, Hao Deng, Qian Chen, Shawn Hinnebusch, Joseph Brown II, and among others. I want to thank them for their generous sharing of their expertise.

I would like to acknowledge funding support from American Makes, Army SBIR and National Science Foundation (NSF), as well as technical support from companies including United Technology Research Center (UTRC), ANSYS, Aerotech, Materials Science Corporation (MSC), Oberg Industry, etc. Specifically, I would like to thank my collaborators Eric Belski and Steve Ludwick from Aerotech Inc., Matt E. Lynch from UTRC, and Jason Oskin and John Lemon from Oberg Inc. The experiments conducted by them allow me to validate the theory proposed in this dissertation.

I owe my deepest and sincere gratitude to my parents, my brother and my girlfriend. Without their selfless support and encouragement, it would not be possible for me to pursue this journey in academia. Your love and support are the strongest pillars in my life.

1.0 Introduction

The primary goal of this work is to propose a design optimization method that can take advantage of the unique capability of AM techniques for novel structures with desirable performance, circumvent the manufacturing constraints, and address the severe issues of current metal AM techniques (i.e. residual stress induced build failure). The main focus of the design objective lies within the fields of solid mechanics (stiffness, yielding and natural frequency) and heat transfer (heat conduction and forced convection heat transfer). From the engineering application point of view, concurrent optimization for the evolution of functional features is also included and discussed in order to achieve better performance for the optimization design. The motivation, background, and research objective will be provided in this chapter.

1.1 Additive Manufacturing

Additive manufacturing (AM) holds the promise to be the next-generation manufacturing technique due to its unique capability to fabricate geometrically complex geometry, such as graded lattice materials. It has experienced significant growth in the past several decades from the rapid prototyping to industrial parts manufacturing for end-use purpose. As defined by ASTM [1], AM is a process to produce a component from the sliced CAD model by depositing material in a layer-by-layer fashion. This differentiates it from traditional subtractive manufacturing techniques, such as milling, turning, and forging, which build a component by combining several different processes. Up to now, more than ten AM techniques have been developed, e.g. selective laser

melting (SLM), stereolithography (SLA), electron beam melting (EBM), selective laser sintering (SLS), fused deposition modeling (FDM), digital light processing (DLP), binder jetting, direct metal laser sintering (DMLS), continuous liquid interface production (CLIP), etc. These techniques are compatible with a broad range of materials including plastic, such as ABS and PLA, and metals, such as stainless steel, and titanium alloys. Several excellent works cover more details about AM technologies can be found in [2-4]. According to the form of feedstock materials utilized, AM techniques can be categorized into four broad groups [4]: (1) liquid, (2) filament/paste, (3) powder, and (4) solid sheet. Details about the categorization of different AM processes can be found in Table 1.1.

Table 1.1: Categories of AM Process [3]

State of starting material	Process	Material preparation	Layer creation technique	Phase change	Typical materials	Applications
Liquid	SLA	Liquid resin in a vat	Laser scanning/ light projection	Photopoly-merization	UV curable resin, ceramic suspension	Prototypes, casting patterns, soft tooling
	MJM	Liquid polymer in jet	Ink-jet printing	Cooling & photopoly-merization	UV curable acrylic plastic, wax	Prototypes, casting patterns
	RFP	Liquid droplet in nozzle	On-demand droplet deposition	Solidification by freezing	Water	Prototypes, casting patterns
Filament/ Paste	FDM	Filament melted in nozzle	Continuous extrusion and deposition	Solidification by cooling	Thermoplastics, waxes	Prototypes, casting patterns
	Robocasting	Paste in nozzle	Continuous extrusion	–	Ceramic paste	Functional parts
	FEF	Paste in nozzle	Continuous extrusion	Solidification by freezing	Ceramic paste	Functional parts
Powder	SLS	Powder in bed	Laser scanning	Partial melting	Thermoplastics, waxes, metal powder, ceramic powder	Prototypes, casting patterns, metal and ceramic preforms (to be sintered and infiltrated)
	SLM	Powder in bed	Laser scanning	Full melting	Metal	Tooling, functional parts
	EBM	Powder in bed	Electron beam scanning	Full melting	Metal	Tooling, functional parts
	LMD	Powder injection through nozzle	On-demand powder injection and melted by laser	Full melting	Metal	Tooling, metal part repair, functional parts
	3DP	Powder in bed	Drop-on-demand binder printing	–	Polymer, Metal, ceramic, other powders	Prototypes, casting shells, tooling
Solid sheet	LOM	Laser cutting	Feeding and binding of sheets with adhesives	–	Paper, plastic, metal	Prototypes, casting models

The unique feature of AM is to manufacture a component from CAD model in a layer-by-layer fashion. Figure 1.1 schematically illustrates the layer-wise manufacturing process for metal powder-bed AM. A customized computer-aided design (CAD) model is being built by rastering of a laser or electron beam selectively over the powder bed. The powder in one layer is locally melted, when the laser/electron beam moves, the melted powder that is left behind cools down and a solid object is created according to the contour of the sliced CAD model. Once a layer is completed, the base plate used to hold the printed part is lowered and a new layer of powder is uniformly deposited by a scraper. Then the new layer is scanned and fused on the previous layer using the same way

until the entire part is built. The powder-bed metal AM is an effective technique of producing metal component, because it only melts material where needed, and thus unprocessed powder can be recycled for next build. In contrast to subtractive manufacturing, such as milling, turning, forging and computer numerical controlled (CNC) machines, powder-bed metal AM can build a component in single process while the others need dozens of subtractive processes. For complex assemblies, AM can build them in a unified design within a single process, which can considerably improve the performance of the component and at the same time reduce the entire cost and development period, which is able to accelerate the application of new design to the market.

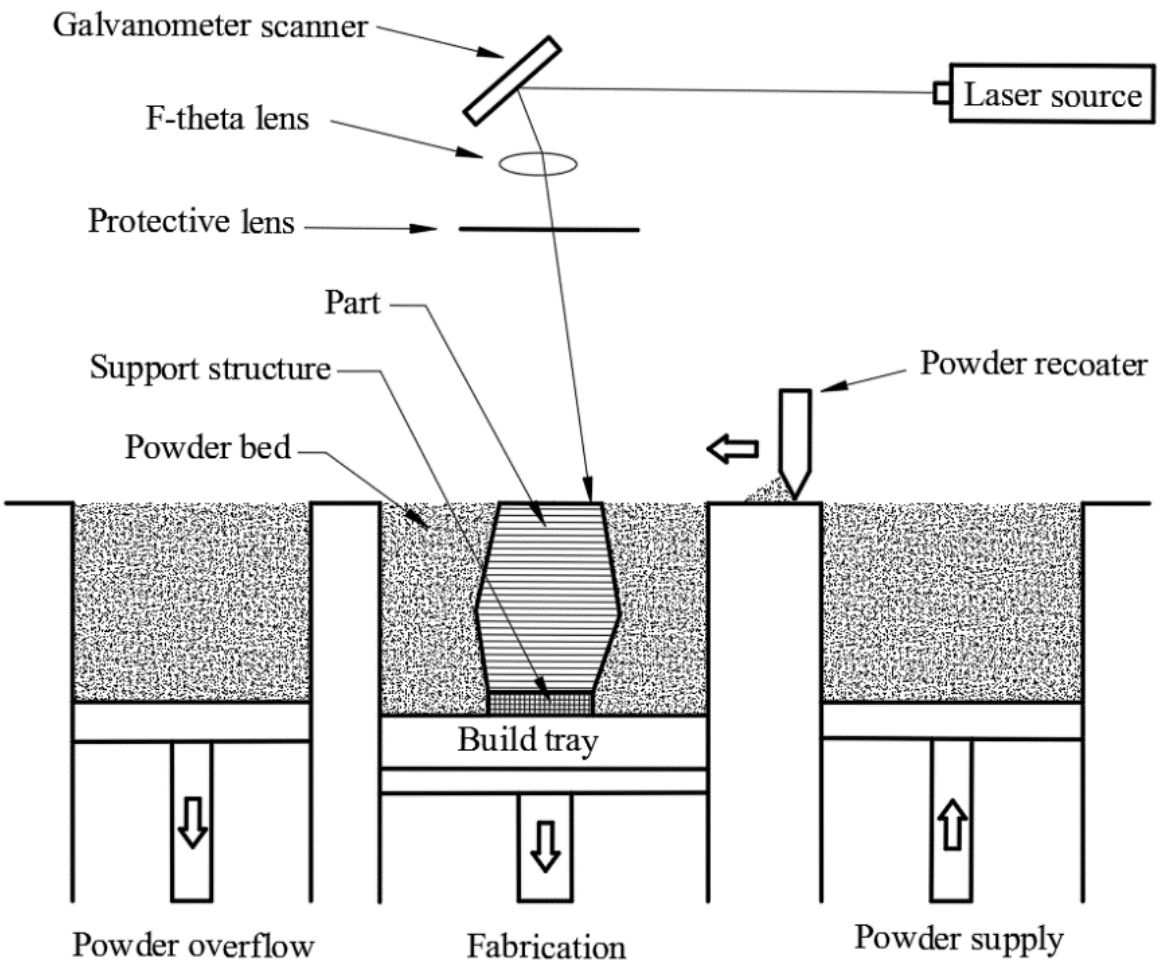

Figure 1.1: Powder-bed Metal Additive Manufacturing [5]

The first commercialized AM machine produced 3D Systems was a stereolithography (SL) system in 1987 [6]. It is a process to solidify the light-sensitive liquid polymer through the ultraviolet (UV) laser. The primary applications of AM are mainly for visual aids, presentation models, and rapid prototyping. Using AM processes, scientists, medical doctors, students, and market researchers can rapidly build and analyze their models in theoretical studies. Hence the requirements for the built parts primarily concern about the geometry from the conceptual point of view. End-use applications are limited due to relatively low quality, dimensional accuracy, and

surface roughness. As reported by Wohlers in 2011 [6], these applications occupy more than 40% of the market of AM. However, as the development of new manufacturing process, i.e. powder-bed fusion, material extrusion, and binder jetting [7], and also the reducing cost of the controller, material price and the open source CAD software, the manufacturing quality has greatly increased and at the same time the manufacturing cost was significantly reduced. This allows AM to be more general use for both consumer market and industry manufacturing. In consumer market, a number of startup companies are creating and available for common applications [6], which results in a significant reduction of the price of the printer and materials. This greatly promotes the wide adoption of AM and development of general platforms, such as Grab CAD and Maker Movement. Some companies i.e. supply chain from Staples, Shapeways and Sculpteo, are beginning to provide printing and shipping services to customers. They allow customers to design and build products by themselves. This further reflects the development of the AM technologies.

For industrial manufacturing, AM techniques not only accelerate the design lifecycle of product development through rapid prototyping, but also fabricate end-use components for practical applications. For example, the fuel nozzle in Figure 1.2 produced by powder-bed metal AM has passed the U.S. Federal Aviation Administration (FAA) and became the first 3D-printed part fly inside the commercial jet engines. The fuel nozzle was originally made up of 20 disparate parts and painstakingly brazed and weld together. However, using AM, it can be built in a single process and a single design, which can reduce 25% weight and be a remarkable five times stronger than conventional manufacturing process. As a critical part in the next generation LEAP engine, the design can help the company save more than $3 million per aircraft per year. This significant enhancement proves that AM has greatly influence the development of manufacturing industry, especially the aerospace sector.

Figure 1.2: Fuel Nozzle Manufactured EOS DMLS from Genetic Electronic Inc.

Another important field of research for AM is the biomedical industry. The main drive for the biomedical field is to fabricate parts that typically cannot be economically realized using conventional manufacturing techniques. There are four high potential application areas for AM in biomedical field, which includ orthopedic implants, dental implants, tissue and organ implants, and prosthetics. According to some estimates from the industry, more than 80% of global implants will be built using AM in two decades [6]. For biomedical, AM solves the challenges that no human body is exactly the same as others, customized implants need to fit perfectly to each patient, in order to reduce patients' pain and improve their life quality [8]. In general, AM can build the implant locally alongside the hospital, which can also help to accelerate the inventory cycle time and reduce the delivering costs [9]. Singare et al [10] have proved that AM can be efficiently used for implant fabrication with high-level accuracy. Winder et al [11] proposed a new method to

combine CT scan with AM to build patients' skull in titanium plates. Excellent works covering the details of AM for biomedical engineering can be found in Refs. [9, 12, 13]. All these prominent applications have demonstrated that AM as a promising manufacturing technique has begun to change the manufacturing industry.

1.1.1 Issues of Current Metal AM

Although metal AM techniques have been gradually accepted to fabricate end-use components, one of the key issues preventing it from broad adoption is residual stress and distortion introduced in the powder melting and solidification processes [2-4]. Residual stress leads to undesirable cracks, delamination, and warpage during AM, which can stop the powder spreading process and result in failure of builds. This leads to a waste of material, energy, and time, but also requires extra efforts for designers to change the design. Figure 1.3(a) illustrates such issue, in which the cracked and deformed component stops the recoater blade and lead to a failed build. Another challenge is the large deformation generated by residual stress after the component is removed from the substrate. The deformation results in limited load resistance, dimensional inaccuracy, and reduction of fatigue performance of the component to more than 10 times compared with conventional bulk material [5, 6]. As illustrated in Figure 1.3(b), an implant was successfully printed out in Ti6Al4V using laser powder-bed AM, but once it was cut from the build tray, the inherent residual stresses lead to undesirable deformation.

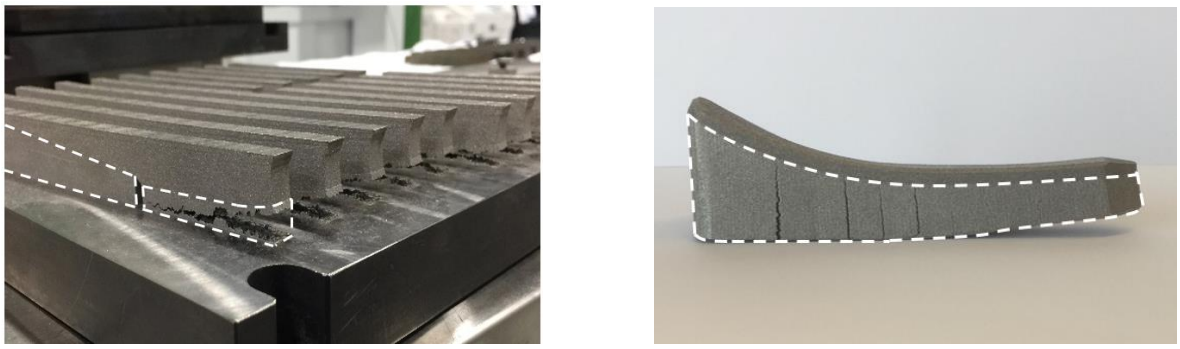

(a) (b)

Figure 1.3: Residual Stress and Large Deformation of Metal AM: (a) Failed Build Due to Residual Stress During Manufacturing; (b) Implant is Deformed after Removal from the Build Chamber.

On the other hand, support structures (e.g. the structures highlighted by white dash line in Figure 1.3) are required in metal AM to support overhangs of the component to ensure manufacturability. These support structures are fabricated simultaneously with the component to anchor the parts and dissipate heat to the build tray in order to prevent distortion/delamination caused by residual stress. There is a number of published works in the past in the area of support structure design for AM techniques. Allen et al [7] proposed the best directional formation for an object to obtain minimal support structure. Frank et al [8] developed an expert system tool to interact with users to select the best build orientation for better performance of the built component. Alexander et al [9] developed a method to optimize part orientation to minimize build cost. Xu et al [10] discussed the section of build orientation for four types of AM processes and proposed an orientation optimization with multiple criteria, such as building inaccuracy, manufacturing time and building cost. Lan et al [11] developed an algorithm for stereolithography apparatus to find a desirable fabrication orientation for a given design based on considerations of surface quality,

build time, and complexity of support structures. Masood et al [12] presented a generic mathematical algorithm to find the best orientation to achieve minimum volumetric error. For fused deposition process, Thrimurthulu et al. [13] applied genetic algorithm to determine an optimum part deposition orientation to enhance part surface finish and reduce build time. Recently, Mumtaz et al [14] developed a method for metal powder-bed AM processes to eliminate the need for supports. Strano et al [15] presented an approach to optimize part-built orientation and support cellular structure. Hussein et al [16] experimentally investigated influences of low-volume fraction lattice structures on the design of support structure for powder-bed direct metal laser sintering (DMLS) machine. Galigonano et al [17] applied Taguchi method to optimize support structure and conducted experiment to investigate the manufacturability of overhanging structures for SLM process. Most recently, Vaidya et al [18] developed an approach for minimizing support structures with space cellular infill combined with Dijkstra's shortest path method to generate optimized support structure. Paul et al [19] proposed a voxel-based framework to generate support structure and developed a multi-objective method to minimize support volume, the cylindricity and flatness errors simultaneously. Following the work of Paul [19], Das et al [20, 21] proposed a method to minimize part errors in AM through the selection of build orientation for optimal support structures.

However, most of these previous research efforts focused on geometric perspectives, and few works have been proposed to take residual stress into consideration for metal AM to ensure manufacturability. For simple geometry, the stress problem can be addressed by manually changing the build orientation by trail-and-error. For component with complex geometry, this empirical approach may not work, and more effective methodology needs to be developed to minimize residual stress. Nevertheless, there are several barriers preventing development of such

optimization method. First, due to the complexity of laser manufacturing process, it is time-consuming to obtain residual stress and distortion distribution through detailed process simulation. In general, it takes tens of hours or days to complete process simulation of a simple component in general. This makes it impractical to find optimal orientation considering hundreds of iterations required by the optimization methods. Second, mesh generation for complex geometry and its support structure is computationally expensive and often error-prone when pure Cartesian grids are desired, or when the bulk component is rotated in the printing space to seek optimal orientation and the layerwise mesh along the building direction is required. Third, problems arise when the mesh generation and finite element analysis (FEA) is considered for support structure. The typically used support structure consists of straight rectangular solid walls or cellular structure [7, 15, 16], which is self-support, lightweight and loose enough to be easily removed. However, from the simulation point of view, it is difficult to generate efficient mesh for these tiny structures, and thus leads to error estimation for residual stress in support structure where most cracks and delamination are observed. Due to these barriers, an efficient approach to ensure manufacturability of AM components through optimization of build orientation is difficult to achieve together with other objectives, such as surface finish [22], dimensional accuracy [7, 19], volume of support structure, [18-20] etc.

Thus, one key goal of this work is to develop a robust computational framework to address the aforementioned problems by systematically optimizing the orientation of a component and design of support structure to reduce the maximum residual stress, and at the same time minimize volume of support structure to reduce manufacturing cost.

1.2 Topology Optimization

Currently, the design methods for AM techniques are mainly developed for traditional manufacturing processes and thus focus on easing the complexity of the manufacturing procedure. To take advantage of the unique capability of AM, new design for manufacturing (DFM) methods need to be developed [14]. Topology optimization (TO) as an efficient approach has been extensively connected to AM due to its excellent performance to obtain exceptional properties under significant material reduction.

The basic concept of topology optimization was introduced by Bendsøe and Kikuchi in 1988[15], and further developed into three branches: Density-based TO, such as Solid Isotropic Material with Penalization (SIMP) [16, 17], Evolutionary Structural Optimization (ESO) [18] and Level set method (LSM) [19, 20]. To promote the development of topology optimization, a considerable number of the theoretical and computational works have been done on the issues like: appearance of gray-scale [21-23], checkerboard patterns [24, 25], problems of mesh independences[26, 27] and the application for geometrical non-linear problems [28]. These theoretical studies also further exploit the potential of topology optimization for a variety of fields, such as frequency [29], heat transfer [30], fluid flow [31], etc. In this work, we will mainly focus on density-based TO method, its extension for concurrent optimization, as well as the application of TO method to address the critical issues of current metal AM techniques. Two fields will be specifically explored: One is the mechanics including minimum compliance, constraint stress and natural frequency, the other one is heat transfer including heat conduction. Following is a brief review of these problems.

1.2.1 Minimum Compliance

Originally, the objective of TO method is to find the material distribution that minimizes the compliance of the structure subject to a volume fraction constraint. To achieve this goal, the objective function is formulated by means of the relative density defined for each element. The optimal distribution can be obtained through the iteratively adjustment of density variable in each element based on the sensitivity analysis. Following the work of Bendsøe and Kikuchi [15], Bendsøe [17] and others further proposed the Solid Isotropic Material with Penalization (SIMP) method, in which a power law was employed to simplify the homogenization in the optimization. The aim of power law in SIMP method is to provide a continuous material interpolation and improve the convergence of TO to 0-1 design. However, this leads to an issue named checkboard pattern when penalizing the design to black-and-white. To address this issue, a filter scheme was proposed to modify the design variable [28] or sensitivity [32] through the weighted average of the value of neighbors. However, the introduction of the filter leads to another problem known as grey transition regions between the lower density and higher density. This problem can be overcome by the so-called projection schemes proposed by Guest et al [33], Sigmund [23] and Xu et al [34], respectively. Note that the simple projection scheme cannot guarantee the convergence of the TO method. It is used to handle the grey area obtained from the filter scheme and ensure the discrete solutions [35]. All these mathematical techniques promote the development of density-based TO and lay the foundation for various problems.

1.2.2 Stress Constraint

Stress constrained optimization as one of the classical problems has been extensively studied in topology optimization because more challenges are encountered. First of all, singularity phenomenon was observed when the elemental density tends to zero in the optimization [36, 37]. This leads to a degenerate regions in the design domain [38]. To address this issue, several relaxation techniques are proposed to eliminate the degenerate region and remedy the singularity problem, e.g. the ϵ-relaxation approach by Cheng and Guo [39]. Duysinx et al [38] and Bruggi et al [40] further develop this approach for continuum structure. Second, the local nature of the stress constraints makes it rather computationally expensive when the constraints need to be satisfied at multiple points in each element. A solution to this difficulties is to replace the local stress constraints with a single continuous approximation, using aggregating function like p-norm or Kreisselmeier-Steinhauser (KS) function [38, 41, 42]. Another approach is to group the elements into multiple clusters and apply stress constraints for each cluster [43-45]. Third, since isotropic material properties are assumed, the yield criteria can work well when the density is equal to 0 or 1. However, if intermediate density is considered during the optimization, the yield criteria may fail to represent real stress distribution. A number of different techniques have been proposed in order to solve this issue. Similar to the material interpolation for minimum compliance problem, Duysinx [38, 46] proposed a power law for the relationship between stress and the stress limit for the whole density range. Le et al [42] further revised the stress constraints and proposed a more general approach. This ensures the continuity of the stress criterion and thus the sensitivity of the stress constraints can be smoothly calculated.

1.2.3 Eigenfrequency

Regarding vibration problem, Diaz and Kikuchi [47] first introduced TO for the maximization of the single eigenfrequency of plane disks. Ma et al [48, 49] proposed an objective function corresponding to multi-eigenfrequency optimization based on homogenization. Pedersen [50] pointed out the localized mode problem of SIMP method for vibration optimization and proposed a discontinuous material interpolation to solve the problem. Subsequently, Du et al [51, 52], Niu [53], Huang [54], Zuo [55], and Xia [56] and their collaborators further proposed the framework of vibration structure optimization from single to multiple eigenfrequences and also the multiscale design using SIMP, ESO and LSM methods, respectively. However, most of these former research works focused on methodology development rather than design issues associated with manufacturing and practical applications. For the design of TO, it is difficult or impossible to manufacture the organic structure by traditional technologies. Even with current AM techniques, extra efforts, such as support structure and post-machining [57-59], are needed to ensure the manufacturability of the design. But these extra works may change the shape of original design or destroy the component when removing the support structure. For vibration design, the problem is even worse since even a little variation from the original design may lead to a remarkable change of the eigenfrequency. To address these issues, a novel material interpolation for lattice material will be proposed and experimental validation will be carried out to examine the accuracy of the optimization design.

1.2.4 Heat Transfer

With regards to heat transfer optimization, TO method have been extensively developed for optimizing the thermal structure by considering conductive [60-67], convective [30, 68-71] and conjugate heat transfers [71-74]. Li et al [75] extended the algorithm of ESO to optimization problem subjected to steady heat conduction. Torquato et al [76] applied TO for the maximization of the simultaneous transport of heat and electricity in three-dimensional. Seung-Hyun Ha [67] and Seonho Cho proposed a topological shape optimization method for heat conduction using level set method. Gersborg-Hansen [61] and Bendose and Sigmund proposed SIMP method for the minimization of thermal resistance. Bruns [68] developed a framework using TO for the nonlinear steady-state heat transfer with convection-dominated problem. Iga et al [30] formulated a surrogate model to represent the heat convection in the optimization method. Matsumori et al [77] extended density-based method for the heat exchanger design considering the coupling of fluid and thermal interactions. Most recently, Yaji et al [72] further applied level set method for the optimization of coupled thermal-fluid problem based on two- and three-dimensional steady-state Navier-Stokes and energy equations. All these methods mainly focus on method development rather than practical applications, and thus most of the numerical examples are limited to two-dimensional problems.

1.2.5 Issues of Topology Optimization for AM

However, there are still some difficulties arising when directly employing topology optimization to design structures for AM techniques. The pillow bracket illustrated in Figure 1.4 is used as an example, where standard topology optimization is performed to minimize the

compliance of the design while constraining the overall volume fraction to a target value. In the mechanical problem, the pillow bracket is subjected to loading acting downward on the hole on top of the bracket while the vertical displacement is fixed on the four bottom holes. Hence essentially, the minimum compliance problem is to maximize the bending stiffness of the pillow bracket given a final overall volume fraction. Figure 1.4 (b) illustrates the result obtained by performing standard topology optimization of the pillow bracket by using the Albany package, a multi-physics analysis package based on the Trilinos framework developed at Sandia National Lab [78, 79]. First, notice that the optimized design changes the shape of the original design. Since AM produces relatively rough surfaces and some deviations from the computer model, the original shape design produced by standard topology optimization makes it very difficult to post-machine the AM component [80, 81]. Second, the optimized structure would likely generate a significant number of overhang structures as shown in Figure 1.4(c). These overhang structures generally need support structures added beneath them in order to prevent them from collapsing during an AM build. Although support structures are useful, it is sometimes difficult to remove them without destroying the component. Third, standard topology optimization algorithm solves the discrete 0/1 (i.e. void/solid) design problem by converting the design variable (i.e. relative density) that varies continuously from 0 to 1. As such, the relative densities obtained from topology optimization may contain a large number of intermediate relative densities (i.e. away from 0 and 1) distributed over the design space. For the pillow bracket design problem, the intermediate densities obtained can be observed as the light blue and yellow regions in Figure 1.4(b). In practice, these intermediate densities are generally converted to 0 or 1 in some ad-hoc ways [16, 82] in order to produce physically meaningful designs.

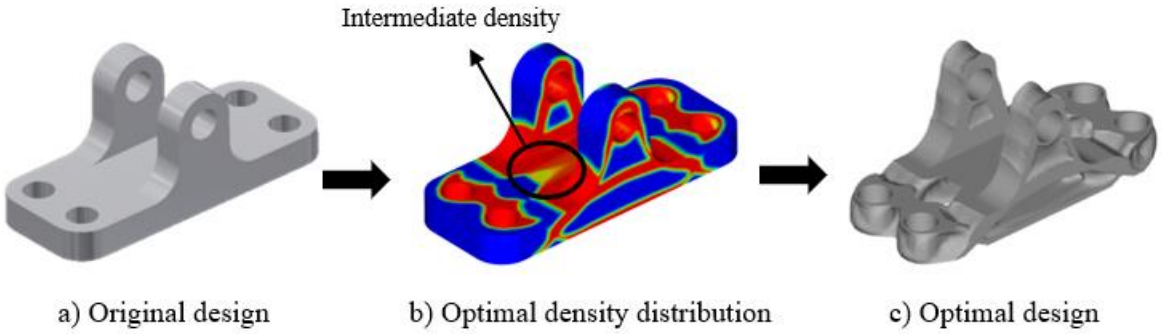

Figure 1.4: Standard Topology Optimization Design for a Pillow Bracket

1.3 Research Objective

Another goal of this research is to develop such a design methodology that can take advantage of the unique capability of AM technologies in the framework of TO method and also take the manufacturing constraints into account. Instead of merely focusing on the geometric perspective, the method in this work depends on the understanding of the AM-related constraints, properties of material manufactured by AM, and the disadvantages introduced in the powder-bed metal AM. One major limitation of AM is that support structure is required to be added beneath the overhangs to ensure the success of manufacturing. Support structure needs to be removed in a post-treatment process. For organic structure generated by TO method, it maybe even impossible to remove the support structure since the machining tool cannot reach tiny surface. Especially for closed structure from TO, support material and powder for metal AM even cannot be pulled out.

To overcome these drawbacks of the existing TO method for AM, a homogenization-based TO method is proposed in this work to integrate open-cell lattice structure into the framework of TO. The intrinsic theory of the design methodology is motivated by microstructure and

constituents of the natural material. Figure 1.5 gives a cross-section of bamboo. It can be seen that bamboo is consisted of microstructure in the same pattern at microscale while variable density at macroscale. This inspires the research in this work to use spatially varying lattice structure to realize the results of TO.

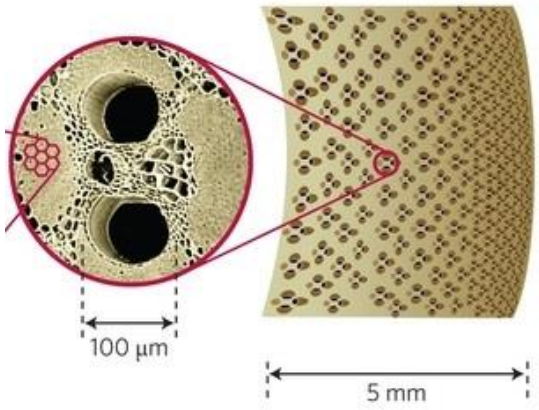

Figure 1.5: Microstructure and Constitutes of Bamboo[83]

Figure 1.6 provides the flowchart of the proposed methodology in this work. As shown in the figure, a given component can be efficiently designed using the proposed LSTO method in four steps: Homogenization, optimization, reconstruction and validation. For lattice structure, the general scheme is to use full-scale simulation with explicit modeling of microstructural features to compute properties including elastic and plastic constants and thermal conductivity, etc. However, the detailed simulation would be time-consuming and much computational expensive due to complex geometry of microstructures. Therefore, an efficient method needs to be employed to calculate the effective properties of lattice materials through the analysis of representative

elementary volume (RVE). As such, the analysis of lattice material can be replaced by the analysis of the material with equivalent properties obtained from RVE model. This can significantly reduce the computational cost and is suitable for LSTO method since the analysis needs to be carried out iteratively. In this proposal, the asymptotic homogenization (AH) method [84-86] is employed to conduct the analysis on the RVE to compute the effective properties. We mainly focus on the mechanical and thermal properties of lattice materials in this work.

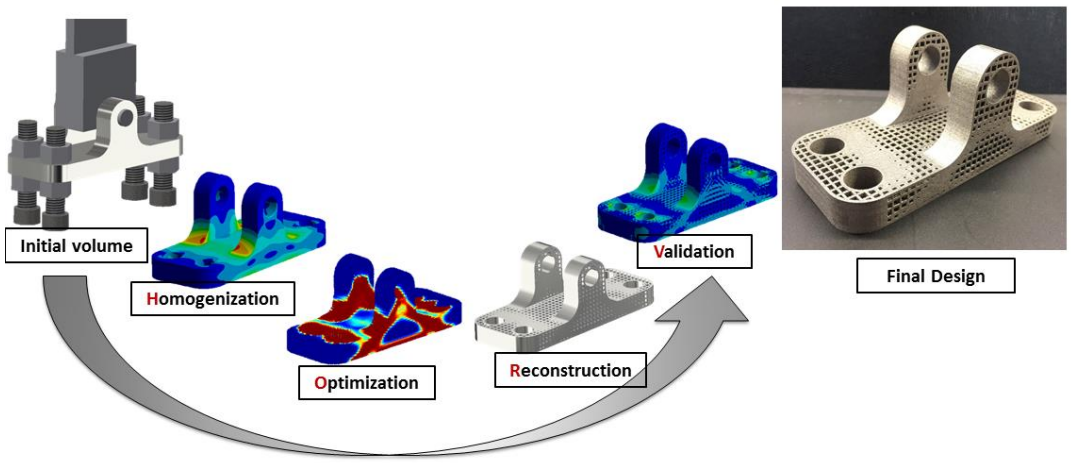

Figure 1.6: Flowchart of the LSTO Method

Once the effective properties of lattice structure are obtained, the model is implemented into the framework density based TO method to replace the power law. Then the sensitivity analysis based on the material model is carried out and the optimization is conducted to obtain the optimal density profile. In the present dissertation, we have proved the proposed framework of LSTO method through the problems including minimum compliance, constrained stress and natural frequency. Both full scale simulations and experiments on the variable density lattice

structure have demonstrated the accuracy and efficiency of the proposed methodology. In practice, we have applied the LSTO method to design and build practical components for companies.

LSTO framework has been proved to be accuracy and efficiency for both mechanical and thermal conduction design. In practice, lattice structure as a type of metal foam has great potential for heat transfer design. Same as the mechanical problem, the framework starts from homogenization of the properties of lattice structure.

On the other hand, there exist some features, such as the bolt holes and cooling channels, which cannot be optimized and reconstructed with lattice structure. But the geometric parameters like the location and angle plays an important role in optimization processes. Especially when the boundary conditions are subjected to these features, the geometric parameters would considerably influence the density profile of the optimal design. Thus, a concurrent scheme coupled with the LSTO method is proposed in the present dissertation in order to simultaneously optimize the lattice infill and the geometric parameters of solid features. In Section 4.0, the concurrent LSTO method has been extensively studied on heat conduction problem. A good agreement is observed, which further valid the accuracy and efficiency of homogenization and the optimization. Specifically, the concept of immersed boundary (IB) method is introduced into the optimization to represent the conformal boundary conditions. The IB strategy is tested on different boundary conditions involving heat flux, heat generation and heat convection. A full-scale simulation on the final design is compared with homogenized results. Comparison shows great agreement for maximum temperature. In particular, we extend the design dependent concurrent LSTO method to cooling channels design, which show significant reduction for the maximum temperature of the structure.

The research that has been done in this dissertation mainly focuses on mechanical and heat conduction designs. We would further apply the framework of LSTO method for multi-physics

problem such as thermomechanical design to mitigate the large deformation and warpage generated in the powder-bed metal AM. As mentioned in Section 1.1.1 , when the residual stress introduced by melting and solidification process in metal AM is large enough, the built components would deform and stop the recoater blade. This is a key factor that leads to build failure of metal AM. To address this problem, we will introduce the LSTO method for support structure design. Here the inherent strain method [87, 88] is used to efficiently perform thermomechanical analysis of the process for powder-bed metal AM at part scale, while LSTO method is employed to optimize the support structure design. The primary goal is to build a framework to efficiently design support structure for powder-bed metal AM to reduce the thermal deformation and increase the successful ratio of the building process.

1.3.1 Outline

The organization of this dissertation is constructed as follows. The homogenization of the lattice materials is introduced in Chapter 2.0 for different problems including effective elastic properties, plastic properties, heat conductivity and forced convection heat transfer coefficient. The mathematical formulation and numerical implementation for the homogenization method is detailed in this chapter. For validation purpose, experiments are conducted on the lattice materials manufactured by both plastic AM processes and powder-bed metal AM processes. The experimental measurement is compared with the prediction from both the homogenized model and full-scale simulation.

Chapter 3.0 provides the proposed LSTO method for various problems ranging from structural design (minimum compliance problem and constrained stress problem), and dynamical design for maximization of natural frequency. Along with introduction of the underlying theory,

each of the design optimization methods is employed for practical applications. The optimal designs of real components are manufactured by advanced AM techniques, and experiments are carried out to compare with prediction from both homogenization and full-scale simulation.

In Chapter 4.0, the developed LSTO method is extended to combined optimization of movable feature evolution with the optimization functionally graded lattice structure infill. Two topics are covered containing in this chapter: 1) Concurrent optimization of the lattice structure infill with design-independent movable features; 2) Coupling design-dependent movable features with LSTO method. Several numerical examples for both practical applications and conceptual validations are studied to illustrate the efficiency of the proposed methodology.

In Chapter 5.0, the methods used to systematically address the residual stress induced build failure are covered. Specifically, a voxel-based methodology for efficiently identifying overhang features and generating Cartesian mesh is proposed. There are two methods developed to solve the build failure problem. One is the build orientation optimization, in which the influence of the microstructure of the lattice structure support on the optimal orientation optimization is discussed on part-scale problem. The other is the support structure optimization aiming to minimize overall weight of the support structure, and at the same time to constrain the maximum stress below the allowable stress (e.g. yield strength). Experiments are conducted on the part-scale problem to explore performance of the proposed methodology.

Chapter 6.0 concludes with the main contributions of my doctoral work dissertation for the design of functionally graded lattice structure for current AM techniques. The potential future works based on the achievement in this dissertation are also provided in this chapter

2.0 Homogenization of Effective Properties for Lattice Structure

In this chapter, the theory of asymptotic homogenization (AH) method will be introduced, including both the mathematical formulation and the numerical implementation. AH method is employed in this work to calculate the effective properties of lattice material through the analysis of RVE for a lattice unit. This chapter will mainly focus on the elasticity, yield strength, thermal conductivity, and forced convection heat transfer of lattice structure. Both full-scale simulations and experiments will be conducted to examine the accuracy of proposed homogenized model.

2.1 Theory of Homogenization

Materials constructed of a lattice structure can be considered as a type of composite-like material, and their mechanical properties can be calculated by analyzing the representative volume element (RVE) through AH approach. The fundamentals of the AH method can be found in the works of Benssousan [89, 90], Willis [91], Bakhvalov and Panasenko [92]. The underlying principle of the AH for lattice material is schematically presented in Figure 2.1. Consider a domain Ω^{γ} infilled with lattice structure, with a traction of $\boldsymbol{t}$ imposed onto the traction boundary Γ_t, a displacement of d added to the boundary Γ_d, and a body force of f uniformly distributed in the entire domain. By means of AH, the lattice unit is taken as the RVE to compute the effective properties, and a surrogate solid structure with equivalent properties is used to represent the original domain by a homogenized body Ω with prescribed external and traction boundaries [93].

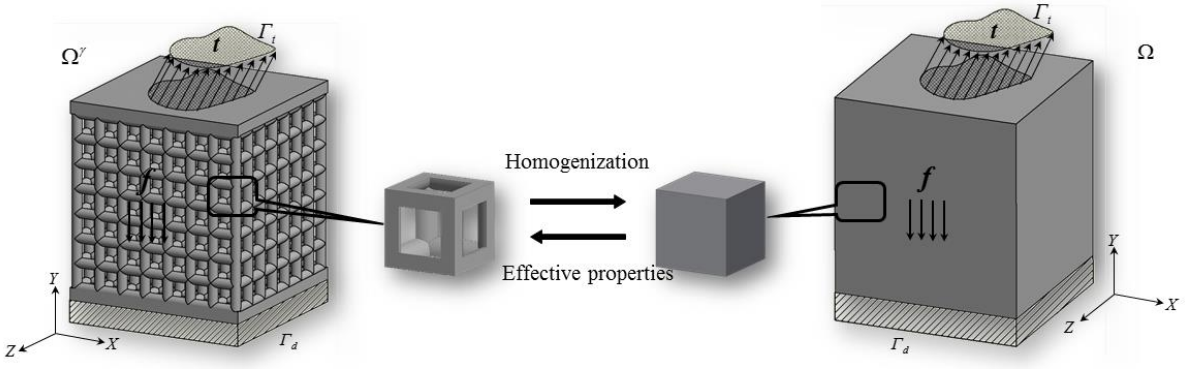

Figure 2.1: Homogenization of Lattice Materials

The AH method is based on perturbation theory and used to study the partial differential equations with rapidly oscillating coefficients [94]. It relies on the assumption that any field quantities, such as displacement, stress and strain, are determined by both the smoothed quantities at macroscale x, and periodic oscillation at microscale, y. The dimensions of these two scales are related by a scale factor β as $y = x/\beta$. Based on AH method, the displacement can be expressed using a two-scale asymptotic expansion as:

$$u^{\beta}(x,y) = u_0(x,y) + \beta u_1(x,y) + \beta^2 u_2(x,y) + \cdots \tag{2.1}$$

where u^{β} is the exact value of the displacement field, u_0 represents the smoothed global displacement while $u_i(i = 1, \ldots n)$ denote the perturbation due to the microscopic heterogeneity.

Substituting the asymptotic expansion in Eq. (2.1) into the strain-displacement equation and performing the standard mechanical analysis with periodic boundary conditions on a unit cell, one can obtain the effective elastic modulus of lattice structure as:

$$\bar{C}_{ijkl} = \frac{1}{|V_{RVE}|}\int_{V_{RVE}} \left(C_{ijkl} - C_{ijpq}\frac{\partial \chi_p^{kl}}{\partial y_q} \right) dV_{RVE} \tag{2.2}$$

Where V_{RVE} is the volume of the smallest representative lattice unit that can be repeated in the lattice structure, $\bar{C}_{ijkl}$ denotes the effective elasticity tensor at macroscopic, and C_{ijkl} represents the elasticity tensor of the constituents at microscale. χ_p^{kl} ($p,k,l \in [1,2,3]$ for 3D and [1,2] for 2D) is the characteristic displacement used to bridge the perturbed displacement in Eq. (2.1) and the macroscopic strain. It can be obtained by solving the following elasticity equation in a unit cell subjected to unit strain and periodic boundary conditions:

$$\int_{V_{RVE}} C_{ijpq} \frac{\partial \chi_p^{kl}}{\partial y_q} \frac{\partial v_i}{\partial y_j} dV_{RVE} = \int_{V_{RVE}} C_{ijkl} \frac{\partial v_i}{\partial y_j} dV_{RVE} \tag{2.3}$$

where v_i is the virtual displacement. Solving the above equation, the stress field at the macroscale can be formulated as:

$$\bar{\sigma}_{ij} = \left(C_{ijkl} - C_{ijpq} \frac{\partial \chi_p^{kl}}{\partial y_q} \right) \frac{\partial u_0}{\partial x_l} \tag{2.4}$$

For practical implementation, finite element analysis (FEA) is used to numerically perform the homogenization for lattice unit, in which the elastic tensor and the averaging stress can be computed using:

$$\bar{C}_{ijkl} = \frac{1}{|V_{RVE}|} \int_{V_{RVE}} C_{ijmn} M_{mnkl} dV_{RVE} \tag{2.5}$$

and

$$\bar{\sigma}_{ij} = \frac{1}{|V_{RVE}|} \int_{V_{RVE}} C_{ijmn} M_{mnkl} dV_{RVE}\, \bar{\varepsilon}_{kl} \tag{2.6}$$

respectively, where $\bar{\varepsilon}_{kl}$ is the global strain at macroscale and M_{mnkl} is the local structural tensor and can be written as:

$$M_{ijkl} = \frac{1}{2} \left(\delta_{ik} \delta_{jl} + \delta_{il} \delta_{jk} \right) - \varepsilon_{ij}^{*kl} \tag{2.7}$$

where $\delta_{ij}$is the Kronecker delta, ε_{ij}^{*kl}denotes the periodicity of the strain field. Further details of calculating ε_{ij}^{*kl} can be found in [94].

2.2 Numerical Homogenization for Lattice Structure

To calculate the effective properties of lattice structures, finite element analysis (FEA) is used to discretize and solve the unit cell problem in Eq. (2.3), and calculate the relationship in Eq. (2.5) and (2.6). In this work, ANSYS v17.2 Mechanical APDL is used to build, mesh and solve the model. After finite element discretization, Eq. (2.3) can be expressed as

$$\boldsymbol{K}\boldsymbol{\chi}^{kl} = \boldsymbol{f}^{kl} \tag{2.8}$$

where $\boldsymbol{\chi}^{kl}$ is the microscopic displacement, $\boldsymbol{f}^{kl}$ represents load vector, and $\boldsymbol{K}$ is the global stiffness matrix. Based on Eq. (2.3), $\boldsymbol{K}$ and $\boldsymbol{f}^{kl}$ are defined as

$$\boldsymbol{K} = \sum_{e=1}^{\boldsymbol{N}} \int_{V_{RVE}} \boldsymbol{B}_e^T \boldsymbol{C}_e \boldsymbol{B}_e dV_{RVE} \tag{2.9}$$

and

$$\boldsymbol{f}^{kl} = \sum_{e=1}^{\boldsymbol{N}} \int_{V_{RVE}} \boldsymbol{B}_e^T \boldsymbol{C}_e \bar{\boldsymbol{\varepsilon}}_{kl} dV_{RVE} \tag{2.10}$$

where $\boldsymbol{B}_e$ represents the strain-displacement matrix, $\boldsymbol{C}_e$ is the constitutive model, $\bar{\boldsymbol{\varepsilon}}_{kl}$is the six unit strains and are chosen to be:

$$\begin{aligned} &\bar{\boldsymbol{\varepsilon}}_{11} = (1,0,0,0,0,0)^T, \bar{\boldsymbol{\varepsilon}}_{22} = (0,1,0,0,0,0)^T, \bar{\boldsymbol{\varepsilon}}_{33} = (0,0,1,0,0,0)^T, \\ &\bar{\boldsymbol{\varepsilon}}_{12} = (0,0,0,1,0,0)^T, \bar{\boldsymbol{\varepsilon}}_{23} = (0,0,0,0,1,0)^T, \bar{\boldsymbol{\varepsilon}}_{31} = (0,0,0,0,0,1)^T \end{aligned} \tag{2.11}$$

Substituting the unit strains given in Eq. (2.11) into Eq. (2.10) and then solving Eq. (2.8), one can obtain the fluctuating strain $\boldsymbol{\varepsilon}^*$, calculate the local structural tensor $\boldsymbol{M}$ in Eq. (2.7), and

compute effective properties of lattice structure using Eq. (2.5). More details about the numerical homogenization is covered in several works of [93, 95, 96].

To calculate the elastic constants of the cubic lattice structure, uniaxial tension and pure shear are applied to the normal and shear direction, respectively. As shown in Figure 2.2, the hexagonal element is used to mesh the cubic lattice unit while periodic boundary conditions for uniaxial tension and pure shear are applied to one direction of the cubic lattice unit.

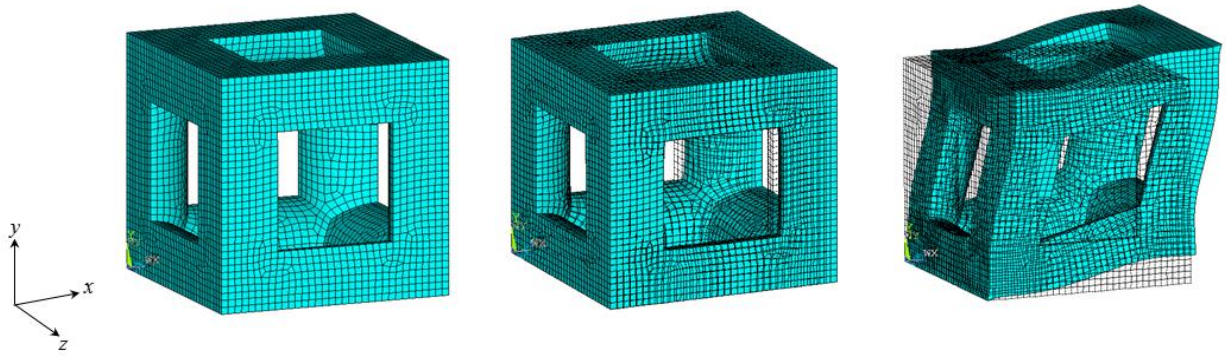

a) Mesh model b) Uniaxial tension along *x* direction c) Pure shear

Figure 2.2: Periodic Boundary Conditions of the Cubic Lattice Unit

2.3 Elasticity

2.3.1 Lattice Structure Printed by SLA

A cellular structure is made up of an interconnected network of solid struts or plates which form the edges and faces of the cells [97, 98]. Compared with a solid part of the same volume, the mechanical properties of cellular solids depend directly on the shape and structure of cells. Except for the detailed cell structure and constituent material, the most important structural characteristic of a cellular solid is its relative density, $\rho_r = \rho_c/\rho^*$ (the ratio of the density of the cellular structure ρ_c and density of the solid material ρ^*). According to the Gibson-Ashby model[97, 98], the elastic modulus E, shear modulus G, and yield strength σ_{pl} of cellular structures are functions of the relative density called "scaling laws". Take the elastic modulus *E* as an example, the scaling law follows the form $\frac{E_c}{E^*} = f(\rho_r)$, where $E^*$is the elastic modulus of the constituent material and $f(\rho_r)$ is either a polynomial or power function of the relative density ρ_r.

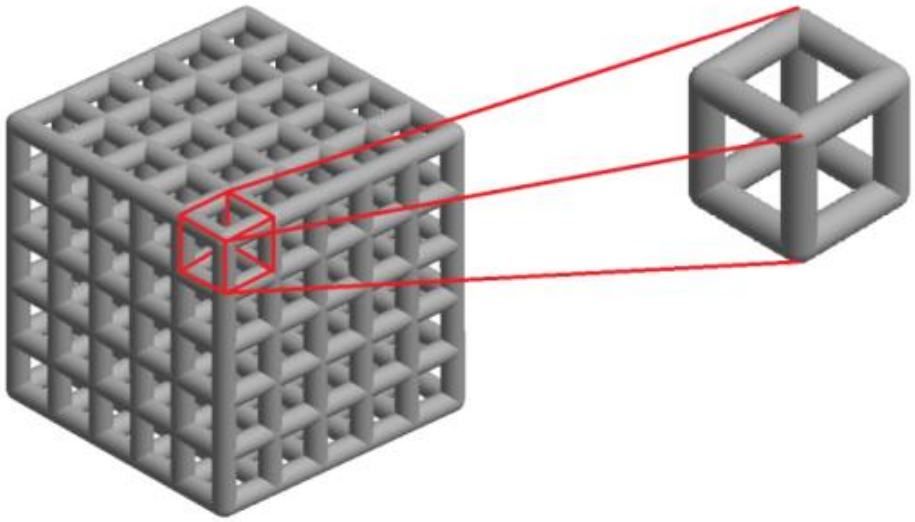

Figure 2.3: A Cubic Cellular Structure and Its Unit Cell

In this work, the cubic cellular structure shown in Figure 2.3 is used as the cellular unit for the LSTO method to optimize the components of interest. In general, the mechanical behavior of a cellular structure is likely to be anisotropic rather than isotropic. According to Simone and Gibson [99], a scaling law for anisotropic cellular structures also exists. In this work, the anisotropic constitutive law $\boldsymbol{\sigma} = \boldsymbol{C\varepsilon}$ is applied, where $\boldsymbol{\sigma}$, $\boldsymbol{C}$ and $\boldsymbol{\varepsilon}$ are the stress, elastic matrix, and strain, respectively. In matrix form in the Cartesian coordinates (x, y, z), these quantities can be written as:

$$\boldsymbol{\sigma} = [\sigma_{11} \quad \sigma_{22} \quad \sigma_{33} \quad \sigma_{12} \quad \sigma_{13} \quad \sigma_{23}]^{\mathrm{T}} \tag{2.12}$$

$$\boldsymbol{\varepsilon} = [\varepsilon_{11} \quad \varepsilon_{22} \quad \varepsilon_{33} \quad \varepsilon_{12} \quad \varepsilon_{13} \quad \varepsilon_{23}]^{\mathrm{T}} \tag{2.13}$$

$$\boldsymbol{C} = \begin{bmatrix} C_{11} & C_{12} & C_{13} & C_{14} & C_{15} & C_{16} \\ C_{12} & C_{22} & C_{23} & C_{24} & C_{25} & C_{26} \\ C_{13} & C_{23} & C_{33} & C_{34} & C_{35} & C_{36} \\ C_{14} & C_{24} & C_{34} & C_{44} & C_{45} & C_{46} \\ C_{15} & C_{25} & C_{35} & C_{45} & C_{55} & C_{56} \\ C_{16} & C_{26} & C_{36} & C_{46} & C_{56} & C_{66} \end{bmatrix} \tag{2.14}$$

For the scaling laws of cubic cellular structures, a polynomial function is used to fit the relationship between the elastic tensor and microstructure characterization parameters (MCPs). In the case of one MCP, e.g. relative density, $\rho_r(x)$, the elastic matrix of cellular structures can be written as:

$$\boldsymbol{C}(\boldsymbol{\rho}_r) = \boldsymbol{C_0} + \boldsymbol{C_1}\boldsymbol{\rho}_r + \boldsymbol{C_2}\boldsymbol{\rho}_r^2 + \cdots \tag{2.15}$$

where $\boldsymbol{C}_i(i = 0,1,2, \dots)$ are the constant symmetric matrices to be determined. For the anisotropic case, Eq.(2.15) gives the relationship of the mechanical properties and relative density.

The cubic structure will be utilized as an example to illustrate the homogenization process. Considering the symmetry of the cubic structure, the relationship of the elastic tensors is: $C_{11} = C_{22} = C_{33}$, $C_{12} = C_{13} = C_{23}$, $C_{44} = C_{55} = C_{66}$ and $C_{14} = C_{15} = C_{16} = C_{24} = C_{25} = C_{26} = C_{34} = C_{35} = C_{36} = 0$. Thus, the elastic matrix can be deduced to have the following form by symmetry:

$$\begin{bmatrix} C_{11} & C_{12} & C_{12} & 0 & 0 & 0 \\ C_{12} & C_{11} & C_{12} & 0 & 0 & 0 \\ C_{12} & C_{12} & C_{11} & 0 & 0 & 0 \\ 0 & 0 & 0 & C_{44} & 0 & 0 \\ 0 & 0 & 0 & 0 & C_{44} & 0 \\ 0 & 0 & 0 & 0 & 0 & C_{44} \end{bmatrix} \tag{2.16}$$

We now illustrate how to obtain the elastic scaling laws for the different elastic constants for the cubic cellular structure. Note that there are only three independent elastic constants C_{11}, C_{12}, and C_{44} for this structure. The effective mechanical behavior of a periodic lattice structure can be obtained using the well-established computational homogenization method [100-103]. In

this method, instead of modeling the entire lattice structure that contains a large number of unit cells and requires substantial amount of computing power, only one-unit cell of the lattice structure is employed in the finite element analysis (FEA) to predict its effective behavior. In order to obtain accurate result, it is of great importance to impose periodic boundary conditions (PBCs) on the unit cell model. To obtain an elastic constant, the most compact stress-strain relationship is deduced for that constant; for example, $\sigma_{xy} = C_{44}\varepsilon_{xy}$ for C_{44}. Then a simulation is run by imposing the strain of interest (e.g. ε_{xy}) to deform the unit cell to obtain the corresponding stress (e.g. σ_{xy}) as shown in Figure 2.2, which allows for the prediction of C_{44}. Since the scaling law is a function of relative density as stated in Eq. (2.15), a number of unit cells with different relative densities will need to be simulated in order to do the fitting. Figure 2.4 illustrates the different models of the cubic structure employed in the present study.

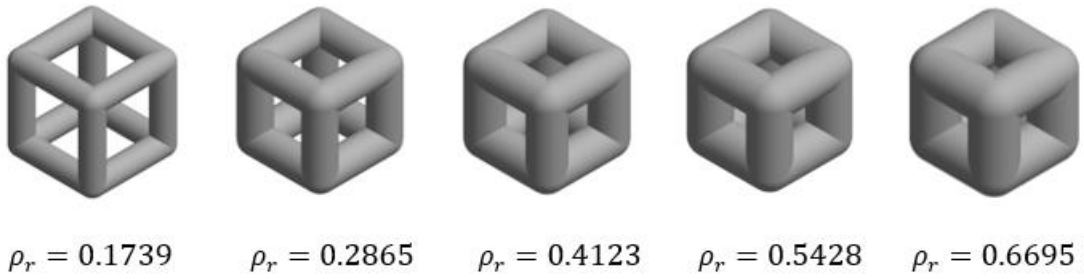

Figure 2.4: Cubic Cellular Structures with Different Relative Densities

Figure 2.5 illustrates the elastic constants versus relative density obtained from simulations and the fitted scaling laws for the cubic structure. Because the elastic scaling laws fitted will be used to perform topology optimization, it is required that they go to unity when $\rho_r = 1$ and go to

zero when $\rho_r = 1$. After some attempts of using different orders of polynomials to fit the simulation data for 15 different common cellular structures, we find that a quartic polynomial without the 3rd order term gives the best combination between accuracy and compactness of the scaling law. The 3rd order term in the quartic polynomial is excluded from quartic polynomial because it may cause the scaling law to become non-monotonic, which may lead to non-optimal result when performing topology optimization. The current form of scaling law is believed to be more robust than the quadratic polynomial employed in our previous work in 2D [104].

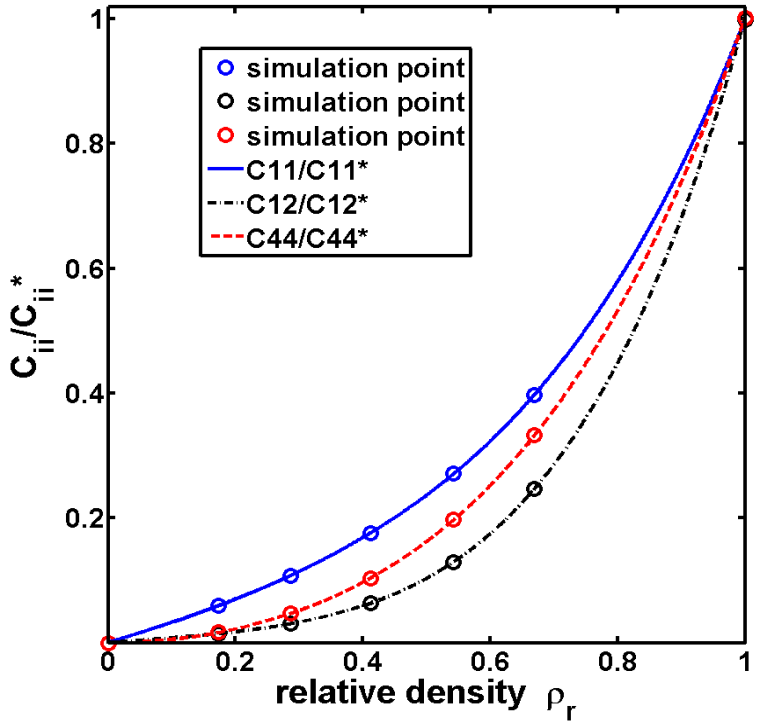

Figure 2.5: Elastic Scaling Law of Cubic Cellular Structures Versus Relative Density

For the cubic structure, the scaling laws for the three independent material constants obtained after fitting to the finite element simulation data are found to be:

$$C_{11}/C_{11}^{*} = 0.4729\rho_r^4 + 0.2266\rho_r^2 + 0.3003\rho_r \tag{2.17}$$

$$C_{12}/C_{12}^{*} = 0.8776\rho_r^4 + 0.0505\rho_r^2 + 0.0713\rho_r \tag{2.18}$$

$$C_{44}/C_{44}^{*} = 0.4727\rho_r^4 + 0.5294\rho_r^2 \tag{2.19}$$

In order to validate the simulation results, compression testing is conducted on some cubic cellular structure specimens fabricated by a 3D printer (Stratasys Connex 260 Objet) using a photopolymer called VeroWhite. The compression test specimen consists of five cubic structure unit cells with lattice constant of 5 mm (see Figure 2.6 for one of the specimens) and the [100] direction oriented along the compression direction. Hence, the elastic modulus along the [100] direction, E_{100}, of the cubic structure is obtained directly from the compression test. The testing is conducted on a load frame (MTS 880) for five different densities and three specimens are tested for each density.

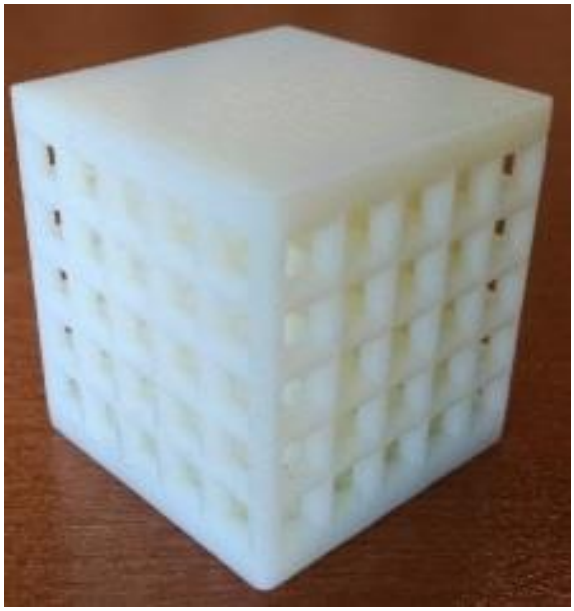

Figure 2.6: Specimens Used to Validate the Elastic Scaling Law

In order to directly compare to experimental results, the elastic modulus in the [100] direction of the unit cell is obtained from the fitted scaling laws from the different elastic constants through the following relationship:

$$\frac{1}{E_{100}} = \frac{C_{11} + C_{12}}{C_{11}^2 + C_{11}C_{12} - 2C_{12}^2} \tag{2.20}$$

Figure 2.7 illustrates the excellent match between the experimental and the simulation results for the cubic structure.

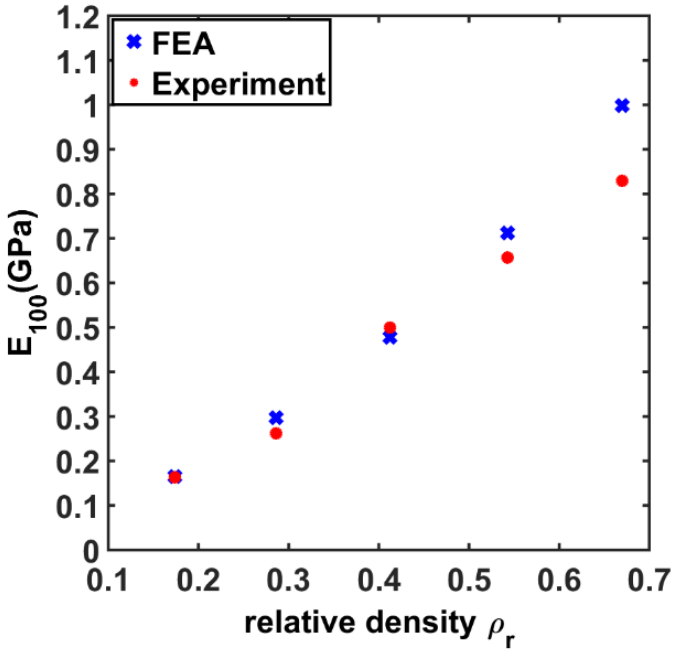

Figure 2.7: Comparison of Elastic Modulus Values Predicted by Finite Element Analysis and those Obtained from Experiments

2.3.2 Lattice Structure Printed by EOS M290 in Metals

Figure 2.8 illustrates the homogenized model of cubic lattice structure with respect to relative density for lattice structure manufactured by metal AM. The normalized three elastic constants (C_{11}, C_{12} and C_{44}) are equal to one (zero) as relative density reaches one (zero). Due to the symmetry of the cubic lattice structure, elastic constant C_{ii} and C_{ij} $(i, j = 1,2,3)$ are equal in x, y and z direction and $C_{11} = \frac{\sigma_{11}}{\varepsilon_{11}}, C_{12} = \frac{\sigma_{22}}{\varepsilon_{11}}$. On the other hand, the shear constant is also equal in any two directions and $C_{44} = \frac{\sigma_{12}}{2\varepsilon_{12}}$. For two-dimensional lattice structure, piecewise function composed of linear and cubic polynomial interpolation is used to fit the constitutive law, which has been proved by Arabnejad [93] and Wang [105]. However, for 3D structure, it is found that

quartic polynomial without 3rd order and constant term is more accurate for the representation of lattice material [106], which is employed in this work.

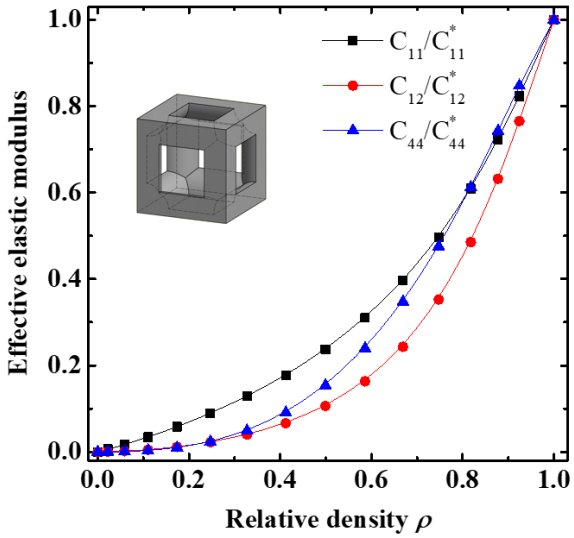

Figure 2.8: Effective Elastic Constants as a Function of Relative Density of the Lattice Structure Manufactured by Metal AM

2.3.2.1 Validation by Experiments for Metal Lattice Structure

Validation of the homogenized model is conducted on the samples printed by EOS DMLS with Ti6Al4V, whose Young's modulus is 110 GPa and Poisson's ratio is 0.3. Based on the AH method, the periodic lattice unit should be as small as possible [107]. However, from the manufacturability point of view, the manufacturable unit size is determined by the resolution of the machine. Hence, the manufactured lattice structure can be neither too small nor too large considering the print quality. Similar to my another work [108] for $AlSi_{10}Mg$, a benchmark is designed and printed out in Ti6Al4V using EOS DMLS to quantify the appropriate size for lattice

structure design, refer to Figure 2.9. Based on the observation on the benchmark in Figure 2.9 (b), it is found that the minimum ligament diameter that can be printed out with clear shape is 0.5 mm, the maximum overhang that can be printed out is 4.25 mm. This means that the design of the lattice structure should satisfy both the maximum overhang constraint and the minimum resolution (i.e. 0.5 mm) to ensure manufacturability of the lattices. Note that the benchmark test also eliminates the weak ligaments that possibly have critical defects in the ligament. This is because the recoater blade of the AM machine would inevitably come into contact with the top of the build, and the weak ligaments would be swiped away. The effects of other defects (micro-voids) on mechanical properties have been captured when the elastic constants are calibrated by tensile testing results on bulk samples. These defects are typically isolated micro-voids that has less than 0.01% volume fraction in DMLS-processed materials, and thus their effects on static mechanical properties are expected to be minimal.

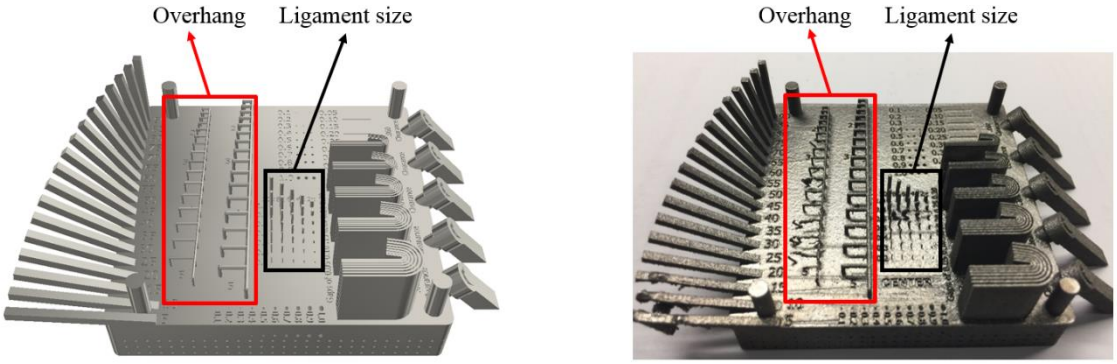

(a) (b)

Figure 2.9: Benchmark Study for the Overhang and Ligament Size. (a) CAD Model of the Benchmark for Ti6Al4V (b) Photo of the Printed-out Benchmark in Ti6Al4V by Using EOS DMLS.

Figure 2.10 illustrates the geometry and AM realization of the tensile samples, in which ASTM E8 standard has been used for sample size selection. The length of the sample is 8 in, with a neck width of 0.5 in and thickness of 0.25 in. As discussed in Refs [109, 110], the scale effect may lead to inaccuracy for the prediction from AH method when there are only a few lattice layers in the test samples. To guarantee the periodicity assumption in AH method and manufacturability discussed in the previous paragraph, the size of the unit cell is set to be 0.125 in or 3.175 mm, in which two layers at the thickness direction and 25 layers along the tensile direction. As mentioned in the work [111], when the layer is larger than 5 along the loading direction, the homogenization results agrees well with that from full-scale simulation. Thus, the unit size selection for the dogbone here is sufficient for validation. Good Agreement (see Fig. 9) between the experiment and the prediction from AH method also proves this point of view. For the tensile testing, samples of four different densities ($\rho = 0.4, 0.5, 0.6, 0.7$) and three specimens for each density are tested on MTS880 load frame.

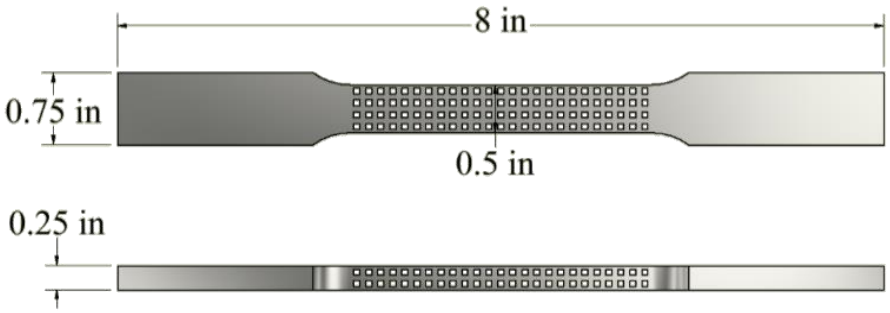

(a)

(b)

Figure 2.10: Specimens Printed by EOS DMLS with Ti6Al4V for Tensile Tests. (a) CAD and Dimension of the Samples; (b) Printed Samples and the Tensile Test.

Figure 2.11 presents the comparison of the experimental results and homogenized model for cubic lattice structure. The solid line denotes the homogenized model of cubic lattice structure computed from Eq. (2.15). The red dots are the experimental results while the blue dots are two known points ($\rho = 0, 1$). As demonstrated in the figure, the homogenized model agrees well with the experimental results, which implies that the homogenization in Eq. (2.15) and Figure 2.11 is reasonably accurate for the representation of lattice structure printed by EOS DMLS with Ti6Al4V. We will use this model for the optimization of lattice structure design.

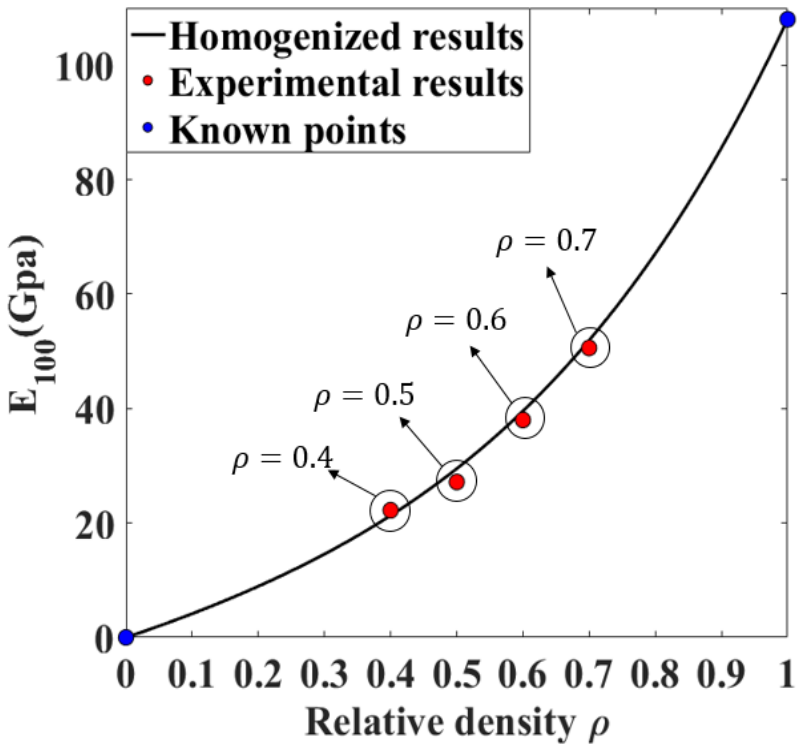

Figure 2.11: Comparison of the Effective Elastic Constants by the Homogenized Model and Experiments.

2.4 Yield Strength

Although homogenized model can be efficiently used for the representation of elastic performance, when the yield criterion is taken into account the obtained stress would apparently cause problem. This is because the local nature of stress constraints, meaning that the detailed stresses at microscale in the lattice structure is much different from the macroscopic stresses calculated by homogenized model. As shown in the Figure 2.12, a constant pressure of 30 MPa along the vertical direction is subjected to the lattice unit and the corresponding homogenized

model at microscale, the bottom surfaces of two models are fixed while the a periodic boundary conditions are subjected to the other four side-surfaces. It can be seen that the stress distribution of homogenized model is much uniform while the stress of detailed simulation for lattice structure is remarkably anisotropic, in which the maximum stress is about 9.0214 times larger than the homogenized model. This means that if the stress of homogenized model as constraints is used for topology optimization, the optimized structure would be much weaker than predicted value.

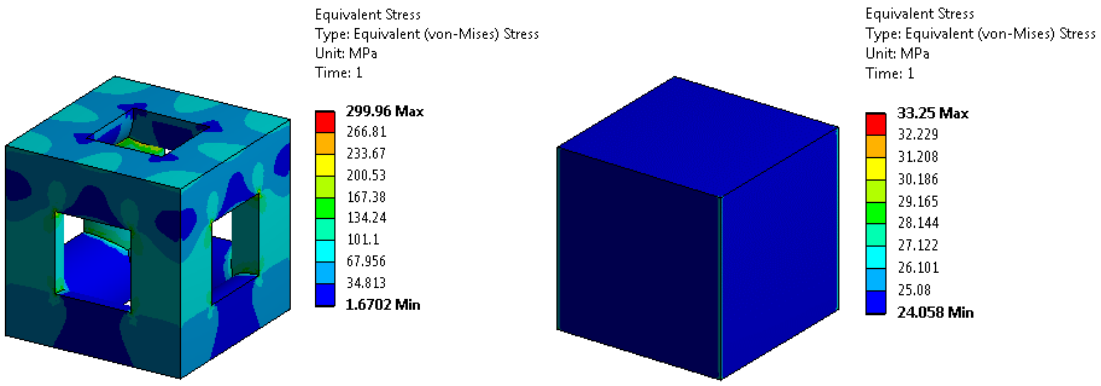

(a) (b)

Figure 2.12: Comparison of Stress Distribution Between Detailed Simulation and Homogenization for RVE. (a) Results of Detailed Simulation; (b) Results of Homogenization.

To ensure the consistency of the yield criterion for lattice structure, it is necessary to establish a model to reflect yield strength of microstructure on microscopic level using macroscopic stresses calculated by homogenized model. The model should not only maintain the local nature of the stress in RVE, but also computational cheap as well. A multiscale failure model

is herein proposed to capture the effective yield strength of lattice structure with predefined relative density ρ in terms of macroscopic stress.

At macroscale, considering the anisotropic properties of lattice material, the modified Hill's yield criterion [112] is employed to describe the yield behavior of lattice structure. As illustrated in Fig. 5, cubic lattice structure is a type of orthotropic material, which has three mutually perpendicular planes of symmetry. Thus, the modified Hill's yield criterion with respect to the principal axes of anisotropy (y_1, y_2, y_3) has the following forms:

$$\phi(\bar{\boldsymbol{\sigma}}) \equiv \bar{\sigma}_d^2 + G\bar{\sigma}_m^2 - 1 = 0 \tag{2.21}$$

where $\bar{\sigma}_d$ and $\bar{\sigma}_m$ represents applied macroscopic stress, and mean principal stress on macroscopic level, respectively, which can be formulated by macroscopic stress as

$$\bar{\sigma}_d^2 \equiv A(\bar{\sigma}_{11} - \bar{\sigma}_{22})^2 + B(\bar{\sigma}_{22} - \bar{\sigma}_{33})^2 + C(\bar{\sigma}_{33} - \bar{\sigma}_{11})^2 + 2D\bar{\sigma}_{12}^2 + 2E\bar{\sigma}_{23}^2 + 2F\bar{\sigma}_{13}^2 \tag{2.22}$$

and

$$\bar{\sigma}_m = \frac{1}{3}(\bar{\sigma}_{11} + \bar{\sigma}_{22} + \bar{\sigma}_{33}) \tag{2.23}$$

where A, B, C, D, E, F and G are material constants used to characterize the anisotropy of lattice structure. $\bar{\sigma}_{ij}(i, j = 1,2,3)$ represent the effective stress obtained via homogenized model. Using matrix notation, the Hill's yield criterion could be expressed as

$$\phi(\bar{\boldsymbol{\sigma}}) \equiv \bar{\boldsymbol{\sigma}}^T \mathbb{M} \bar{\boldsymbol{\sigma}} - 1 = 0 \tag{2.24}$$

where $\mathbb{M}$ represents an orthotropic fourth-order symmetric tensor satisfying both the minor and major symmetries, $\bar{\boldsymbol{\sigma}}$ denotes the macroscopic stress tensor. In Cartesian coordinate system (x_1, x_2, x_3), $\mathbb{M}$ can be expressed as

$$\mathbb{M} = \begin{bmatrix} A+C+1/9\,G & 1/9\,G-A & 1/9\,G-C & 0 & 0 & 0 \\ 1/9\,G-A & A+B+1/9\,G & 1/9\,G-B & 0 & 0 & 0 \\ 1/9\,G-C & 1/9\,G-B & B+C+1/9\,G & 0 & 0 & 0 \\ 0 & 0 & 0 & 2N & 0 & 0 \\ 0 & 0 & 0 & 0 & 2M & 0 \\ 0 & 0 & 0 & 0 & 0 & 2L \end{bmatrix} \tag{2.25}$$

According to the symmetry of cubic lattice structure, the total number of the material constants can be reduced to two independent constants, i.e. $A = B = C = K$ and $2D = 2E = 2F = Q$. The yield criterion in Eq. (2.24) can be simplified to

$$\begin{aligned} \phi(\boldsymbol{\sigma}) \equiv K[(\bar{\sigma}_{11}-\bar{\sigma}_{22})^2 + (\bar{\sigma}_{22}-\bar{\sigma}_{33})^2 + (\bar{\sigma}_{33}-\bar{\sigma}_{11})^2] \\ + Q[\bar{\sigma}_{12}^2 + \bar{\sigma}_{23}^2 + \bar{\sigma}_{13}^2] + G\bar{\sigma}_m^2 - 1 = 0 \end{aligned} \tag{2.26}$$

And $\mathbb{M}$ becomes

$$\mathbb{M} = \begin{bmatrix} 2K+1/9\,G & 1/9\,G-K & 1/9\,G-K & 0 & 0 & 0 \\ 1/9\,G-K & 2K+1/9\,G & 1/9\,G-K & 0 & 0 & 0 \\ 1/9\,G-K & 1/9\,G-K & 2K+1/9\,G & 0 & 0 & 0 \\ 0 & 0 & 0 & Q & 0 & 0 \\ 0 & 0 & 0 & 0 & Q & 0 \\ 0 & 0 & 0 & 0 & 0 & Q \end{bmatrix} \tag{2.27}$$

At microscale, the solid material consisting of lattice structure is assumed to be an isotropic, elastic-perfectly plastic solid of Young's modulus E^*, Poisson's ratio ν^* and yield strength σ_y^*. It is note that the buckling of lattice structure is ignored in the calculation of yield strength at microscale. For validation purpose, the solid material of lattice structure is assumed to be VeroWhitePlus printed out by Objet Connex 260, with $\mathrm{E}^* = 1745$ MPa, $\nu^* = 0.3$ and $\sigma_y^* = 65$ MPa. The FEA calculation of the yield strength for RVE is based on J_2 flow theory. The macroscopic yield strength of lattice structure are calculated at the peak of the curve of macroscopic stress versus strain. The yielding model of lattice structure can be obtained at different

relative densities through the uniaxial, shear and hydrostatic loadings under periodic boundary conditions, as shown in Figure 2.13.

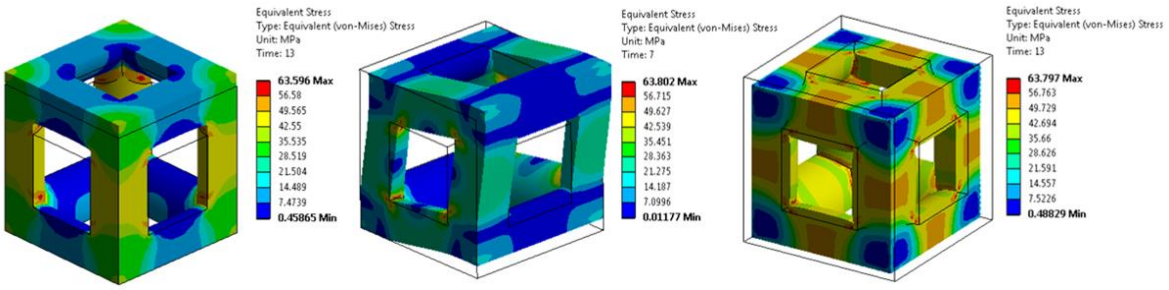

Figure 2.13: Yield Simulation for Cubic Lattice Structure on RVE. (a) Uniaxial Loading, (b) Pure Shear Loading and (c) Hydrostatic Loading.

FEA analysis on ten relative densities are performed to obtain the macroscopic yields, and a fourth order polynomial without the constant term are employed to achieve the curve fitting for the three-independent yield strengths in terms of relative density as follows:

$$\sigma_{kk}^{Y} \equiv \frac{\bar{\sigma}_{11}^{Y}}{\sigma_{\mathrm{y}}^{*}} = \frac{\bar{\sigma}_{22}^{Y}}{\sigma_{\mathrm{y}}^{*}} = \frac{\bar{\sigma}_{33}^{Y}}{\sigma_{\mathrm{y}}^{*}} = b_1\rho + b_2\rho^2 + b_3\rho^3 + b_4\rho^4 \tag{2.28}$$

$$\sigma_{ij}^{Y} \equiv \frac{\sqrt{3}\bar{\sigma}_{12}^{Y}}{\sigma_{\mathrm{y}}^{*}} = \frac{\sqrt{3}\bar{\sigma}_{23}^{Y}}{\sigma_{\mathrm{y}}^{*}} = \frac{\sqrt{3}\bar{\sigma}_{13}^{Y}}{\sigma_{\mathrm{y}}^{*}} = c_1\rho + c_2\rho^2 + c_3\rho^3 + c_4\rho^4 \tag{2.29}$$

and

$$\sigma_{m}^{Y} \equiv \frac{\bar{\sigma}_{m}^{Y}}{\sigma_{\mathrm{y}}^{*}} = d_1\rho + d_2\rho^2 + d_3\rho^3 + d_4\rho^4 \tag{2.30}$$

where $\bar{\sigma}_{ij}^{Y}$ $(i,j = 1,2,3)$ represent the macroscopic yield strength and $\bar{\sigma}_{m}^{Y}$ denotes the hydrostatic yield strength of cubic lattice structure, b_k, c_k and d_k $(k = 1,2,3,4)$ are the constants used for the curve fitting. σ_{kk}^{Y}, σ_{ij}^{Y} and σ_{m}^{Y} are used to represent the normalized uniaxial strength, shear strength and the hydrostatic strength, respectively.

Figure 2.14 illustrates curve fitting of the three-normalized yield strength of cubic lattice structure. It is seen the normalized yield strengths are also monotonic function within the whole range of relative density, which implies when density tends to zero, the material constants tends to be infinite, while when density tends to one, the material constants converge to one. From physical point of view, it is reasonable since the effective yield strengths are singly determined by the relative density and the relationship is monotonic.

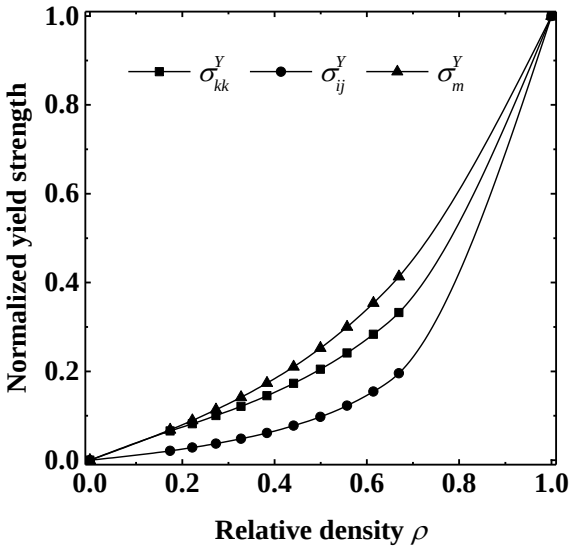

Figure 2.14: Material Constants of Macroscopic Yields for Cubic Lattice Structure in Terms of Relative Density.

Substituting Eq. (2.28)-(2.30)into the Eq. (2.26), and solving for the material constants K, Q and G, the function of the three material constants can be expressed in terms of relative density as:

$$K(\rho) = \frac{1}{2(\bar{\sigma}_{11}^{Y})^2} - \frac{G(\rho)}{18} \tag{2.31}$$

$$Q(\rho) = \frac{1}{(\bar{\sigma}_{12}^{Y})^2} \tag{2.32}$$

and

$$G(\rho) = \frac{1}{(\bar{\sigma}_{m}^{Y})^2} \tag{2.33}$$

Without losing the generality, the material constants are normalized by the yield strength of solid material, and the normalized material constants can be formulated as:

$$\frac{K(\rho)}{K^*} = \frac{1}{2(\sigma_{kk}^{Y} + \eta)^2} - \frac{G(\rho)}{18G^*(\sigma_{kk}^{Y} + \eta)^2} \tag{2.34}$$

$$\frac{Q(\rho)}{Q^*} = \frac{1}{\left(\sigma_{ij}^{Y} + \eta\right)^2} \tag{2.35}$$

and

$$\frac{G(\rho)}{G^*} = \frac{1}{(\sigma_{m}^{Y} + \eta)^2} \tag{2.36}$$

where K^*, Q^* and G^* represent the material constants of solid material, η is a smaller positive number to avoid the singularity when relative density is equal to zero.

Again, to examine accuracy of the proposed plastic model, yield strength of the uniaxial direction obtained from compression tests are used to compare with the prediction from the model

in Eq. (2.34)-(2.36). The yield strength along the [100] can be calculated by means of the material constants as:

$$\sigma_{100}^{Y}(\rho) = \frac{1}{\sqrt{2K(\rho) + \frac{1}{9}G(\rho)}} \tag{2.37}$$

Figure 2.15 illustrates the comparison. As can be seen, yield strength of cubic lattice structure along [100] direction at different relative densities are in a good agreement with the estimation from Eq. (2.43). It means that the modified Hill's model can provide reasonably accurate description for the yield performance of cubic lattice structure.

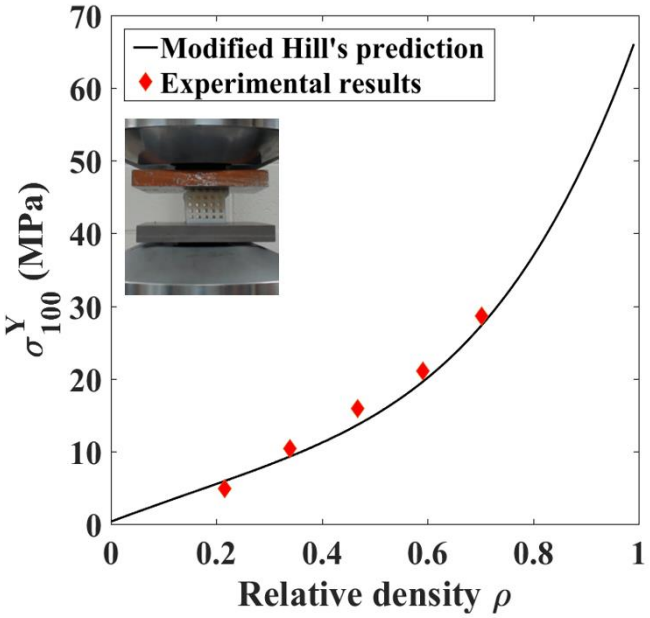

Figure 2.15: Experimental Verification of the Plastic Scaling Law

Based on homogenized model in Eq. (2.6), the macroscopic stress can be calculated by

$$\bar{\boldsymbol{\sigma}} = \overline{\boldsymbol{C}}\bar{\boldsymbol{\varepsilon}} \tag{2.38}$$

The substitution of Eq. (2.44) into Eq. (2.24), one can obtain

$$\phi(\bar{\boldsymbol{\varepsilon}}) = \bar{\boldsymbol{\varepsilon}}^T \overline{\boldsymbol{C}}^{\boldsymbol{T}} \mathbb{M} \overline{\boldsymbol{C}} \bar{\boldsymbol{\varepsilon}} - 1 \tag{2.39}$$

The modified Hill's yield criterion can be expressed as macroscopic strain-based formulation as

$$\phi(\bar{\boldsymbol{\varepsilon}}) = \bar{\boldsymbol{\varepsilon}}^T \mathbb{R} \bar{\boldsymbol{\varepsilon}} - 1 = (\bar{\sigma}^H)^2 - 1 \tag{2.40}$$

where

$$\bar{\sigma}^H = (\bar{\boldsymbol{\varepsilon}}^T \mathbb{R} \bar{\boldsymbol{\varepsilon}})^{\frac{1}{2}} \tag{2.41}$$

where $\mathbb{R}$ represents tensor used to describe yield performance of lattice structure under macroscopic strain, and $\mathbb{R} = \overline{\boldsymbol{C}}^{\boldsymbol{T}} \mathbb{M} \overline{\boldsymbol{C}}$. Since $\overline{\boldsymbol{C}}$ and $\mathbb{M}$ are function of relative density, $\mathbb{R}$ is the function of relative density.

Instead of penalizing the stress in the standard TO, the sensitivity analysis of stress constraint in this work is based on real material properties (e.g. $\overline{\boldsymbol{C}}$, $\mathbb{M}$ and $\mathbb{R}$). This is one of most different aspects in this work from the former studies [38, 40, 42, 43, 45]. $\bar{\sigma}^H$ is the modified Hill's stress used to estimate the yielding of the structure. $\bar{\sigma}^H \geq 1$ means that the structure has yielded, otherwise the structure is safe under the prescribed loading.

2.5 Thermal Conductivity

The governing equation for Fourier's heat conduction law can be written as:

$$\begin{cases} K\nabla^2 u(\boldsymbol{x}) + f = 0 \\ q(\boldsymbol{x}) = -K\nabla u(\boldsymbol{x}) \end{cases} \tag{2.42}$$

where q is the heat flux, K denotes the effective thermal conductivity and f represents the internal heat generation in the design domain. Substituting the derivatives of the temperature field in Eq. (2.1) with respect to x into the governing equation of Eq. (2.42). Following similar procedure of homogenization in elasticity[94], one can obtain the effective thermal conductivity as:

$$\overline{K}_{ij} = \frac{1}{|V_{RVE}|}\int_{V_{RVE}} K_{ik} M_{kj} dV_{RVE} \tag{2.43}$$

where $\overline{K}_{ij}$ $(i, j = 1,2,3)$ denotes the effective thermal conductivity, V_{RVE} indicates the RVE volume and M_{kj} represents the local structure tensor which is defined as follows:

$$u_{,i} = M_{ij}\bar{u}_{,j} \tag{2.44}$$

The local structure tensor M_{ij} is used to relate the average temperature gradient $\bar{u}_{,j}$and the local temperature gradient $u_{,i}$. As illustrated in Figure 2.16, cubic lattice structure saturated with air is taken as the objective structure.

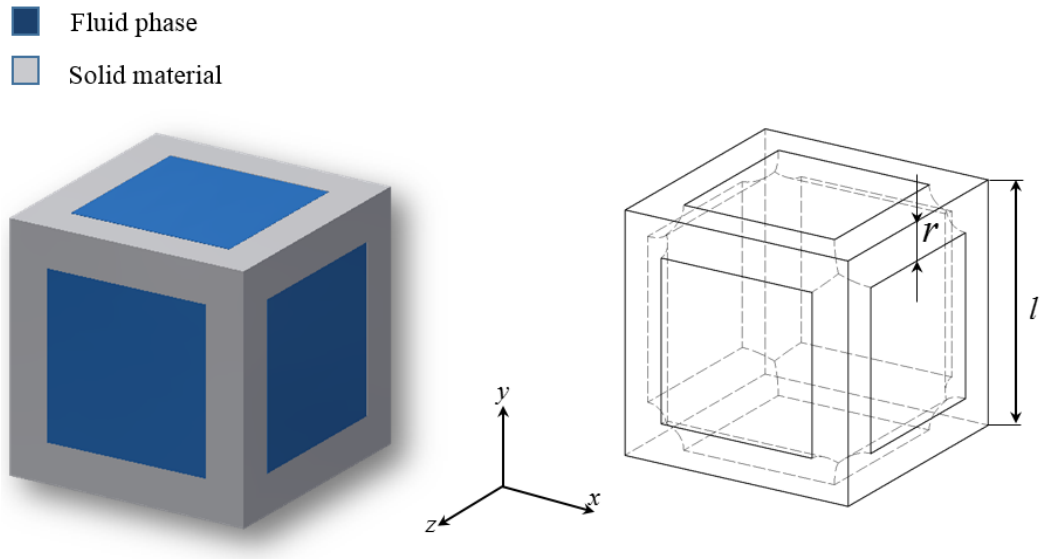

Figure 2.16: Cubic Lattice Unit Saturated with Fluid Phase.

Numerical homogenization is employed to obtain the effective thermal conductivity of the lattice. For the homogenization analysis, only one lattice unit is analyzed, since the periodic assumption gives the same results of any number of cells. Figure 2.17 gives the mesh model and boundary conditions of the cubic lattice unit. ANSYS v17.0 was used to conduct the finite element analysis for the model.

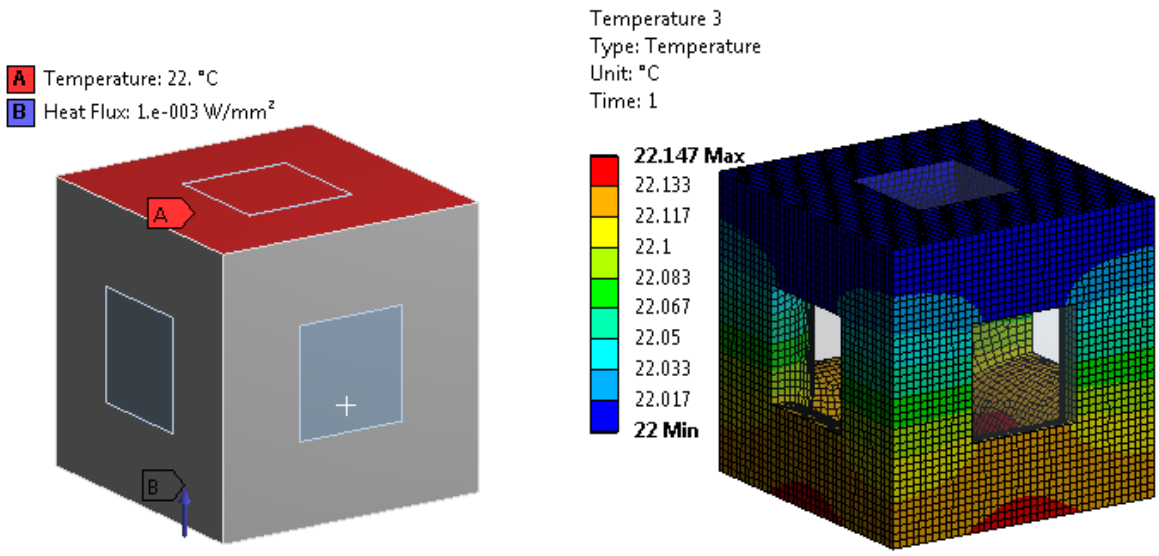

Figure 2.17: FEA Model of the Cubic Lattice Unit

Based on the homogenization theory, the effective thermal conductivity of lattice material is expressed as a function of relative density ρ. In order to ensure smooth convergence of the optimization procedure, a monotonic function is needed to fit to the FEA results. Hence a fourth-order polynomial without third-order and zero-order (constant) terms is used to fit the relationship [106].

$$\overline{K}_r(\rho) = a_1\rho + a_2\rho^2 + a_4\rho^4 \tag{2.45}$$

where $\overline{K}_r$ denotes the normalized effective conductivity ($\overline{K}_r = \overline{K}/K_s$, $\overline{K}$ and K_s are the effective conductivity and the conductivity of solid material, respectively). The coefficients $a_i (i = 1,2,4)$ are the constants used to fit the polynomial. Figure 2.18 illustrates the effective conductivity obtained via numerical homogenization. It can be seen the fitted curve is monotonic in the entire range of the relative density.

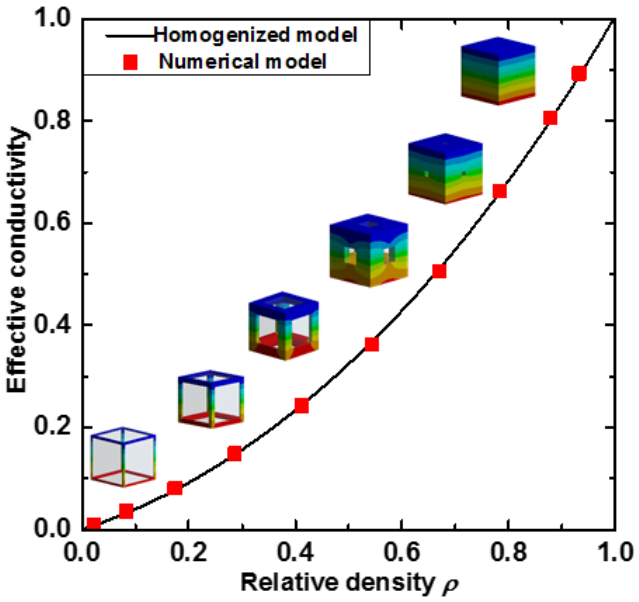

Figure 2.18: Normalized Effective Thermal Conductivity of Cubic Lattice Material as a Function of Relative Density.

3.0 Lattice Structure Topology Optimization (LSTO)

In this chapter, the framework of lattice structure topology optimization will be introduced including both the workflow and the reconstruction for the proposed LSTO methodology. Following the basic theory of the LSTO method, the extensions of LSTO for various problems including minimum compliance, constraint stress, natural frequency, and forced convection heat transfer are explored. Several numerical examples for each problem are designed using the proposed framework and experiments on the 3D printed lattice structure designs are conducted to demonstrate the efficiency and accuracy of the proposed framework.

3.1 Theory of LSTO Method

3.1.1 Design Methodology

The proposed design methodology for cellular structured components is illustrated in the flowchart shown in Figure 3.1 and each step is detailed in the follows.

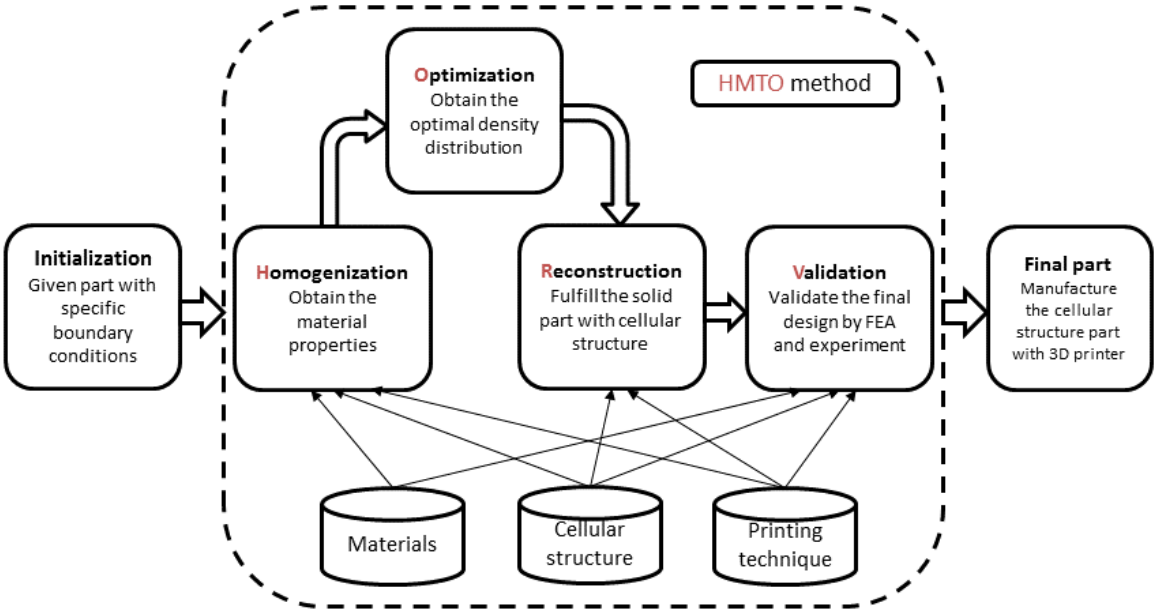

Figure 3.1: Flowchart of the Lattice Structure Design Optimization Methodology.

(i) Initialization: The design component with the given boundary conditions and the corresponding mechanical model are specified in preparation for the cellular structure design, optimization, and reconstruction processes. The material, cellular structure type, and the printing technique are initialized as the input parameters for homogenization and optimization.

(ii) Homogenization, Optimization, Reconstruction, and Validation:

In the cellular structure optimization reconstruction section, four steps are implemented to redesign the specific component with variable-density cellular structures.

a) Homogenization: The material type, cellular type, and AM techniques are determined as input parameters for the material model function to calculate the material table required for the cellular topology optimization process. The material table holds the mechanical properties of the cellular structures with the specific material types and

orientations. The material table is also used as the material model for the finite element analysis (FEA) in the design validation and assessment.

b) Optimization: Once the homogenized material model is obtained from step (a), the geometry optimization of the cellular structures can be cast into the revised topology optimization algorithm of the equivalent continuous solid model. The optimized density distribution is then obtained after conducting the optimization calculation, which is used as the input parameters of the cellular structure reconstruction.

c) Reconstruction: For the given component, the cellular structure reconstruction software would identify the boundaries of the parts and automatically generate the variable-density mesh according to the optimal density distribution. As illustrated in Figure 3.2, pillow bracket is reconstructed with variable-density cubic cellular structures.

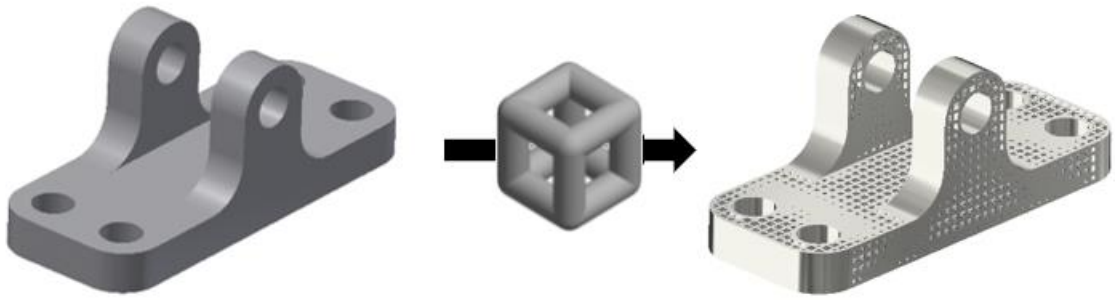

Figure 3.2: Reconstruction of the Variable-Density Cellular Structure in the Pillow Bracket.

d) Validation: In order to further validate reconstructed part, both numerical simulation and experiments are conducted to validate the optimized design.

(iii) Finalization: In addition to the FEA and experiments, the optimization algorithm, design criteria, and cellular reconstruction algorithm all need to be assessed and reevaluated. Some necessary adjustments and modification should be made to the optimal design until the design requirements are satisfied. For example, the regions where loads are being applied should be kept as solid instead of converting into cellular structure to maintain good structural integrity. This was done around the bolt holes of the pillow bracket design shown in Figure 3.2. As another example, it may be desirable to insert a skin layer to cover certain regions of the design, sometimes to cover up the truncated ligaments in the lattice, while sometimes for aesthetic purpose. A successful model obtained from the above three steps does not mean that the cellular structured component is qualified for AM production. After the solid component is discretized with the specific cellular structures, there may be many sharp corners that exist in the internal parts which will cause stress concentrations. Fillets are required to avoid these stress concentrations and a surface skin may need to be added to cover the cellular structures depending on the components specific utilization. The specific AM processing conditions and limitations such as large overhangs and unsupported geometries need to be considered and adjusted in the designed cellular structure component[113]. After the CAD model is finalized, the reconstructed cellular structure component can be manufactured using the proper AM process and applied to industry.

3.1.2 Reconstruction

Having obtained the optimal density distribution over the part geometry, the next step in the design process is to reconstruct the CAD model of the cellular structured component for AM. In the reconstruction, a periodic lattice of the given cellular structure is generated to span the design space. The lattice constant should be chosen to ensure that the resulting cellular structure is

manufacturable using the AM process of interest. Next, each individual ligament in the lattice is reconstructed according to the relevant optimized relative densities, followed by a union operation over all the generated ligaments to obtain the final variable-density structure. Note that each individual ligament is modeled as a tapered cylinder with rounded ends, the radius of each end is determined according to the optimized relative density at that end (Figure 3.3 illustrates the way to obtain the variable density cellular structure). This is achieved by using the relationship between the radius of ligament and relative density for the given cellular structure. To obtain this relationship, the radius of ligament is varied at small regular intervals to generate different unit cells of the given structure, from which the corresponding relative densities can be computed using a CAD program. As an example, the normalized radius (i.e. ratio of radius of ligament and lattice constant) versus relative density of the cubic lattice structure is shown in Figure 3.3. Since the data shows a quite non-linear relationship in the low-density range and high-density range, three cubic spline functions are employed to fit the data in the low, medium, and high density ranges for the cubic lattice structure:

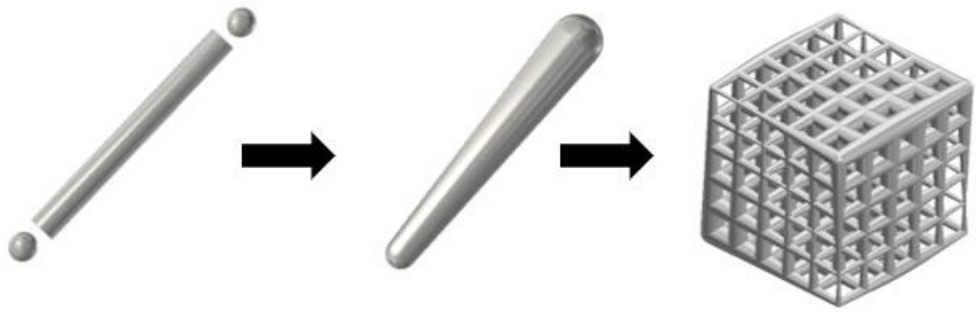

Figure 3.3: Procedure to Generate Variable Density Cellular Structure

$$
\begin{aligned}
R/l_e &= 38.481\rho_r{}^3 - 13.612\rho_r{}^2 + 2.095\rho_r && (0 < \rho_r \le 0.1162) \\
R/l_e &= 0.098\rho_r{}^3 - 0.236\rho_r{}^2 + 0.541\rho_r + 0.060 && (0.1162 < \rho_r \le 0.5428) \\
R/l_e &= 1.006\rho_r{}^3 - 1.715\rho_r{}^2 + 1.344\rho_r - 0.085 && (0.5428 < \rho_r \le 0.9420)
\end{aligned} \tag{3.1}
$$

where R is the radius of ligament, l_e is the lattice constant, and ρ_r is the relative density. Based on our experience, up to three cubic spline functions is needed to fit the data for the entire range of relative density in order to obtain an accurate fit. In the reconstruction of the variable-density cellular structure, the function obtained is employed to determine the radius of the tapered ligament from the optimized relative density at each lattice point. Figure 3.4 shows the process of reconstructing the variable-density cubic cellular structure for the minimum compliance 3-point bending beam.

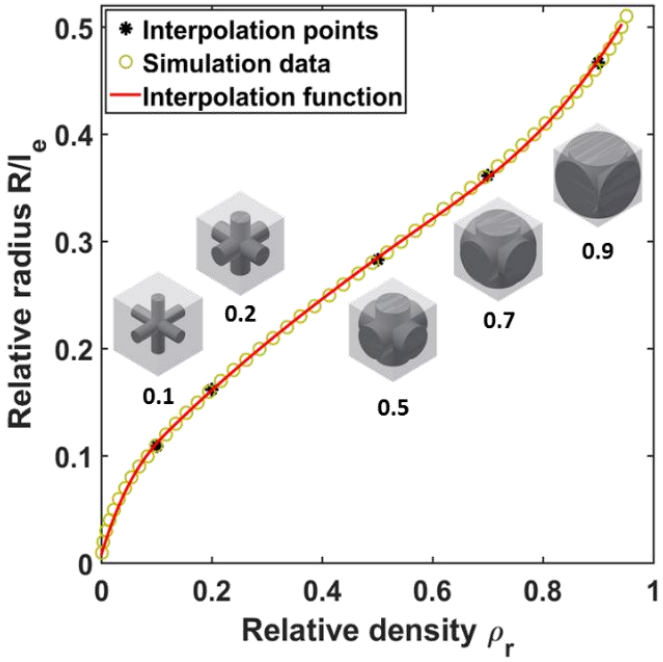

Figure 3.4: Fitted Function of Relative Radius Versus Relative Density.

As illustrated in Figure 3.4, the relationship between the ratio of the vertex radius versus ligament length and relative density is a smooth spline, which ranges from 0 to 0.942 for the cubic structure. The green circles are simulation data obtained by computing the relative density of the joint with respect to the radius in the CAD program. Taking the reconstruction of MBB problem as an example shown in Figure 3.5, an optimal density distribution is smoothly transformed into a variable density lattice infill.

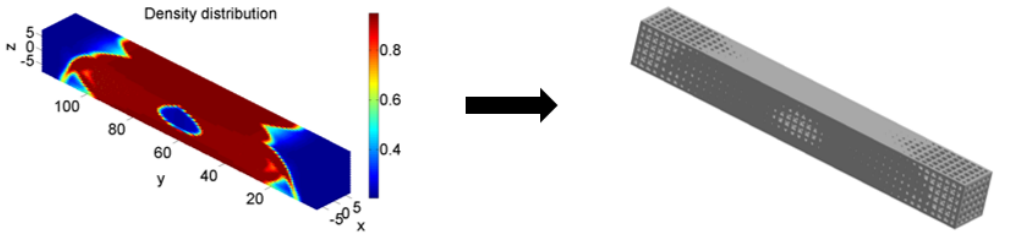

a) Optimal density distribution b) Optimal cellular structured design

Figure 3.5: Reconstruction of the Variable-Density Cubic Cellular Structure for the Optimized 3-Point Bending Beam.

3.2 Minimum Compliance Problem

3.2.1 Problem Statement

In this section, we illustrate how the elastic scaling law will be utilized to obtain the minimum compliance cellular structure for a mechanical component. Since the effective

mechanical properties can be represented as a function of relative density of a given cellular structure through the scaling law, the relative density is the design variable in our optimization problem. Typically, the underlying mechanical equilibrium problem is solved by the finite element method. Hence the design domain Ω is discretized by N finite elements, where each element e will be assigned a relative density $\rho_r \in [0,1]$. Employing the relative density vector $\boldsymbol{\rho}_r$, the global stiffness matrix for the discretized problem can be rewritten as $\mathbf{K}(\boldsymbol{\rho}_r)$. Let the external loading denoted by the vector $\boldsymbol{f}$ and the displacement vector by $\mathbf{u}$, the discretized equilibrium equation can be written as:

$$\mathbf{K}(\boldsymbol{\rho}_r)\mathbf{u} = \mathbf{f} \tag{3.2}$$

Hence the minimum compliance problem takes the following mathematical form:

$$\begin{aligned} \min_{u\in U,\rho_r} \; & c(\rho_r) = \mathbf{u}^{\mathbf{T}}\mathbf{K}\mathbf{u} = \sum_{e=1}^{N} u_e^T k_e u_e \\ s.t. \quad & \mathbf{K}\mathbf{u} = \mathbf{f}; \\ & \mathbf{C} = \mathbf{C}(\rho_r); \\ & \sum_{e=1}^{N} \rho_r v_e = V; \\ & 0 \le \rho_{\min} \le \rho_r \le \rho_{\max} \le 1 \end{aligned} \tag{3.3}$$

where $\boldsymbol{C}(\boldsymbol{\rho}_r)$ is the objective function, $\mathbf{u}_e$ the elemental displacement vector, $\mathbf{k}_e$ the elemental stiffness matrix, and v_e the element volume for element e, while V is the total designed volume. As can be seen, there are four constraints in this minimum compliance problem. The first constraint is the equilibrium equation. The second constraint is the elastic scaling law as discussed in Chapter 2.0. The third constraint is that the total design volume is constrained to V, whose value should be equal to or less than the volume of the design space. The fourth constraint requires that

the relative density is bounded by the minimum and maximum relative density ρ_{min} and ρ_{max}, respectively.

3.2.2 Numerical Examples

The optimization problem stated in Eq. (3.3) is almost identical to the standard minimum compliance problem (i.e. 0/1 design), but the physical meaning they carry are quite different. In the standard problem, the second constraint is a fictitious elastic scaling law that is employed to drive the design variable to zero (void) or unity (solid) during the optimization process. Standard techniques such as the Solid Isotropic Material with Penalization (SIMP) approach have no real physical meaning in standard topology optimization. In contrast, in the proposed approach for cellular structure design, the second constraint in Eq. (3.3) utilizes the elastic scaling law that represents the real mechanical property of the underlying cellular structure as a function of relative density. Hence, a major advantage of the proposed approach is that all the intermediate densities obtained from the optimization can be realized into cellular structures with the corresponding densities. It is not possible to achieve this in standard topology optimization.

Due to their similarity, standard topology optimization algorithms can be easily adopted to solve the current minimum compliance problem posed in Eq. (3.3). In this work, the non-gradient-based Proportional Topology Optimization (PTO) method is employed to solve the problem [114]. Interested readers should refer to that work for further details.

In order to demonstrate the effectiveness of the proposed method, the classic three-point bending beam design problem is solved. Figure 3.6 shows the basic dimensions of the beam model with size 120 x 15 x 15 mm^3. In the FEA model, a vertical displacement is applied onto the middle

of the upper face of the beam. The displacements are fixed at the supports located at the left bottom face of the beam and at the right bottom face as indicated in the figure.

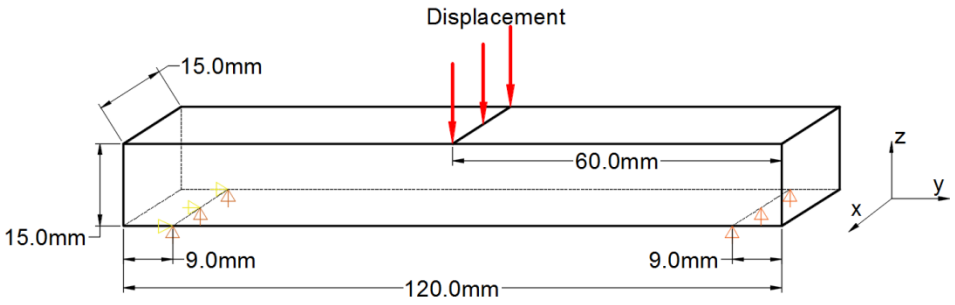

Figure 3.6: Dimension of the 3-point Bending Beam.

As illustrated in Figure 3.7, the finite element mesh of the 3-point bending beam consists of 55,594 ten-node hexahedron elements with an average element size of 0.8 mm and total number of nodes of 62,000. More elements are distributed in the area where the boundary constrains are applied and at the supports to ensure the accuracy of the FEA. The values employed for the various material parameters are as follows: E=2100 Mpa for Young's modulus and υ=0.3 for Poisson's ratio, which are the properties of the material that we will be printing in. The scaling law of the cubic cellular structure used for topology optimization is given in Eqns. (3.2) and (3.3). The initial relative density for all the elements is set to 0.5 in the beginning of the optimization. The convergence criterion is when the change in total compliance is less than 0.0001.

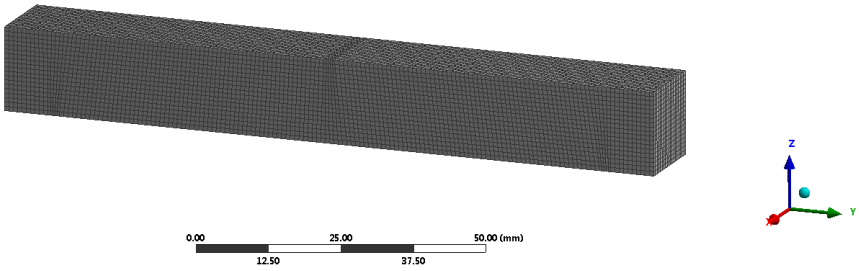

Figure 3.7: Finite Element Mesh of the 3-Point Bending Beam.

Figure 3.8 gives the stiffness of the beam model versus the number of iterations. As illustrated in the figure, the total compliance of the beam model converges to the optimal density distribution after 28 iterations. As illustrated in Figure 3.8, the stiffness of the structure increases from 106.8 N/mm to 239.4 N/mm, which represents an increase of 124.3%. This result proves that the structure becomes stiffer than before.

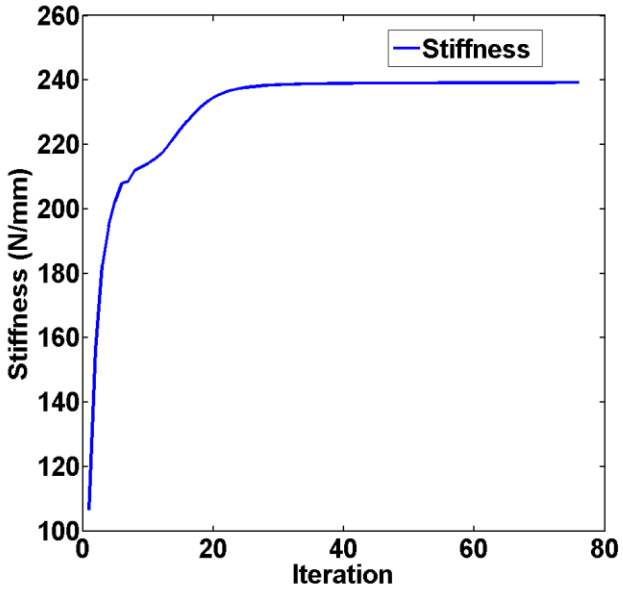

Figure 3.8: Convergence History of the Beam Stiffness in the Optimization

The evolution of the relative density distribution in the beam during the optimization is shown in Figure 3.9. In the figure, red color indicates the larger relative density while blue color indicates lower relative density.

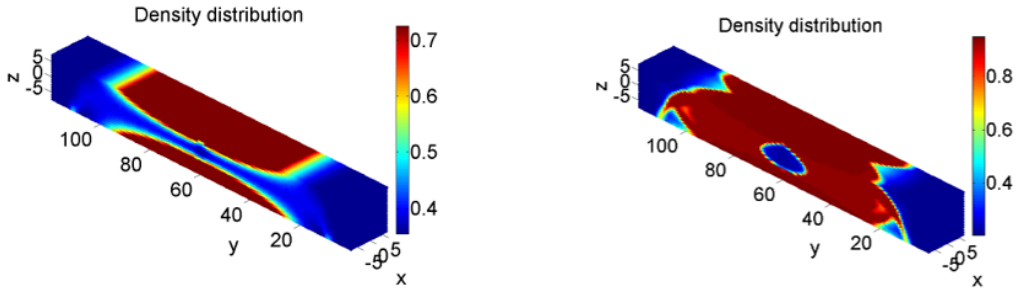

(1) (28)

Figure 3.9: Density Distribution in the Beam at Different Iterations in the Optimization

3.2.2.1 Verification

In order to validate the proposed design method, both full scale simulation and experiments are conducted on the 3-point bending beam before and after minimum compliance optimization with the overall volume fraction constrained to 50% of the original beam. Note that the un-optimized beam has a uniform cubic structure of 50% relative density. To be consistent with the 3-point bending experiment, support structures are added to the bottom surface of the beams as shown in Figure 3.10(a).

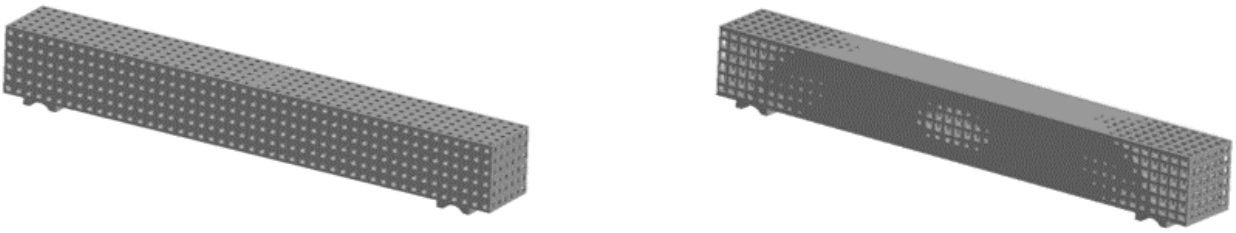

a) Cellular structured model of s uniform and non-uniform beam (volume fraction=0.5)

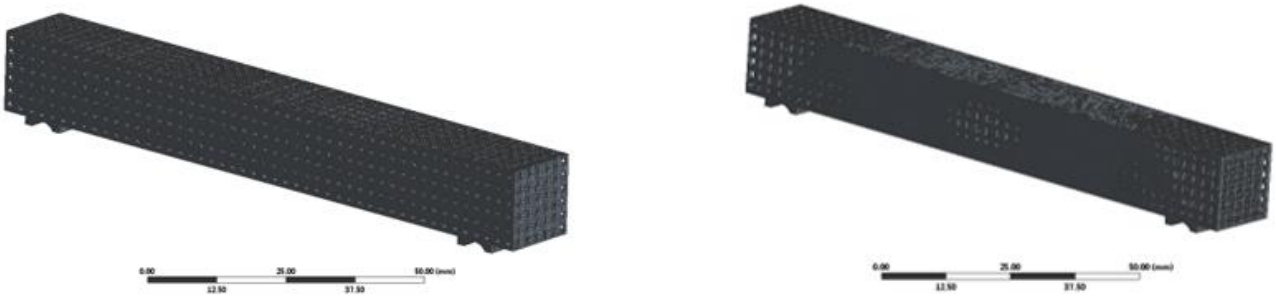

b) Mesh model of s cellular structured uniform and non-uniform beam (mesh type: triangular)

Figure 3.10: The Mesh Model of the Uniform 3-Points Bending Beam.

3.2.2.2 Simulation

To conduct the full scale FEA, the uniform and optimized cellular structured beam is meshed with 570,713 tetrahedral elements (1,041,711 nodes) and 533,262 elements (956,692 nodes), respectively. The material properties employed are identical to those used in the optimization, where E=2100 Mpa and υ=0.3. The beam is assumed to be pinned supported at the bottom. Displacement is applied in the middle of the upper beam surface at an increment of 1 mm, and the reaction force is recorded so that the force-displacement curve obtained can be compared directly with experiment.

3.2.2.3 Experiment

For the 3-point bending experiment, five specimens of each of the uniform and optimized non-uniform beams are printed in VeroWhite using an Objet260 Connex (Stratasys Inc.) as shown in Figure 3.11(a,b). The comparison between the CAD models and the printed beams is illustrated in Figure 3.11.

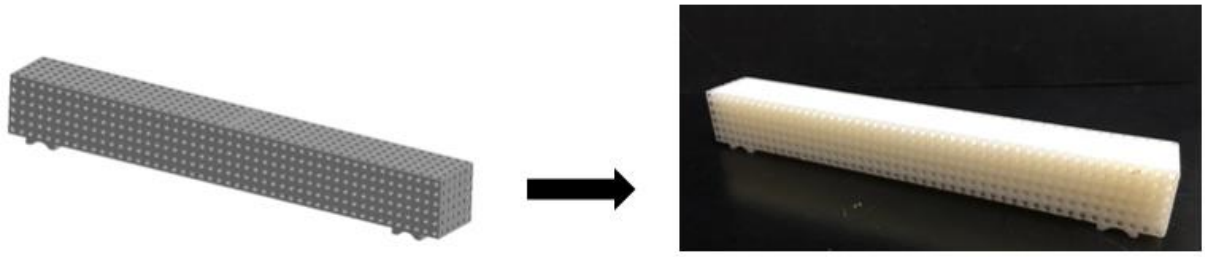

a) Uniform cellular beam CAD model printed by Objet260

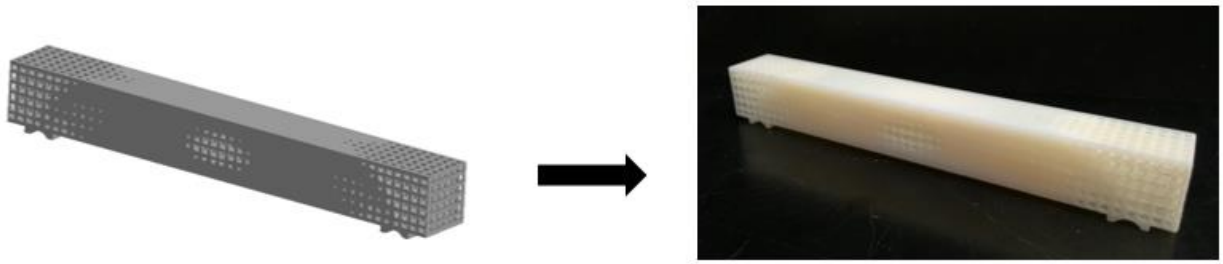

b) Optimized cellular beam CAD model printed by Objet260

Figure 3.11: Comparison Between the CAD Models of the Reconstructed Beams and the Printed Beams by Objet260.

The experiment on the 3D-printed beams is conducted on a 3-point bending fixture on a load frame (MTS880 system). The beams are loaded at rate of 0.2mm/s until failure. After the beam is fractured, the pressure head automatically retracts to the original position. The

displacements and the corresponding loads are recorded by the data acquisition system that is part of the loading system. Figure 3.12 shows a snapshot of the experimental apparatus during the testing of the uniform and optimized non-uniform cellular structured beams.

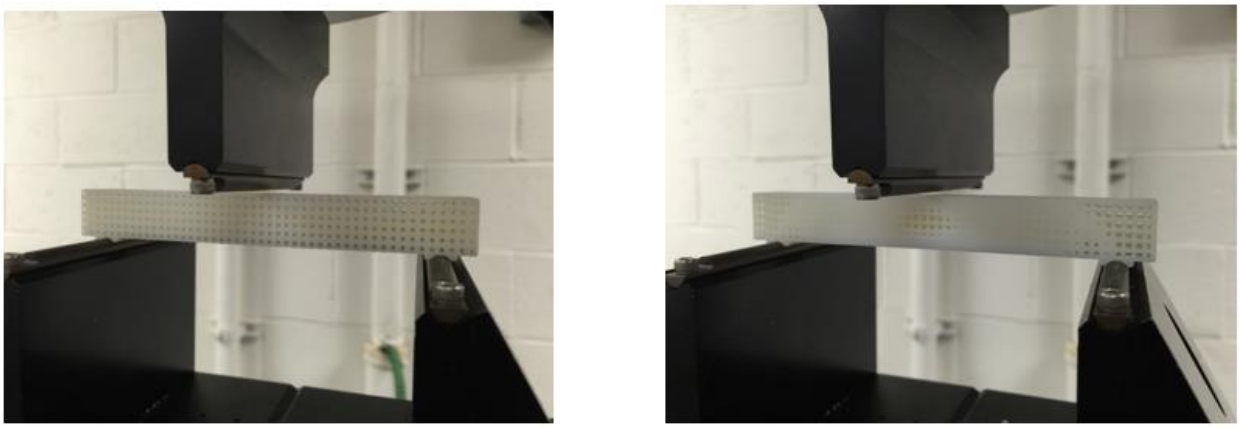

a) 3-point bending test for uniform beam b) 3-point bending beam test for optimized beam

Figure 3.12: Experiment setup of the 3-point Bending Test.

3.2.2.4 Results

Figure 3.13 illustrates the simulation and experimental load-displacement curves for the uniform and optimized non-uniform beams, respectively. Table 3.1 tabulates the tangent stiffness in the linear elastic region obtained from full scale simulation, homogenized model, and experiment. From Table 3.1, it can be seen that the predicted stiffness values from the homogenized model is close to those obtained from both the full-scale simulation and experiment for both cases. The homogenized and full-scale simulation results are especially close for the

uniform beam (1.65% difference), but not as close in the case of non-uniform beam (10.7% difference). This observation alone would suggest that the homogenized model is not as predictive for variable-density cellular structures. However, the simulation results using the homogenized model are actually closer to the experiment results than the full-scale simulation are for both beams. Hence, the homogenized model should be reasonably accurate for modeling variable-density cellular structures. It is likely that the finite element mesh of the cellular structure beams in the full-scale simulation is not accurate due to the geometric complexity of the structure, resulting in its worse performance than the homogenized model, especially for the non-uniform beam.

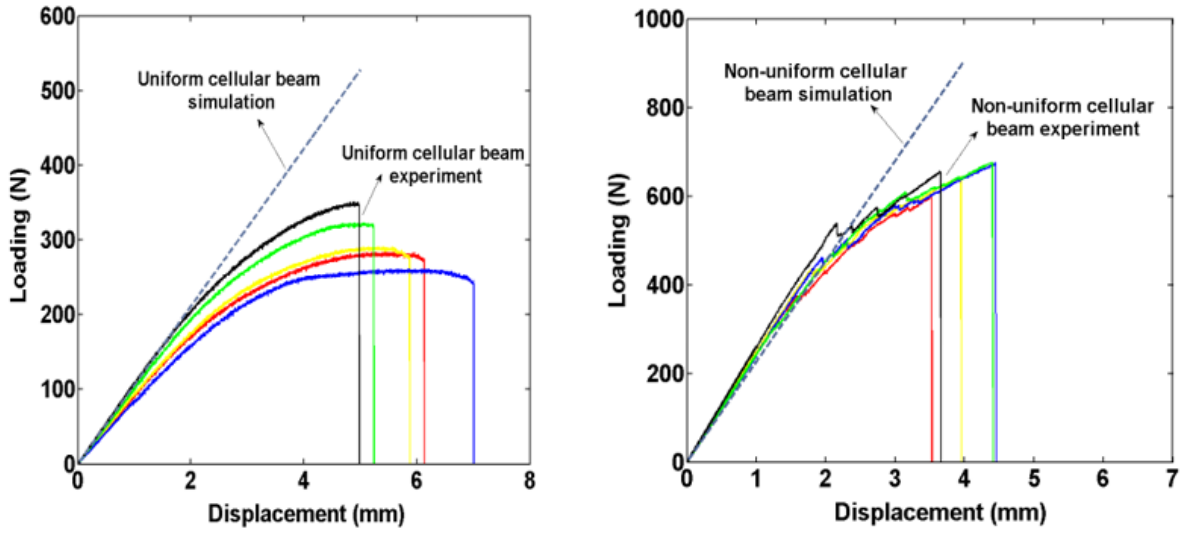

a) Uniform beam result

b) Optimized beam result

Figure 3.13: Comparison Between the Simulation and Experiment of the 3-Point Bending Beam for the Uniform Beam and Optimized Non-Uniform Beam.

Table 3.1: Linear Tangent Stiffness Values Obtained from Full Scale Simulation, Homogenized Model, and Experiment.

Test structure	Full scale simulation	Homogenized model	Experiment
Uniform beam	108.46 N/mm	106.67 N/mm	96.34 N/mm
Non-uniform beam	216.05 N/mm	239.24 N/mm	247.01 N/mm

Next we compare the experimental results between the uniform beam and optimized non-uniform beam, where the load-displacement curves are shown in Figure 3.14 and the initial tangent stiffness and strength are tabulated in Table 3.2. Recall that both beams are designed to have the same weight (i.e. 50% volume fraction of the original solid beam). Note that the non-uniform beam is much stiffer than the uniform beam (i.e. 156.5% increase) as it should be since the former is optimized for minimum compliance. Besides, the strength of the non-uniform beam is also 115.2% higher than the uniform beam. These results show the effectiveness of the proposed homogenization-based design method.

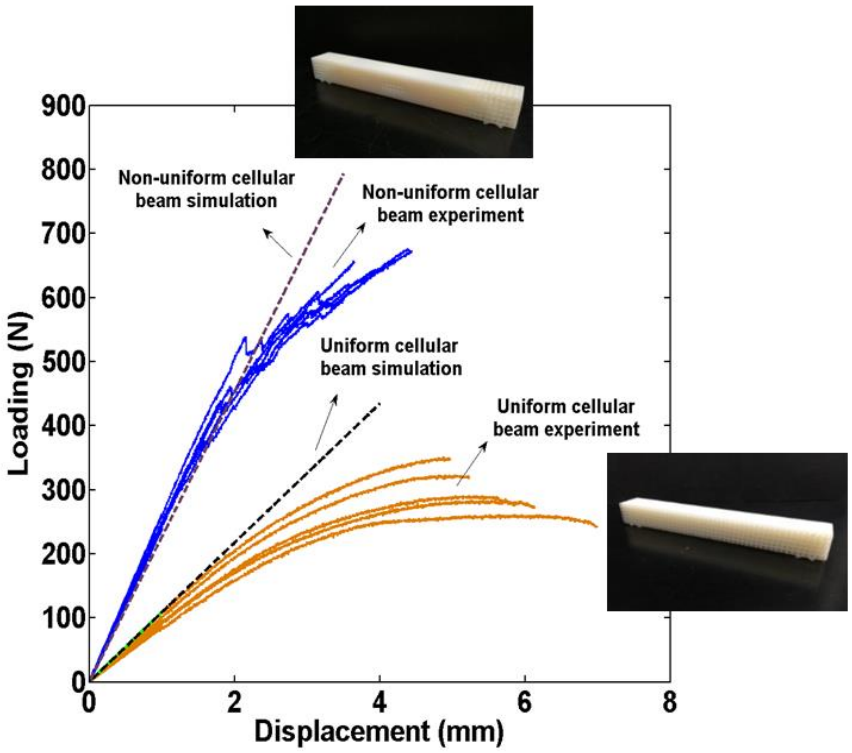

Figure 3.14: Comparison of the 3-Point Bending Tests Between the Uniform Cellular Beam and a Non-Uniform Cellular Beam.

Table 3.2: Comparison of Mechanical Properties of the Uniform and Optimized Beams.

Property	Uniform beam	Optimized non-uniform beam	Enhancement (%)
Average stiffness (N/mm)	96.34	247.1	156.5%
Average strength (N)	302.3	650.7	115.2%

3.2.3 Practical Application

Further application of the LSTO method is carried out through the design of the pillow bracket (Figure 3.15), which is a conventional component in industry. The design optimization process for the pillow bracket is shown in Figure 3.15: (a) Homogenization of the cubic cellular structure, (b) topology optimization for the pillow bracket using the specific scaling law, (c) reconstruction of the variable-density cubic cellular structure, and (d) validation by both simulation and experiment.

The pillow bracket is designed for flexural loading and Figure 3.16 shows the experimental apparatus used to conduct the experiment. The experiment apparatus consists of two main parts. The first part is the lower plate used to fix the pillow bracket in place using four bolts and eight nuts as shown in Figure 3.16. The other part is the upper plate, which is connected to the pillow bracket through a pin that is inserted through the hole of the plate between the ears of the bracket. In the experimental setup, the distance from the bottom part to the upper plate is equal to the distance to the two ears of the pillow bracket to avoid the flexural deformation of the pin as much as possible. During the experiment, both the upper and lower plates are fixed to the load frame (MTS 880), and hence by moving the upper plate downward, a vertical downward force is applied onto the ears of the pillow bracket through the pin.

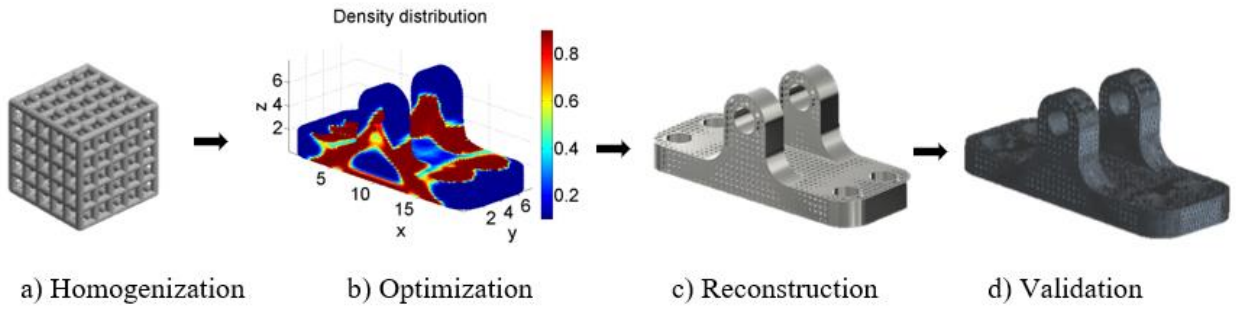

Figure 3.15: Procedure to Optimize Design of the Pillow Bracket.

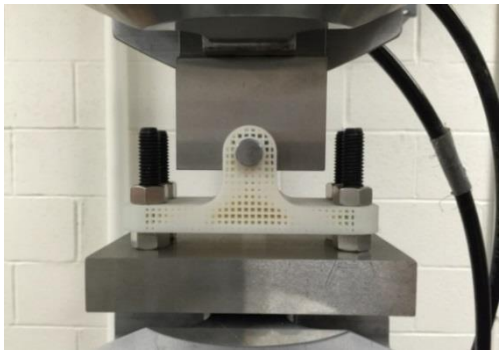

Figure 3.16: Experimental Setup for the Pillow Bracket.

The bracket specimens used for the bending test are printed by the same 3D printer and material as before. Figure 3.17 shows the specimens of the pillow bracket with uniform and the optimized variable-density structures, respectively. The two parts are designed for the same volume fraction of 50% of the original fully dense bracket. For both bracket designs, a thin skin layer is employed to cover the curved surfaces, where the broken ligaments are formed from the non-conformity between the bracket shape and the underlying lattice structure. As a result, the final volume fraction of the uniform and non-uniform brackets becomes 54% of the original fully dense bracket. In the compression testing, four specimens for both the uniform and non-uniform

bracket designs are printed using the same process parameters and build orientations to ensure that they are produced under the same conditions. The print direction of the pillow bracket is along its upright position.

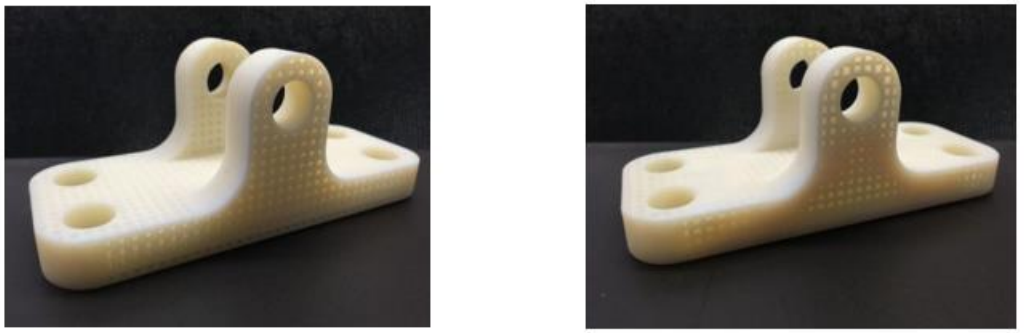

(a) Uniform density bracket (b) Optimized non-uniform bracket

Figure 3.17: 3D Printed Pillow Bracket Designs

Figure 3.18 shows the experimental results of the compression test for the uniform and optimized non-uniform pillow brackets, while Table 3.3 tabulates the initial tangent stiffness and strength values of the two designs. Note that the optimized non-uniform beam is much stiffer than the uniform beam (i.e. 119.7% increase) as it should be since the former is optimized for minimum compliance. Besides, the strength of the non-uniform beam increases by 75.4% over the uniform beam. Through this comparison, it is obvious that the LSTO method is a powerful tool to reduce the weight of the component while enhancing its stiffness and strength.

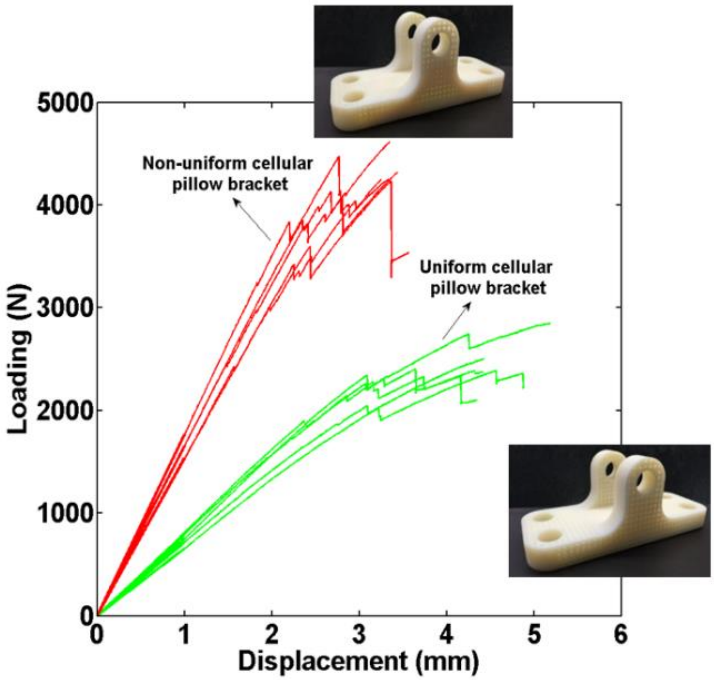

Figure 3.18: Loading Curves for the Uniform and Optimized Non-Uniform Cellular Structured Pillow Brackets.

Table 3.3: Comparison of Mechanical Properties of the Uniform and Optimized Brackets.

Property	Uniform	Optimized non-uniform	Enhancement (%)
Average stiffness (N/mm)	740.45	1626.9	119.7%
Average strength (N)	2497.2	4379.1	75.4%

3.2.4 Summary

In this work, a homogenization-based topology optimization method is proposed to optimize the design of variable-density cellular structure efficiently. Through this research, the following conclusions can be drawn:

- The proposed method effectively resolves the issues of intermediate densities and overhang structure seen in designs produced by standard topology optimization for additive manufacturing.
- Both numerical simulation and experiments demonstrate the accuracy of the elastic scaling law that takes the form of a quartic polynomial without the third order term.
- Mechanical properties of the component designed by the proposed method can be enhanced significantly after optimization; e.g. stiffness increases by more than 100% and strength increases by more than 75%.

There are still several issues that need to be resolved to further improve the propose optimization method for additive manufacturing. These issues include considering build orientation, anisotropic yield properties, and residual distortion in the optimization method. These and other issues are under active investigation.

3.3 Stress Constrained Problem

3.3.1 Stress Measure

The prominent characterization of stress constraint for topology optimization is the local nature of the stress. From the continuum mechanics point of view, the ideal way to enforce the stress constraint is to do this at every material point, which is known as local constraint strategy [38]. However, this may lead to a very large number of constraints for most engineering problems. Considering the highly non-linear dependency of stress constraint, this results in a very complicated sensitivity analysis and thus high computational cost. To reduce the number of constraints, several numerical methods, such as global stress measure [42, 115] and cluster/block stress measure [42-44], are proposed to formulate and control the stress in the structural design. The global stress measure aggregates the large number of local constraints into a single function by means of the P-norm or the Kreisselmeier-Steinhauser (KS) function, and significantly reduce the computational expense. The block/cluster stress measure is employed to divide the stresses into several clusters/blocks and enforces the P-norm stress for each cluster/block, in order to reduce the computational cost of local constraint scheme and poor local control of the global constraint. To simplify the calculation, the P-norm global stress measure is employed in this work to implement the stress constraint due to its conservative nature.

In the global stress measure, the original N local constraints are formulated by a single maximum stress constraint as:

$$\bar{\sigma}_{max}^{H} = \max_{e=1\cdots N}\left(\bar{\sigma}_{e}^{H}\right) \leq 1 \tag{3.4}$$

where $\overline{\sigma}_{max}^{H}$ is the maximum Hill's stress in the design domain, $\overline{\sigma}_{e}^{H}$ $(e = 1, \cdots N)$ represents the modified Hill's stress on element e, and N denotes total number of elements in the design domain. Since the formulation in Eq. (3.4) is non-differentiable, a smooth P-norm function is alternatively used to approximate the global maximum stress measure, and the constraint yields:

$$\sigma^{PN} = \left(\sum_{e=1}^{N} \left(\overline{\sigma}_{e}^{H}\right)^{P}\right)^{\frac{1}{P}} \leq 1 \tag{3.5}$$

where P represents factor of P-norm used to control smoothness of the approximation, σ^{PN} denotes P-norm stress used to estimate yielding of the structure. When $P \to 1$, the P-norm stress measure is the average stress of the design domain; when $P \to \infty$, σ^{PN} approaches to $\overline{\sigma}_{max}^{H}$. Note that the stress measure in Eq. (3.5) is a conservative measure as it overestimates the maximum local stress

$$\max_{e=1\cdots N}\left(\overline{\sigma}_{e}^{H}\right) \leq \left(\sum_{e=1}^{N}\left(\overline{\sigma}_{e}^{H}\right)^{P}\right)^{\frac{1}{P}}$$

In practical implementation, P can only be set as a limited value, since a large P would lead to even higher non-linearity for the stress constraints [42]. Hence, the control of P-norm in Eq. (3.6) on the actual maximum local stress is lacking. To address this issue, the adaptively scaling constraint proposed in [42, 116, 117] is adapted to reformulate Eq. (3.5) as:

$$\sigma^{PN} \leq \gamma^{I} \tag{3.6}$$

where γ is calculated iteratively, and I $(I \geq 1)$ represents the iteration number.

$$\gamma^{I} = \beta^{I} \frac{\left(\sigma^{PN}\right)^{I}}{\left(\overline{\sigma}_{max}^{H}\right)^{I}} \tag{3.7}$$

where $\beta^{I} \in (0,1)$. As can be seen, when $\beta^{I} = 1$, the inequality in Eq. (3.6) is equivalent to Eq. (3.4) and the optimization converges to the optimal solution. During the optimization, $\beta^{I} = 0.5$,

when γ^I oscillates between two successive iterations, otherwise $\beta^I = 1$. It is noted that Eq. (3.7) is a heuristic scheme to stabilize the convergence of the optimization. The expression of γ is non-differentiable [42], and the sensitivity would not include the derivatives.

3.3.2 Problem Formulation

3.3.2.1 Problem Statement

Using the global stress measure proposed in section 3 and the modified Hill's stress in Section 2.4, the mass minimization optimization with stress-constraint can be formulated by the discretization form as:

$$minimize \quad m(\boldsymbol{\rho}) = \sum_{e=1}^{N} \rho_e v_e \tag{3.8}$$

$$w.r.t \qquad \rho_e$$

$$such\ that \begin{cases} \boldsymbol{K}\boldsymbol{u} = \boldsymbol{f} \\ \overline{\boldsymbol{C}} = \overline{\boldsymbol{C}}(\boldsymbol{\rho}) \\ \sigma^{PN} \leq \gamma^I \\ 0 < \underline{\rho} \leq \rho_e \leq \overline{\rho} \leq 1, \qquad e = 1, \dots, N \end{cases} \tag{3.9}$$

where $m(\boldsymbol{\rho})$ is the objective function of the optimization problem, which represents the total mass of the structure. $\boldsymbol{\rho}$ is the density vector saving the relative density of element in the design domain. $\boldsymbol{K}$, $\boldsymbol{u}$ and $\boldsymbol{f}$ in the equilibrium equation denote stiffness matrix, global displacement and prescribed external loads, respectively. ρ_e is the relative density of element e , while v_e is its corresponding elemental volume. The design variable ρ_e is limited by the upper bound $\overline{\rho}$ and lower bound $\underline{\rho}$. $\overline{\boldsymbol{C}} = \overline{\boldsymbol{C}}(\boldsymbol{\rho})$ represents effective elastic model proposed in Section 2.3. The stress measure used in this work is the P-norm form formulated using Hill's stress proposed in Section 2.4.

3.3.2.2 Sensitivity Analysis

In this section, the sensitivity analysis of the optimization problem in Eq. (3.8) and Eq. (3.9) is derived. The Method of Moving Asymptotes (MMA) proposed by Svanberg [118] is employed to solve the optimization problem. The implementation of the MMA requires the first order derivatives of objective function and constraints, which are derived as follows.

The sensitivity of the objective function, $m(\boldsymbol{\rho})$, is

$$\frac{\partial m(\boldsymbol{\rho})}{\partial \rho_e} = v_e \tag{3.10}$$

The stress constraints in Eq. (3.6) is employed, and its first order derivative to the relative density can be calculated using the following chain rule:

$$\frac{\partial \sigma^{PN}}{\partial \rho_e} = \sum_{e=1}^{N} \frac{\partial \sigma^{PN}}{\partial \bar{\sigma}_e^H} \frac{\partial \bar{\sigma}_e^H}{\partial \rho_e} \tag{3.11}$$

In Eq. (3.11), the first term $\frac{\partial \sigma^{PN}}{\partial \bar{\sigma}_e^H}$ can be calculated as follows,

$$\frac{\partial \sigma^{PN}}{\partial \bar{\sigma}_e^H} = \left(\sum_{e=1}^{N} \left(\bar{\sigma}_e^H\right)^P\right)^{\left(\frac{1}{P}-1\right)} \left(\bar{\sigma}_e^H\right)^{P-1} \tag{3.12}$$

while the term $\frac{\partial \bar{\sigma}_e^H}{\partial \rho_e}$ can be calculated from Eq. (3.3) as

$$\frac{\partial \bar{\sigma}_e^H}{\partial \rho_e} = \frac{\partial \left[\left(\bar{\boldsymbol{\varepsilon}}^T \mathbb{R} \bar{\boldsymbol{\varepsilon}}\right)^{1/2}\right]}{\partial \rho_e} = \frac{1}{2}\left(\bar{\boldsymbol{\varepsilon}}^T \mathbb{R} \bar{\boldsymbol{\varepsilon}}\right)^{-\frac{1}{2}} \frac{\partial\left(\bar{\boldsymbol{\varepsilon}}^T \mathbb{R} \bar{\boldsymbol{\varepsilon}}\right)}{\partial \rho_e} = \frac{1}{2\bar{\sigma}_e^H}\left(2\bar{\boldsymbol{\varepsilon}}^T \mathbb{R} \frac{\partial \bar{\boldsymbol{\varepsilon}}}{\partial \rho_e} + \bar{\boldsymbol{\varepsilon}}^T \frac{\partial \mathbb{R}}{\partial \rho_e} \bar{\boldsymbol{\varepsilon}}\right) \tag{3.13}$$

According to the strain-displacement formulation, the macroscopic strain tensor on element e can be computed as

$$\bar{\boldsymbol{\varepsilon}} = \boldsymbol{B}\boldsymbol{u} \tag{3.14}$$

where $\boldsymbol{B}$ represents strain-displacement matrix and $\boldsymbol{u}$ is the vector of displacements. Substituting Eq. (3.14)into second term in Eq. (3.13),the derivatives can be expressed as:

$$2\bar{\boldsymbol{\varepsilon}}^T\mathbb{R}\frac{\partial\bar{\boldsymbol{\varepsilon}}}{\partial\rho_e}=2\bar{\boldsymbol{\varepsilon}}^T\mathbb{R}\frac{\partial(\boldsymbol{Bu})}{\partial\rho_e}=2\bar{\boldsymbol{\varepsilon}}^T\mathbb{R}\boldsymbol{B}\frac{\partial\boldsymbol{u}}{\partial\rho_e} \tag{3.15}$$

Based on the equilibrium equation in Eq. (3.9), the derivatives of $\frac{\partial\boldsymbol{u}}{\partial\rho_e}$ can be computed as

$$\frac{\partial\boldsymbol{u}}{\partial\rho_e}=\boldsymbol{K}^{-1}\frac{\partial\boldsymbol{f}}{\partial\rho_e}-\boldsymbol{K}^{-1}\frac{\partial\boldsymbol{K}}{\partial\rho_e}\boldsymbol{u} \tag{3.16}$$

For design-independent problem considering in this work, $\frac{\partial\boldsymbol{f}}{\partial\rho_e}=0$, we have $\frac{\partial\boldsymbol{u}}{\partial\rho_e}=-\boldsymbol{K}^{-1}\frac{\partial\boldsymbol{K}}{\partial\rho_e}\boldsymbol{u}$. Substituting it into Eq. (3.15) and replacing $\boldsymbol{K}$ with $\boldsymbol{K}=\boldsymbol{B}^T\bar{\boldsymbol{C}}\boldsymbol{B}$, Eq. (3.15) can be written as

$$2\bar{\boldsymbol{\varepsilon}}^T\mathbb{R}\frac{\partial\bar{\boldsymbol{\varepsilon}}}{\partial\rho_e}=-2\bar{\boldsymbol{\varepsilon}}^T\mathbb{R}\boldsymbol{B}\boldsymbol{K}^{-1}\boldsymbol{B}\frac{\partial\bar{\boldsymbol{C}}}{\partial\rho_e}\bar{\boldsymbol{\varepsilon}} \tag{3.17}$$

Substituting Eq. (3.17) back into Eq. (3.13) yields:

$$\frac{\partial\bar{\sigma}_e^H}{\partial\rho_e}=-\frac{1}{\bar{\sigma}_e^H}\bar{\boldsymbol{\varepsilon}}^T\mathbb{R}\boldsymbol{B}\boldsymbol{K}^{-1}\boldsymbol{B}\frac{\partial\bar{\boldsymbol{C}}}{\partial\rho_e}\bar{\boldsymbol{\varepsilon}}+\frac{1}{2\bar{\sigma}_e^H}\bar{\boldsymbol{\varepsilon}}^T\frac{\partial\mathbb{R}}{\partial\rho_e}\bar{\boldsymbol{\varepsilon}} \tag{3.18}$$

Substituting Eq. (3.12) and Eq. (3.18) into Eq. (3.11) yields:

$$\begin{aligned}\frac{\partial\sigma^{PN}}{\partial\rho_e}&=\sum_{e=1}^{N}\left[\left(\sum_{e=1}^{N}\left(\bar{\sigma}_e^H\right)^P\right)^{\left(\frac{1}{P}-1\right)}\left(\bar{\sigma}_e^H\right)^{P-1}\left(-\frac{1}{\bar{\sigma}_e^H}\bar{\boldsymbol{\varepsilon}}^T\mathbb{R}\boldsymbol{B}\boldsymbol{K}^{-1}\boldsymbol{B}\frac{\partial\bar{\boldsymbol{C}}}{\partial\rho_e}\bar{\boldsymbol{\varepsilon}}+\frac{1}{2\bar{\sigma}_e^H}\bar{\boldsymbol{\varepsilon}}^T\frac{\partial\mathbb{R}}{\partial\rho_e}\bar{\boldsymbol{\varepsilon}}\right)\right]\\&=-\sum_{e=1}^{N}\left(\sum_{e=1}^{N}\left(\bar{\sigma}_e^H\right)^P\right)^{\left(\frac{1}{P}-1\right)}\left(\bar{\sigma}_e^H\right)^{P-2}\bar{\boldsymbol{\varepsilon}}^T\mathbb{R}\boldsymbol{B}\boldsymbol{K}^{-1}\boldsymbol{B}\frac{\partial\bar{\boldsymbol{C}}}{\partial\rho_e}\bar{\boldsymbol{\varepsilon}}+\\&\quad\frac{1}{2}\sum_{e=1}^{N}\left(\sum_{e=1}^{N}\left(\bar{\sigma}_e^H\right)^P\right)^{\left(\frac{1}{P}-1\right)}\left(\bar{\sigma}_e^H\right)^{P-2}\bar{\boldsymbol{\varepsilon}}^T\frac{\partial\mathbb{R}}{\partial\rho_e}\bar{\boldsymbol{\varepsilon}}\end{aligned} \tag{3.19}$$

where $\frac{\partial\mathbb{R}}{\partial\rho_e}$ can be calculated from the definition, $\mathbb{R}=\bar{\boldsymbol{C}}^{\boldsymbol{T}}\mathbb{M}\bar{\boldsymbol{C}}$, as:

$$\frac{\partial\mathbb{R}}{\partial\rho_e}=\frac{\partial\bar{\boldsymbol{C}}^T}{\partial\rho_e}\mathbb{M}\bar{\boldsymbol{C}}+\bar{\boldsymbol{C}}^T\frac{\partial\mathbb{M}}{\partial\rho_e}\bar{\boldsymbol{C}}+\bar{\boldsymbol{C}}^T\mathbb{M}\frac{\partial\bar{\boldsymbol{C}}}{\partial\rho_{\boldsymbol{e}}}=2\frac{\partial\bar{\boldsymbol{C}}^T}{\partial\rho_e}\mathbb{M}\bar{\boldsymbol{C}}+\bar{\boldsymbol{C}}^T\frac{\partial\mathbb{M}}{\partial\rho_e}\bar{\boldsymbol{C}} \tag{3.20}$$

To calculate derivatives in Eq. (3.19), an adjoint variable $\boldsymbol{\mu}$ is introduced and defined as:

$$\boldsymbol{\mu}^T = \sum_{e=1}^{N}\left(\sum_{e=1}^{N}\left(\bar{\sigma}_e^H\right)^P\right)^{\left(\frac{1}{P}-1\right)}\left(\bar{\sigma}_e^H\right)^{P-2}\bar{\boldsymbol{\varepsilon}}^T\mathbb{R}\boldsymbol{B}\boldsymbol{K}^{-1} \tag{3.21}$$

$\boldsymbol{\mu}$ can be computed by solving the following adjoint equation:

$$\boldsymbol{K}\boldsymbol{\mu} = \sum_{e=1}^{N}\left(\sum_{e=1}^{N}(\bar{\sigma}_e^H)^P\right)^{\left(\frac{1}{P}-1\right)}(\bar{\sigma}_e^H)^{P-2}\boldsymbol{B}^T\mathbb{R}\bar{\boldsymbol{\varepsilon}} \tag{3.22}$$

Once $\boldsymbol{\mu}$ is obtained from Eq. (3.21), the derivative of P-norm stress measure in Eq. (3.18) can be expressed as:

$$\frac{\partial\sigma^{PN}}{\partial\rho_e} = -\bar{\boldsymbol{\varepsilon}}_{\boldsymbol{\mu}}^T\frac{\partial\bar{\boldsymbol{C}}}{\partial\rho_e}\bar{\boldsymbol{\varepsilon}} + \frac{1}{2}\sum_{e=1}^{N}\left(\sum_{e=1}^{N}\left(\bar{\sigma}_e^H\right)^P\right)^{\left(\frac{1}{P}-1\right)}\left(\bar{\sigma}_e^H\right)^{P-2}\bar{\boldsymbol{\varepsilon}}^T\left(2\frac{\partial\bar{\boldsymbol{C}}^T}{\partial\rho_e}\mathbb{M}\bar{\boldsymbol{C}} + \bar{\boldsymbol{C}}^T\frac{\partial\mathbb{M}}{\partial\rho_e}\bar{\boldsymbol{C}}\right)\bar{\boldsymbol{\varepsilon}} \tag{3.23}$$

where $\bar{\boldsymbol{\varepsilon}}_{\boldsymbol{\mu}}$ represent the "strain" of adjoint variable $\boldsymbol{\mu}$ and it can be calculated by $\bar{\boldsymbol{\varepsilon}}_{\boldsymbol{\mu}} = \boldsymbol{B}\boldsymbol{\mu}$. It can be seen from the derivative in Eq. (3.23), the sensitivity of the P-norm stress constraint is consisted of two parts: one is from the adjoint equation, the other is from the structure itself.

3.3.3 Numerical Examples and Experimental Validation

In this section, two three-dimensional (3D) examples are presented to examine efficiency and accuracy of the proposed homogenization based LSTO method for constrained stress problem. The objective of the optimization is to minimize the total mass of the structure under the constraint of allowable stress represented by modified Hill's stress. The optimization method is implemented

in MATLAB R2015a, and the MMA method [118] is applied as the optimizer to solve the constrained stress problem. Considering the high non-linearity of the stress constraint, the move limit of MMA is narrowed to ensure the convergence of the optimization. The initial volume fraction of the structure in the two examples is set to $\boldsymbol{V} = 0.9$. The optimization terminates if the differences of the objective function among three successive iterations is smaller than 1×10^{-3}, while the stress constraint is satisfied. It is assumed the lattice structured design is printed out by Objet Connex 260 in VeroWhitePlus, which has a Young's modulus of 1,747 MPa, Poisson's ratio of 0.3 and yield strength of 65 MPa.

3.3.3.1 Three-dimensional L-bracket Design

The first numerical example is the established L-bracket design problem, which is used here to examine the proposed framework for the structure with reentrant corner. Figure 3.19 illustrates dimension and boundary conditions of the L-bracket. The cross section of L-bracket is $15 \times 15\ \text{mm}^2$ with a side length of $45\ \text{mm}$. A mesh of 16,875 eight-node hexahedron elements is used to discretize the design domain and solve the FEA model. A load of 130 N is initially distributed over the two rows of elements as shown in the figure, and the relative densities of these elements are set to solid during the optimization. A fixed boundary condition is subjected to the upper surface of L-bracket. The lower and upper density limits of the lattice structure in the design domain is set to be $\underline{\rho} = 0.15$ and $\overline{\rho} = 0.95$, respectively. Note that the number of P in P-norm is set to 11 in this case to get P-norm value closer to the maximum local stress and capture the stress concentration at reentrant corner.

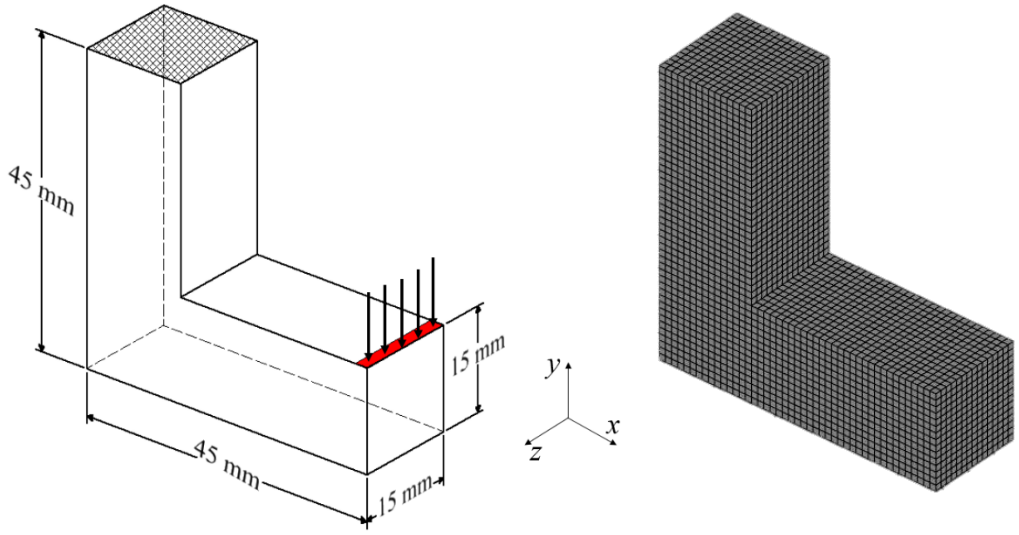

(a) (b)

Figure 3.19: Boundary Conditions and Dimensions of an L-Bracket. (a) Dimension of L-Bracket and (b) Mesh of the L-Bracket for Static Analysis.

The optimization results of the 3D L-bracket are presented in Figure 3.20, including density evolution and the evolution of the Hill's stress. As shown in the figure, more materials are distributed on the vertical surface of bracket, while on the horizontal surface materials are removed to form a lower density area. This is different from results in the two-dimensional design, in which a curved boundary is generated along the reentrant corner to avoid the stress concentration. There are two reasons leading to the difference. First, the anisotropy of cubic lattice structure results in the materials tends to distribute along the vertical and horizontal directions, which can provide stronger load path comparing with shear direction. Second, for 3D L-bracket, the loading applied to the solid edge tends to transform from the bottom and side surfaces of the bracket and leads to higher density concentration. Another interesting phenomenon is that there are a great number of intermediate densities existing in the transformation between the high-density region and the low-

density region. This implies that the stress based LSTO method tends to generate intermediate density to smooth the stress concentration. The evolution of Hill's stress distribution also supports this observation. As the density is optimized along the surface of the structure, the stress concentration is gradually reduced and averaged in the whole design domain.

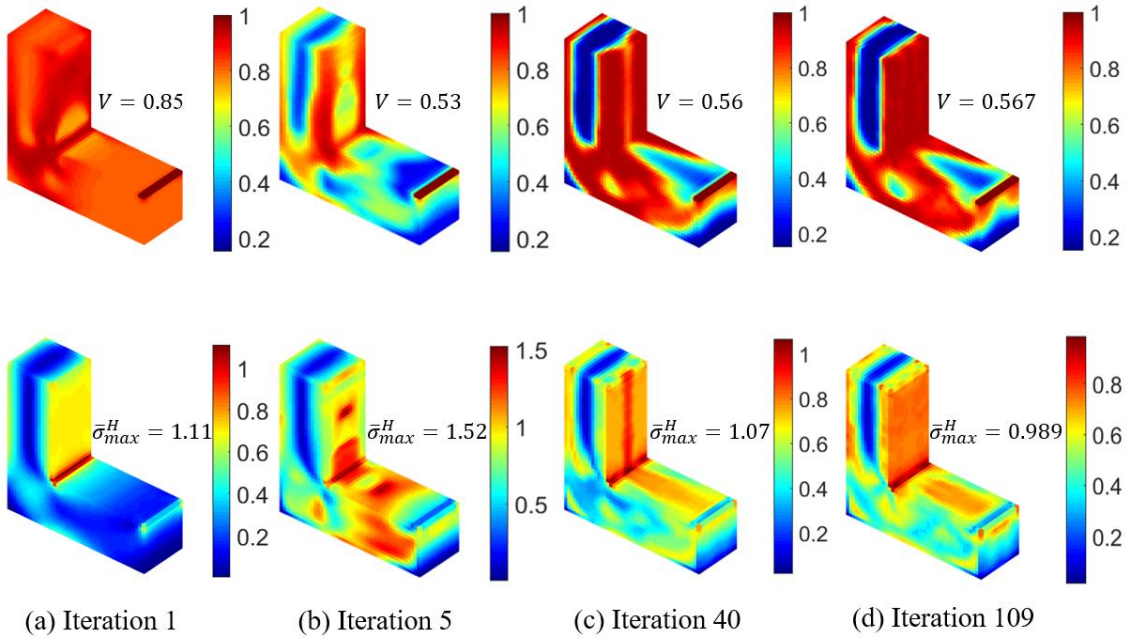

Figure 3.20: Density and Hill's Stress Evolution of the L-bracket Design: (a) Iteration 1, (b) Iteration 5, (c) Iteration 40 and (d) Iteration 105.

Figure 3.21 illustrates convergence history of the P-norm stress, maximum Hill's stress, and the objective function of the structure. As shown in Figure 3.21(a), using the adaptive constraint scheme for P-norm stress in Eq. (3.7), the maximum Hill's stress converges from 1.11 to 0.989 with the predefined limit of 1, while the P-norm stress converge to 1.55. This demonstrates that the proposed adaptive scheme can efficiently avoid the over-conservative global stress

measure and ensure approximation of the maximum stress to the predefined limit. It is also found the maximum stress oscillates remarkably in the first 20 iterations due to the existence of the reentrant corner. Simultaneously, the volume fraction of the structure is significantly reduced, and leads to the maximum stress first increases and then decreases. Finally, the volume fraction of the structure converges from 0.9 to 0.568 with a decrease of 36.89%. The volume fraction of the structure decreases from 0.9 to 0.568 after 105 iterations. It can be deduced that the optimization tends to remove material from the reentrant corner first, and then redistribute material to smoothly lower the maximum stress. As the iteration proceeds, the volume fraction increases to the convergent value, and the maximum stress converges to the predefined limit.

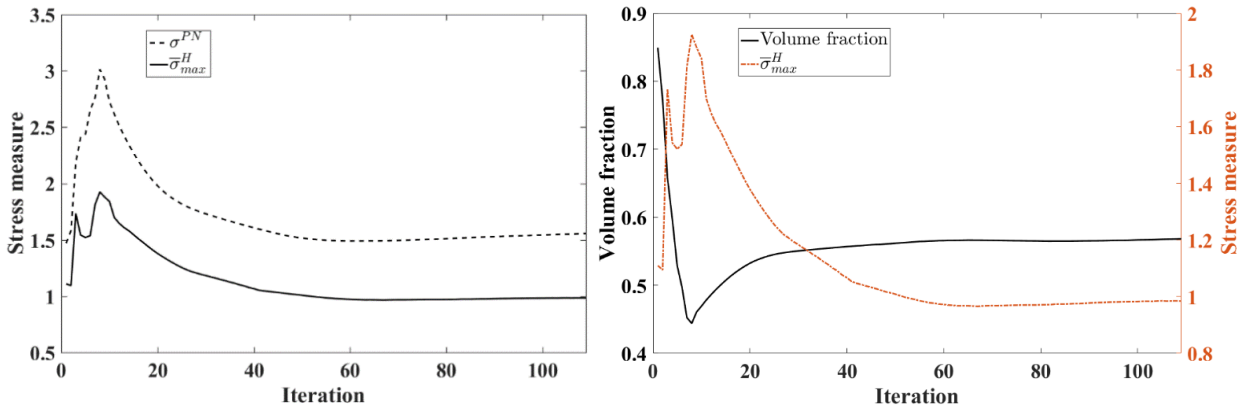

(a) (b)

Figure 3.21: Convergence History of Objective Function and Hill's Stress. (a) P-Norm Stress and Hill's Stress (b) Mass of the Structure and Maximum Hill's Stress.

Figure 3.22 illustrates various reconstructed designs of L-bracket with lattice unit sizes of 2, 2.5, and 3 mm. With decrease of the unit size, the density distribution of lattice structure tends

to converge to the density profile from optimization. Note that the unit size should be smaller than the size of the element used to discretize the design domain to ensure validity of the homogenization theory.

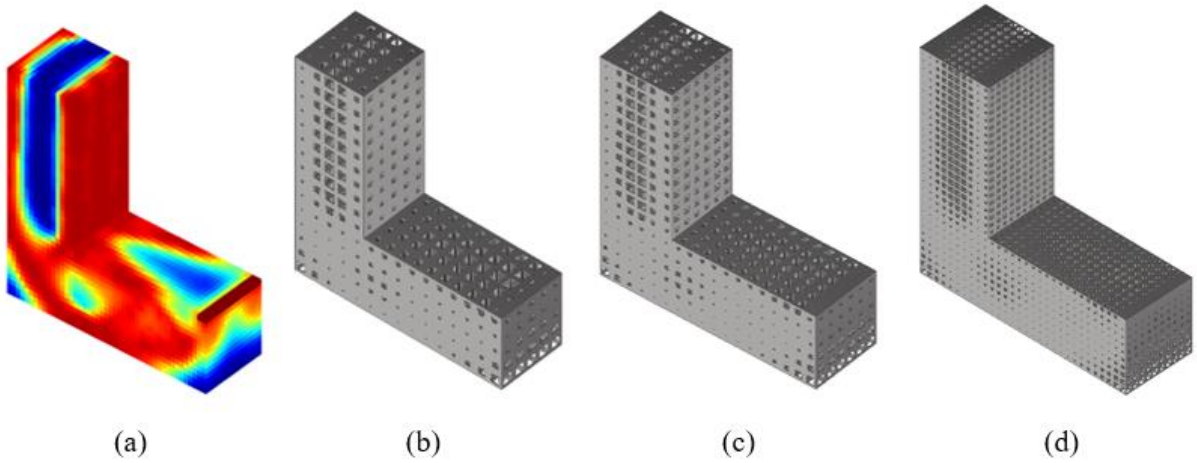

Figure 3.22: Reconstruction of the L-Bracket with Variable Density Lattice Structure. (a) Density Profile, (b) Design with Ligament Length of 3 mm, (c) Design with Ligament Length of 2.5 mm And (d) Design with Ligament Length of 2 mm.

3.3.3.2 Optimization of Three-point Bending Beam and Corresponding Experiments

The second example is a three-point bending beam used to validate stress-based LSTO method experimentally, due to its simplicity and accuracy for experiment measurement. Figure 3.23 illustrates the dimension and boundary conditions of the beam. The beam has a cross section of 15×15 mm^2 with a length of 120 mm. A remote displacement is applied to lower surface of the beam with a distance of 9 mm from the two sides of the beam. A load of 600 N is applied to

the center of the upper surface along the $-y$ direction. The elements used for the loading boundary are set to be solid during the optimization. A mesh of 27,000 eight-node hexahedron elements is used to discretize design domain and solve FEA model. The lower and upper bounds of the relative density for design domain is set to be [0.2, 0.95]. The P-norm of the stress constraint is set to be 10 in this case to get P-norm value closer to the maximum local stress.

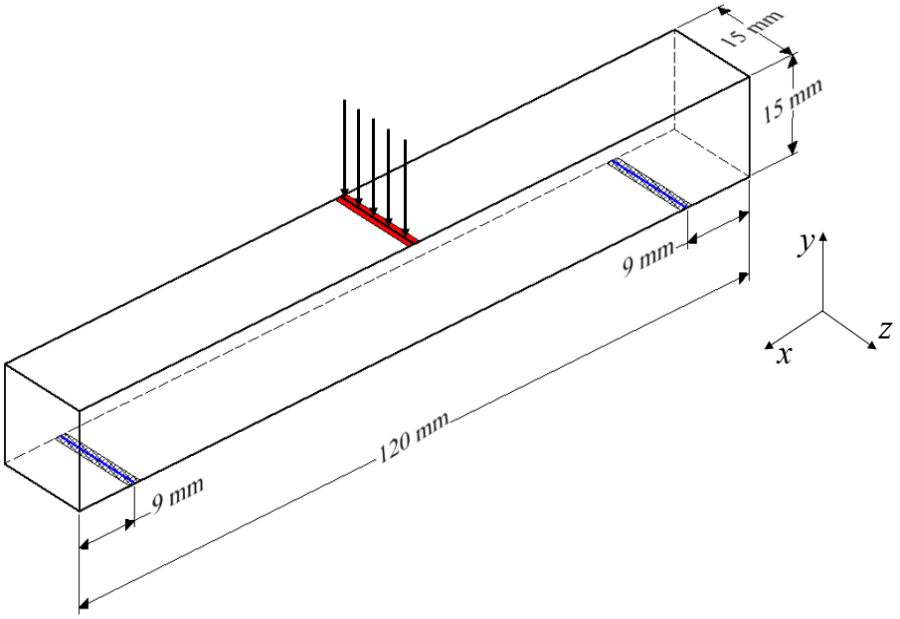

Figure 3.23: Dimension and Boundary Condition of 3-Point Bending Beam for Constrained-Stress Problem.

The iterative history of the optimization including relative density profile and Hill's stress profile are given in Figure 3.24 and Figure 3.25. As illustrated in the Figure 3.24, more materials are distributed on the position, where boundary conditions are applied, and higher density are concentrated along the loading paths between those boundaries. Differentiating from the result of the SIMP method, LSTO method tends to form structure based on anisotropy of material

properties, such as the cubic-like material distribution around the two support boundaries. The stress distributions in Fig. 18 prove this point of view. It can be seen that instead of transferring loading along connection of the boundaries, there exists a high stress band transferring loading in the vertical direction. Similar to the density distribution of L-bracket, there are a great number of intermediate densities existing between the high-density area and low-density area. The formation of these transformation area implies that the implementation of real material properties tends to form intermediate densities rather than 0-1 design. This is because the highly non-linearity of Hill's stress tends to generate smooth density distribution to transfer the loads.

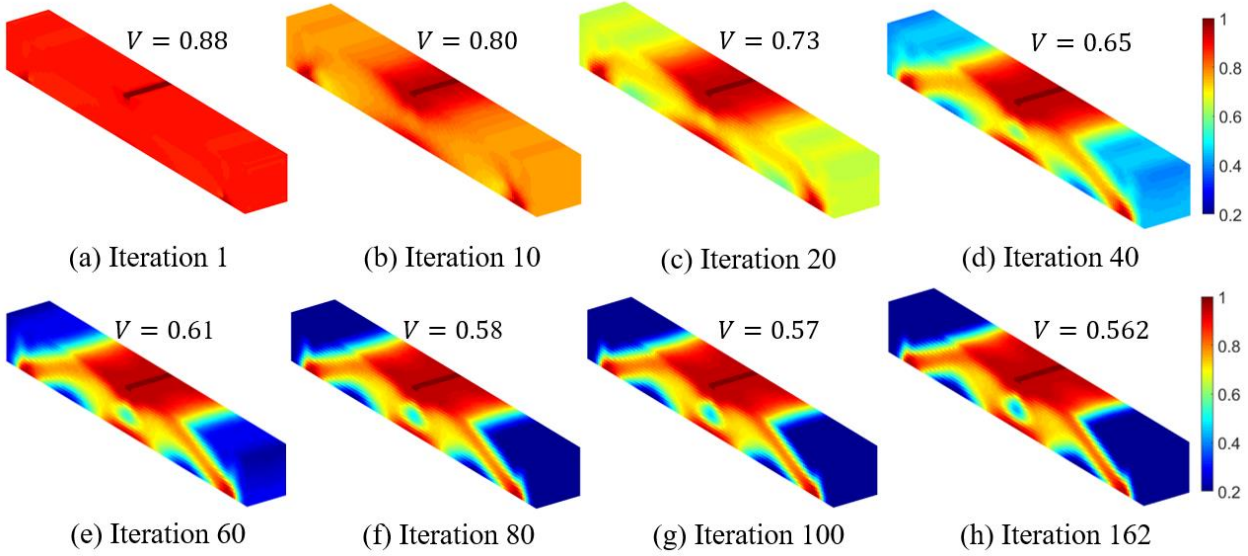

Figure 3.24: Density Evolution of Three-point Bending Beam Design.

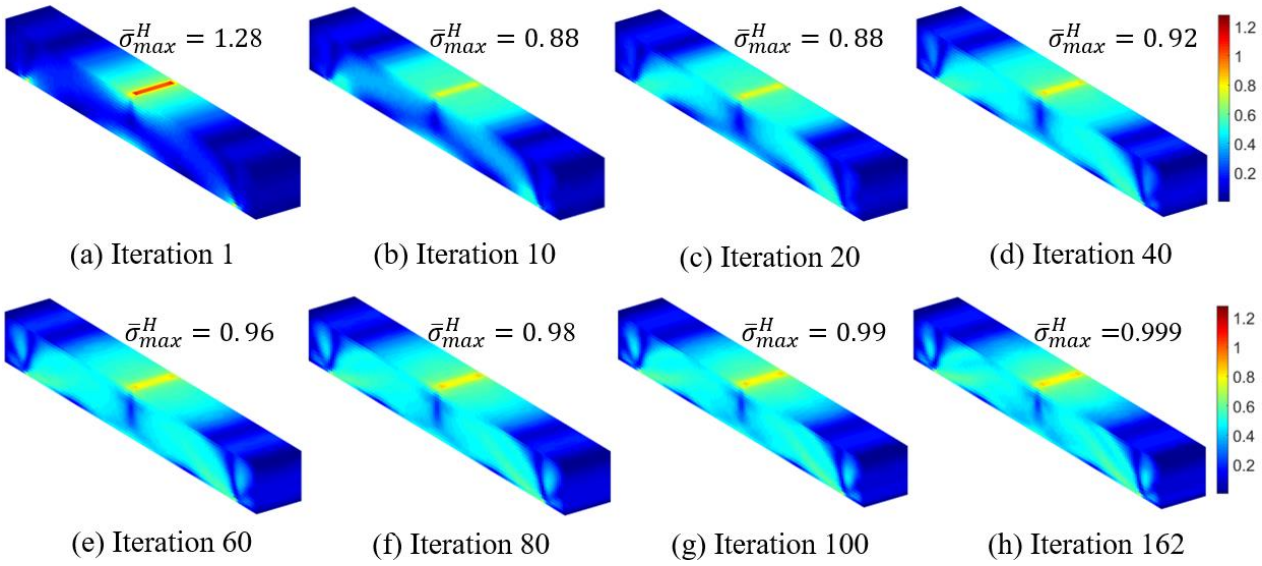

Figure 3.25: Hill's Stress Evolution of Three-Point Bending Beam Design.

The convergence history of the total volume and maximum stress is shown in Figure 3.26. As illustrated in the figure, the volume fraction of the structure converges from 0.9 to 0.562 after 162 iterations, while the maximum Hill's stress reduces from 1.28 to 0.999, as well as the P-norm stress from 1.68 to 1.44. In contrast to the optimization of L-bracket, the volume fraction of the three-point bending beam reduces smoothly and finally converges to the optimal design without oscillation, while the maximum Hill's stress first reduces to a smaller value than the predefined limit and then converges to 1. This implies that for a structure without reentrant corners, the optimization tends to smoothly evolves to the optimal design, and the Hill's stress gradually converges to the predefined limit.

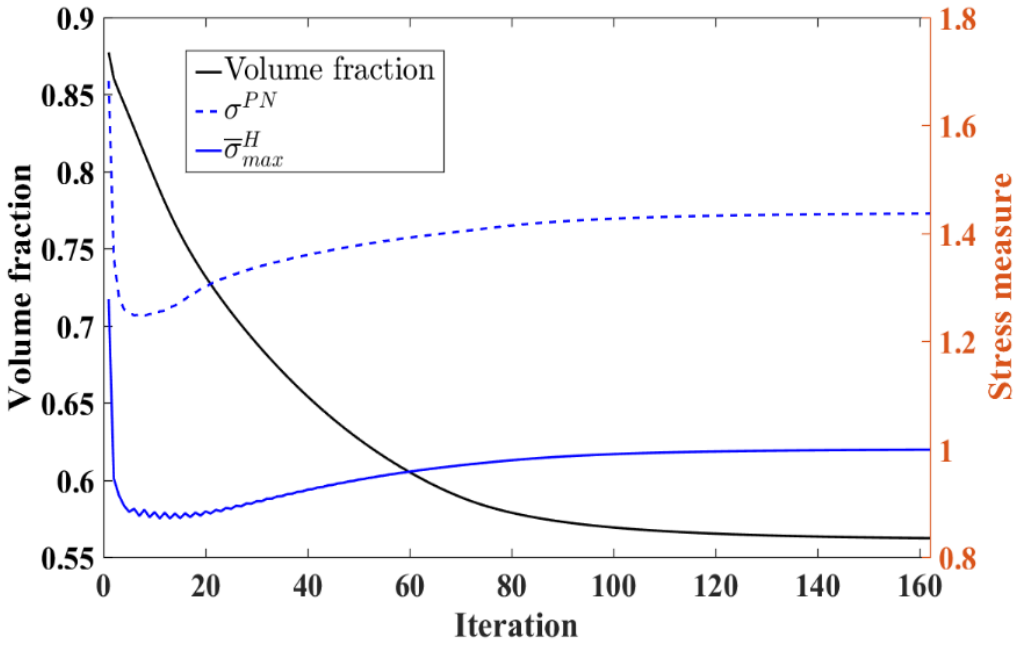

Figure 3.26: Convergence of the Maximum Hill's Stress and Overall Mass in the Optimization.

To examine accuracy of the design, the optimal three-point bending beam is reconstructed with variable density lattice structure and printed out in the VeroWhitePlus material using the Objet Connex 260 printer. For comparison purpose, a uniform beam with the same volume fraction is designed and manufactured to explore performance of the optimized design. Figure 3.27 illustrates the CAD models of the optimal design, uniform design, and their samples printed out for experiments. Three specimens of each design are printed out to lower the uncertainty of the experiments.

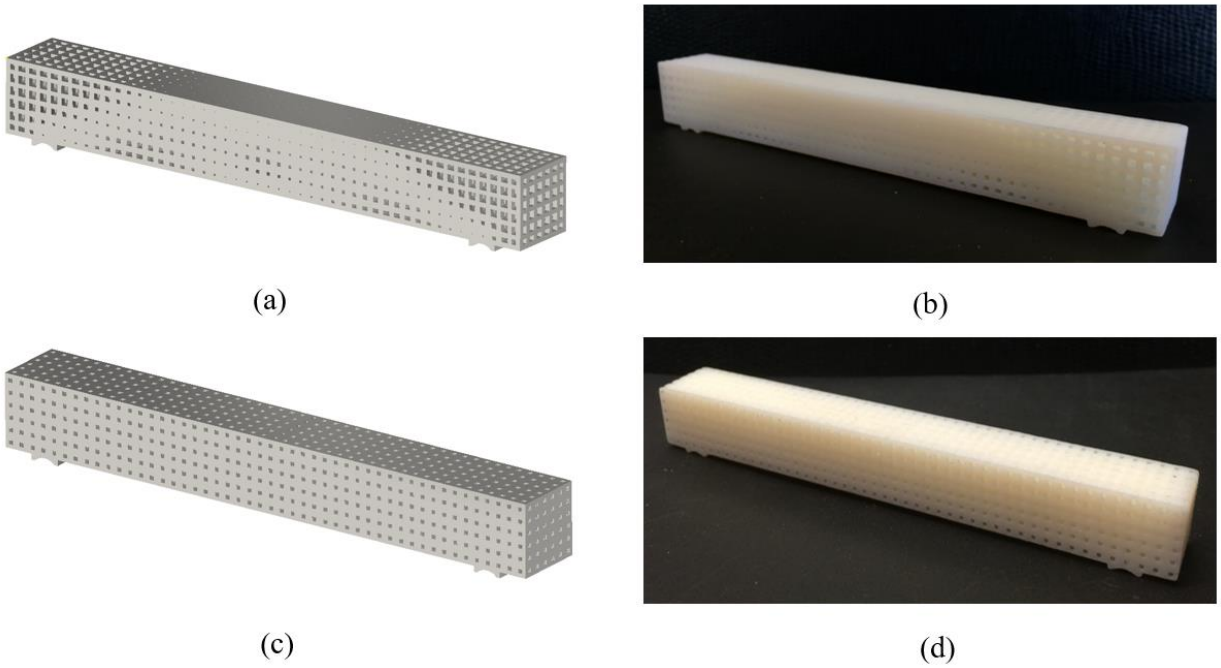

Figure 3.27: CAD Model and Printed Samples for Experiment. (a) CAD Model of Optimal Beam Infilled with Variable-Density Lattice Structure (b) Printed-out Optimal Beam (c) CAD Model of Uniform Beam (d) Printed-out Uniform Beam.

The experiments on the beams are conducted on a 3-point bending fixture on a load frame of MTS 880 system. The beams are loaded at a rate of 0.1 mm/s until failure. Once the beams are fractured, the displacements and corresponding loads are recorded by a data acquisition system for analysis. The experimental results of the optimal beams are presented in Figure 3.28. The designed loading of 3-point test is plotted using the dot dash line in the figure, the stiffness from the homogenized model is represented by the dash line, and the experimental results of the three samples are presented by the solid line. It can be observed that the stiffness predicted by homogenized model agrees well with the experiments. For the stress constraints, the design loading is 600 N, which implies that yielding of the beams should begin around that loading. As illustrated

in the figure, the yield point of the three beams is around 600 N. This demonstrates that the proposed homogenized model and modified Hill's yield criterion can be efficiently used for the variable-density lattice structure. Note that the macroscopic yield employed here is an approximation of the local yield of the structure. The primary purpose of this optimization scheme is to provide insight to the designer into the yield strength of the structure.

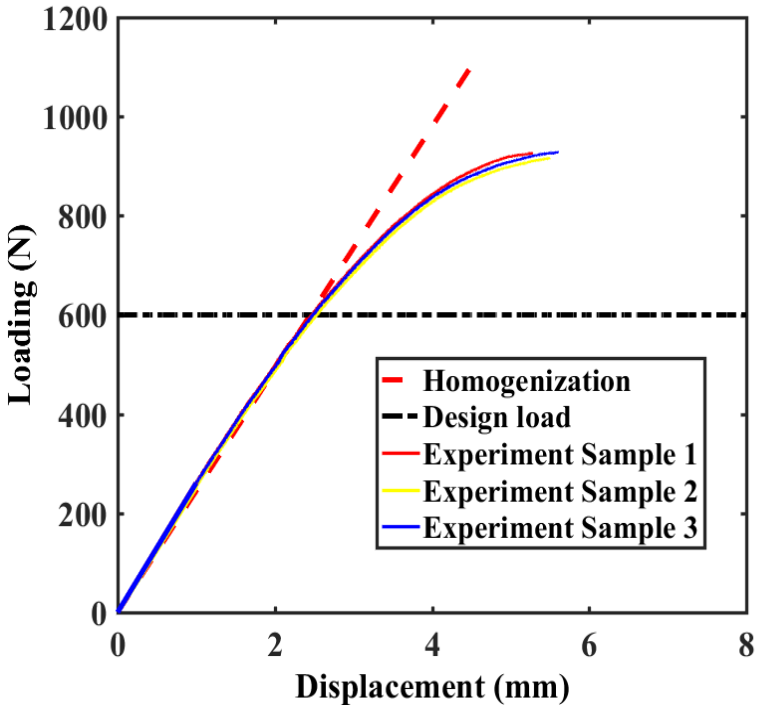

Figure 3.28: Experimental Results of the Optimal Beams.

The comparison of the experimental results between the optimal beam and uniform beam is illustrated in Figure 3.29, while the detailed mechanical properties from the experiments are tabulated in Table 3.4. As illustrated in the figure and table, the mean stiffness of the structure

increases from 96.34 N/mm to 258.3 N/m, which represents an increase of 168.1%. The mean yield loading of the optimal beam is 602.6 N, while the uniform beam is 150.8 N, which is an increase of 303.6%. This implies that the proposed methodology can significantly enhance yield performance of the structure with same volume fraction. The mean ultimate strength of the optimal beam is 926.9 N, while the mean value for uniform beam is 302.3 N, which represents an increase of 206.6%. For energy absorption, the increment is 173.6%, from 3.24 J to 1.184 J. These results show that the structure designed via the proposed optimization framework for lattice structure can achieve superior performance on mechanical properties, such as stiffness, yield loading, ultimate loading, and energy absorption, comparing with the uniform design. Especially considering the stress constraint, the proposed homogenized model coupled with modified Hill's yielding criterion can provide reasonably accurate representation for the performance of graded lattice design.

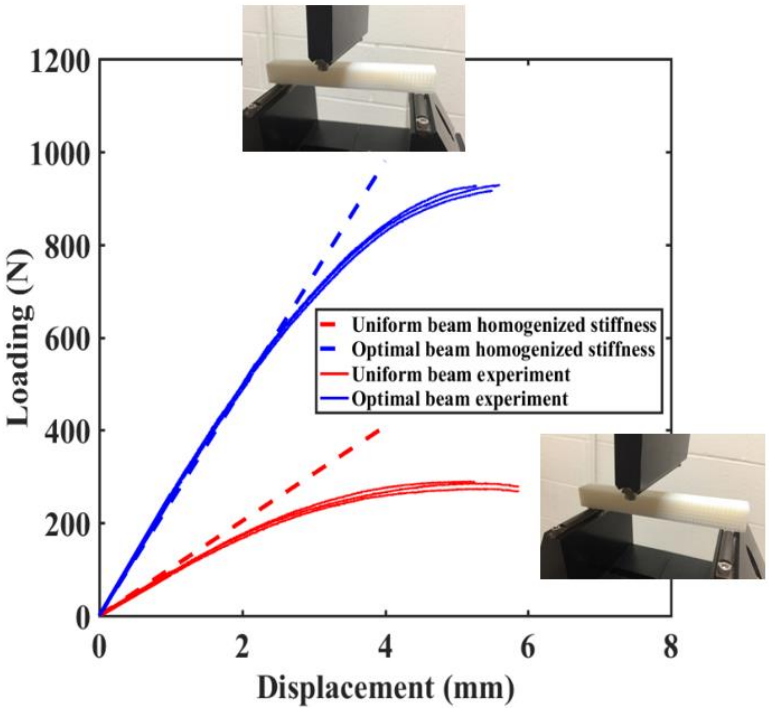

Figure 3.29: Comparison of the Testing for the Uniform Beam and Optimal Beam.

Table 3.4: Comparison of Mechanical Properties of Uniform Beam and Optimal Beam.

Item	Uniform beam	Non-uniform beam	Increment (%)
Average stiffness (N/mm)	96.34	258.3	168.1%
Average yield loading (N)	150.8	602.6	303.6%
Average ultimate strength (N)	302.3	926.9	206.6%
Average energy absorption (J)	1.184	3.240	173.6%

3.3.4 Summary

In this work, the authors proposed a framework for stress-based lattice structure topology optimization for additive manufacturing. Instead of using the SIMP material interpolation, asymptotic homogenization method is employed to efficiently obtained the effective elastic properties of lattice structure in terms of relative density, and a forth order polynomial is proposed for the curve fitting in whole density range. For the effective yield strength, the modified Hill's yield criterion considering the hydrostatic loading is applied to estimate the plastic performance of lattice structure. The material constants in the Hill's formulation are assumed to be the function of relative density. The uniaxial, pure shear and hydrostatic loading are applied to RVE of lattice structure to capture the three-independent yield strengths. A polynomial function is proposed to formulate normalized yield strength of the lattice structure with respect to relative density. Experimental validation for both the elastic and plastic properties demonstrate that the proposed constitutive models can accurately describe mechanical properties of lattice structure. In the optimization, the proposed material interpolation is used for the stress-based LSTO method. The

sensitivity analysis based on the proposed elastic and plastic model are derived for the optimization. Finally, two three-dimensional numerical examples are designed using the proposed stress based LSTO framework. The first example is the canonical L-bracket with a reentrant corner, which is used to investigate performance of methodology for structure with stress concentration. It can be observed that there are a great number of intermediate densities existing between the high-density area and low-density area. The material in the L-bracket tends to distribute according to the anisotropy of lattice structure. The second example is a three-point bending beam, which is designed for experimental validation. In the experiments, it is found that the yield loading of the optimal design falls within the yield band in the load-displacement curve. This implies that the proposed homogenized model and modified Hill's yield criterion based on the assumption of periodicity can also be efficiently used for the description of graded lattice structure. Moreover, we also compare optimal design with the uniform design of the same volume fraction. It can be observed from the experiments that the stress-based lattice design can significantly enhance both the elastic and plastic properties of the structure. These results further demonstrate the effectiveness of the proposed methodology.

3.4 Natural Frequency Problem

3.4.1 Governing Equation and Material Interpolation

In this section, the governing equations of the harmonic oscillations and their discretization using finite element analysis with the material interpolation model of lattice structures are presented.

Assume that a design domain $\Omega_r$bounded by a boundary of Γ, the equation of vibratory motion of a generic structure can be expressed in a continuum form as [119, 120]:

$$\varrho \boldsymbol{U}_{,tt}(\boldsymbol{x},t) + D\boldsymbol{U}_{,t}(\boldsymbol{x},t) + L\boldsymbol{U}(\boldsymbol{x},t) = \boldsymbol{F}(\boldsymbol{x},t), \quad \boldsymbol{x} \in \Omega_r \, , t > 0 \tag{3.24}$$

where $\boldsymbol{U}(\boldsymbol{x},t)$ is the displacement of the domain Ω_r at point $\boldsymbol{x}$ and time t. $D(\boldsymbol{x})$ denotes the viscous damping effect and $L(\boldsymbol{x})$ represents the linear partial differential operator, $\varrho(\boldsymbol{x})$ denotes the physical density of the base material. $\boldsymbol{F}(\boldsymbol{x},t)$ is the dynamic load. The subscribed comma in $\boldsymbol{U}_{,tt}$ and $\boldsymbol{U}_{,t}$ indicate the derivatives of displacement with respect to time.

Considering the steady-state response, the time-dependent terms in Eq. (3.24) can be replaced by $\boldsymbol{U}(\boldsymbol{x},t) = \boldsymbol{\phi}(\boldsymbol{x})e^{i\omega t}$ and $\boldsymbol{F}(\boldsymbol{x},t) = \boldsymbol{f}(\boldsymbol{x})e^{i\omega t}$. The time dependency of the dynamic problem can thus be simplified to:

$$-\omega^2 \varrho \boldsymbol{\phi}(\boldsymbol{x}) + i\omega D\boldsymbol{\phi}(\boldsymbol{x}) + L\boldsymbol{\phi}(\boldsymbol{x}) = \boldsymbol{f}(\boldsymbol{x}), \quad \boldsymbol{x} \in \Omega_r \tag{3.25}$$

where $\boldsymbol{\phi}(\boldsymbol{x})$ is the complex displacement, $\boldsymbol{f}(\boldsymbol{x})$ denotes the harmonic load, ω represents the vibration frequency, and i is the imaginary unit, satisfying the formulation, $i^2 = -1$. In this work, the aim is to optimize the first eigenfrequency of the structure without considering the damping term and external forces. Thus, the governing equation can be written as:

$$-\omega^2 \varrho \boldsymbol{\phi}(\boldsymbol{x}) + L\boldsymbol{\phi}(\boldsymbol{x}) = 0, \qquad \boldsymbol{x} \in \Omega_r \tag{3.26}$$

Multiplying the virtual displacement $\boldsymbol{\psi}(\boldsymbol{x})$ on both sides of Eq. (3.26) and integrating it over the domain Ω_r, one can obtain the following weak form of the governing equation as:

$$\int_{\Omega_r} C_{ijkl}\varepsilon_{kl}(\boldsymbol{\phi})\varepsilon_{ij}(\boldsymbol{\psi})d\Omega = \omega^2 \int_{\Omega_r} \varrho\phi_i\psi_i d\Omega \tag{3.27}$$

Appling the FEA scheme for the above equation, the state equation of the eigenfrequency can be expressed in a discretized form as:

$$\mathbf{K}\boldsymbol{\phi} = \omega^2\mathbf{M}\boldsymbol{\phi} \tag{3.28}$$

where **K** and **M** denotes the global stiffness and mass matrix, respectively. The calculation of these two matrixes can be carried out by assembling the element matrix as:

$$\mathbf{K} = \sum_e \boldsymbol{k}_e = \sum_{\boldsymbol{e}} \int_{\Omega_e} \boldsymbol{B}^T \boldsymbol{C}(\rho_e)\boldsymbol{B}d\Omega \tag{3.29}$$

$$\mathbf{M} = \sum_e \boldsymbol{m}_e = \sum_{\boldsymbol{e}} \int_{\Omega_e} \rho_e\varrho\boldsymbol{N}^T\boldsymbol{N}d\Omega \tag{3.30}$$

where $\boldsymbol{k}_e$ and $\boldsymbol{m}_e$ represent the stiffness and mass matrix of e^{th} element, respectively. $\boldsymbol{B}$ is the strain-displacement matrix and $\boldsymbol{N}$ is the shape function matrix. Instead of using power law in SIMP method, the homogenized model, $\boldsymbol{C}(\rho_e)$, proposed in section 2.3 is employed for the description of the constitutive model in terms of relative density. The real mass of the e^{th} element can be calculated by the production of relative density ρ_e and mass density ϱ of the isotropic base material.

Note that the artificial localized mode is an important issue in the SIMP method and occurs when the relative density in a local region is small enough. The reason of the problem has been well documented and explained by Pedersen [50]. When the relative density tends to void, the extremely high ratio of the penalization model of mass over stiffness leads to the artificial localized modes. Therefore, some modification for the penalization function is proposed to

eliminate the problem at low-density areas, referring to the works of [50, 52, 121]. For LSTO method, the quartic polynomial interpolation used in this work can be expressed as the following form:

$$\boldsymbol{C}(\boldsymbol{\rho}) = \boldsymbol{a}\boldsymbol{\rho}^4 + \boldsymbol{b}\boldsymbol{\rho}^2 + \boldsymbol{c}\boldsymbol{\rho} \tag{3.31}$$

where $\boldsymbol{a}$, $\boldsymbol{b}$ and $\boldsymbol{c}$ are the constants vector used to fit the polynomial formulation for elastic modulus. Based on Eq. (3.31), the ratio of the mass over stiffness can be written as:

$$\frac{\boldsymbol{\rho}}{\boldsymbol{C}(\boldsymbol{\rho})} = \frac{1}{\boldsymbol{a}\boldsymbol{\rho}^3 + \boldsymbol{b}\boldsymbol{\rho}^1 + \boldsymbol{c}} \tag{3.32}$$

When the relative density approximates to zero, the ratio tends to be a constant $1/\boldsymbol{c}$. As mentioned by [50, 52, 53], this can avoid the localized mode problem. Moreover, the purpose of the optimization is to infill the component with variable-density lattice structure rather than a black and white design black and white structure (0/1 design). For manufacturability, the lower bound of relative density in our problem is larger than zero, i.e. $\rho > 0.1$. Therefore, the artificial localized modes are not a problem in the proposed methodology.

3.4.2 Methodology of Lattice Structured Topology Optimization

3.4.2.1 Optimization Formulation

The problem of maximizing fundamental eigenfrequency of vibration elastic structures can be expressed as:

$$\max_{\rho_1,\cdots,\rho_{N_e}} J = \left\{ \min_{i=1,\cdots,I} \{\lambda_i = \omega_i^2\} \right\} \tag{3.33}$$

$$s.t. \begin{cases} \boldsymbol{K}\phi_i = \omega_i^2 \boldsymbol{M}\phi_i, & i = 1, \dots, I \\ \phi_i^T \boldsymbol{M}\phi_k = \delta_{ik}, i \geq k, & k, i = 1, \dots, I \\ \boldsymbol{C} = \boldsymbol{C}(\boldsymbol{\rho}) \\ \sum_{j=1}^{N_e} \rho_j v_j \leq V^*, & j = 1, \dots, N_e \\ 0 \leq \rho_L \leq \rho_j \leq \rho_U \leq 1 \end{cases} \tag{3.34}$$

where J is the objective function and equal to the fundamental eigenvalue. ω_i and ϕ_i are the i^{th}eigenfrequency of the structure and the corresponding eigenvector, respectively. $\boldsymbol{K}$ and $\boldsymbol{M}$ are the global stiffness matrix and mass matrix, which are formulated in Eq. (3.29) and Eq.(3.30), respectively. $\boldsymbol{C}(\boldsymbol{\rho})$ is the constitutive law of lattice structure obtained in Section 2.3. $\boldsymbol{\rho}$ indicates the elemental density vector, ρ_j and v_j are the relative density and elemental volume of j^{th} element, and N_e represents the total number of the elements in the design domain. ρ_L and ρ_U denote the lower bound and upper bound of the relative density, which is restricted in the range of [0, 1]. The first equality formula is the governing equation while the second equality is the assumption of $\boldsymbol{M}$ orthonormalization, where δ_{ik} is the Kronecker delta. The third equality is the scaling law of lattice structure. The first inequality constrains the volume fraction of the admissible design domain to a predefined value, V^*. In the optimization procedure, since the order of fundamental eigenfrequency can change, a number of I candidate eigenfrequencies are taken into account in each iteration.

3.4.2.2 Sensitivity Analysis

Using the Lagrangian multiplier method, the optimization problem subject to the volume fraction constraint is of the following form:

$$\mathcal{L} = J + \alpha\left(\sum_{j=1}^{N_e} \rho_j v_j \leq V^*\right) \tag{3.35}$$

where α denotes the Lagrangian multiplier of volume constraints. In the optimization process, the variable α is fixed first and we solve the problem of Eq. (3.33)-(3.34) to obtain the design variable ρ_j, then α is updated and the termination criteria is checked. If the termination criteria are satisfied, the optimization result is obtained, otherwise, the iteration continues until the results converge.

In the admissible design domain, the sensitivity of the i^{th} eigenvalue λ_i with respect to the j^{th} design variable ρ_j can be calculated as:

$$\frac{\partial J}{\partial \rho_j} = \frac{\partial \lambda_i}{\partial \rho_j} = \boldsymbol{\phi}_i^T\left(\frac{\partial \boldsymbol{K}}{\partial \rho_j} - \lambda_i \frac{\partial \boldsymbol{M}}{\partial \rho_j}\right)\boldsymbol{\phi_i} \tag{3.36}$$

where the derivatives of the stiffness matrix and the mass matrix can be computed explicitly from the material interpolation in Eq. (3.29) and Eq. (3.30) as:

$$\frac{\partial \boldsymbol{K}}{\partial \rho_j} = \sum_{j=1}^{N_e}\left(\int_{\Omega_j} \boldsymbol{B}^T \frac{\partial \boldsymbol{C}(\rho_j)}{\partial \rho_j}\boldsymbol{B} d\Omega\right) \tag{3.37}$$

$$\frac{\partial \boldsymbol{M}}{\partial \rho_j} = \sum_{j=1}^{N_e}\left(\int_{\Omega_j} \varrho \boldsymbol{N}^T \boldsymbol{N} d\Omega\right) \tag{3.38}$$

However, as for repeated natural frequencies of adjacent orders, the sensitivity analysis with respect to the design variables cannot be derived straightforwardly, because the eigenvector associated with multiple natural frequencies of an identical value may not unique [122]. Assume that the eigenvalue problem in Eq. (3.34) yields a repeated frequency problem with N-fold multiple eigenvalues as:

$$\tilde{\lambda} = \lambda_i = \omega_i^2, i = 1, \dots, N \tag{3.39}$$

where $\tilde{\lambda}$ represents the N-fold multiple eigenvalues, N is the number of repeated first natural frequencies and $N > 1$. Here, it assumes that $N \leq I$, the number of eigenfrequencies considered in the optimization problem.

Following the work of Du [52], for the structure with multiple repeated eigenfrequencies, the sensitivity analysis of the topology optimization problem can be solved by means of a mathematical perturbation analysis of multiple eigenvalues and the corresponding eigenvectors shown in the following equation:

$$det[\boldsymbol{f}_{sk}^T \Delta\rho - \delta_{sk}\Delta\rho] = 0, \quad s, k = 1, \dots, N \tag{3.40}$$

where δ_{sk} denotes the Kronecker delta while $\boldsymbol{f}_{sk}$ is the generalized gradient whose expression can be written as:

$$\boldsymbol{f}_{sk} = \left\{ \boldsymbol{\phi}_s^T \left(\frac{\partial \boldsymbol{K}}{\partial \rho_1} - \tilde{\lambda} \frac{\partial \boldsymbol{M}}{\partial \rho_1} \right) \boldsymbol{\phi}_k, \dots, \boldsymbol{\phi}_s^T \left(\frac{\partial \boldsymbol{K}}{\partial \rho_{N_e}} - \tilde{\lambda} \frac{\partial \boldsymbol{M}}{\partial \rho_{N_e}} \right) \boldsymbol{\phi}_k \right\}^T, \quad s, k = 1, \dots, N \tag{3.41}$$

where $\frac{\partial \boldsymbol{K}}{\partial \rho_j}$ and $\frac{\partial \boldsymbol{M}}{\partial \rho_j}$ $(j = 1, \dots, N_e)$ can be calculated from the Eq. (2.44) and Eq. (2.45).

In the case of the *N*-multiplicity natural frequency, in order to assume a particular case, all the scalar products in Eq. (3.38), except the diagonal ones are 0, that is:

$$\boldsymbol{f}_{sk}^T \Delta\rho = 0, \qquad s \neq k, \quad s, k = 1, \dots, N \tag{3.42}$$

In this special case, the increment $\Delta\lambda_i$ of a natural eigenfrequency $\lambda_i = \omega_i^2$ can then be determined:

$$\Delta\lambda_i = \boldsymbol{f}_{ii}^T \Delta\rho \tag{3.43}$$

Based on Eq. (3.39) , the item $\boldsymbol{f}_{ii}$ takes the following form:

$$\boldsymbol{f}_{ii} = \left\{ \boldsymbol{\phi}_i^T \left(\frac{\partial \boldsymbol{K}}{\partial \rho_1} - \tilde{\lambda} \frac{\partial \boldsymbol{M}}{\partial \rho_1} \right) \boldsymbol{\phi}_i, \dots, \boldsymbol{\phi}_i^T \left(\frac{\partial \boldsymbol{K}}{\partial \rho_{N_e}} - \tilde{\lambda} \frac{\partial \boldsymbol{M}}{\partial \rho_{N_e}} \right) \boldsymbol{\phi}_i \right\}^T, \qquad i = 1, \dots, N \tag{3.44}$$

Thus, if the optimum increments of density $\Delta\rho$ satisfy Eq. (3.40), the generalized gradient $\boldsymbol{f}_{ii}$ has the same form with the case of a unique eigenfrequency.

Given all the discussions above, the modified mathematical model of the maximization of first eigenfrequency problem through topology optimization can be formulated as:

$$\max_{\beta, \Delta\rho_1, \dots, \Delta\rho_{N_e}} \{\beta\} \tag{3.45}$$

$$s.t. \begin{cases} \beta - [\lambda_i + \boldsymbol{f}_{ii} \Delta\rho] \le 0 \quad if \;\; i = I = N \\ \beta - [\lambda_i + \Delta\lambda_i] \le 0 \qquad\qquad i = 1, \dots, N \\ det[\boldsymbol{f}_{sk} \Delta\rho - \delta_{sk} \Delta\lambda] = 0, \qquad s, k = 1, \dots, N \\ \sum_{j=1}^{N_e} (\rho_j + \Delta\rho_j) v_j \le V^* \\ 0 < \rho_L \le \rho_j + \Delta\rho_j \le \rho_U, \qquad j = 1, \dots, N_e \end{cases} \tag{3.46}$$

where β is the new objective function and $\Delta\rho_j$ are the practical variables to proceed the optimization process. In the numerical implementation, after the multiplicity of the first natural eigenfrequency is determined, the model can be reformed into a corresponding case to implement the sensitivity analysis.

3.4.3 Numerical Examples and Experimental Validation

In this section, two numerical examples are presented to examine the accuracy of the homogenized model and the effectiveness of the LSTO method. The optimized design is reconstructed using variable-density lattice structure, and both full-scale simulations and experiments are conducted to validate the proposed methodology. The purpose of the optimization

is to maximize the first eigenfrequency of the structure under the constraint of volume fraction. The optimization terminates if the difference of the first eigenfrequency of the structure within two successive iterations is smaller than 1×10^{-3} while the constraint of the volume fraction is satisfied. If not specified, density limits of the lattice structure are defined as $\rho_L = 0.25$ and $\rho_U = 0.9$. It assumes the lattice structure is printed by the EOS M290 with Ti6Al4V, of which the Young's modulus is 108 Gpa, the Poisson's ratio is 0.3, and the physical density is $4430\ \mathrm{kg/m^3}$. It is also mentioned that numerical sub-optimization problem is solved by the Method of Moving Asymptotes (MMA) [123, 124] while the FEA is performed using ANSYS v17.2.

3.4.3.1 Cantilever Beam

As a verification of the proposed optimization algorithm, a simple canonical problem of a cantilever beam is considered first. Figure 3.30 illustrates the CAD model of the cantilever beam, as well as the meshed and the FEA model. The beam has a square cross section with a dimension of $15\ \mathrm{mm} \times 15\mathrm{mm}$ and the length of the beam is $120\ \mathrm{mm}$. A mesh of 38437 eight-node hexahedron elements is used to discretize the design domain and solve the modal analysis. The volume fraction of the structure is restricted to $V^* = 0.6$. In the problem, one end of the beam is fixed while the other surfaces are free.

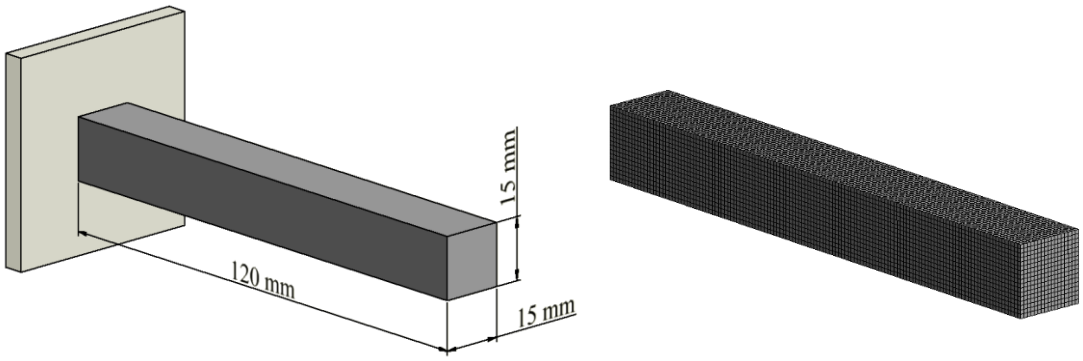

(a) (b)

Figure 3.30: Model of a Cantilever Beam: (a) CAD Model and Boundary Condition; (b) Meshed Model.

Figure 3.31 gives the optimization results of cantilever beam including optimal density distribution, optimized design and the iteration history of the first eigenfrequency. After the optimization, higher densities tend to concentrate near the fixed boundary while lower densities are distributed at the opposite direction. There are a number of intermediate densities between the higher density and lower density, shown as the yellow area. A section view of the optimal density distribution is given in Figure 3.31(b), where it is seen that more materials are distributed along the surface of the beam than at center region of the beam, which leads to a larger stiffness of the beam and thus the increase of the eigenfrequency. The first eigenfrequency of the structure increases from 671.5 Hz to 1281.3 Hz after 55 iterations, with an increment of 90.81%. This illustrates the efficiency of the proposed method for the maximization of the fundamental frequency.

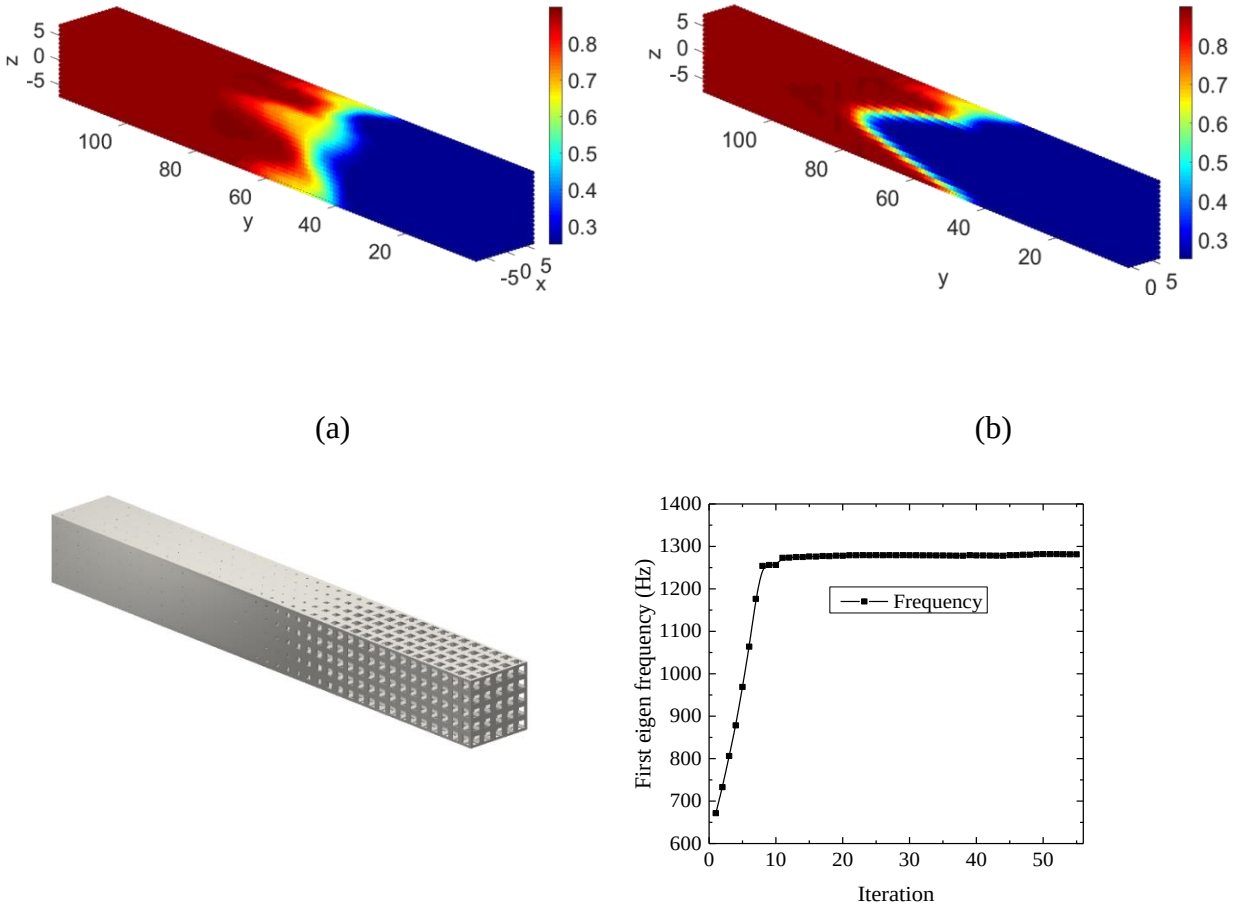

Figure 3.31: Optimization Results: (a) Optimized Density Distribution of the Beam; (b) Section View of the Density Distribution at $x > 0$; (c) Optimized Design Using Variable-Density Lattice Structure; (d) Iteration History of the First Eigenfrequency.

To examine the accuracy of the optimization, full-scale simulations for both the uniform and optimized beam infilled with lattice structure are carried out to compare with the homogenized results. The uniform beam is meshed using 197712 elements and the simulation results are given in Figure 3.32. The first eigen-frequency of the uniform beam is 676.4 Hz, which is 4.9 Hz or 0.73% different from the homogenized result. For the optimized beam, a mesh of 506841 elements

is used to solve the modal analysis and the result is illustrated in Figure 3.33. The first eigenfrequency of the optimized beam is 1245.3 Hz and the difference from the homogenized model is 36.0 Hz or 2.81%. It can be seen that full-scale simulations are in good agreement with the homogenized results. This implies that the homogenization is reasonably accurate for the description of the design by LSTO method.

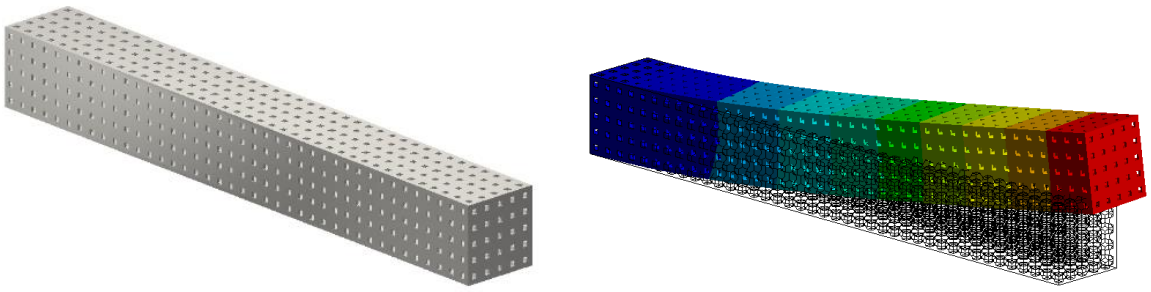

(a) (b)

Figure 3.32: Full-scale Simulation for the Cantilever Beam with Uniform Lattice Structure ($V^* = 0.6$). (a) CAD Model of the Uniform Beam; (b) First Mode of the Cantilever Beam, $\omega_1 = 676.4$ Hz.

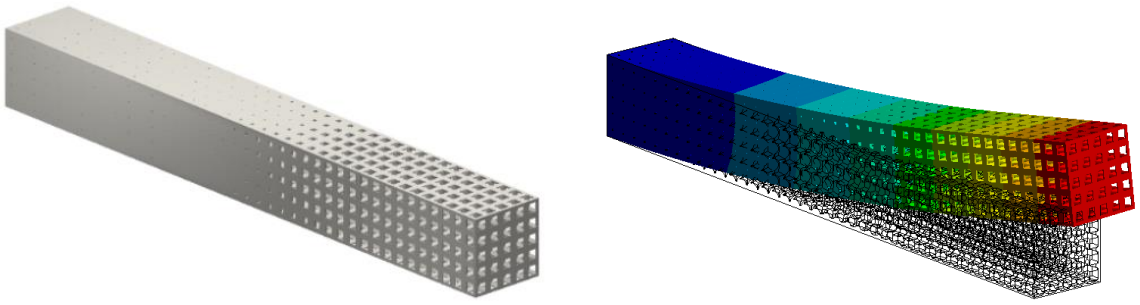

(a) (b)

Figure 3.33: Full-scale Simulation for the Cantilever Beam with Optimized Lattice Structure ($V^* = 0.6$): (a) CAD Model of the Non-Uniform Beam; (b) First Mode of the Optimized Beam, $\omega_1 = 1245.3$ Hz.

The original purpose of the methodology is to promote the optimized design with predictable properties for practical application using current AM techniques. To examine the performance of the design, both the uniform and optimized beam were printed for vibration tests. However, since the ideal fixed boundary conditions subjected to the cantilever beam are difficult to realize, a fixture with four bolt holes is added to the boundary end of the CAD models of the two beams, Figure 3.34. The photos of the printed-out beams are given in Figure 3.35, in which the fixture is merged with the beam and printed as a unified component.

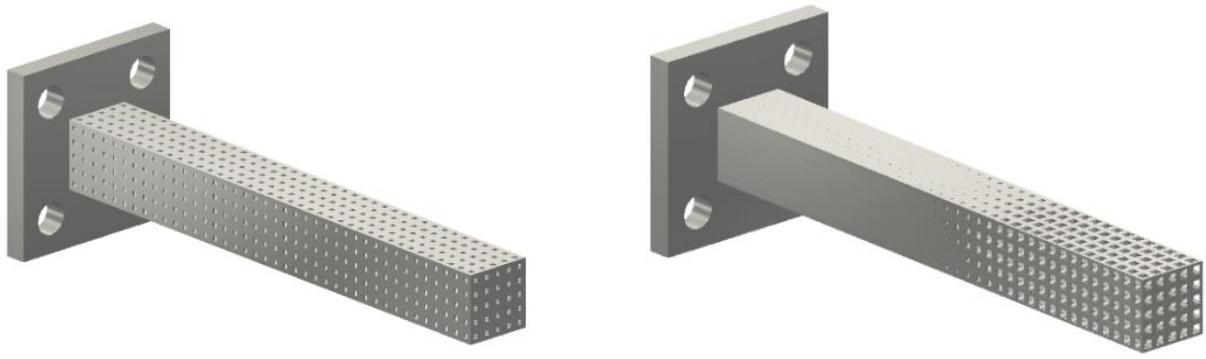

(a) (b)

Figure 3.34: CAD Model of the Cantilever Beams with the Fixture for Experiments: (a) Uniform Lattice Structured Beam; (b) Optimized Lattice Structured Beam.

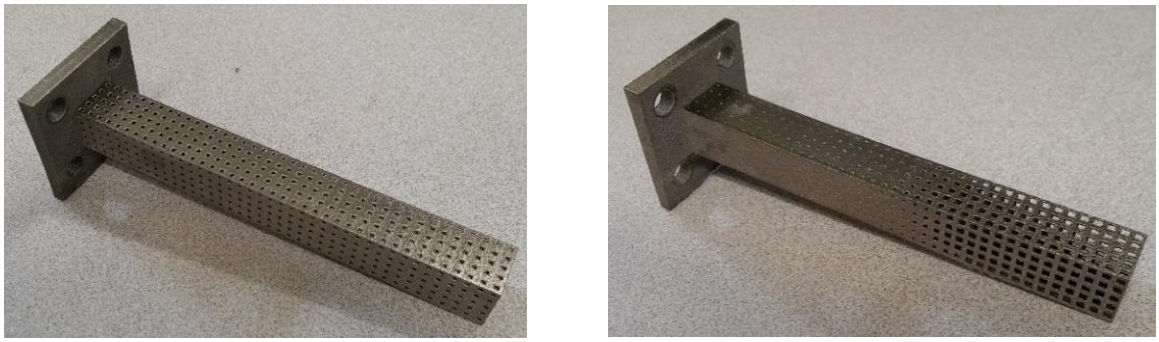

(a) (b)

Figure 3.35: Beams Printed by EOS M290 with Ti6Al4V: (a) Uniform Lattice Structured Beam (b) Optimized Lattice Structured Beam.

Although the fixture ensures the flexibility of the experiments, the mode of the structure is changed due to the variation of the CAD model. To demonstrate the optimized design, a full-scale simulation is conducted on the beams unified with the fixtures. Figure 3.36 illustrates the simulation results, in which the first eigenfrequency of the uniform beam is 631.8 Hz while the

value of optimized beam is 1094.3 Hz. This implies that the additional fixture leads to the decrease of the first eigenfrequency of the structure.

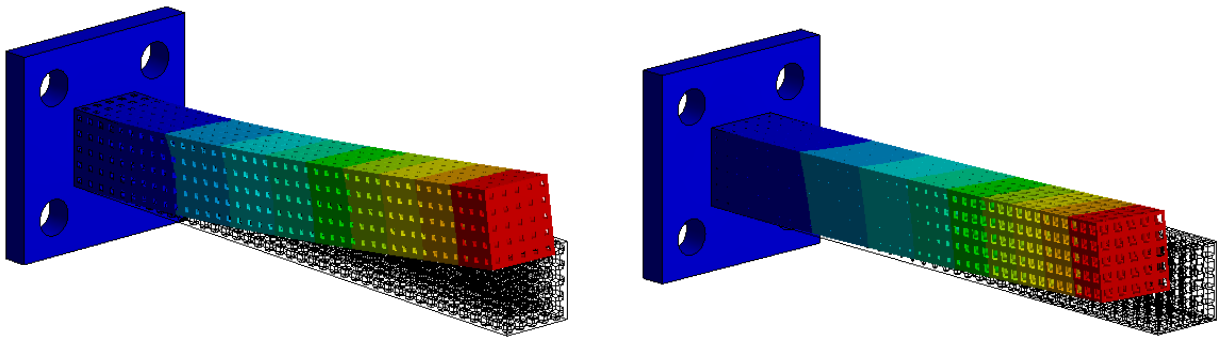

(a) (b)

Figure 3.36: Full-Scale Simulation for the Beams with Fixture. (a) Uniform Beam, $\omega_1 = 631.8$ Hz (b) Optimized Beam, $\omega_1 = 1094.3$ Hz.

The experiments used to measure the eigenfrequency of the printed beams for comparison with the full-scale simulation are given in Figure 3.37. For the stationary, two beams are mounted to a heavy part fixed on the ground by four M6 bolts. An Agilent 35670A Dynamic Signal Analyzer is used to capture the modal data, and a modal hammer of PCB Impulse Hammer Model #086C02 is used for testing, of which the sensitivity is 54.0 mV/lbf. The accelerometer used for the experiments is the PCB 352C65_L with a sensitivity of 100 mV/g.

(a) (b)

Figure 3.37: Vibration Tests for Two Beams. (a) Uniform Beam (b) Optimized Beam

Figure 3.38 illustrates the experimental results of the testing and the results are tabulated in Table 3.5. It is seen that the first eigenfrequency of the uniform beam is 624.5 Hz with a difference of 1.16% from the simulation results. For the optimized beam, the first eigenfrequency is 1080.8 Hz with a difference of 1.23% from the simulation and an increase of 73.07% from the uniform design. This proves that the proposed methodology can significantly improve the first eigenfrequency of the structure, and the homogenized model can provide accurate estimation of the dynamic performance for printed components. Furthermore, through experiments and simulations, it is demonstrated the homogenization under periodicity assumption can be efficiently employed for the description of graded lattice structures.

Table 3.5: Results of the Cantilever Beam

	AH model (Hz)	Simulation for the beam (Hz)	Difference (%)	Simulation for the beam with fixture (Hz)	Experiments (Hz)	Difference (%)
Uniform beam	671.5	676.4	0.73%	631.8	624.5	1.16%
Optimized beam	1281.3	1245.3	2.81%	1094.3	1080.8	1.23%
Increment	609.8 (↑90.81%)	568.9 (↑84.11%)		462.5 (↑73.20%)	456.3 (↑73.07%)	

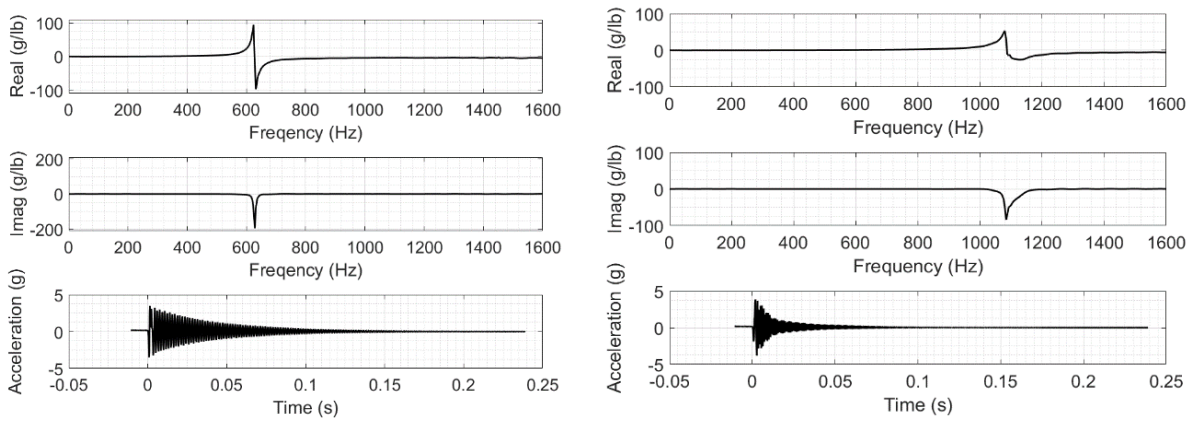

(a) (b)

Figure 3.38: Vibration Experiments for the Two Beams. (a) Uniform Beam; (b) Optimized Beam.

3.4.3.2 Dual Side Fixed Beam

For the same beam, now fixed boundary conditions are applied to both ends of the beam, see Figure 3.39. The volume fraction of the structure is restricted to $V^* = 0.55$.

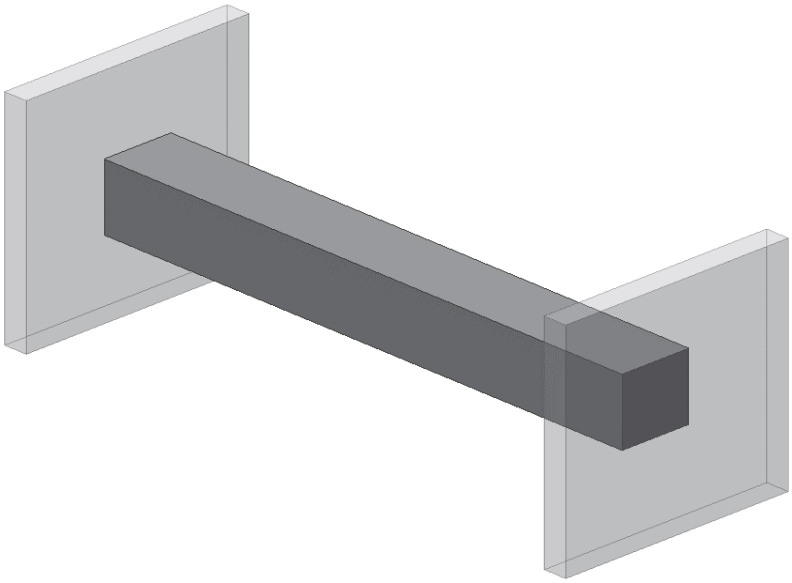

Figure 3.39: Model of a Dual-fixed Beam.

The optimization results of the dual fixed beam are presented in Figure 3.40 including the optimal density distribution, lattice structured design and convergence history. It is seen that higher densities are located on the two-fixed boundary while lower densities are distributed near the central region of the beam. A number of intermediate densities can be found between the transitional region between higher densities and lower densities. The first eigenfrequency increases from 3,699.9 Hz with volume fraction of 0.55, to a value of 5,121.7 Hz within 51 iterations,

representing an increase of 1,421.8 Hz or 38.42%. This demonstrates that the proposed framework can significantly increase the dynamical performance of the structure.

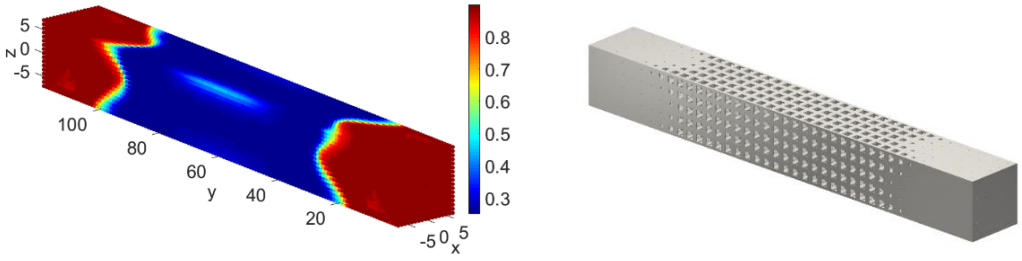

(a) (b)

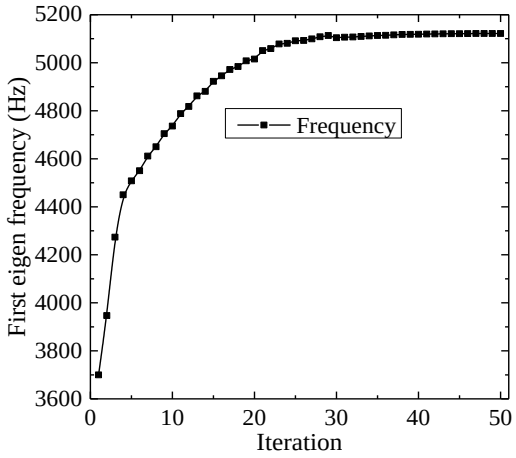

(c)

Figure 3.40: Optimization Results of the Dual-Fixed Beam: (a) Optimized Density Distribution; (b) Optimized Design Using Variable-Density Lattice Structure; (c) Convergence History of First Eigenfrequency.

Again, for the dual-fixed beam, both uniform design and variable-density design are reconstructed using cubic lattice structure and the CAD models are given in Figure 3.41(a) and Figure 3.41(b), respectively. As shown in reconstruction of the optimal beam, more material is distributed on the both sides of the beams. This leads to a stiffer structure at the fixed boundary and thus a higher eigenfrequency design compared with the uniform design of same volume fraction. Full-scale simulations are conducted on both the uniform and optimized design for dual-fixed beam (see Table 3.6). As illustrated in Figure 3.41, the first eigenfrequency of the uniform beam is 3,730.9 Hz with a difference of 31.0 Hz or 0.84% from the homogenized model prediction. For the optimized beam, the first eigenfrequency is 5,208.6 Hz and the difference from the homogenization is 86.9 Hz or 1.70%. Compared with the uniform beam with same volume fraction, the first eigenfrequency increases 1,477.7 Hz or 39.61% after optimization using the proposed method. This demonstrates the homogenized model is accurate in describing the elastic properties of both uniform and non-uniform lattice structure generated by the LSTO method.

Table 3.6: Simulation and Experimental Results of The Dual Fixed Beam

	Volume fraction	AH model (Hz)	Simulation for the beam (Hz)	Difference (%)	Simulation for the beam with fixture (Hz)	Experiments (Hz)	Difference (%)
Uniform beam	0.55	3,699.9	3,730.9	0.84%	3,501.4	3,504.6	0.091%
Optimized beam	0.55	5,121.7	5,208.6	1.70%	4,610.1	4,480.9	2.80%
Increase		1,421.8 (↑38.42%)	1,477.7 (↑39.61%)		1,108.7 (↑31.66%)	975.3 (↑27.83%)	

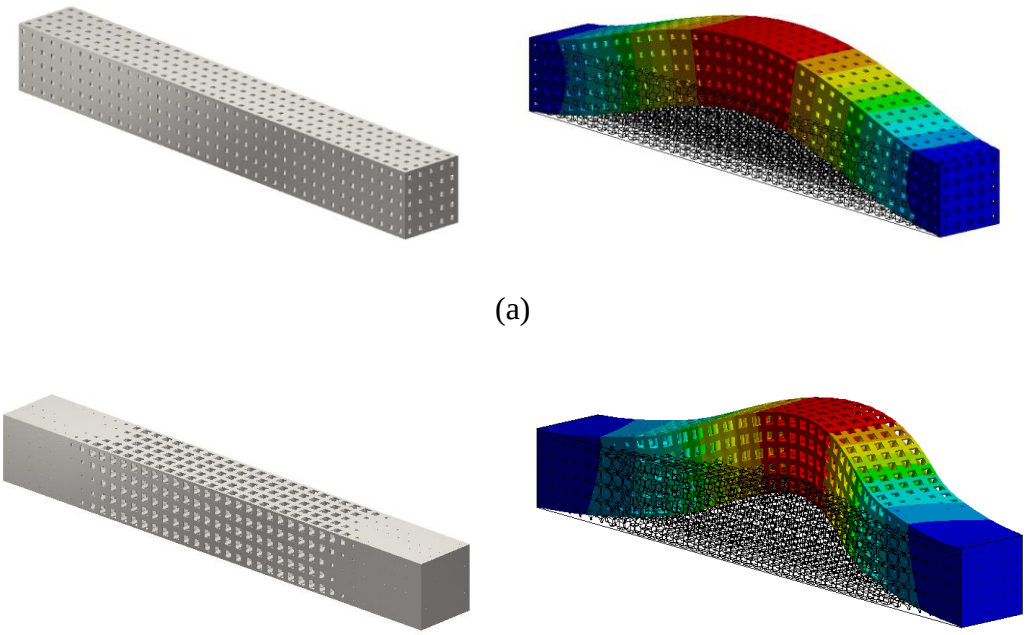

(a)

(b)

Figure 3.41: Full-scale Simulations for the Dual-Fixed Beam: (a) CAD Model of Uniform Beam and Vibration Mode of First Eigenfrequency $\omega_1 = 3,730.9$ Hz; (b) CAD Model of Optimized Beam and Vibration Mode of First Eigenfrequency $\omega_1 = 5,208.3$ Hz.

The fixture used for cantilever beam is also added to the dual-fixed beams, see in Figure 3.42. The printed beams are illustrated in Figure 3.43, while the corresponding simulation results are given in Figure 3.44. The first eigenfrequency of the uniform beam obtained by simulation is 3,501.4 Hz and the optimal beam is 4,610.1 Hz. Compared with the result in Figure 3.41, the fixture leads to a higher decrease of first eigenfrequency of the optimized beams than the uniform one, 229.5 Hz lower for the uniform beam and 598.5 Hz lower for the optimized beams.

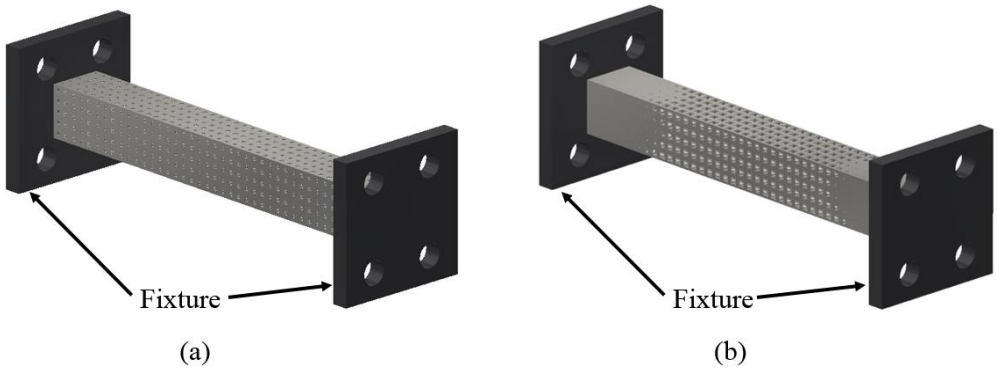

Figure 3.42: CAD Model of Dual-Fixed Beams after Assembling with the Fixtures Used for Experiments: (a) Uniform Beam and (b) Optimized Beam.

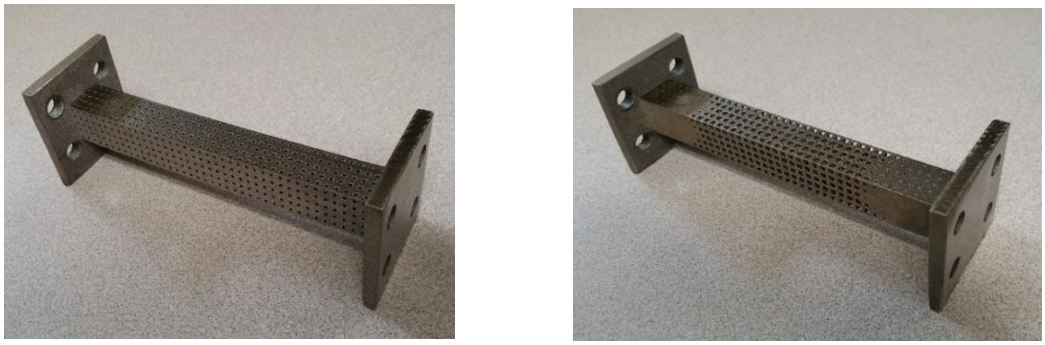

(a) (b)

Figure 3.43: Dual-fixed Beams Printed by EOS M290 with Ti6Al4V: (a) Uniform Beam and (b) Optimized Beam.

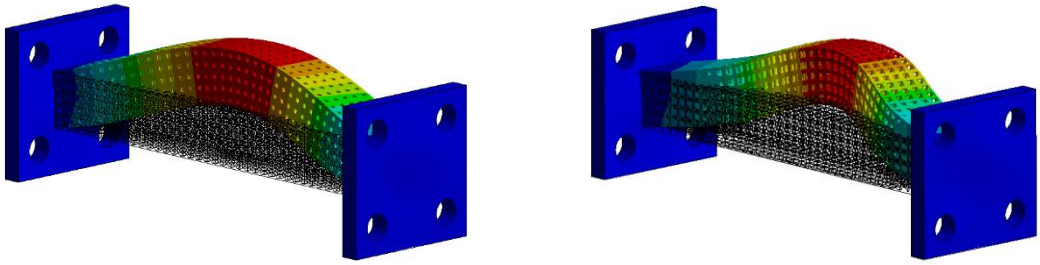

(a) (b)

Figure 3.44: Full-scale Simulations for the Dual-Fixed Beams with the Fixtures: (a) Uniform Beam, $\omega_1 = 3,501.4$ Hz; (b) Optimized Beam, $\omega_1 = 4,610.1$ Hz.

The experimental setup for the dual-fixed beams is shown in Figure 3.45, in which the beams were mounted to two huge metal bases fixed on the ground. The accelerometer, modal hammer and the signal analyzer were same as the former case. Figure 3.46 illustrates the experimental results of the testing and the key results are again tabulated in Table 3.6. The first eigenfrequency is 3,504.6 Hz for the uniform beam and 3.2 Hz or a 0.091% difference from the full-scale simulation. For the optimized beam, the first eigenfrequency is 4,480.9 Hz and the difference from the simulation is 129.2 Hz or 2.80%. Compared with the uniform beam with the same volume fraction, the structure designed by LSTO method represents an increase of 975.3 Hz or 27.83%. This further demonstrates that the structure designed by the proposed optimization method can achieve a significant increase of dynamical performance, and the homogenization approach proposed in section 2.3 can be efficiently used to represent the mechanical performance for both the uniform and graded lattice material.

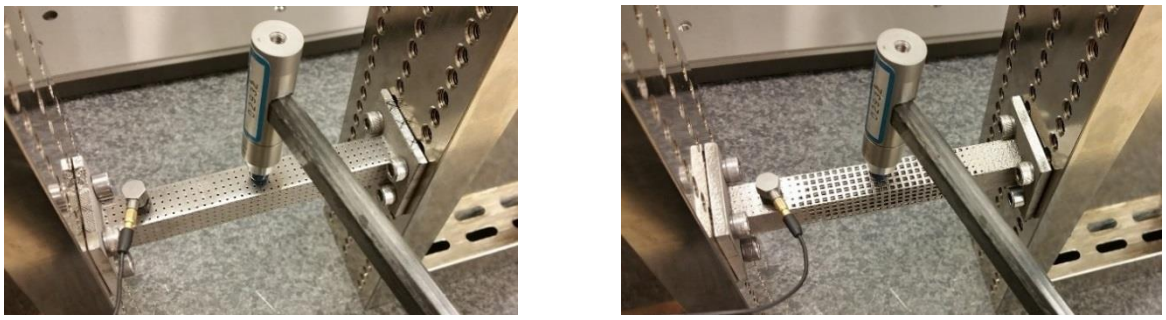

(a) (b)

Figure 3.45: Experimental Setup for the Dual-fixed Beam: (a) Uniform Beam; (b) Optimized Beam.

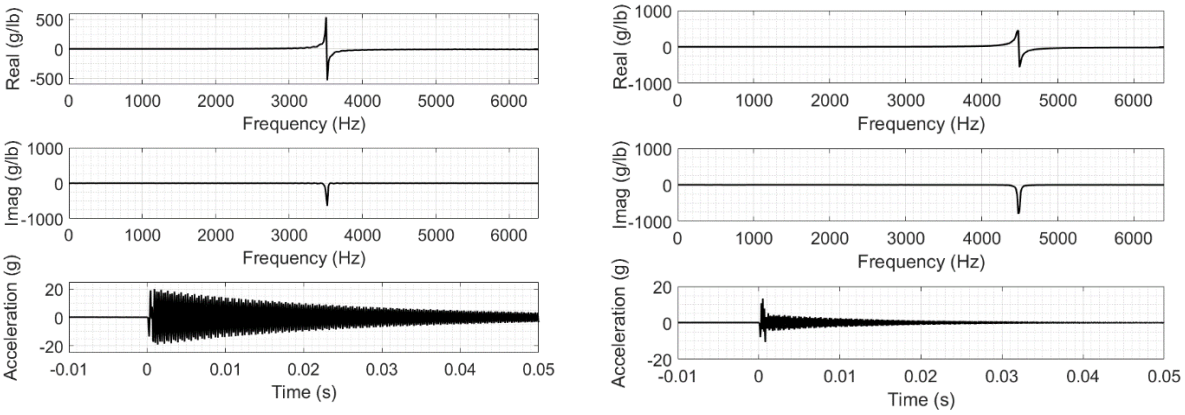

(a) (b)

Figure 3.46: Experimental Results of the Dual-fixed Beams: (a) Uniform Beam, $\omega_1 = 3,504.6$ Hz; (b) Optimized Beam, $\omega_1 = 4,480.9$ Hz.

3.4.3.3 Part-scale Validation

In addition to the beam validation, this case aims to apply the optimization framework to a more complex test component. The CAD model and corresponding mesh of the test part are given

in Figure 3.47. Fixed boundary conditions are applied to the two bolt holes highlighted by red color in the figure. The dimension of the base plate is $80 \times 20 \times 12$ mm^3, while the protruding feature has the dimension of $36 \times 20 \times 12$ mm^3. The diameter of the three bolt holes is 8 mm and a chamfer of 5 mm is added to the two top corners of the protruding feature. A mesh of 53,044 eight-node tetrahedral elements is used to discretize the design domain and solve the dynamic problem. The volume fraction of the design domain for the optimization is set to be $V^* = 0.5$.

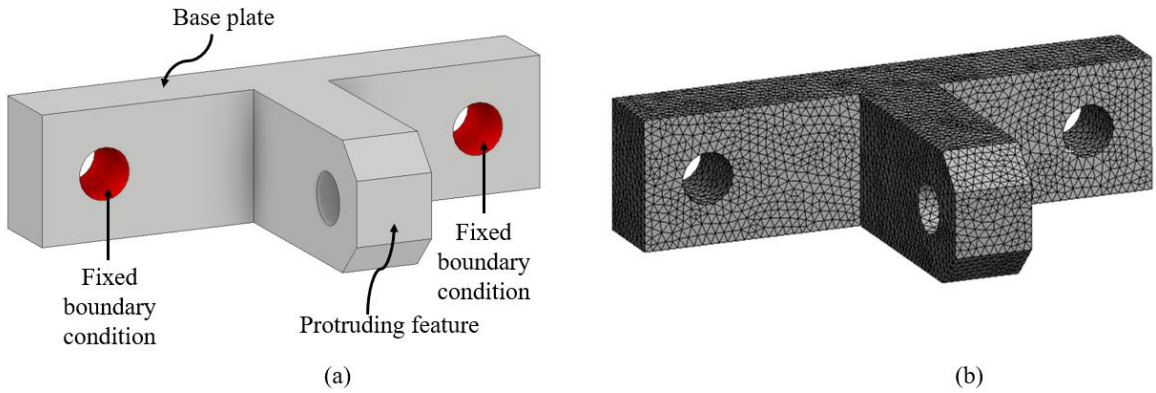

Figure 3.47: Model of Test Component: (a) CAD Model and Boundary Conditions and (b) Mesh Model

The optimization results of the test component including the optimal density distributions and the convergent history of the first eigenfrequency are illustrated in Figure 3.48. After 49 iterations, the first eigenfrequency of the structure is improved from 2,865.8 Hz to 3,745.8 Hz, representing an increase of 30.71%. More material is distributed around the two bolt holes while less material is distributed at the center region of the base plate and region of the protruding feature. This leads to a stiffer structure around the fixed boundary conditions and thus a higher frequency is obtained. Note that for this part-scale problem, a larger fraction of intermediate densities is

generated in the optimization, refer to Figure 3.48 (a). The advantage of LSTO method makes it possible to realize this design with variable-density lattice infill without changing the original shape. For 0/1 design, the protruding feature may be removed after the optimization.

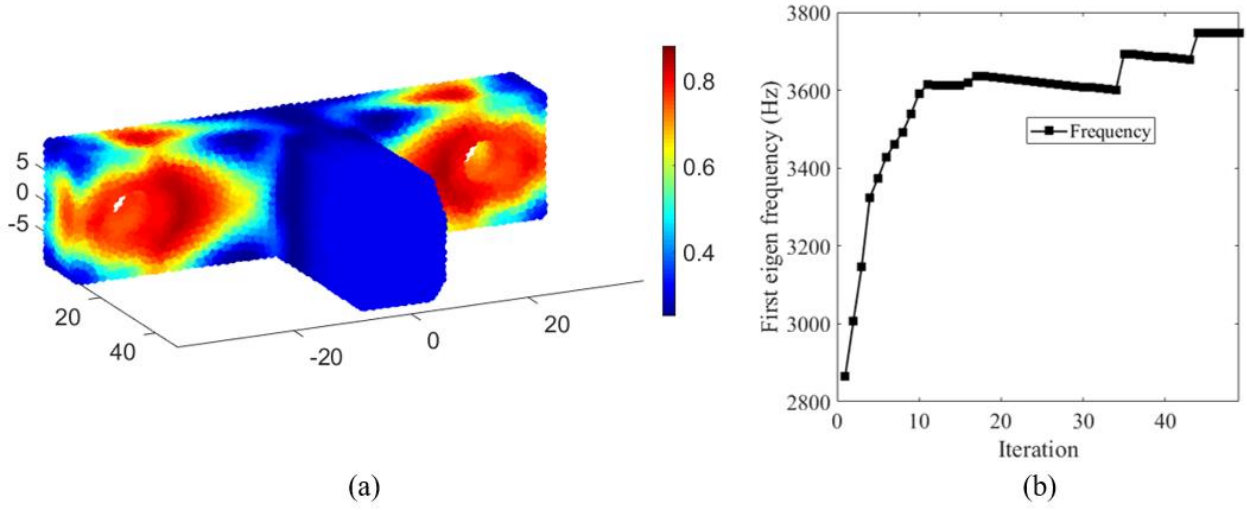

Figure 3.48: Optimization Results for the Test Component: (a) Optimal Density Distribution and (b) Convergent History of First Eigenfrequency.

For validation purpose, both the optimal design and uniform design of volume fraction equal to 0.5 are reconstructed using cubic lattice structure. A solid shell with thickness of 0.5mm is added to cover the broken ligaments at the chamfer and bolt holes, refer to Fig. 29(a) and (b). Full-scale simulations are carried out to examine the performance of the two designs, and the results are illustrated in Figure 3.49(c) and (d) and tabulated in Table 3.7. As can be seen, with the additional shell, the first eigenfrequency of the uniform design obtained from full-scale simulation is 3.29% larger than the prediction from AH model, while for the optimal design, the difference is

0.87%. This implies that addition of the solid shell leads to an increase of eigenfrequency for uniform design and a little decrease for the optimal design. On the other hand, based on the result from full-scale simulation, the first eigenfrequency of the test component increases by 753.1 Hz or 25.44% compared to the uniform design of the same volume fraction. This demonstrates that the proposed methodology can also be efficiently employed to improve natural frequency of a component by designing the variable-density lattice structure infills.

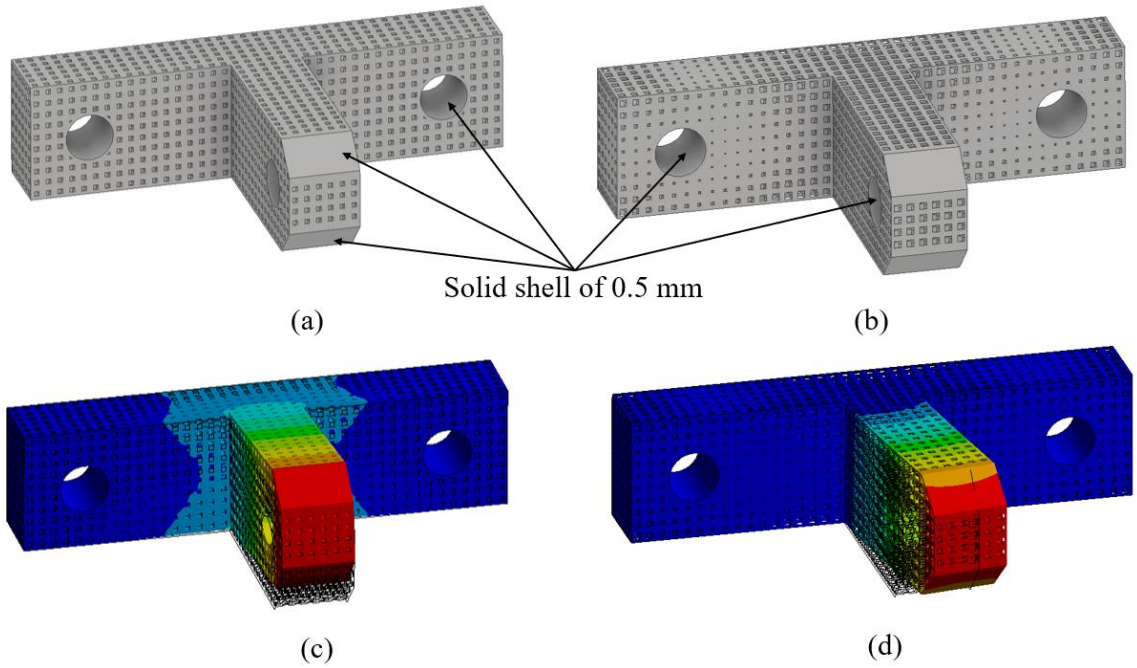

Figure 3.49: Reconstruction of Lattice Infills and Full-scale Simulation for Uniform Design and Optimal Designs: (a) CAD Model of Reconstructed Uniform Design ($V^* = 0.5$), (b) CAD Model of Reconstructed Optimal Design ($V^* = 0.5$), (c) Full-scale Simulation Of Uniform Part, $\omega_1 = 2,960$ Hz, And (d) Full-scale Simulation of Optimized Part, $\omega_1 = 3,713.1$ Hz.

Table 3.7: Simulation Results of the Test Part

	Volume fraction	AH model (Hz)	Simulation for the test part with solid shell (Hz)	Difference (%)
Uniform design	0.5	2,865.8	2,960	3.29%
Optimal design	0.5	3,745.8	3,713.1	0.87%
Enhancement		30.71%	25.44%	

3.4.4 Summary

This work proposed the LSTO method for maximization of the first eigenfrequency of the structure infilled with an optimized lattice structure. At the microscopic level, numerical AH approach is employed to calculate the effective elastic modulus of lattice structures manufactured by metal AM technologies. To examine the accuracy of the AH model, tensile tests are carried out on the printed samples to compare with the results predicted by the homogenized model, which shows great agreement with experimental results. At macroscale, the AH model is implemented into the framework of density-based topology optimization to optimize the relative density distribution of lattice structure. In particular, the repeated eigenfrequency and change of the order of the eigenfrequencies are taken into account to ensure the maximization of the fundamental eigenfrequency. Once the optimized density profile is obtained, variable-density lattice structure infill based on the profile is used to realize the graded lattice design. This can not only maintain the original shape of the component, but also ensure the precise conversion of the intermediate densities. Two 3D numerical examples are provided to demonstrate the accuracy and efficiency of

the proposed methodology for vibration structure optimization. The first example is a simple cantilever beam with square cross section. By means of LSTO, the first eigenfrequency of the beam is increased from 671.5 Hz to 1281.3 Hz with an increment of 90.81%. A full-scale simulation is conducted to compare with the homogenized result. It is found that the differences for both the uniform beam and the optimized beam are smaller than 3%. The two cantilever beams were also printed using the EOS M290 with Ti6Al4V for the experimental tests. Comparing with the simulation results, the first eigenfrequency of the uniform beam and optimized beam is in good agreement, and in either of the two cases the difference is less than 1.3%. Another example is a beam with fixed support boundary conditions on both ends. By means of LSTO, the first eigenfrequency increases from 3699.9 Hz to 5121.7 Hz with an improvement of 1421.8 Hz or 38.42%. Both full-scale simulations and experiments are carried out on the uniform and optimized lattice structure design for comparison. Similar conclusions are made based on the comparison. Both of the two cases demonstrate that the LSTO method is accurate and efficient for the optimization of the first eigenfrequency of lattice structure design.

4.0 Concurrent Lattice Structure Topology Optimization Part

In this chapter, the framework of concurrent LSTO method is proposed. Since the solid features, such as cooling channel and bolt holes cannot be realized by lattice structure, a methodology that optimizes the layout of the feature coupled with lattice structure is explored. The content in this chapter mainly focus on the representation of the movable feature with design-independent boundary and with design-independent boundary conditions.

4.1 Movable Feature Representation

4.1.1 Implicit Level Set Representation of Functional Features

Feature representation under the density-based framework is possible but the related sensitivity calculation is nontrivial. Instead, the level set method shows its advantage that both the parametric feature representation and sensitivity calculation can be straightforwardly conducted [125].

Specifically, the level set function $\phi(\boldsymbol{x})$ describes an arbitrary design domain Ω as follows:

$$\begin{cases} \phi(\boldsymbol{x}) > 0 & for\ \boldsymbol{x} \in \Omega \backslash \partial\Omega \\ \phi(\boldsymbol{x}) < 0 & for\ \boldsymbol{x} \notin \Omega \\ \phi(\boldsymbol{x}) = 0 & for\ \boldsymbol{x} \in \partial\Omega \end{cases} \tag{4.1}$$

where Ω indicates the material domain while $\partial\Omega$ represents the boundary. $\boldsymbol{x}$ is the coordinate vector in Ω. $\phi(\boldsymbol{x}) > 0$, $\phi(\boldsymbol{x}) < 0$ and $\phi(\boldsymbol{x}) = 0$ represent the solid, void and interface areas, respectively. Note that, the smeared-out Heaviside function $H(x)$ and the Dirac delta function $\delta(x)$ are used in the numerical implementation to approximate the domain and boundary integrations, which is given as.

$$H(x) = \begin{cases} \epsilon, & x < -\Delta \\ \frac{3(1-\epsilon)}{4}\left(\frac{x}{\Delta} - \frac{x^3}{3\Delta^3}\right) + \frac{1+\epsilon}{2}, & -\Delta \leq x < \Delta \\ 1, & x \geq \Delta \end{cases} \tag{4.2}$$

$$\delta(x) = \frac{d}{dx}H(x) = \begin{cases} \frac{3(1-\epsilon)}{4\Delta}\left(1 - \frac{x^2}{\Delta^2}\right), & |x| \leq \Delta \\ 0, & |x| > \Delta \end{cases} \tag{4.3}$$

In Eq. (4.2) and (4.3), Δ is a tunable parameter defined to smooth the level set function projection. ϵ is a small positive number used to avoid singularity problem. During the concurrent optimization, the shape of the moving features is maintained while their geometric parameters (positions, angles, etc.) evolve in every step. Thus, the level set function used to represent the moving features can be further parameterized in terms of geometrically meaningful variables $\{c_i\}$ and denoted as $\phi(\boldsymbol{x}, \boldsymbol{c}(t))$, where $\boldsymbol{x}$ is the spatial variable and $\boldsymbol{c}(t) = \{c_1(t), c_2(t), \dots, c_{Nc}(t)\}$ is a set of geometric parameters.

For more complex geometry, the R-functions are employed to construct the geometric shape by Boolean operation for the primitive features [126, 127]. Specifically, the basic R-functions including conjunction ⋀ and disjunction ⋁ [126] are applied; refer to Eq.(4.4) and (4.5):

$$f_1 \wedge_0 f_2 \equiv f_1 + f_2 - \sqrt{f_1^2 + f_1^2} \tag{4.4}$$

$$f_1 \vee_0 f_2 \equiv f_1 + f_2 + \sqrt{f_1^2 + f_1^2} \tag{4.5}$$

Note that $f_1 \wedge_0 f_2$ is positive when both f_1 and f_2 are positive, and $f_1 \vee_0 f_2$ is positive if one of the functions f_1 or f_2 is positive. An example of a component constructed through the combination of level-set function and R-functions is given in fig. 9, including the composition of the operations, the level-set representation and the normalized level-set representation. It is seen that the new structure is constructed by four primitive level-set functions, which are expressed as follows:

$$\phi_1(x,y) = R_1 - \sqrt{(x-c_1)^2 + (y-c_2)^2};$$

$$\phi_2(x,y) = a - |x-c_3|; \phi_3(x,y) = b - |y-c_4|;$$

$$\phi_4(x,y) = R_2 - \sqrt{(x-c_5)^2 + (y-c_6)^2};$$

$$\phi_5(x,y) = R_3 - \sqrt{(x-c_7)^2 + (y-c_8)^2}.$$

where $\phi_i (i = 1,2,\dots,5)$ represents the level set function of the primitive features, $R_j (j = 1,2,3)$ indicates the radius of the three circles, a and b denote the length and width of the rectangle, and c_l $(l = 1,2,\dots,8)$ are the geometric variables of the primitive features.

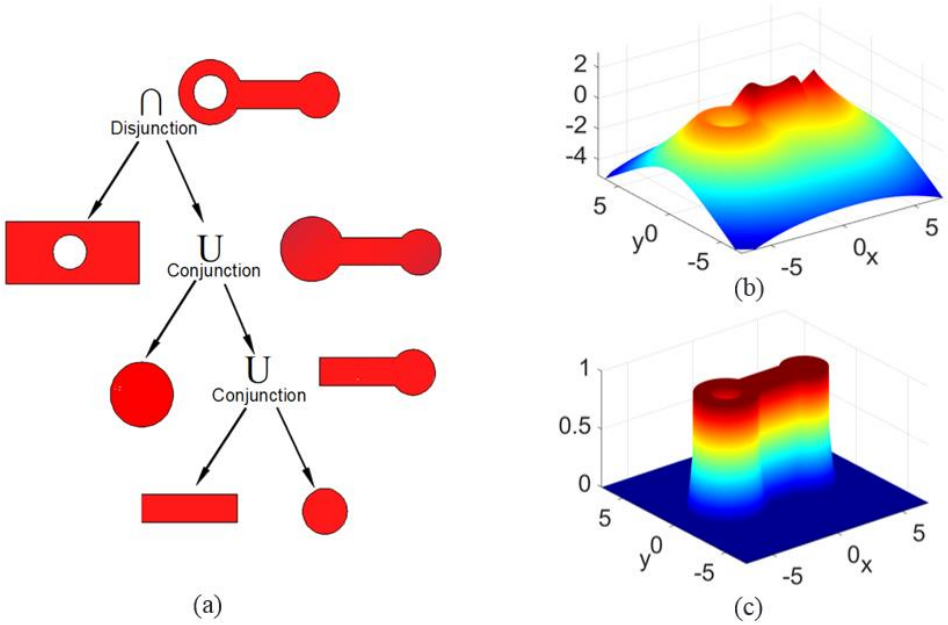

Figure 4.1: Representation of Complex Geometry Using Level Set Function and R-Function. (a) Construction of Complex Geometry by Primitive Features Through R-Functions (b) Level Set Function Constructed by R-Functions, and (c) Implicit Representation after Heaviside Mapping.

4.1.2 Immersed Boundary Representation

The immerse boundary (IB) [128-130] method has been widely applied to solve fluid-structure interaction problems numerically. The IB method allows the Eulerian fluid domain and Lagrangian solid domain to overlap by incorporating the effects of the overlap into the governing equations of each description. Hence IB method does not need remeshing to solve fluid-structure interaction problems, as compared to methods using a single description. In this work, the

underlying concept of IB method is used to implicitly represent a movable feature with conforming boundaries.

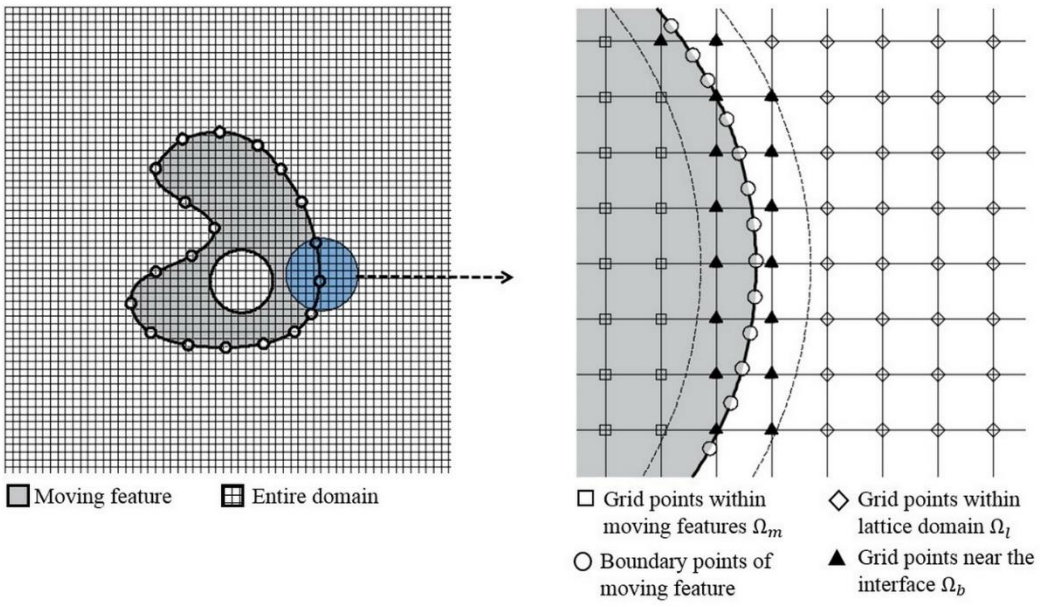

(a) (b)

Figure 4.2: (a) Parameterization of the IB Representation of the Movable Features, (b) Zoom View of The Vicinity of the Interface Where the Points are Divided Into Different Groups.

As shown in Figure 4.2, the design domain is divided into three groups: Grid points lying within the movable features Ω_m, grid points on the boundary Ω_b, grid points within the lattice structure domain Ω_l. For the surface boundary given in Eq. (4.3), the boundary integral is performed on the domain Ω_b, which is a band between the two dashed lines in Figure 4.2(b). For volume boundary in (4.2), the boundary integral is performed on the domain consisting of Ω_b and

Ω_m. To mathematically impose these integrals, the Heaviside function and Dirac delta function are employed for surface boundary and volume boundary, respectively, which are given as:

$$\int_{\Omega_b} G(x)\delta(\phi(x))|\nabla\phi(x)|d\Omega \tag{4.6}$$

And

$$\int_{\Omega_b+\Omega_m} G(x)H(\phi(x))d\Omega \tag{4.7}$$

where $G(x)$ represents a given function for the integration, i.e. heat flux or heat convection for surface boundary and internal heat generation for volume boundary. $H(\phi(x))$ and $\delta(\phi(x))$ denote the Heaviside function and Dirac delta function, respectively, and $\phi(x)$ is the level set function used to mathematically describe boundary of the movable features, Thus, the integration in Eq. (4.6) and Eq. (4.7) can be written as:

$$l(t) = \int_{\partial\Omega^{f(t)}} f(\boldsymbol{x},t)dS = \int_{\Omega} f\delta(\phi)|\nabla\phi|d\Omega \tag{4.8}$$

$$v(t) = \int_{\Omega^{F(t)}} F(\boldsymbol{x},t)dV = \int_{\Omega} FH(\phi)d\Omega \tag{4.9}$$

where $\Omega^f(\mathrm{t}) = \{\boldsymbol{x}|\phi(x,t) > 0, \boldsymbol{x} \in \Omega\}$ represent the domain of the moving features. t indicates a pseudo time used to update level set function.

Using the operation of R-functions for feature representation , the level set function can be further parameterized in terms of geometrically meaningful variables $\{c_i\}$ (e.g. position and angle), and denoted as $\phi(\boldsymbol{x},\boldsymbol{c}(t))$, where $\boldsymbol{x}$ is the spatial variable and $\boldsymbol{c}(t) = \{c_1(t), c_2(t), \dots, c_{Nc}(t)\}$ is a set of the geometric parameters. Hence, Eq. (4.8) and Eq. (4.9) can be further expressed as:

$$l(t) = \int_{\Omega} f\delta(\phi(\boldsymbol{x}, \boldsymbol{c}(t)))|\nabla\phi|dV \tag{4.10}$$

$$v(t) = \int_{\Omega} FH(\phi(\boldsymbol{x}, \boldsymbol{c}(t))dV \tag{4.11}$$

For the purpose of illustration, boundaries represented by Eq. (4.10) and (4.11) are verified by the following two examples.

Figure 4.3 gives the first example, a block with a hole in the center. Temperature of $T_0 = 10℃$ is assigned to the outer surface of the block while a heat flux of $q_0 = 1\ \mathrm{W/mm^2}$ is applied on the internal surface of the hole. A Dirac delta function shown in Figure 4.3(b) is substituted into Eq. (4.10) and is employed to implicitly attribute heat flux in a fixed mesh. The obtained results from both direct numerical simulation (DNS) and the IB method are given in Figure 4.4. It is seen that the results obtained by the IB method is in good agreement with the results of DNS. However, the number of elements used in the IB method is just 20,000, which is only 23.89% of that used in DNS, while the size of the element of the IB model is two times that in the DNS. It shows that the IB method can be efficiently used for surface boundary representation. Note that the hole in the IB method is treated as a feature consisting of weak material, of which the thermal conductivity is $0.0001\ \mathrm{W/(m \cdot K)}$.

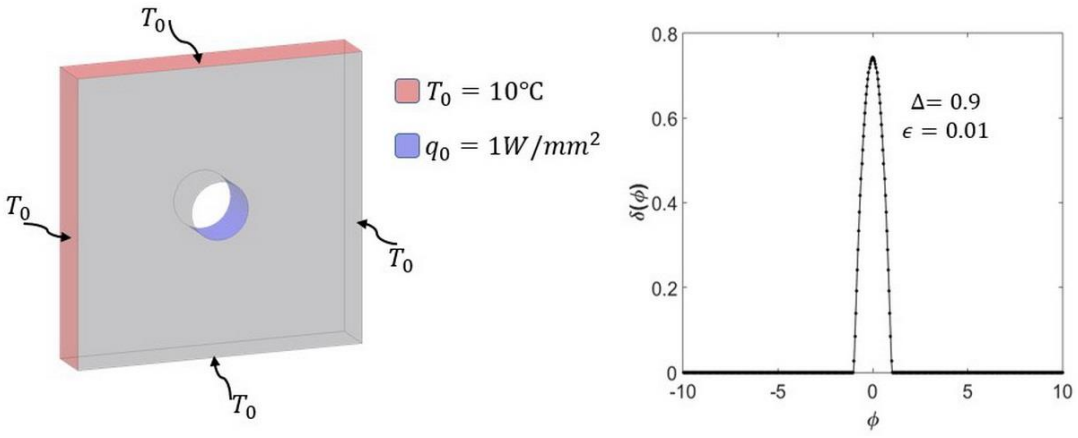

(a) (b)

Figure 4.3: Verification Problem #1 for the Proposed IB Method: (a) Geometry with Boundary Conditions and (b) Diract Delta Function Used for Boundary Mapping.

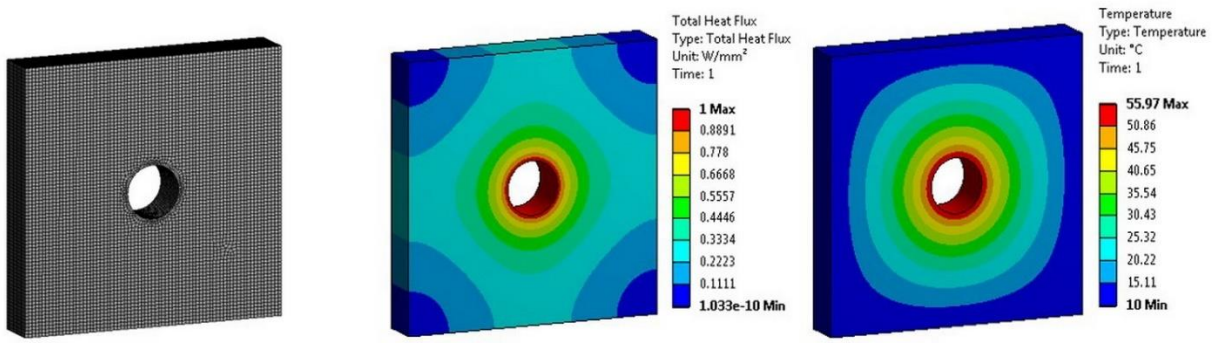

(a)

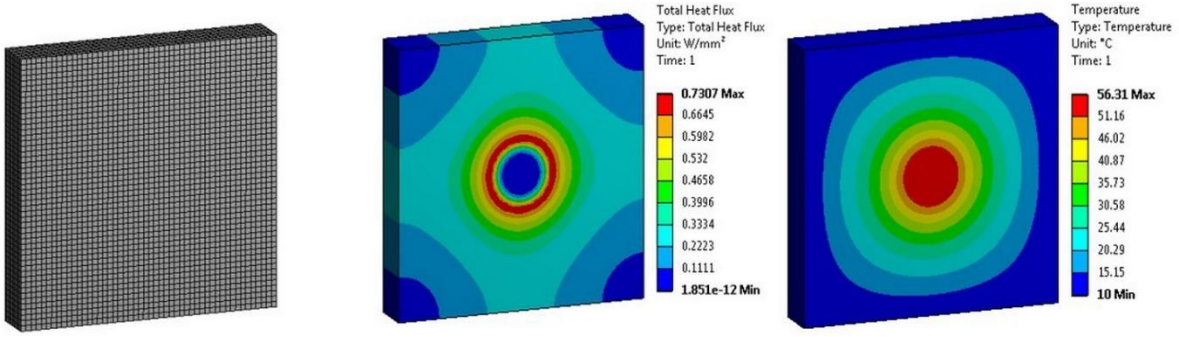

(b)

Figure 4.4: Comparison between IB Method and DNS for the Verification Problem: (a) DNS Results Including the Mesh (83,700 Hexagonal Elements), Heat Flux Distribution, and Temperature Distribution; (b) IB Results Including the Mesh (20,000 Hexagonal Elements), Heat Flux Distribution and Temperature Distribution.

The second example is to examine the efficiency of IB method for volume boundary representation in Eq. (4.11). Figure 4.5 provides the geometry with boundary conditions and the Heaviside function used for the volume representation. As shown in Figure 4.6, the results obtained by IB method shows good agreement with DNS; however, the mesh used for IB method can significantly reduce the computational cost compared with the detailed simulation.

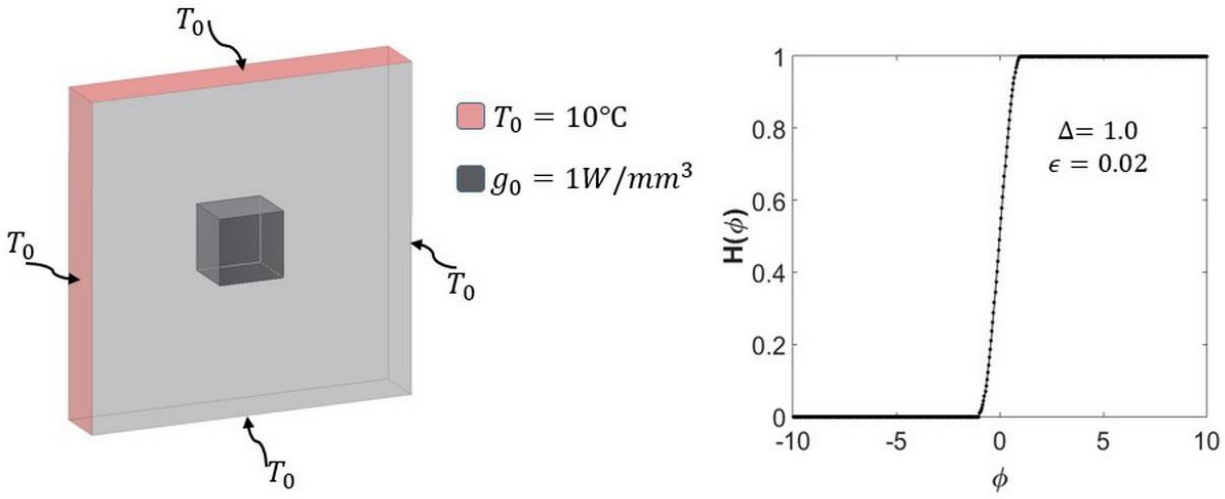

(a) (b)

Figure 4.5: Verification Problem #2 for the Proposed IB Method: (a) Geometry with Boundary Conditions and (b) Heaviside Function Used for The Boundary Mapping.

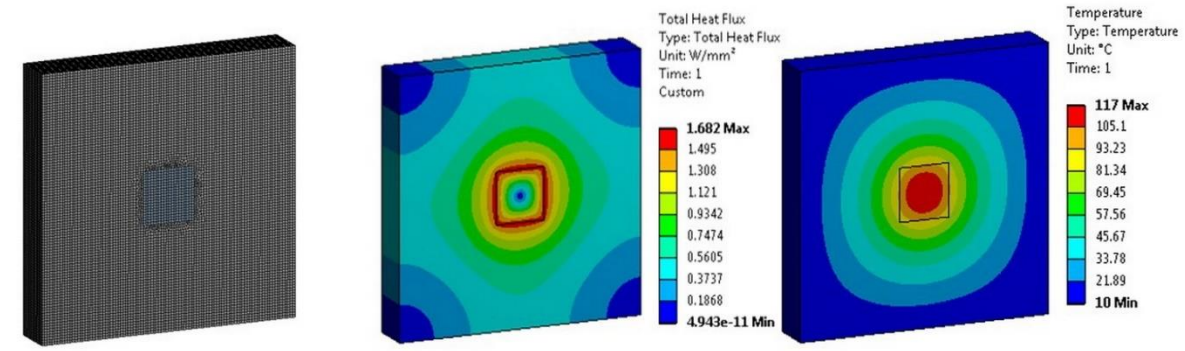

(a)

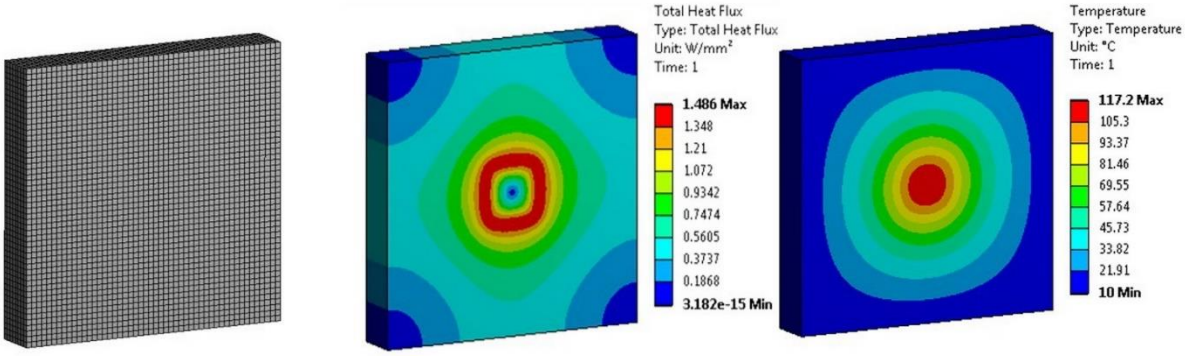

(b)

Figure 4.6: Comparison between IB Method and DNS for the Verification Problem: (A) DNS Results Including the Mesh (171887 Hexagonal Elements), Heat Flux Distribution, and Temperature Distribution; (B) IB Results Including the Mesh (20,000 Hexagonal Elements), Heat Flux Distribution and Temperature Distribution.

4.2 Concurrent Optimization for Design-independent Feature for Heat Conduction

4.2.1 Material Interpolation

The surrogate model developed in Section 2.5 is employed to represent the effective thermal conductivity of the lattice material. Accordingly, the element-wise thermal conductivity tensor and volume fraction are analytically expressed in Eq. (4.12). Different from the 0/1 SIMP interpolation, the adopted surrogate model allows continuous density variation:

$$\begin{cases} \boldsymbol{D}_e^l = \boldsymbol{D}(\rho_e) \\ v_e = \rho_e v_0 \end{cases} \tag{4.12}$$

where $\boldsymbol{D}_e^l$ denotes the thermal conductivity tensor of an arbitrary element e, where the tensor components are all functions of the relative density ρ_e. v_e indicates the volume fraction of element e, which is a linear combination of the full volume v_0 and relative density ρ_e.

Regarding the elements around the feature areas, the material properties and volume fraction can be expressed as follows:

$$\begin{cases} \boldsymbol{D}_e^f = H(\phi(\boldsymbol{x}, \boldsymbol{c}(t))\boldsymbol{D} \\ v_e = H(\phi(\boldsymbol{x}, \boldsymbol{c}(t))v_0 \end{cases} \tag{4.13}$$

where $\boldsymbol{D}_e^f$ denotes the effective conductivity of the element e, and $\boldsymbol{D}$ is the conductivity tensor of a full solid element. $H(\phi(\boldsymbol{x}, \boldsymbol{c}(t))$ indicates the Heaviside projection, in which $\boldsymbol{c}(t)$ denotes the vector of the geometric variables including position and orientation. In the case that multiple features are involved that are potentially composed of different material types, the material interpolation model in Eq. (4.13) can be further extended as follows:

$$\begin{cases} \boldsymbol{D}_e^c = \sum_{k=1}^{N_c} H(\phi_k(\boldsymbol{x}, \boldsymbol{c}(t))\boldsymbol{D}_k \\ v_e = \sum_{k=1}^{N_c} H(\phi_k(\boldsymbol{x}, \boldsymbol{c}(t))v_0 \end{cases} \tag{4.14}$$

where N_c represents the total number of features, $\phi_k(\boldsymbol{x}, \boldsymbol{c}(t))$ denotes the level set function of the k^{th} feature and its corresponding material properties are represented by $\boldsymbol{D}_k$. Based on Eq. (4.12) and Eq. (4.14), The unified material model considering both the lattice domain and the multiple functional features can be constructed as:

$$\begin{cases} \boldsymbol{D}_e = (1-\zeta)\boldsymbol{D}(\rho_e) + \zeta \boldsymbol{D}_k \\ v_e = (1-\zeta)\rho_e v_0 + \zeta v_0 \end{cases} \tag{4.15}$$

where ζ is the interpolation weight of movable feature areas as specified below:

$$\zeta = H(\bigvee_{k=1}^{N_c} \phi_k(\boldsymbol{x}, \boldsymbol{c}(t)) \tag{4.16}$$

This represents a combination of level-set function of movable features, which implies that the value of level-set function is converted into 0-1 binary value. $\zeta = 0$ indicates that the point is in the lattice structure domain and thus the material interpolation from homogenization is being used; when $\zeta = 1$, it means that the point in the movable features domain and the material interpolation in Eq. (4.14) is being employed. Thus, the material interpolation for multi-component system can be written as Eq. (4.15).

4.2.2 Problem Statement

4.2.2.1 Governing Equation

In this work, steady-state heat conduction problems are considered. Suppose a design domain Ω bounded by a closed surface Γ which is dominated by heat conduction. Then the temperature field T is governed by the following heat equation in steady state as:

$$-\nabla \cdot (\boldsymbol{k}\nabla T) = g \tag{4.17}$$

where g denotes the internal heat generation in Ω. Using the virtual temperature field $\tilde{T}$, Eq. (4.17) can be transformed in the weak form as:

$$\int_{\Omega} \nabla\tilde{T}\boldsymbol{k}\nabla T d\Omega - \int_{\Gamma} \tilde{T}\boldsymbol{k}\frac{\partial T}{\partial n} d\Gamma - \int_{\Omega} \tilde{T} g d\Omega = 0 \tag{4.18}$$

In the present work, the boundaries on the surface of Γ are composed of Dirichlet boundary Γ_T and Neumann boundary Γ_q as follows:

$$\Gamma = \Gamma_T + \Gamma_q \tag{4.19}$$

Defining the following bilinear and linear form

$$a(T, \tilde{T}) = \int_{\Omega} \nabla\tilde{T}\boldsymbol{k}\nabla T d\Omega \tag{4.20}$$

$$L(\tilde{T}) = \int_{\Gamma} q\tilde{T} d\Gamma + \int_{\Omega} g\tilde{T} d\Omega \tag{4.21}$$

where q is the heat flux on the boundary of Γ. Thus, the equilibrium equation can be rewritten as

$$a(T, \tilde{T}) = L(\tilde{T}) \tag{4.22}$$

4.2.2.2 Optimization Formulation

The purpose of the optimization is to find optimal distribution of the lattice together with the optimal geometric parameters of the functional features simultaneously. The objective of the optimization is to minimize the thermal potential energy of the structure under volume constraints. The general formulation of the problem using finite element (FE) discretization can be expressed as follows:

$$\text{Minimum: } J(\rho, \boldsymbol{c}(t)) = \frac{1}{2}\boldsymbol{T}^T \boldsymbol{K_c} \boldsymbol{T} \tag{4.23}$$

$$Subject\ to: \quad \boldsymbol{KT} = \boldsymbol{q} + \boldsymbol{G} + \boldsymbol{H} \tag{4.24}$$

$$V(\rho) \leq V^* \tag{4.25}$$

$$V_l(\phi((\boldsymbol{x}, \boldsymbol{c}(t))) = -\sum_{e=1}^{N} (\zeta v_e) + V_c \leq 0 \tag{4.26}$$

$$\underline{\rho} \leq \rho_e \leq \overline{\rho} \tag{4.27}$$

where $\boldsymbol{K}$ is the heat conduction matrix; $\boldsymbol{q}$, $\boldsymbol{G}$ and $\boldsymbol{H}$ denote the heat flux vector, internal heat generation vector, and heat transfer vector after FE discretization, respectively. ρ_e is the relative density of the e^{th} element. $\underline{\rho}$ and $\overline{\rho}$ are the lower and upper bound of the elemental density. The first constraint in Eq. (4.24) denotes the equilibrium equation used to calculate the temperature field of the design domain. The second constraint in Eq. (4.25) implies that the allowable volume fraction is limited to V^*. Following the work of [131], the third inequality constraint in Eq. (4.26) is used to avoid overlap of multi component design, in which V_c denotes the total volume of the movable features. The global conductivity matrix and the heat transfer matrix can be calculated by assembling the elemental matrix, as given below:

$$\boldsymbol{K} = \sum_{\Omega} \boldsymbol{k}_e = \sum_{e} \int_{\Omega_e} \boldsymbol{B}_e^T \boldsymbol{D}_e \boldsymbol{B}_e d\Omega \tag{4.28}$$

where $\boldsymbol{k}_e$ is the elemental conduction matrix of element e, $\boldsymbol{D}_e$ represents the corresponding material model proposed in Section 2.5. $\boldsymbol{B}_e$ indicates the gradient of the shape function in FEM and Ω_e is the elemental domain.

4.2.2.3 Sensitivity Analysis

In this section, the solution process of the concurrent optimization is described. Note that, the density variables and the position variables are separately treated, where the former plus the volume constraint are solved with the OC method and the latter plus the non-overlap constraint are addressed through the Lagrange multiplier method. In this way, movement of the features will slightly perturb convergence of the lattice density field but would not damage the overall convergence, which can be concluded from the later demonstrated convergence curves.

In the lattice domain, the sensitivity of the objective function with respect to the relative density can be computed as:

$$\frac{\partial J}{\partial \rho_e} = -\frac{1}{2} \boldsymbol{T}_e^T \frac{\partial \boldsymbol{k}_e}{\partial \rho_e} \boldsymbol{T}_e \tag{4.29}$$

Substitution of Eq. (4.12) into $\frac{\partial \boldsymbol{k}_e}{\partial \rho_e}$, one can obtain:

$$\begin{aligned} \frac{\partial \boldsymbol{k}_e}{\partial \rho_e} &= \int_{\Omega_e} \boldsymbol{B}_e^T \frac{\partial \boldsymbol{D}_e}{\partial \rho_e} \boldsymbol{B}_e d\Omega \\ &= (1-\zeta) \int_{\Omega_e} \boldsymbol{B}_e^T \frac{\partial \boldsymbol{D}(\rho)}{\partial \rho_i} \boldsymbol{B}_e d\Omega \end{aligned} \tag{4.30}$$

The sensitivity of the volume fraction V with respect to the element density can be calculated as:

$$\frac{\partial V}{\partial \rho_e} = (1-\zeta)v_e \tag{4.31}$$

With all the sensitivity results obtained above, the lattice densities can be solved with the optimality criteria (OC) method, which has been widely applied for the single volume constraint problem [132, 133]. Following the work of [133], an update of the relative density in the lattice structure domain can be expressed as

$$\rho_e^{new} = \begin{cases} \max(\underline{\rho}, \rho_e - m) & \text{if } \rho_e B_e^{\gamma} \leq \max(\underline{\rho}, \rho_e - m) \\ \min(\overline{\rho}, \rho_e + m) & \text{if } \rho_e B_e^{\gamma} \geq \min(\overline{\rho}, \rho_e - m) \\ \rho_e B_e^{\gamma} & \text{otherwise} \end{cases} \tag{4.32}$$

where $m = 0.15$ represent a positive move-limit and $\gamma = 0.5$ is a damping coefficient. The term B_i is defined as

$$B_e = -\frac{\frac{\partial J}{\partial \rho_e}}{\lambda \frac{\partial V}{\partial \rho_e}} \tag{4.33}$$

Given the feature parameters, the Lagrangian can be constructed as:

$$L = J\big(\boldsymbol{c}(t)\big) + \eta\left(-\sum_{e=1}^{N}(\zeta v_e) + V_c\right) \tag{4.34}$$

where η is the Lagrange multiplier for the non-overlap constraint.

The sensitivity of the objective function with respect to the pseudo time can be calculated as:

$$\frac{\partial J}{\partial t} = \boldsymbol{T}^T \boldsymbol{K} \frac{\partial \boldsymbol{T}}{\partial t} + \frac{1}{2}\boldsymbol{T}^T \frac{\partial \boldsymbol{K}}{\partial t}\boldsymbol{T} \tag{4.35}$$

Calculating the derivatives of the geometric variables on both sides of the equilibrium equation, we have

$$\frac{\partial \boldsymbol{K}}{\partial t}\boldsymbol{T} + \boldsymbol{K}\frac{\partial \boldsymbol{T}}{\partial t} = \frac{\partial(\boldsymbol{q}+\boldsymbol{G}+\boldsymbol{H})}{\partial t} \tag{4.36}$$

Thus, one can obtain $\frac{\partial \boldsymbol{T}}{\partial t}$ as

$$\frac{\partial \boldsymbol{T}}{\partial t} = \boldsymbol{K}^{-1}\frac{\partial(\boldsymbol{q}+\boldsymbol{G}+\boldsymbol{H})}{\partial t} + \boldsymbol{K}^{-1}\frac{\partial \boldsymbol{K}}{\partial t}\boldsymbol{T} \tag{4.37}$$

By substituting Eq. (4.37) into Eq. (4.35), we can obtain the sensitivity for the geometric variables as:

$$\frac{\partial J}{\partial t} = \boldsymbol{T}^T\frac{\partial(\boldsymbol{q}+\boldsymbol{G}+\boldsymbol{H})}{\partial t} - \frac{1}{2}\boldsymbol{T}^T\frac{\partial \boldsymbol{K}}{\partial t}\boldsymbol{T} \tag{4.38}$$

In this work, the design-independent boundary condition is considered, and hence the sensitivity of functional features can be further rewritten as:

$$\frac{\partial J}{\partial t} = -\frac{1}{2}\boldsymbol{T}^T\frac{\partial \boldsymbol{K}}{\partial t}\boldsymbol{T} \tag{4.39}$$

Using Eq. (4.13), the derivation of $\frac{\partial \boldsymbol{K}}{\partial t}$ can be calculated as:

$$\begin{aligned}\frac{\partial \boldsymbol{K}}{\partial t} = \sum_{k=1}^{N_c}\sum_{j=1}^{M_k}\Bigg(\sum_{\Omega}\int_{\Omega_e}\boldsymbol{B}_e^T\Bigg(-\frac{\partial \zeta}{\partial \phi_k(\boldsymbol{x},\boldsymbol{c}(t))}\cdot\frac{\partial \phi_k(\boldsymbol{x},\boldsymbol{c}(t))}{\partial c_j}\cdot\frac{\partial c_j}{\partial t}\cdot\boldsymbol{D}(\rho_e) + \\ \frac{\partial \zeta}{\partial \phi_k(\boldsymbol{x},\boldsymbol{c}(t))}\cdot\frac{\partial \phi_k(\boldsymbol{x},\boldsymbol{c}(t))}{\partial c_j}\cdot\frac{\partial c_j}{\partial t}\cdot\boldsymbol{D_k}\Bigg)\boldsymbol{B}_e d\Omega\Bigg)\end{aligned} \tag{4.40}$$

where M_k is the number of geometric variable for the k^{th} movable feature and c_j represents the j^{th} geometric variable of the k^{th} movable feature.

The substitution of Eq. (4.40) into Eq. (4.39), the sensitivity of the objective function to the pseudo-time is

$$\frac{\partial J}{\partial t} = \sum_{k=1}^{N_c}\sum_{j=1}^{M_k}\left(\sum_{\Omega}\frac{1}{2}\boldsymbol{T}_e^T\int_{\Omega_e}\boldsymbol{B}_e^T\left(\frac{\partial\zeta}{\partial\phi_k(\boldsymbol{x},\boldsymbol{c}(t))}\cdot\frac{\partial\phi_k(\boldsymbol{x},\boldsymbol{c}(t))}{\partial c_j}\cdot\frac{\partial c_j}{\partial t}\cdot\boldsymbol{D}(\rho_e) - \frac{\partial\zeta}{\partial\phi_k(\boldsymbol{x},\boldsymbol{c}(t))}\cdot\frac{\partial\phi_k(\boldsymbol{x},\boldsymbol{c}(t))}{\partial c_j}\cdot\frac{\partial c_j}{\partial t}\cdot\boldsymbol{D_k}\right)\boldsymbol{B}_e d\Omega\,\boldsymbol{T}_e\right) \tag{4.41}$$

For the non-overlap constraint, the sensitivity of the constraint with respect to the geometric parameters is

$$\frac{\partial V_l}{\partial t} = \sum_{e=1}^{N}\left(\frac{\partial\zeta}{\partial t}v_e\right) = -\sum_{k=1}^{N_c}\sum_{j=1}^{M_k}\left(\sum_{e=1}^{N}\left(\frac{\partial\zeta}{\partial\phi_k(\boldsymbol{x},\boldsymbol{c}(t))}\cdot\frac{\partial\phi_k(\boldsymbol{x},\boldsymbol{c}(t))}{\partial c_j}\cdot\frac{\partial c_j}{\partial t}\cdot v_e\right)\right) \tag{4.42}$$

Thus, the sensitivity of the Lagrangian expression in Eq. (4.34) with respect to the pseudo time is

$$\frac{\partial L}{\partial t} = \frac{\partial J}{\partial t} + \eta\frac{\partial V_l}{\partial t} =$$
$$\sum_{k=1}^{N_c}\sum_{j=1}^{M_k}\left(\sum_{\Omega}\frac{1}{2}\boldsymbol{T}_e^T\int_{\Omega_e}\boldsymbol{B}_e^T\left(\frac{\partial\zeta}{\partial\phi_k(\boldsymbol{x},\boldsymbol{c}(t))}\cdot\frac{\partial\phi_k(\boldsymbol{x},\boldsymbol{c}(t))}{\partial c_j}\cdot\boldsymbol{D}(\rho_e) - \frac{\partial\zeta}{\partial\phi_k(\boldsymbol{x},\boldsymbol{c}(t))}\cdot\right. \tag{4.43}$$
$$\left.\frac{\partial\phi_k(\boldsymbol{x},\boldsymbol{c}(t))}{\partial c_j}\cdot\boldsymbol{D_k}\right)\boldsymbol{B}_e d\Omega\,\boldsymbol{T}_e - \eta\sum_{e=1}^{N}\left(\frac{\partial\zeta}{\partial\phi_k(\boldsymbol{x},\boldsymbol{c}(t))}\cdot\frac{\partial\phi_k(\boldsymbol{x},\boldsymbol{c}(t))}{\partial c_j}\cdot v_e\right)\Bigg)\frac{\partial c_j}{\partial t}$$

A decent direction of the objective function can therefore be found[125] by

$$\frac{\partial c_j}{\partial t} = \sum_{\Omega}\frac{1}{2}\boldsymbol{T}_e^T\int_{\Omega_e}\boldsymbol{B}_e^T\left(-\frac{\partial\zeta}{\partial\phi_k(\boldsymbol{x},\boldsymbol{c}(t))}\cdot\frac{\partial\phi_k(\boldsymbol{x},\boldsymbol{c}(t))}{\partial c_j}\cdot\boldsymbol{D}(\rho_e) + \frac{\partial\zeta}{\partial\phi_k(\boldsymbol{x},\boldsymbol{c}(t))}\cdot\frac{\partial\phi_k(\boldsymbol{x},\boldsymbol{c}(t))}{\partial c_j}\cdot\boldsymbol{D_k}\right)\boldsymbol{B}_e d\Omega\,\boldsymbol{T}_e + \eta\sum_{e=1}^{N}\left(\frac{\partial\zeta}{\partial\phi_k(\boldsymbol{x},\boldsymbol{c}(t))}\cdot\frac{\partial\phi_k(\boldsymbol{x},\boldsymbol{c}(t))}{\partial c_j}\cdot v_e\right) \tag{4.44}$$

The Lagrange multiplier method is employed to solve the problem, which can be expressed as follows:

$$c_j^{(t+1)} = c_j^{(t)} + \Delta t\left(\frac{\partial c_j}{\partial t}\right)^{(t)} \tag{4.45}$$

$$\eta^{(t+1)} = \eta^{(t)} + \beta_t(-\sum_{i=1}^{N}(\zeta v_i) + V_c)^{(t)} \tag{4.46}$$

where Δt and β_t are positive to control the update of the geometric parameter and the Lagrange multiplier, respectively.

4.2.2.4 Numerical Implementation

The flowchart of the optimization is given in Figure 4.7. At the beginning, homogenized model of thermal conductivity obtained in Section 2.5 is implemented in the FEM program. In the second step, the equilibrium equation is calculated to obtain the temperature distribution and its corresponding gradient. In the third step, the objective of the optimization and the volume constraint are computed. If the stop criteria are satisfied, the optimization terminates, and optimal result is obtained. If not, the sensitivity of objective for both lattice density and geometric parameters are calculated. In the concurrent optimization, the optimality criteria (OC) [132, 134] method given in Eq. (4.32)-(4.33)is employed to evolve the lattice density, while the geometric parameters of functional features are updated by the Lagrange multiplier method proposed in Eqs.(4.45)-(4.46). A Boolean operation is performed in the internal iteration of OC to combine the movable feature with lattice structure to guarantee the volume constraint. Once the optimization in OC is completed, the program will go to the next iteration until the stop criterion is satisfied.

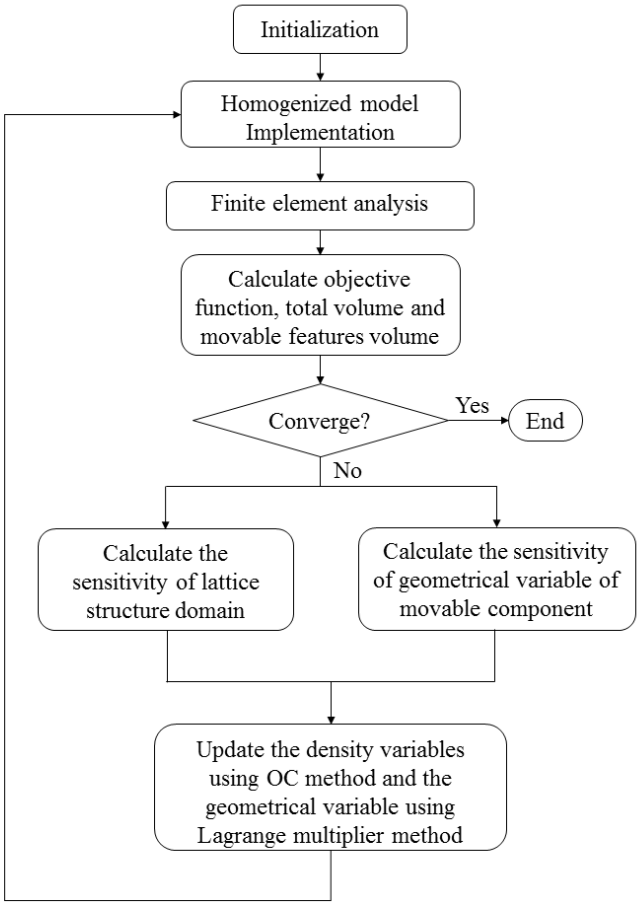

Figure 4.7: Flowchart of the Concurrent Optimization Process.

4.2.3 Convergence Study of AH Method

Once the optimal material distribution is obtained through the proposed concurrent LSTO approach, a reconstruction program is developed to realize the final design for manufacturing. As introduced earlier, AH method is employed, which means that the RVE units should be periodically distributed and the size of the RVE unit should be small [107]. On the other hand, from the manufacturability point of view, the minimum size of the lattice units that can be produced using AM processes is determined by the resolution of the machines. Therefore, both

aspects should be considered in reconstruction to ensure accuracy of the AH representation and manufacturability of the part.

First, we numerically examine the size effect of the lattice structure on accuracy of the homogenization model. A simple cube example is studied as shown in Figure 4.8(a). It has a size of $30 \times 30 \times 30\ \text{mm}^3$ and its top and bottom surfaces are attached with two solid plates of 0.5 mm thickness each. The temperature is 22℃ at the top surface, a heat flux of $0.1\ \text{W/mm}^2$ is applied to the bottom surface, and all other surfaces are perfectly insulated. The base material is $AlSi_{10}Mg$ with a thermal conductivity of $110\ \text{W/m} \cdot ℃$, and the volume fraction of the cube is set to be $V = 0.4$. Accordingly, the homogenized thermal conductivity is $26.15\ \text{W/m} \cdot ℃$, and the simulation result with homogenization is illustrated in Figure 4.8 (b), where the temperature at the bottom surface is about 138.1 ℃.

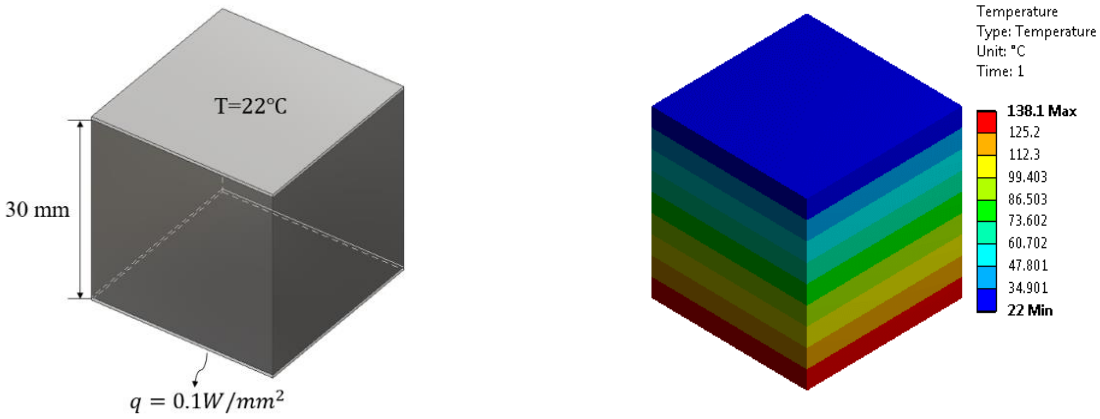

(a) (b)

Figure 4.8: FEA Model of the Cubic for Examination of Homogenization. (a) FEA Model of the Cube and (b) Temperature Profile of the Cube with Volume Fraction of 0.4.

For comparison purpose, the unit sizes of 2mm, 3mm, 5mm, 6mm, 10mm, 15mm and 30 mm are used to fill the part and the corresponding full-scale FEAs are carried out to compare with the accuracy of the homogenization model; see Figure 4.9. The temperature profile of the bottom surface gradually approaches the homogenization result with the decrease in unit cell size, as presented in Figure 4.10. Especially when the cell number is larger than five in the heat transfer direction, the difference between homogenization and full-scale simulation becomes less than 2%.

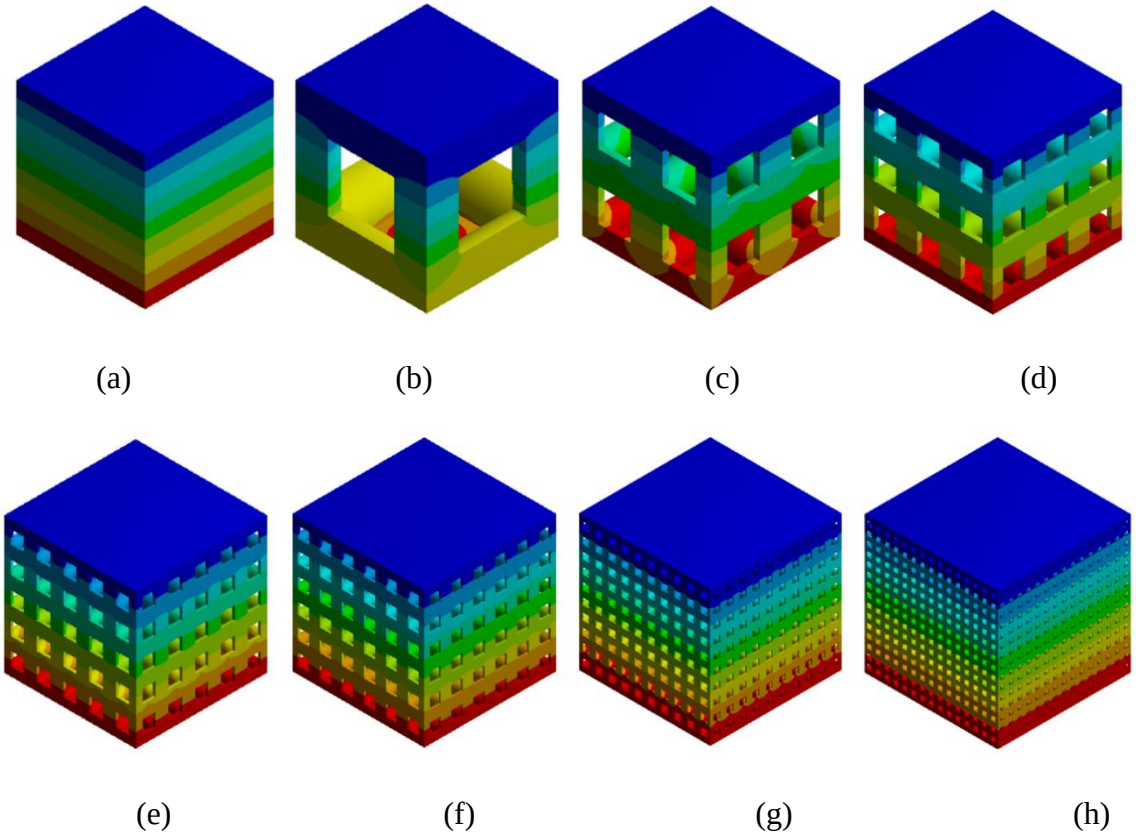

Figure 4.9: Temperature Profile of Lattice Infill Design with Various Cell Size. (a) Homogenized Model, (b) $l_0 = 30$ mm (c) $l_0 = 15$ mm (d) $l_0 = 10$ mm (e) $l_0 = 6$ mm (f) $l_0 = 5$ mm (g) $l_0 = 3$ mm (h) $l_0 = 2$ mm.

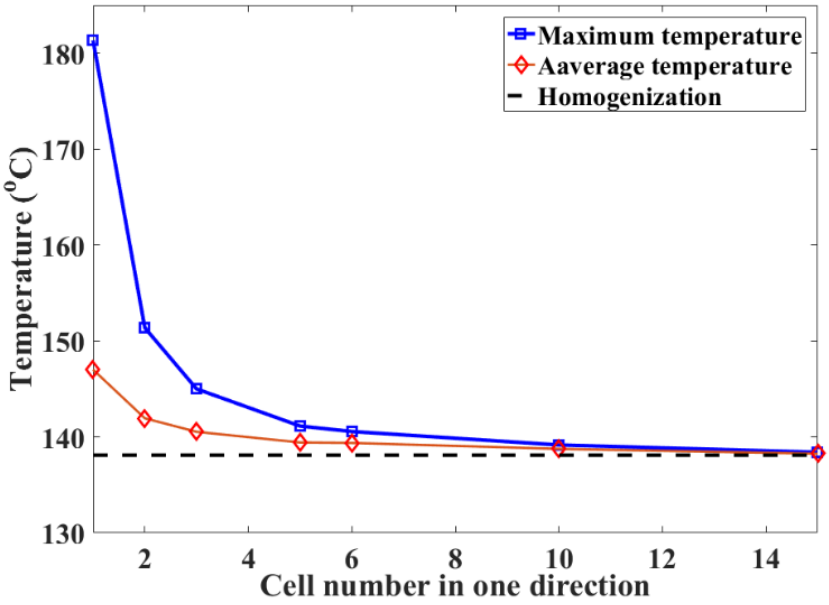

Figure 4.10: Maximum Temperature and Average Temperature Associated with Cell Number along One Direction

From the manufacturability point of view, the unit cell size can neither be too small nor too large. This is because below a certain value, the printing quality will drastically decrease and beyond some value, the unit cells cannot be self-supported. To quantify the design constraints, a test part is designed and printed out using the laser powder-bed metal AM process. Figure 4.11 demonstrates both the CAD model and the print-out in $AlSi_{10}Mg$. By analyzing the print-out, it is found that the minimum ligament diameter that can be printed out with regularity is 0.5 mm and the corresponding maximum overhang length is 3.5 mm. Therefore, the minimum unit size is set to 3.5 mm in length and the related lower bound of relative density is $\underline{\rho} = 0.15$.

In summary, the lattice unit size and the relative density range have been properly determined to maximize the accuracy of the AH model and at the same time, address the manufacturability issue.

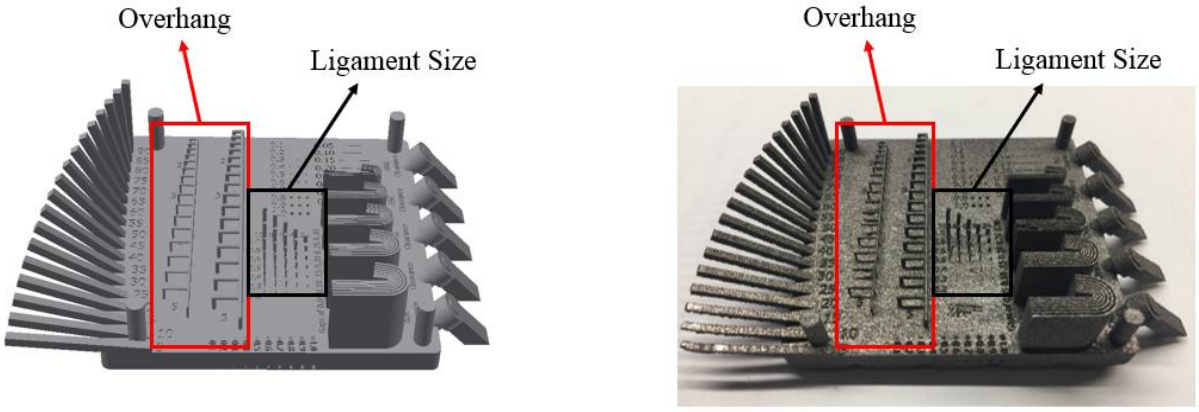

(a) (b)

Figure 4.11: Benchmark Study for the Overhang and Ligament Size. (a) CAD Model of the Benchmark (b) Photo of the Printed Sample in Ti64 Using EOS DMLS.

Once the proper lattice unit size is determined, the procedure of reconstructing the CAD model is illustrated in Figure 4.12. The key steps include converting the density distribution into the radius distribution at the joints, and then connect the joints through a linear loft of the radii to avoid discontinuity along the ligaments. The reconstruction process has been experimentally validated for different AM processes and more details about the reconstruction process can be found in [106, 135, 136].

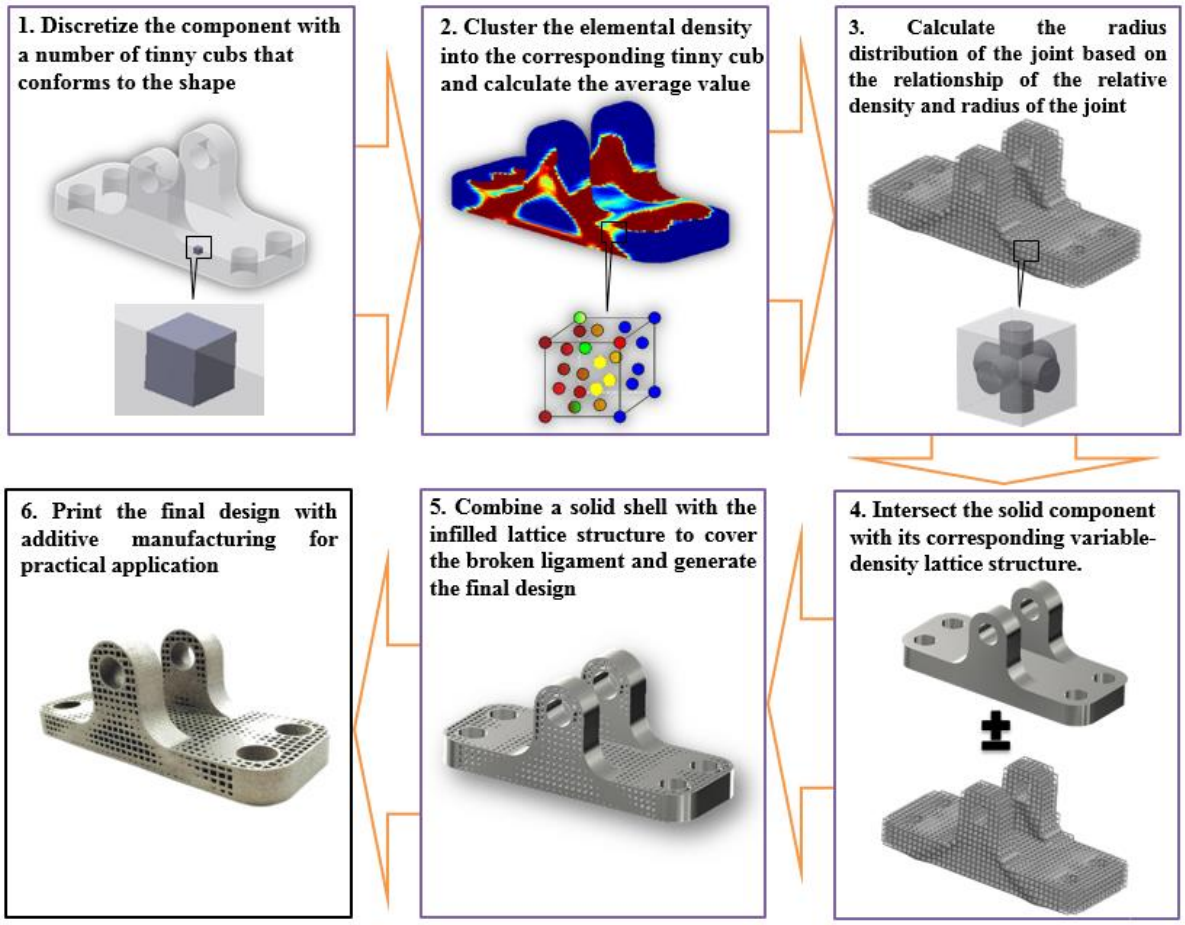

Figure 4.12: Reconstruction Procedure to Obtain the End-usable Component

4.2.4 Numerical Examples and Validation

In this section, several numerical examples are provided to demonstrate accuracy of the homogenized model and effectiveness of the proposed concurrent optimization method. The optimization problem is to minimize the potential thermal energy of the structure under the volume fraction constraint. Note that a sensitivity filter technique [137] is applied to in the LSTO to avoid the checkboard problem. If not specified, the volume fraction of the structure is set to be $V^* = 0.5$. The optimization terminates when the relative difference of the objective functions between two

successive iterations is smaller than 1×10^{-5} and when the volume constraint is satisfied when the relative difference between successive iterations is less than 1×10^{-4}. A thermal conductivity value of $110\ \mathrm{W/m \cdot ℃}$ will be employed in the simulation; this value corresponds to the thermal conductivity of aluminum alloy $AlSi_{10}Mg$ samples printed by the EOS DMLS M290 system.

Case 1: LSTO without Functional Feature

The first test case of a plate with a heat source and constant temperature boundary conditions is designed to verify accuracy of the homogenized model and investigate the affect the density bounds on the final design. As illustrated in Figure 4.13, two different temperatures are imposed on the four corners of the plate, while a heat flux of $1\ \mathrm{W/mm^2}$ is uniformly applied on the surface of the rectangular hole located in the middle of the plate. A structured mesh consisting 48,246 eight-node hexagonal element is used to discretize the design domain.

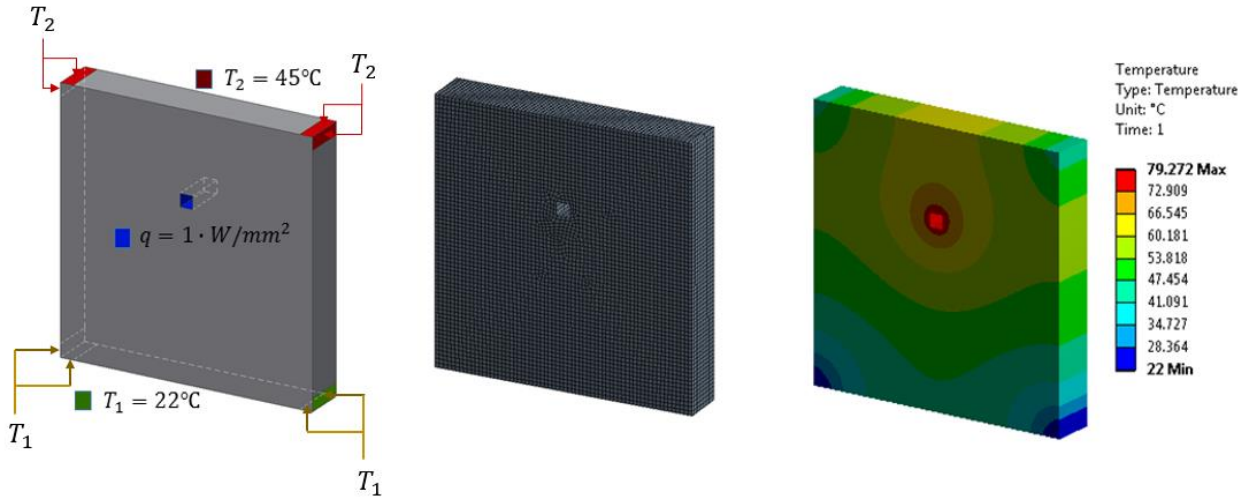

(a) (b) (c)

Figure 4.13: FEA Model of the Plate. (a) Boundary Conditions, (b) Structured Mesh Model and (c) Temperature Distribution of the Solid Plate.

To verify the proposed homogenized model for graded lattice design, the model in Figure 4.13 is optimized using LSTO method without embedded features. The density range of the infilled lattice is set to be $\underline{\rho} = 0.2$ and $\overline{\rho} = 0.92$. The optimization results are given in Figure 4.14, including the density distribution, temperature distribution and convergence history. During the optimization, the material tends to concentrate on the bands that connect the heat flux boundary and corner temperature boundaries, in order to promote the heat transfer of the heat source. As illustrated in the iteration history, the objective function converges to 1.756×10^8 W · K after 36 iterations, while the maximum temperature decreases from 170.68 ℃ to 100.56 ℃ (i.e. 41.08% reduction).

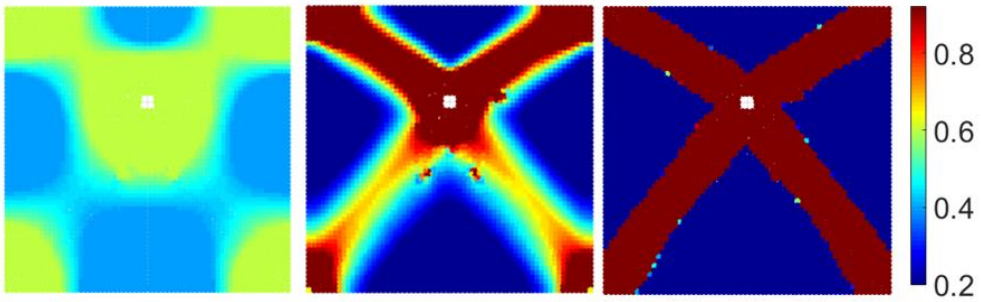

(a) Iteration 1 (b) Iteration 4 (c) Iteration 36

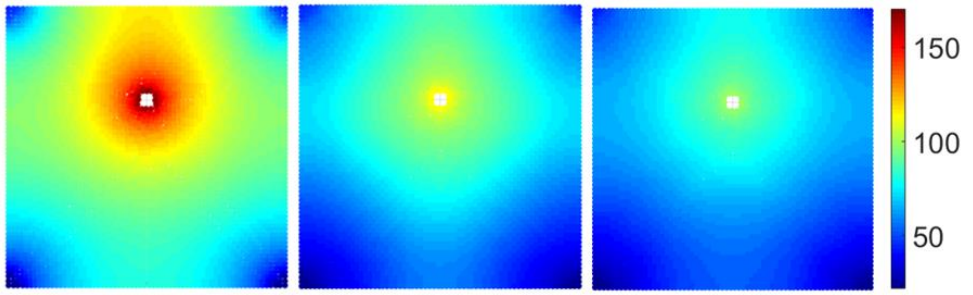

(d) Iteration 1 (e) Iteration 4 (f) Iteration 36

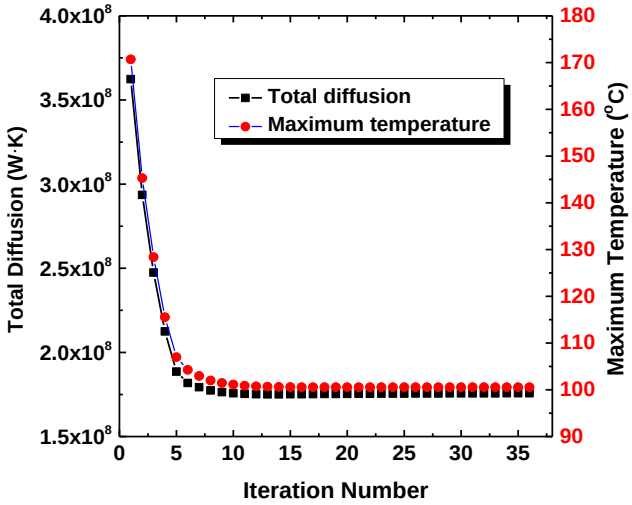

(g)

Figure 4.14: Optimization Result of Case 1. (a)-(c) Snapshot of Relative Density Distribution at Different Iteration Number. (d)-(f) Snapshot of Temperature Distribution at Different Iteration Number. (g) Convergence of Objective Function and Maximum Temperature.

Next, the optimized density distribution in Figure 4.14(c) is used to reconstruct the plate with variable-density lattice structure, where the result is shown in Figure 4.15(a). A full-scale simulation on the lattice design is conducted to verify the proposed homogenization. The detailed optimal design is discretized using 838,858 elements and simulated using FEA in order to compare with the temperature field obtained by homogenization. As shown in Figure 4.14(f) and Figure 4.15 (b), the temperature profiles from the two models are in good agreements with each other. For instance, the maximum temperature obtained by homogenization is 100.56 ℃, while the value of full-scale simulation is 101.01 ℃, and hence the difference is about 0.45%. This test case demonstrates that the homogenized model is reasonably accurate for modeling variable-density lattice structure.

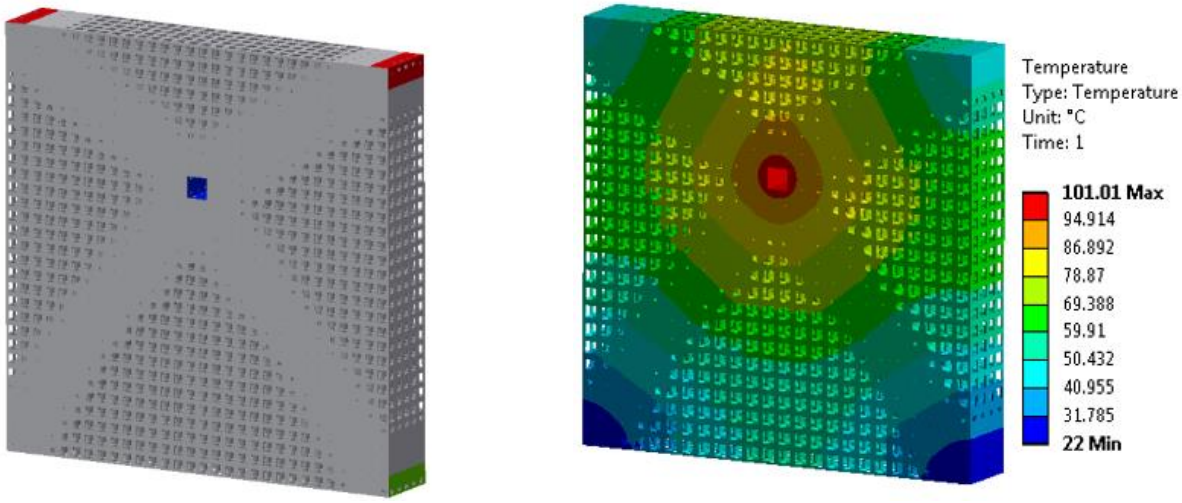

(a) (b)

Figure 4.15: Variable-density Lattice Structure Design for Case 1. (a) CAD Model of Graded Lattice Infill (b) Temperature Field of the Full-scale Simulation.

To explore the effect of the density range on the final design, given the same volume fraction ($V^* = 0.5$), three different density ranges are studied: (1) [0.1 0.9], (2) [0.1 0.8] and (3) [0.2 0.8], and the optimization results are demonstrated in Figure 4.16 and Table 4.1. As illustrated, the decrease of lower bound results in a reduction of objective function and maximum temperature, while the decrease of the upper bound leads to an increase of these values. The reason lies in that, either decreasing the lower limit and increasing the upper limit effectively expands the design space. Note that the volume fraction should be larger than the lower bound of the density range, because when the volume fraction is smaller than the lower bound, the volume constraint cannot be satisfied and thus convergence cannot be obtained.

Table 4.1: Optimization Result of the Problem for Case 1 with Various Density Range

	$V^* = 0.5$ $\rho \in [0.1, 0.9]$	$V^* = 0.5$ $\rho \in [0.1, 0.8]$	$V^* = 0.5$ $\rho \in [0.2, 0.8]$
Objective function ($\mathrm{W \cdot K}$)	1.714×10^8	1.967×10^8	2.038×10^8
Maximum Temperature from homogenization (℃)	97.95	107.14	109.8
Maximum Temperature from simulation (℃)	98.7	107.3	110.1

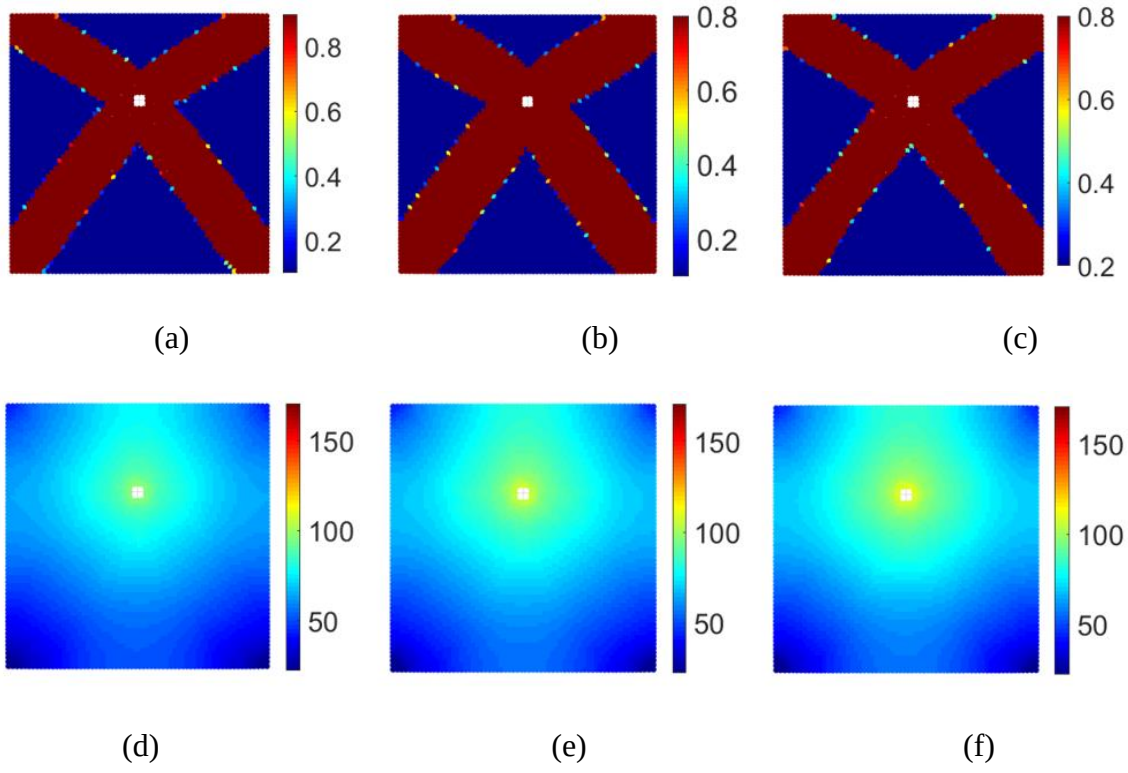

Figure 4.16: Optimization Result of the Design with Various Density Range. (a) Optimal Density Distribution for $\boldsymbol{\rho} \in [\mathbf{0.1}, \mathbf{0.9}]$ (b) Optimal Density Distribution for $\boldsymbol{\rho} \in [\mathbf{0.1}, \mathbf{0.8}]$ (c) Optimal Density Distribution for $\boldsymbol{\rho} \in [\mathbf{0.2}, \mathbf{0.8}]$; (d) Temperature Profile for $\boldsymbol{\rho} \in [\mathbf{0.1}, \mathbf{0.9}]$, (e) Temperature Profile for $\boldsymbol{\rho} \in [\mathbf{0.1}, \mathbf{0.8}]$ and (f) Temperature Profile for $\boldsymbol{\rho} \in [\mathbf{0.2}, \mathbf{0.8}]$.

A full-scale simulation is conducted on the variable-density lattice structure designs for the three different density ranges. The temperature distributions are illustrated in Figure 4.17, which agree well with the homogenization model result. It implies that the proposed homogenization model can be effectively used to analyze the graded lattice structure, which therefore can significantly reduce the computational cost compared with the detailed simulation. For instance, the element number used for these three full-scale simulations are all more than 500,000, which is ten times larger than the homogenization model.

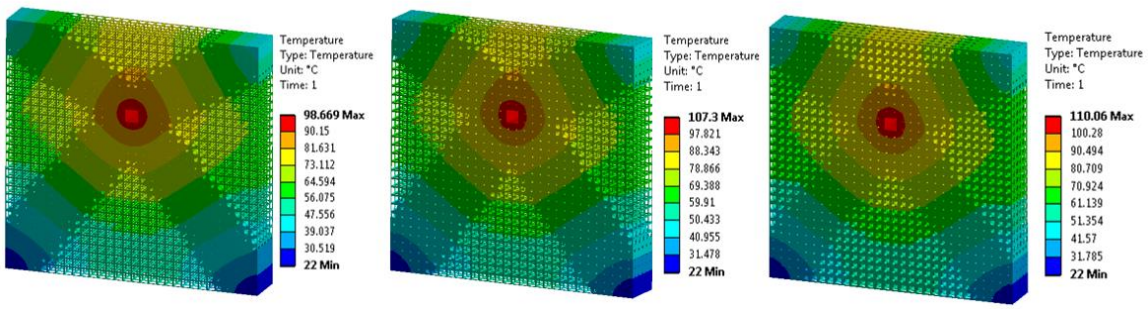

Figure 4.17: Full Scale Simulation for Problem of Case 1. (a) Temperature Distribution of $\boldsymbol{\rho} \in [\mathbf{0.1}, \mathbf{0.9}]$ (b) Temperature Distribution of $\boldsymbol{\rho} \in [\mathbf{0.1}, \mathbf{0.8}]$ (c) Temperature Distribution of $\boldsymbol{\rho} \in [\mathbf{0.2}, \mathbf{0.8}]$.

Case 2. Concurrent LSTO with Non-overlap Constraints

The second test case is used to verify the non-overlap constraint proposed in Eq. (4.26) for multi-component design. The model and boundary conditions are identical to case 1, except that a solid cylinder and a solid rectangle are initially placed within the base plate and allowed to move around. As illustrated in Figure 4.18, the two features are initially placed at the same positions with coordinates $(x = 2\ \text{mm}, y = -6\ \text{mm})$ and the initial angle of the cube is set to $\theta = 0°$. Assuming that the two movable features are composed of copper alloy with thermal conductivity of $399\ \text{W/m} \cdot \text{K}$, which is about 3.5 times larger than the base material, $\text{AlSi}_{10}\text{Mg}$. The diameter of the cylinder is 3 mm and the side length of the cube is 3 mm. The cylinder is at the center of the rectangle. The density range of base plate is set to be $\underline{\rho} = 0.2$ and $\overline{\rho} = 0.9$, respectively.

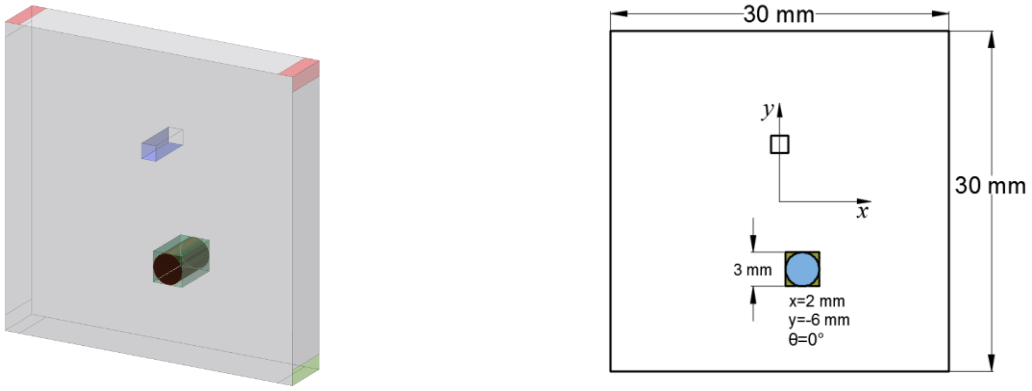

(a) (b)

Figure 4.18: CAD Model for the Problem in Case 2. (a) Cylinder and Cub are Initially Placed in the Base Plate (b) Coordinate and Dimension of the Cylinder and Cub.

For comparison purpose, an optimization without considering the non-overlap constraint is first performed. The optimization results including the density evolution and temperature history are presented in Figure 4.19. It can be seen that the solid cylinder tends to move together with the rectangle during the optimization. This is because the material of the two features are the same to each other. In the result, the two features are positioned inside a high-density band. Figure 4.20 illustrates the convergence history of the objective function, maximum temperature, and the evolution of coordinates of the two features. After 50 iterations, the objective function converges from 3.618×10^8 W · K to 1.772×10^8 W · K, a 51% decrease, and the maximum temperature decreases from 170.13 ℃ to 100.95 ℃. The rectangle is finally positioned at $(x = 3.59 \text{ mm}, y = -3.78 \text{ mm}, \theta = -0.14 \text{ rad})$ and the cylinder finally moves to$(x = 3.3 \text{ mm}, y = -1.84 \text{ mm})$.

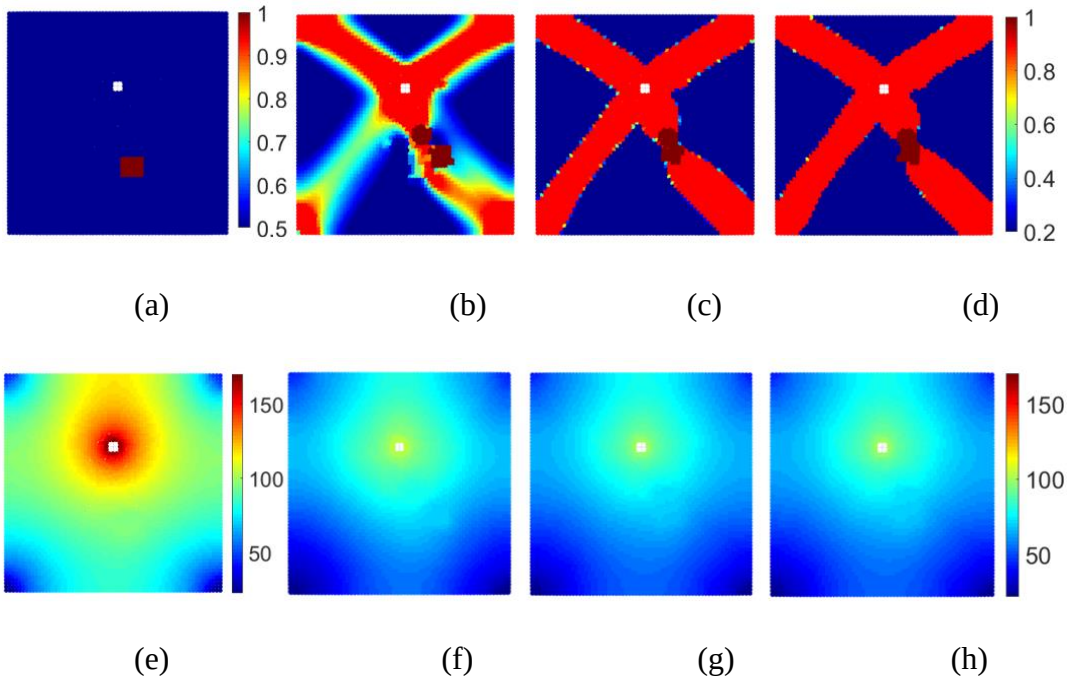

Figure 4.19: Optimization Results of Case 2 without Non-overlap Constraint. (a)-(d) Optimal Density Distribution of Iteration (0), (5), (20) and (50); (e)-(f) Temperature Distribution of Iteration (0), (5), (20) and (50).

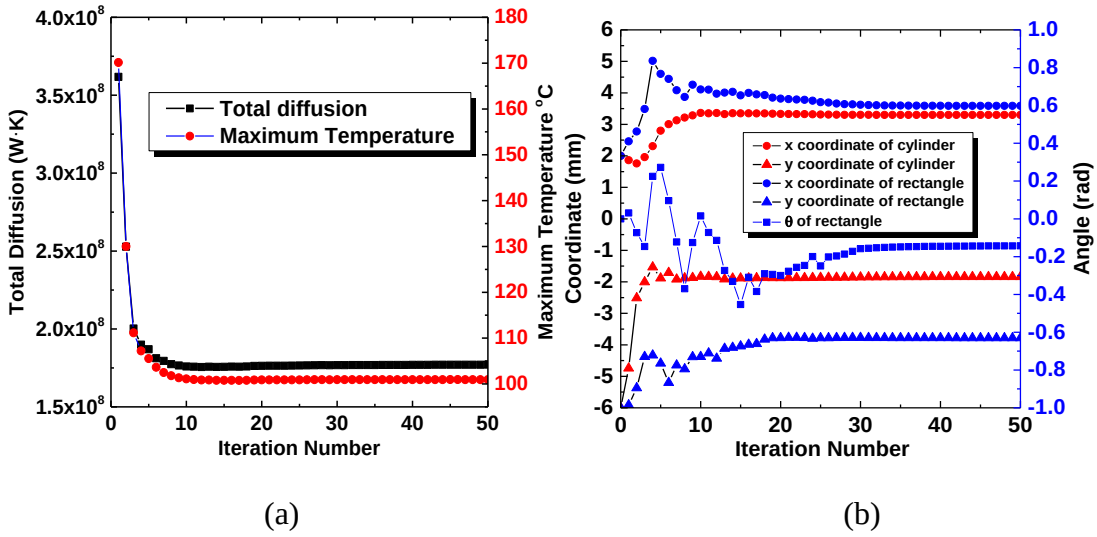

Figure 4.20: Convergence History of Case 2 without Non-overlap Constraint. (a) Objective Function and Maximum Temperature (b) Position Coordinate of Two Features.

The optimization result with non-overlap constraint is presented in Figure 4.21. It can be found that the rectangle moves towards the left side of the high-density area, while the cylinder ends up at the right side of the high-density area. Different from the results without non-overlap constraint, the two features are separated from each other and moves towards the nearest high-density band. As illustrated in Figure 4.22(a), the objective function converges to 1.733×10^8 W · K with a decrease of 52.1% and the maximum temperature is decreased from 170.13 ℃ to 99.53 ℃. In the final design, the cylinder moves to the right side with a coordinate of $(x = 2.45 \text{ mm}, y = -1.78 \text{ mm})$, while the rectangle is positioned at $(x = -4.30 \text{ mm}, y = -1.30 \text{ mm}, \theta = 0.47 \text{ rad})$. The rectangle and the cylinder are separated from each other, which demonstrates the efficiency of the proposed non-overlap constraint. In Figure 4.21(d), there exists a hole area around the solid cylinder, because the thermal conductivity of the cylinder is much larger than the base material and the temperature gradient at that area is very small.

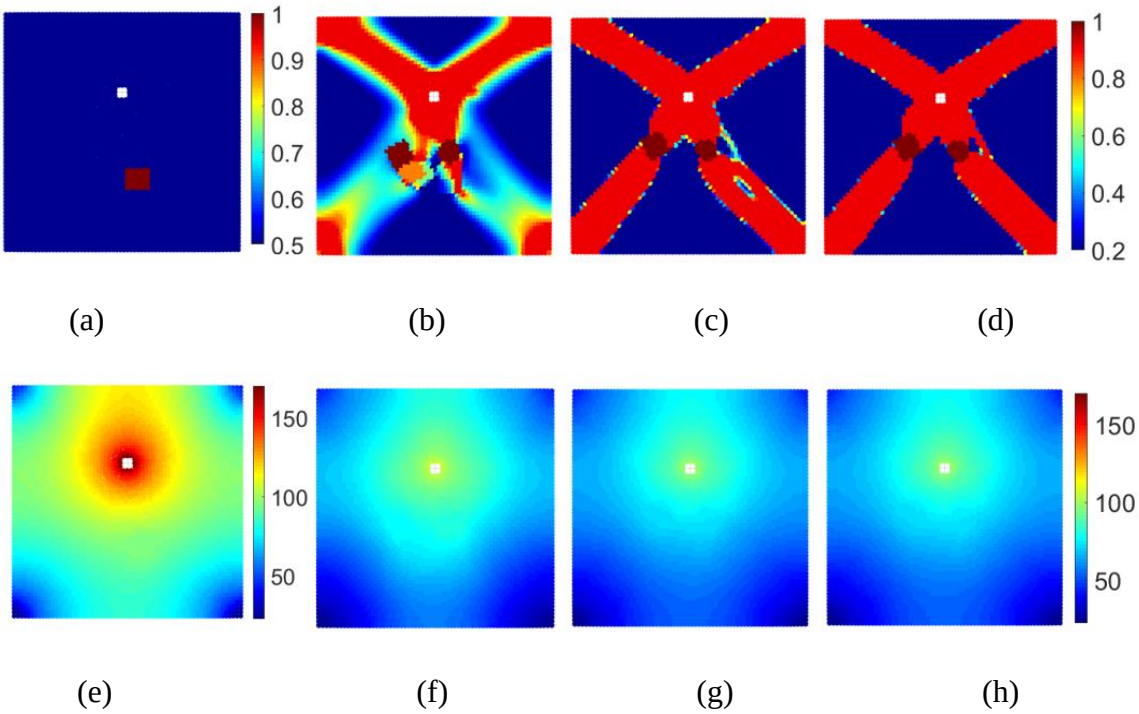

Figure 4.21: Optimization Results of Case 2 Under Non-overlap Constraint. (a)-(d) Optimal Density Distribution of Iteration (0), (5), (20) and (46); (e)-(f) Temperature Distribution of Iteration (0), (5), (20) and (46).

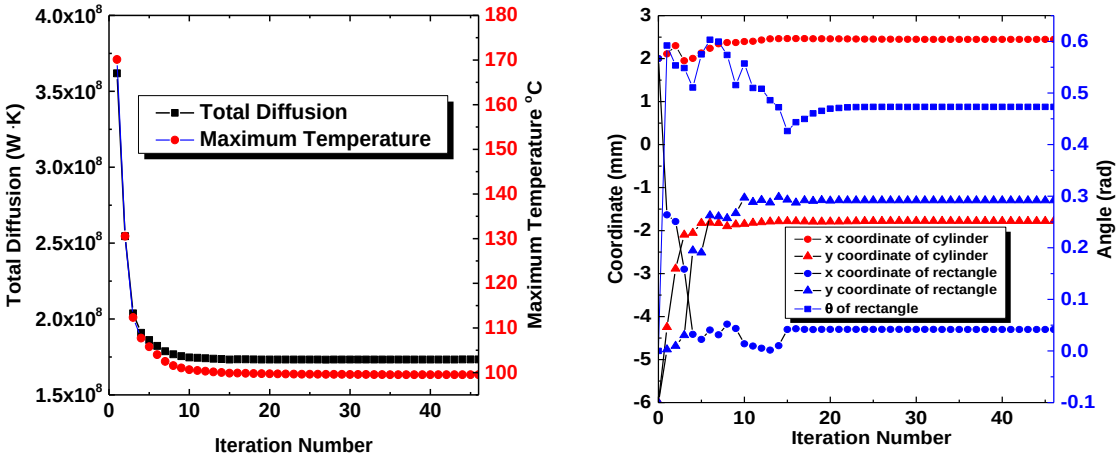

(a) (b)

Figure 4.22: Convergence History of Case 2 under Non-overlap Constraint. (a) Objective Function and Maximum Temperature (b) Position Coordinate of Two Features.

To examine the performance of the two designs for case 2, full scale simulations are conducted to compare with the prediction from homogenization. As illustrated in Figure 4.23, the maximum temperature of the design under non-overlap constraint is 100.41 ℃ while the design without the non-overlap design is 101.52 ℃. This is because the overlap of the two features leads to a decrease of the volume of the embedded features and thus an increase of the maximum temperature. Comparing with the prediction from homogenization, the difference of the maximum temperature for the overlap design is 0.54 ℃, while for the non-overlap design is 0.88 ℃. These results further prove that the proposed homogenized model can be efficiently used to optimize graded lattice structure embedded with movable features.

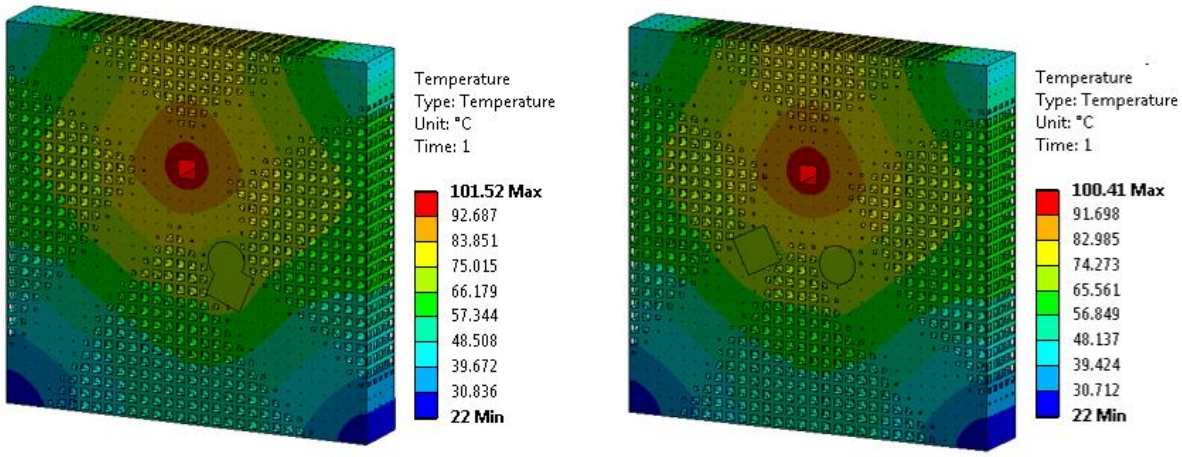

(a) (b)

Figure 4.23: Full Scale Simulation of Case 2. (a) Design without Non-overlap Constraint; (b) Design under Non-overlap Constraint.

Case 3. Concurrent LSTO Method with Different Initial Position

In the third case, a solid cylinder is randomly placed in the base plate and different starting positions will be investigated to explore the initial guess dependency issue. Figure 4.24 shows the CAD model and initial positions to be explored. Due to the symmetry of the design domain, the cylinder is only randomly placed at the right side of the host plate. The boundary conditions and material property of the host lattice structure are the same as case 1. The radius of the cylinders is 1.5 mm and its material is $AlSi_{10}Mg$. The density range of the lattice structure at base plate is set to be $\underline{\rho} = 0.2$ and $\overline{\rho} = 0.9$, respectively. The volume fraction of the design domain including the movable feature is set to be $V^* = 0.5$.

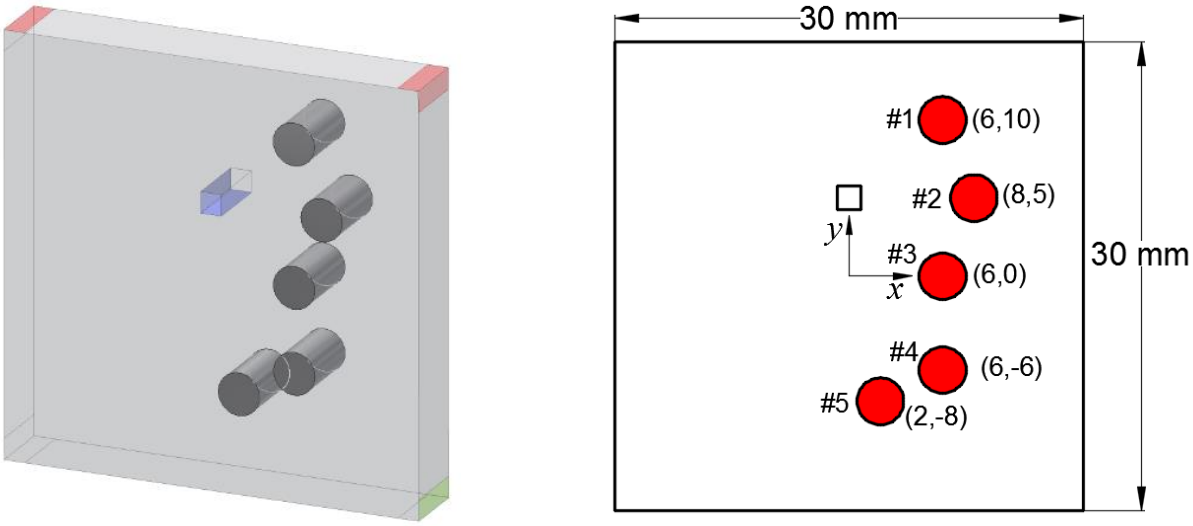

(a) (b)

Figure 4.24: CAD Model and Initial Position of the Cylinder for the Problem of Case 3. (a) CAD Model and (b) Five Random Positions of the Cylinder.

The optimization results are presented in Figure 4.25. As illustrated in the figure, these five cylinders move towards to the nearest high-density area and end up with merging into the high-density band. This implies that the concurrent optimization is a type of local optimal design, in which the movable features tend to be positioned locally rather than globally. The detailed optimization results are tabulated in Table 4.2. It is found that, for the given problem, due to the difference of the initial positions, there are some but small differences of the objective function and maximum temperature. For cylinder #2, both the objective function and the maximum temperature is the lowest. This is because the solid cylinder is nearest to the heat source. Cylinder #5 shows the worst performance since it is farthest from the heat source. This implies that the initial position plays an important role in the performance of the final design.

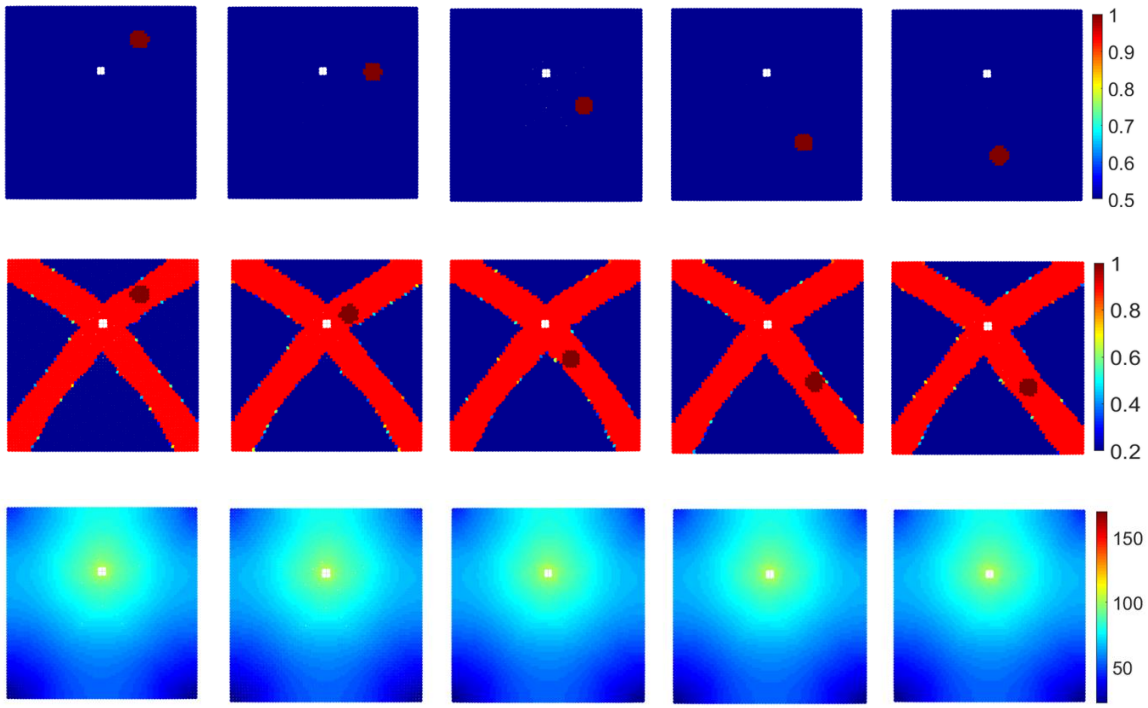

(a) (b) (c) (d) (e)

Figure 4.25: Optimization Results of Problem for Case 3. (a) Initial State, Optimal Density Distribution of #1 (b) Initial State, Optimal Density Distribution of #2 (c) Initial State, Optimal Density Distribution of #3 (d) Initial State, Optimal Density Distribution of #4 (e) Initial State, Optimal Density Distribution of #5.

Table 4.2: Optimization Results of Problem for Case 3

	#1	#2	#3	#4	#5
Initial position (mm)	(6,10)	(8,5)	(6,0)	(6,-6)	(2,-8)
Final position (mm)	(5.75, 9.58)	(3.45, 6.62)	(4.23, -0.46)	(7.91, -4.42)	(6.45, -4.54)
Objective function $(W \cdot K)$	1.80×10^8	1.79×10^8	1.80×10^8	1.80×10^8	1.80×10^8
Maximum temperature from homogenization (℃)	101.1	100.9	101.2	101.2	101.3
Maximum temperature from detailed simulation (℃)	101.4	101.2	101.4	101.4	101.5

The detailed simulation for the lattice structure design is given in Figure 4.26. It can be seen that the maximum temperature of different schemes is in good agreement with the prediction from the homogenized model. This proves that the homogenized model is reasonably accurate for the description of graded lattice structure with embedded solid component.

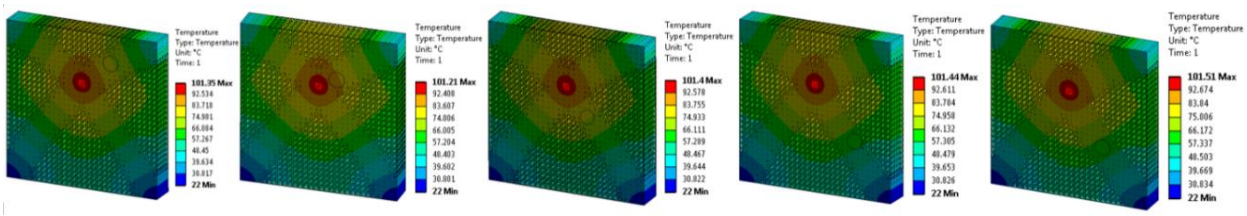

(a) (b) (c) (d) (e)

Figure 4.26: Full-scale Simulation for Case 3. (a)-(e) Temperature Profile of Cylinder #1 to #5.

Case 4. LSTO Includes Multi Features with Multiphase Materials

In the third case, using the same base plate, we consider multi features consisting of multiphase materials. As illustrated in Figure 4.27, there are three different features initially placing in the design domain: a cross, a cylinder and a rectangular. The cross filled with $AlSi_{10}Mg$ is initially placed at $(x = -10\ \text{mm}, y = 4\ \text{mm}, \theta = 0°)$. The stainless steel cylinder having thermal conductivity of $23\ \text{W}/(\text{m} \cdot \text{K})$ is initially placed at $(x = 2\ \text{mm}, y = -7\ \text{mm})$. The coppers rectangular is initially placed at $(x = 4\ \text{mm}, y = -7\ \text{mm}, \theta = 0°)$. In addition to position of the features, the orientation angle of the cross and rectangular is also taken into account in the concurrent optimization, and the parametric representations of these two features are formulated through the combination of R-functions with level-set function. In this case, the upper bound and lower bound of the density in the base plate are set to $\underline{\rho} = 0.2$ and $\overline{\rho} = 0.9$.

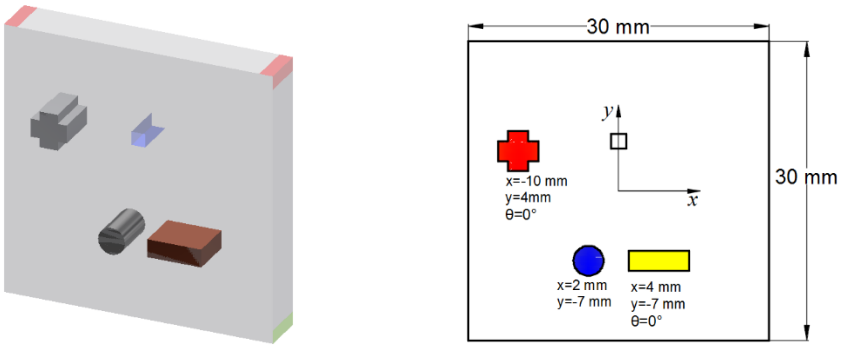

(a) (b)

Figure 4.27: Model of the Optimization for the Plate with Multi Features (a) CAD Model of the Plate and Features (b) Initial Position and Angle of the Features

Figure 4.28(a)-(f) provides the intermediate and final results of the optimization iterations, including the density distribution and the corresponding temperature field. After optimization, the three solid features tend to move towards the higher density path, however, the final position and angle are different due to their different thermal conductivities. The aluminum cross finally moves into the high-density band of the base plate since the material is the same as the base plate. The stainless-steel cylinder moves to the interface of the high and low-density regions, since the thermal conductivity of stainless steel is between the upper and lower bound of the density range. The copper rectangle orients its longitudinal axis and migrates toward the heat source along the high-density band, while the band narrows around the rectangle due to its very high conductivity. Figure 4.28(e) illustrates the iteration history of the objective function and maximum temperature obtained from the homogenized model. The objective function converges to 1.75×10^8 $(W \cdot K)$ after 43 iterations, while the maximum temperature reduces from 169.68℃ to100.72℃. The objective function decreases by 51.52%, while the maximum temperature drops by 40.61%.

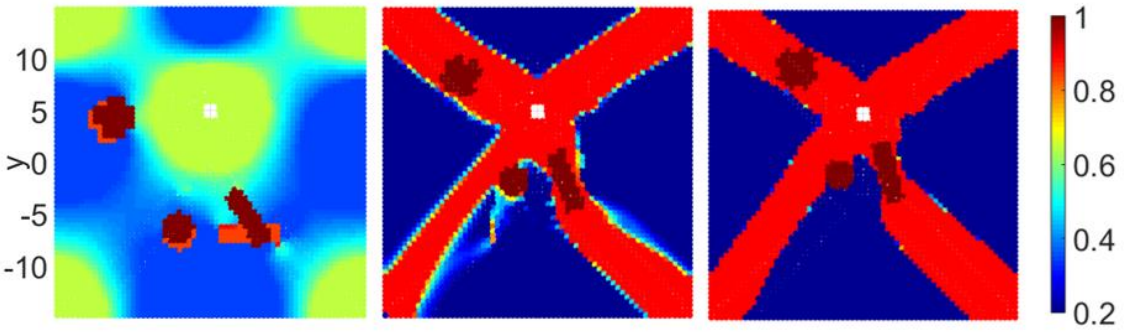

(a) Iteration 1 (b) Iteration 10 (c) Iteration 43

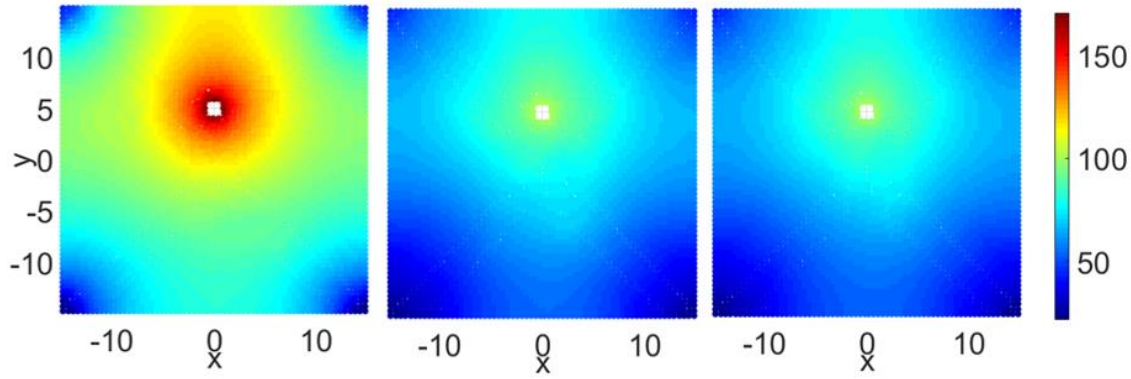

(d) Iteration 1 (e) Iteration 10 (f) Iteration 43

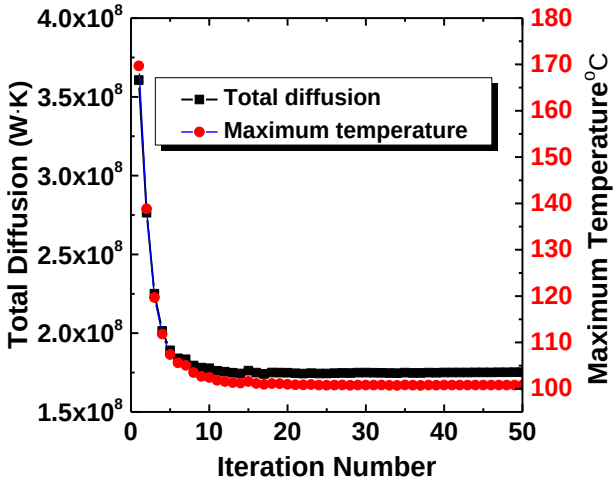

(g)

Figure 4.28: Optimization Results of Case 3. (a)-(c) Iteration History of Relative Density Distribution. (d)-(f) Iteration History of Temperature Distribution. (g) Convergence of Objective Function and Maximum Temperature

For comparison purpose, we conduct the optimization for the same model without evolving the three embedded features. The optimization results are provided in Figure 4.29 including density distribution of lattice structure, temperature distribution and the convergence history of objective function and maximum temperature of the design domain. As shown in the figure, the objective function converges to 1.79×10^8 $(\mathrm{W} \cdot \mathrm{K})$ after 40 iterations, while the maximum temperature is reduced to 102.51 ℃. Compared with the results of concurrent design, the objective function is 2.3% larger, while the maximum temperature is 1.8 ℃ higher. This demonstrates that the concurrent optimization scheme can further enhance the performance of the optimal design.

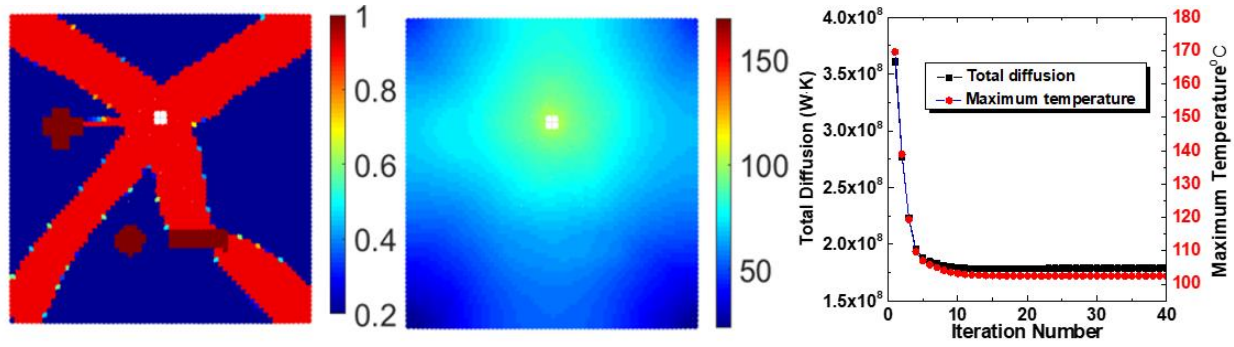

(a) (b) (c)

Figure 4.29: Optimization Results of Case 3 Without Evolving the Geometric Parameters of the Features. (a) Optimal Density Distribution (b) Temperature Distribution (c) Convergence of Objective Function and Maximum Temperature

Again, full-scale detailed FEA is conducted on the optimal design after the reconstruction with variable density lattice structure. The temperature field of the simulation is given in Figure 4.30. As shown, the temperature profile shows good agreement with the homogenized model for

both the movable design and non-movable design. For the concurrent design, the difference of the maximum temperature is about 0.37 ℃ or 0.367%. For the non-movable design, the difference of the maximum temperature is about 1.01 ℃ or 0.985%. This demonstrates that the proposed methodology is also efficient and accurate for optimization with multi features and multiphase materials.

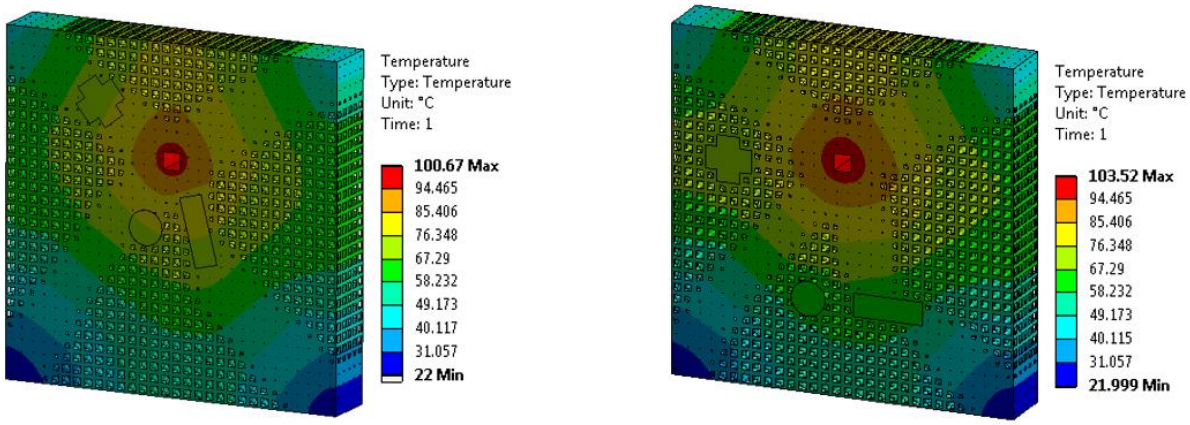

(a) (b)

Figure 4.30: Temperature Distribution of Full-Scale Simulation for Case 4. (a) Movable Design (b) Non-Movable Design

Case 5. LSTO with Movable Features in 3D Setting

In this case, we focus on optimization of lattice density and layout of movable functional feature in a three-dimensional (3D) setting. Figure 4.31 presents the base model, including the boundary conditions and mesh for FEA. Four temperatures are imposed on the four corners of the upper surface of the block, while a heat flux of $0.5\ \mathrm{W/mm^2}$ is applied to a small region on the

bottom surface. A mesh of 99,530 eight-node hexahedral elements is used to discretize the design domain. The dimension of the block is 60×60×60 mm^3 and the area of the heat flux is 20×20 mm^2. The lower and upper density bounds of lattice structure in the block are $\underline{\rho} = 0.2$ and $\overline{\rho} = 0.9$ The material employed for the base block is $AlSi_{10}Mg$.

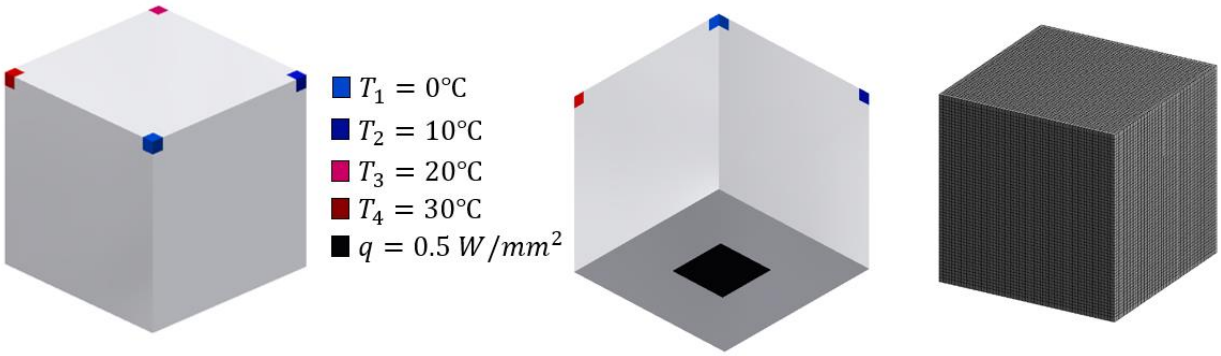

(a) (b) (c)

Figure 4.31: Finite Element Model of the Block. (a) and (b) Boundary Conditions of the Model. (c) Mesh Model for FEA

Two solid $AlSi_{10}Mg$ spheres of different radii are initially placed within the block. As illustrated in Figure 4.32, the original position of the two spheres are: Sphere #1 is at (*x*,*y*,*z*)=(0,-10,30) mm and Sphere #2 is placed at (0,10,30) mm.

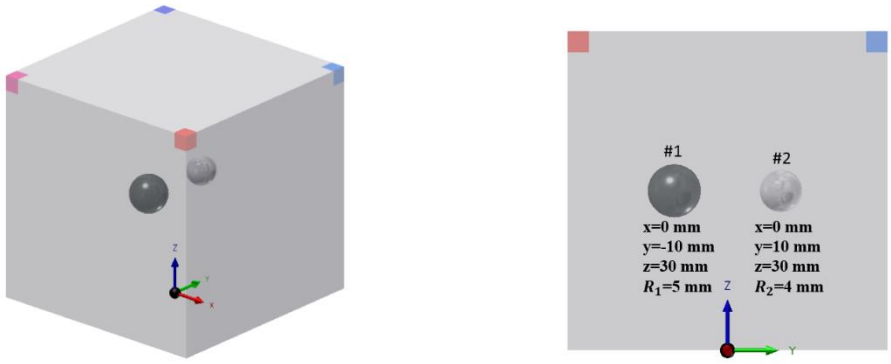

(a) (b)

Figure 4.32: Initial State of the Functional Features (a) Three-Dimensional View of the Two Spheres (b) Initial Position and Radius of the Two Features

The optimized results are presented in Figure 4.33, including the density distribution of different iterations, the corresponding temperature distribution, as well as the convergence history of objective function and maximum temperature. As illustrated in the figure, more materials are distributed along the bands directly connecting the heat source and temperature boundaries to promote the thermal diffusion and reduce the thermal potential energy of the structure. It can also be seen that the two spheres move from the initial position to closer to the heat source of the model. This leads to a reduction of total thermal energy of the structure from 2.357×10^8 W · K to 1.068×10^8 W · K, which is a 54.69% reduction, while the maximum temperature reduces from 364.9℃ to 167.5℃. The final positions of Sphere #1 and #2 are (-1.78, -9.81, 19.10) mm and (-5.07, 13.65, 14.85) mm, respectively. It is reasonable because the solid spheres move toward the heat source and into the area with high density.

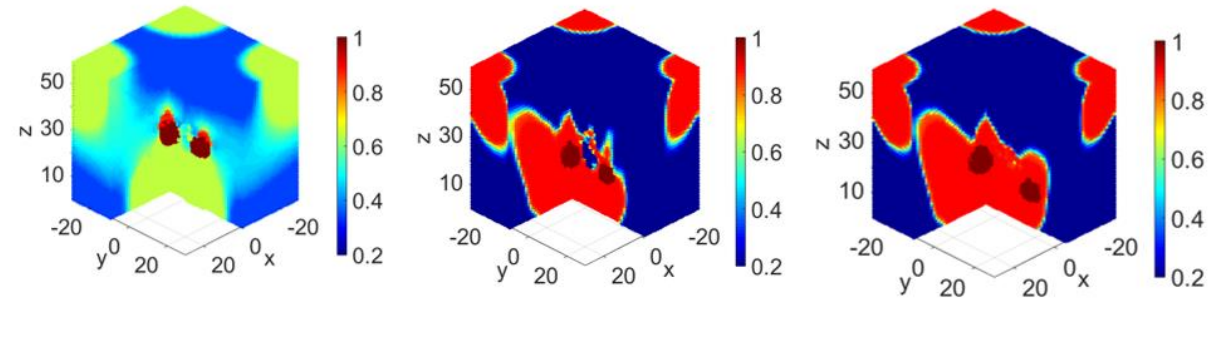

(a) Iteration 1 (b) Iteration 10 (c) Iteration 31

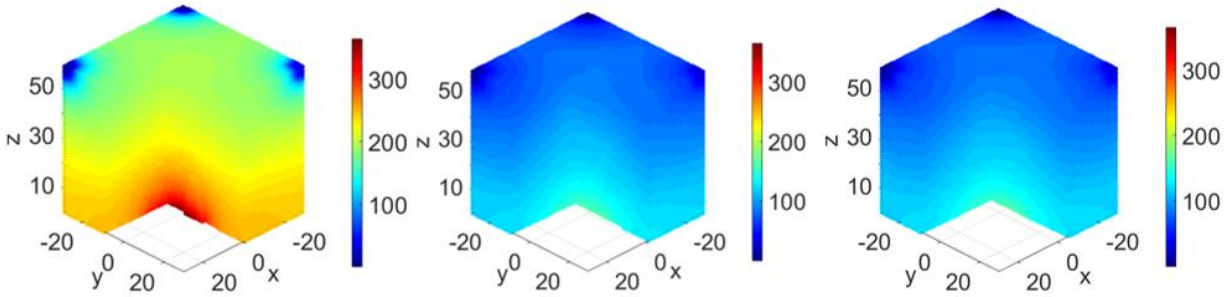

(d) Iteration 1 (e) Iteration 10 (f) Iteration 31

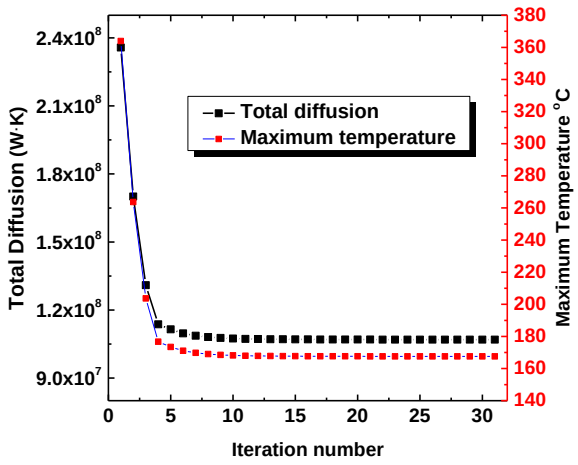

(g)

Figure 4.33: Optimized Solution of Case 4. (a)-(c) Iteration History of Relative Density Distribution. (d)-(f) Iteration History of Temperature Distribution. (g) Convergence of Objective Function and Maximum Temperature

To check the accuracy of the optimization result, a full-scale detailed FEA of the final design infilled with variable density lattice structure is conducted. As illustrated in Figure 4.34, the maximum temperature of direct numerical simulation is 166.82℃, and the difference with the homogenized model is 0.68℃ or 0.41%. This very good agreement of the maximum temperature further demonstrates accuracy of homogenized model and effectiveness of the proposed method.

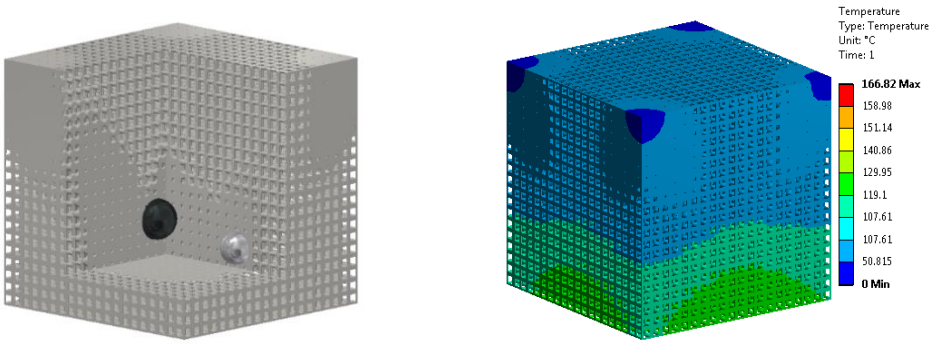

(a) (b)

Figure 4.34: Verification of the Optimization Result by Full Scale Simulation. (a) Section View of the CAD Model. (b) Temperature Field of Corresponding Design.

To verify manufacturability of the designs without inserting additional support structure, the optimal design shown in Figure 4.35is printed by two different AM technologies. Specifically, the plastic sample was printed by Objet260 Connex (Stratasys. Inc) in VeroWhite, while the metal one was printed by EOS M290 DMLS in TiAl6V4, see Figure 4.35. Since the lattice structure is self-support for the small cell, the variable density design can be printed out without any extra efforts. It demonstrates that the proposed concurrent optimization can be applied for practical application directly.

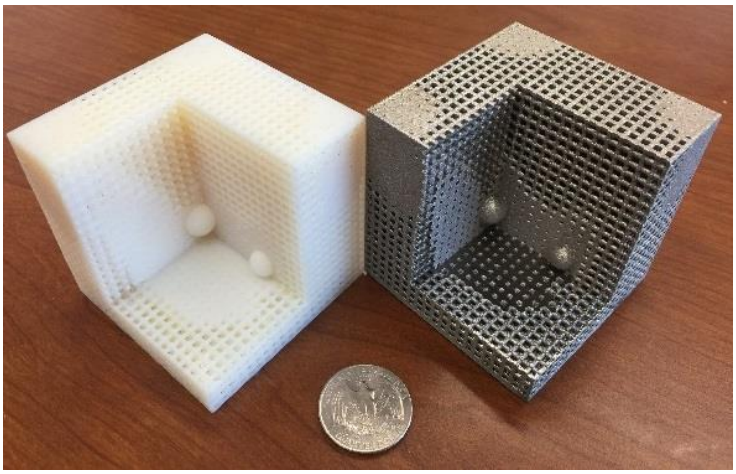

Figure 4.35: Illustration of the Manufacturability of the Optimal Design Printed by Both Plastic and Metal Additive Manufacturing

4.2.5 Summary

This work has presented a novel method to concurrently optimize the density distribution of the lattice infill and the layout of functional features. To ensure continuous material interpolation, asymptotic homogenization is employed to obtain the effective thermal conductivity of lattice structure in terms of the relative density. The homogenized model is embedded into the framework of density-based TO to replace the conventional fictitious material interpolation in SIMP method, in order to obtain the design with predictable properties. Regarding the functional features, the parametric level-set functions together with R-functions are employed to implicitly represent the geometric shape. The technique not only provides implicitly mathematical representation of the features, but also flexibly integrates with LSTO approach for multi-feature optimization. All the 3D numerical experiments including single features, multi features, and multi features composed of multiphase materials show good agreement with the results obtained by full

scale detailed finite element simulation for lattice infill design. In particular, the optimized design in the last case is printed out by both plastic 3D printer and metal 3D printer without adding support structure. This further demonstrates the great potential of the proposed methodology for practical application using current AM technique. Currently, this work focuses on the evolution of features on which there are no boundary conditions impose. In the future, we plan to extend the proposed methodology to features attached with boundary conditions, and the problem will become the combination of free form optimization with design-dependent feature evolution.

4.3 Concurrent Optimization for Design-dependent Feature for Heat Conduction

4.3.1 Problem Formulation

4.3.1.1 Problem Statement

The purpose of the optimization is to simultaneously find the optimal structure of the lattice layout and optimize geometric parameters of the features attributed with boundary conditions. The objective function is minimizing the total thermal potential energy [30] of the structure under the prescribed volume constraints. The general formulation of the problem are written as follows:

$$\text{Minimum: } J = L(\tilde{T}) - \frac{1}{2}a(T, \tilde{T}) \tag{4.47}$$

$$\text{Subject to: } a(T, \tilde{T}) = L(\tilde{T}) \tag{4.48}$$

$$\int_{\Omega} v_e d\Omega \leq V^* \tag{4.49}$$

where $\int_{\Omega} v_e d\Omega$ is the volume of the structure with v_e is given in Eq. (4.12), while $a(T, \tilde{T})$ and $L(\tilde{T})$ are given in Eq. (4.20) and Eq. (4.21), respectively.

Finite element method (FEM) is employed to discretize and solve the thermal problem. The discretized form of the problem can be mathematically expressed as:

$$\text{Minimum: } J(\rho, \boldsymbol{c}(t)) = \boldsymbol{T}^T(\boldsymbol{q} + \boldsymbol{G} + \boldsymbol{H}) - \frac{1}{2}\boldsymbol{T}^T(\boldsymbol{K_c} + \boldsymbol{K_h})\boldsymbol{T} \tag{4.50}$$

$$\text{Subject to: } (\boldsymbol{K_c} + \boldsymbol{K_h})\boldsymbol{T} = \boldsymbol{q} + \boldsymbol{G} + \boldsymbol{H} \tag{4.51}$$

$$V(\rho) = \sum_{i=1}^{N}((1-\zeta)\rho_i v_i + \zeta v_i) \leq V^* \tag{4.52}$$

$$\underline{\rho} \leq \rho_i \leq \overline{\rho} \tag{4.53}$$

where $\boldsymbol{K_c}$ and $\boldsymbol{K_h}$ are the thermal conductivity matrix and heat convection matrix, respectively. $\boldsymbol{q}$, $\boldsymbol{G}$ and $\boldsymbol{H}$ indicate the heat flux vector, internal heat generation vector, and heat transfer vector after discretization. ρ_i is the relative density of the i^{th} element. $\underline{\rho}$ and $\overline{\rho}$ are the lower and upper bound of the relative density for the element in lattice domain. The first equality denotes the equilibrium equation used to calculate the temperature field. The first inequality implies that the allowable total material volume fraction is limited to V^*. The global conductivity matrix and the heat transfer matrix can be calculated by assembling the element matrix, as given below:

$$\boldsymbol{K_c} = \sum_e \boldsymbol{k}_e^c = \sum_e \int_{\Omega_e} \boldsymbol{B}_e^T \boldsymbol{D}_e^c \boldsymbol{B}_e d\Omega \tag{4.54}$$

$$\boldsymbol{K}_h = \sum_e \boldsymbol{k}_e^h = \sum_e \int_{\Gamma_e} h_e \boldsymbol{N}^T \boldsymbol{N} d\Gamma \tag{4.55}$$

where $\boldsymbol{k}_e^c$ and $\boldsymbol{k}_e^h$ are the conductivity matrix and convection matrix of element e, $\boldsymbol{D}_e^c$ represents the material model and h_e is the heat-transfer or convection coefficient. $\boldsymbol{N}$ represents the shape function and $\boldsymbol{B}_e$ indicates the gradient of the shape functions in FEM and Ω_e is the element domain.

4.3.1.2 Sensitivity Analysis

In the concurrent optimization, there exist the lattice structure domain and movable feature domain. Since the surface/volume boundary conditions are attached on these features, sensitivity analysis of the moving boundaries described in Eq. (4.10) and Eq. (4.11) plays an important role in the evolution of the features. To promote the implementation of sensitivity, the shape derivatives of two types of boundaries are given within the level set framework, while the lattice design variables are calculated in the density-based methodology.

(a) Sensitivity of Surface Integral

Considering the integral of surface boundary conditions given in Eq. (4.10):

$$l(t) = \int_{\Omega} f\delta(\phi(\boldsymbol{x}, \boldsymbol{c}(t)))|\nabla\phi|dV$$

The derivative of the surface integral with respect to geometric variables yields:

$$\frac{\partial l}{\partial t} = \int_{\Omega} \left(\frac{\partial f}{\partial t}\right)\delta(\phi)|\nabla\phi|dV + \int_{\Omega} \left[f\delta(\phi)'\left(\frac{\partial\phi}{\partial \boldsymbol{c}}\frac{\partial \boldsymbol{c}}{\partial t}\right)|\nabla\phi| + f\delta(\phi)\frac{\nabla\phi\cdot\nabla\left(\frac{\partial\phi}{\partial \boldsymbol{c}}\frac{\partial \boldsymbol{c}}{\partial t}\right)}{|\nabla\phi|}\right]dV \qquad (4.56)$$

which can be further simplified by considering the fact that $\boldsymbol{n} = -\nabla\phi/|\nabla\phi|$ and $\nabla\cdot\boldsymbol{n} = \gamma$ (where γ is the curvature of the structural boundary curve). The derivatives of the surface integral have been given in [138] and listed here:

$$\frac{\partial l}{\partial t} = \int_{\Omega} \left(\frac{\partial f}{\partial t}\right)\delta(\phi)|\nabla\phi|dV - \int_{\Omega} \delta(\phi)\gamma f\left(\frac{\partial\phi}{\partial \boldsymbol{c}}\frac{\partial \boldsymbol{c}}{\partial t}\right)dV - \int_{\Omega} \delta(\phi)\left(\frac{\partial\phi}{\partial \boldsymbol{c}}\frac{\partial \boldsymbol{c}}{\partial t}\right)\boldsymbol{n}\cdot\nabla f dV \qquad (4.57)$$

Since in the present work the surface boundary condition f maintains a constant during the optimization and $\frac{\partial f}{\partial t} = 0$ and $\nabla f = 0$, the derivatives in Eq. (4.57) can be simplified as:

$$\frac{\partial l}{\partial t} = -\int_{\Omega} f\delta(\phi)\gamma\left(\frac{\partial\phi}{\partial \boldsymbol{c}}\frac{\partial \boldsymbol{c}}{\partial t}\right)dV \qquad (4.58)$$

(b) Sensitivity of Volume Integral

For the derivative of the volume integral given in Eq. (4.11),

$$v(t) = \int_{\Omega} FH(\phi(\boldsymbol{x}, \boldsymbol{c}(t))dV$$

It follows the similar process that

$$\frac{\partial v}{\partial t} = \int_{\Omega} \left(\frac{\partial F}{\partial t}\right) H(\phi)dV + \int_{\Omega} F\delta(\phi)|\nabla\phi| \left(\frac{\partial \phi}{\partial \boldsymbol{c}} \frac{\partial \boldsymbol{c}}{\partial t}\right) dV \tag{4.59}$$

By similar work in Eq. (4.57), we have

$$\frac{\partial v}{\partial t} = \int_{\Omega} F\delta(\phi)|\nabla\phi| \left(\frac{\partial \phi}{\partial \boldsymbol{c}} \frac{\partial \boldsymbol{c}}{\partial t}\right) dV \tag{4.60}$$

(c) Sensitivity of Objective Function

The sensitivity of lattice domain is described in this section. Using the Lagrange multiplier method, the Lagrangian of the problem in this article can be written as:

$$L = J(\rho, \boldsymbol{c}(t)) + \lambda(\sum_{i=1}^{N}((1-\zeta)\rho_i v_i + \zeta v_i) - V^*) \tag{4.61}$$

where λ represents the Lagrange multiplier for the volume constraint.

In the lattice domain, the sensitivity of the objective function with respect to the relative density can be computed as:

$$\frac{\partial J}{\partial \rho_i} = -\frac{1}{2}\boldsymbol{T}^T \frac{\partial \boldsymbol{K_c}}{\partial \rho_i}\boldsymbol{T} \tag{4.62}$$

Substituting Eq. (4.15) into $\frac{\partial \boldsymbol{K_c}}{\partial \rho_i}$, one can obtain:

$$\begin{aligned} \frac{\partial \boldsymbol{K_c}}{\partial \rho_i} &= \boldsymbol{B}_e^T \frac{\partial \boldsymbol{D}_e^c}{\partial \rho_i} \boldsymbol{B}_e v_e \\ &= \boldsymbol{B}_e^T \frac{\partial \boldsymbol{D}(\rho)}{\partial \rho_i} \boldsymbol{B}_e v_e \end{aligned} \tag{4.63}$$

where v_e is the volume of element e.

The sensitivity of the volume fraction V with respect to the element density can be calculated as:

$$\frac{\partial V}{\partial \rho_i} = v_i \tag{4.64}$$

In the movable feature domain, the sensitivity of the objective function with respect to the geometric features can be expressed as:

$$\frac{\partial J}{\partial t} = \boldsymbol{T}^T(\boldsymbol{K_c} + \boldsymbol{K_h})\frac{\partial \boldsymbol{T}}{\partial t} + \frac{1}{2}\boldsymbol{T}^T\frac{\partial(\boldsymbol{K_c}+\boldsymbol{K_h})}{\partial t}\boldsymbol{T} \tag{4.65}$$

Calculating the derivatives of the geometric variables in both sides of the equilibrium equation, we have

$$\frac{\partial(\boldsymbol{K_c}+\boldsymbol{K_h})}{\partial t}\boldsymbol{T} + (\boldsymbol{K_c} + \boldsymbol{K_h})\frac{\partial \boldsymbol{T}}{\partial t} = \frac{\partial(\boldsymbol{q}+\boldsymbol{G}+\boldsymbol{H})}{\partial t} \tag{4.66}$$

Thus, one can further write $\frac{\partial \boldsymbol{T}}{\partial t}$ as:

$$\frac{\partial \boldsymbol{T}}{\partial t} = (\boldsymbol{K_c} + \boldsymbol{K_h})^{-1}\frac{\partial(\boldsymbol{q}+\boldsymbol{G}+\boldsymbol{H})}{\partial t} - (\boldsymbol{K_c} + \boldsymbol{K_h})^{-1}\frac{\partial(\boldsymbol{K_c}+\boldsymbol{K_h})}{\partial t}\boldsymbol{T} \tag{4.67}$$

Via substitution of Eq. (4.67) into Eq. (4.65), we can obtain the sensitivity for the geometric variables as:

$$\frac{\partial J}{\partial t} = \boldsymbol{T}^T\frac{\partial(\boldsymbol{q}+\boldsymbol{G}+\boldsymbol{H})}{\partial t} - \frac{1}{2}\boldsymbol{T}^T\frac{\partial(\boldsymbol{K_c}+\boldsymbol{K_h})}{\partial t}\boldsymbol{T} \tag{4.68}$$

where the derivatives of the design-dependent boundary with respect to geometric variables are specified as follows:

$$\frac{\partial \boldsymbol{q}}{\partial t} = -\boldsymbol{N}^T q_0 \delta_k^q(\phi_k^q)\gamma\left(\frac{\partial \phi_k^q}{\partial \boldsymbol{c}_k^q}\frac{\partial \boldsymbol{c}_k^q}{\partial t}\right)v_e \tag{4.69}$$

$$\frac{\partial \boldsymbol{G}}{\partial t} = \boldsymbol{N}^T g_0 \delta_k^g\left(\phi_k^g\right)\left|\nabla\phi_k^g\right|\left(\frac{\partial \phi_k^g}{\partial \boldsymbol{c}_k^g}\frac{\partial \boldsymbol{c}_k^g}{\partial t}\right)v_e \tag{4.70}$$

$$\frac{\partial \boldsymbol{H}}{\partial t} = -\boldsymbol{N}^T h_0 T_{am}\delta_k^h(\phi_k^h)\gamma\left(\frac{\partial \phi_k^h}{\partial \boldsymbol{c}_k^h}\frac{\partial \boldsymbol{c}_k^h}{\partial t}\right)v_e \tag{4.71}$$

where δ_k^q, δ_k^g and δ_k^h indicate the Diract delta functions used for the representation of the heat flux boundary, internal heat generation, and heat convection boundary, respectively. q_0 and g_0 are the heat flux rate and internal heat generation rate applied on the movable features, while h and T_{am} represent the heat convection coefficient and ambient temperature subjected to the moving heat convection boundary. ϕ_k with different upper subscript (q, g, h) represents the k^{th} level set function attached with heat flux, heat generation and heat convection boundary conditions, and $\boldsymbol{c}_k$ is the corresponding parametric variable. Using the Eq. (4.54) and Eq. (4.55), the derivation of $\frac{\partial(\boldsymbol{K_c}+\boldsymbol{K_h})}{\partial t}$ can be calculated as:

$$\frac{\partial(\boldsymbol{K_c}+\boldsymbol{K_h})}{\partial t} = \boldsymbol{B}_e^T \left(\frac{\partial H_k(\phi_k)}{\partial \phi_k} \cdot \frac{\partial \phi_k}{\partial \boldsymbol{c}_k} \cdot \frac{\partial \boldsymbol{c}_k}{\partial t} \cdot D_k\right) \boldsymbol{B}_e v_e - \delta_k^h(\phi)\gamma \left(\frac{\partial \phi_k^h}{\partial \boldsymbol{c}_k^h}\frac{\partial \boldsymbol{c}_k^h}{\partial t}\right) \cdot h v_e \boldsymbol{N}^T \boldsymbol{N} \tag{4.72}$$

Following Eq. (4.58) to Eq. (4.60), the sensitivities of the objective function in terms of the parametric variables can be expressed as:

$$\frac{\partial J}{\partial t} = \sum_{\Omega_e \in \Omega} \frac{\partial J_e}{\partial t} \tag{4.73}$$

where

$$\begin{aligned}\frac{\partial J_e}{\partial t} = &-\boldsymbol{T}_e^T \boldsymbol{N}^T q_0 \delta_k^q(\phi_k^q)\gamma \left(\frac{\partial \phi_k^q}{\partial \boldsymbol{c}_k^q}\frac{\partial \boldsymbol{c}_k^q}{\partial t}\right) v_e + \boldsymbol{T}_e^T \boldsymbol{N}^T g_0 \delta_k^g(\phi_k^g)\left|\nabla \phi_k^g\right| \left(\frac{\partial \phi_k^g}{\partial \boldsymbol{c}_k^g}\frac{\partial \boldsymbol{c}_k^g}{\partial t}\right) v_e \\ &- \boldsymbol{T}_e^T \boldsymbol{N}^T h_0 T_{am} \delta_k^h(\phi_k^h)\gamma \left(\frac{\partial \phi_k^h}{\partial \boldsymbol{c}_k^h}\frac{\partial \boldsymbol{c}_k^h}{\partial t}\right) v_e - \frac{1}{2}\boldsymbol{T}_e^T \boldsymbol{B}_e^T \left(\delta_k^h(\phi_k^h)\frac{\partial \phi_k}{\partial \boldsymbol{c}_k}\frac{\partial \boldsymbol{c}_k}{\partial t} D_k\right) \boldsymbol{B}_e \boldsymbol{T}_e \\ &+ \frac{1}{2}\boldsymbol{T}_e^T \boldsymbol{N}^T \delta_k^h(\phi_k^h)\gamma \frac{\partial \phi_k^h}{\partial \boldsymbol{c}_k^h}\frac{\partial \boldsymbol{c}_k^h}{\partial t} h_0 \boldsymbol{N} \boldsymbol{T}_e\end{aligned}$$

To ensure the objective function to evolve along a decent direction iteratively, the motion of the conforming boundaries can be given in different conditions as:

$$\frac{\partial \boldsymbol{c}_k^q}{\partial t} = \sum_{\Omega_e \in \Omega} \left[\boldsymbol{T}_e^T \boldsymbol{N}^T q_0 \delta_k^q(\phi_k^q)\gamma \frac{\partial \phi_k^q}{\partial \boldsymbol{c}_k^q} + \frac{1}{2}\boldsymbol{T}_e^T \boldsymbol{B}_e^T \left(\delta_k^h(\phi_k^h)\frac{\partial \phi_k}{\partial \boldsymbol{c}_k} D_k\right) \boldsymbol{B}_e \boldsymbol{T}_e\right] v_e$$

$$\frac{\partial \boldsymbol{c}_k^g}{\partial t} = \sum_{\Omega_e \in \Omega} \left[-\boldsymbol{T}_e^T \boldsymbol{N}^T g_0 \delta_k^g(\phi_k^g) |\nabla \phi_k^g| \frac{\partial \phi_k^g}{\partial \boldsymbol{c}_k^g} + \frac{1}{2} \boldsymbol{T}_e^T \boldsymbol{B}_e^T \left(\delta_k^h(\phi_k^h) \frac{\partial \phi_k}{\partial \boldsymbol{c}_k} D_k \right) \boldsymbol{B}_e \boldsymbol{T}_e \right] v_e$$

$$\frac{\partial \boldsymbol{c}_k^h}{\partial t} = \sum_{\Omega_e \in \Omega} \left[\boldsymbol{T}_e^T \boldsymbol{N}^T h_0 \delta_k^h(\phi_k^h) \gamma \frac{\partial \phi_k^h}{\partial \boldsymbol{c}_k^h} T_{am} + \frac{1}{2} \boldsymbol{T}_e^T \boldsymbol{B}_e^T \left(\delta_k^h(\phi_k^h) \frac{\partial \phi_k}{\partial \boldsymbol{c}_k} D_k \right) \boldsymbol{B}_e \boldsymbol{T}_e \right.$$

$$\left. - \frac{1}{2} \boldsymbol{T}_e^T \boldsymbol{N}^T \delta_k^h(\phi_k^h) \gamma \frac{\partial \phi_k^h}{\partial \boldsymbol{c}_k^h} h_0 \boldsymbol{N} \boldsymbol{T}_e \right] v_e$$

The flowchart of the optimization is given in Figure 4.36. In the beginning, the homogenized model of thermal conductivity obtained in Section 2.5 is implemented into the FEM program. In the second step, the equilibrium equation is solved to obtain the temperature field and temperature gradient. In the third step, the objective function of the optimization and the volume constraint are computed. If the convergence criteria is satisfied, the optimization terminates and the optimal result is obtained. Otherwise, the sensitivity of the problem will continue. In the concurrent optimization, the optimality criteria (OC) method is employed to evolve the lattice density, while the upwind scheme is used to update the geometric parameters of the movable features through the level set scheme.

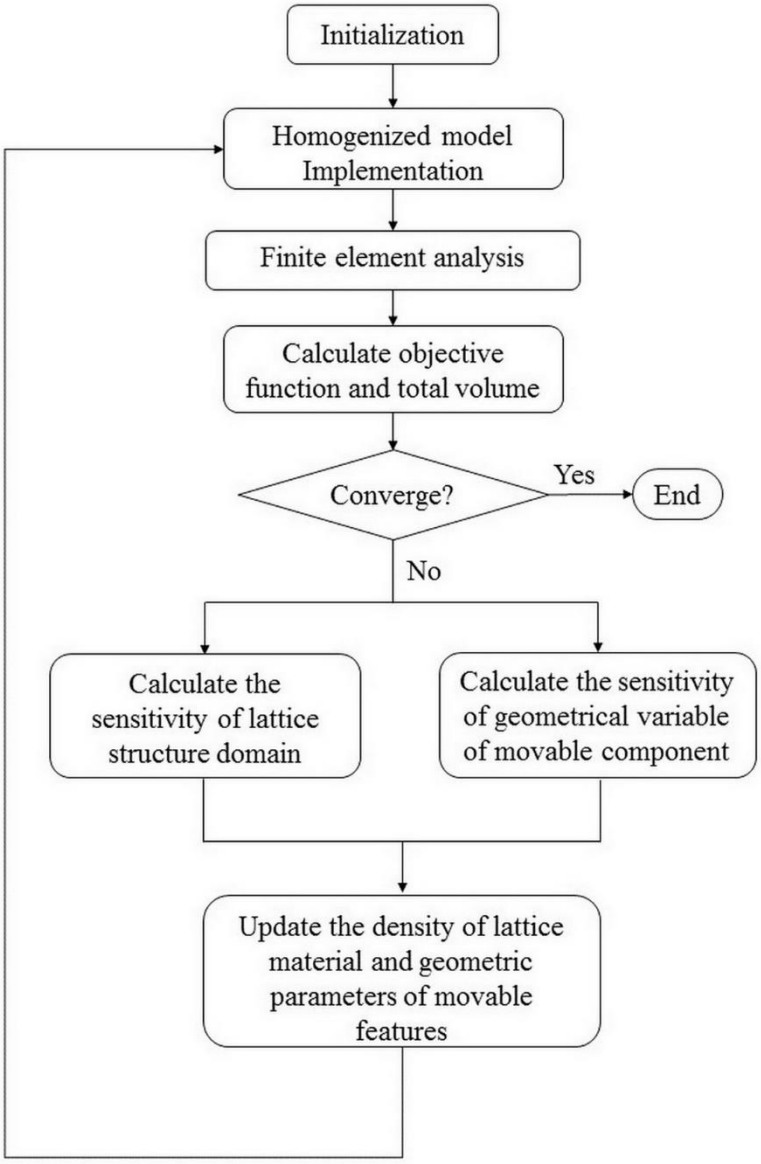

Figure 4.36: Flowchart of the Concurrent Optimization Process

4.3.2 Numerical Examples and Validation

To demonstrate the effectiveness of the proposed optimization method, several numerical examples are presented and discussed in this section. Unless otherwise specified, the volume

fraction restriction is set to be $V^* = 0.5$. The optimization terminates if the relative difference of the objective function between two successive iterations is smaller than 1×10^{-4}, while the volume fraction constraint is satisfied at the same time. It is assumed that the properties of an aluminum alloy AlSi10Mg printed by the EOS DMLS system are used in all the following simulations; specifically, thermal conductivity is set to $110\,\mathrm{W/m \cdot ℃}$. The FEA in all the following examples have been performed in ANSYS V17.2.

4.3.2.1 Variable-density LSTO with a Single-type Design-dependent Boundary

In the first example, one type of the following three design-dependent surface/volumetric conditions is considered in each optimization: 1) heat flux and 2) heat generation. The IB method described in Section 4.1.2 is used to implicitly impose these conditions. As shown in Figure 4.37, the design domain has a dimension of 60×60×12 mm^3, while four void features including two blocks and two cylinders are initially placed inside the design domain to make the thermal load path assymetric. All the undefined surfaces are considered adiabatic. The design domain is discretized with a mesh of 84,180 eight-node elements. The density range of the lattice cells is set to be $\underline{\rho} = 0.2$ and $\overline{\rho} = 0.9$.

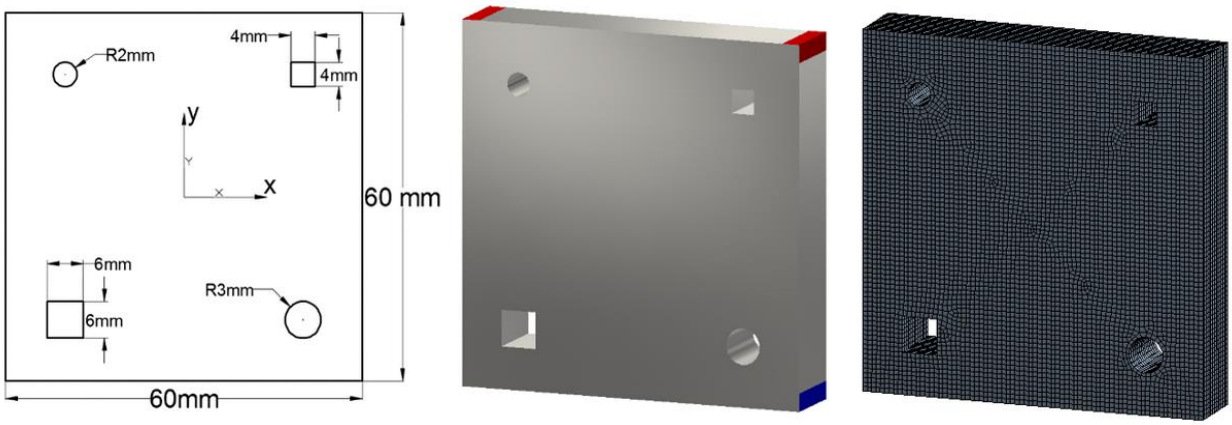

Figure 4.37: CAD Model for the First Three Examples. (a) Dimension of the Plate at the Top View; (b) CAD Model of the Plate with Thickness of 12 mm; (c) Mesh Model of the Plate.

4.3.2.2 Heat Flux Boundary Condition

As illustrated in Figure 4.38, a solid cylinder is positioned inside the base plate and a uniform heat flux of $q = 0.5\text{W/mm}^2$ is imposed on the surface of the solid cylinder. In addition, the four corners of the plate have fixed temperatures in different magnitudes. The intial position of the cylinder is (x=0, y=2) mm and its radius is $R = 3$ mm. The optimization problem is to minimize the thermal potential energy of the structure by finding the optimal position of the cylinder and the optimal lattice density distribution simultaneously.

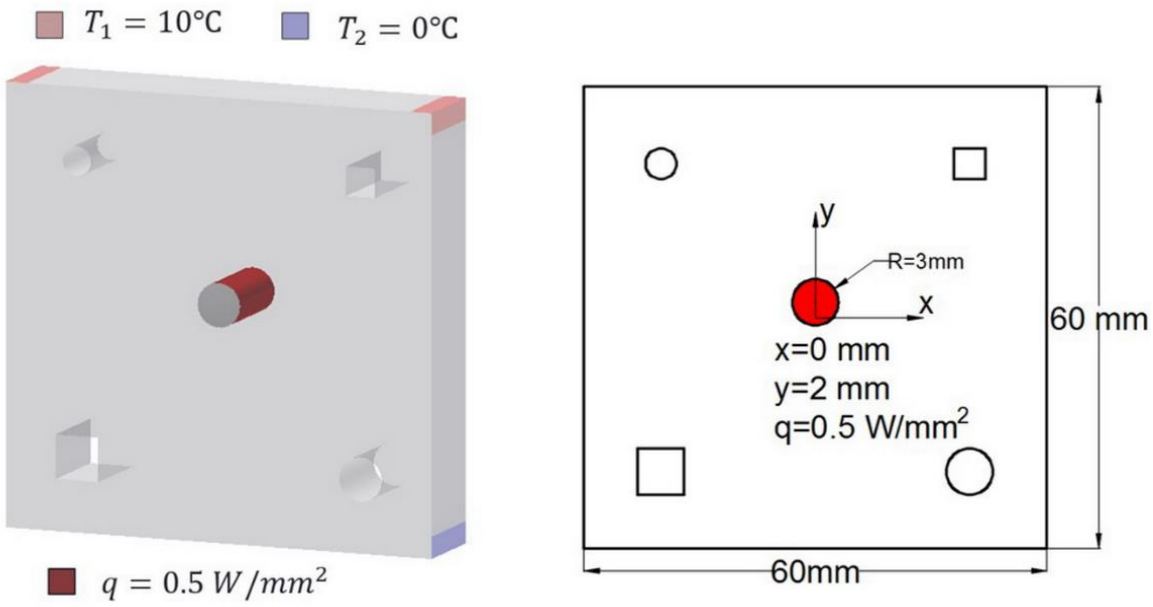

Figure 4.38: Optimization Problem Involving a Movable Cylinder with Heat Flux Boundary Condition.

Figure 4.39 presents the optimization results, including the lattice density distribution and the corresponding temperature field. It can be seen that the solid cylinder moves towards the lower left corner of the plate, since the temperatures at the lower corners are smaller than those of the upper corners, and the top left cylinder void can provide better thermal condution path than the top right block void. The results also show that the lattice density distribution depends strongly on the position of the cylinder to form the effective thermal conduction path. Figure 4.40 gives the convergence history of the objective function and the maximum temperature, as well as the position of the cylinder. The objective function of the concurrent design decreases from 1.8×10^8 W · K to 8.3×10^7 W · K (53.7% decrease), while the maximum temperate is reduced from 204.2℃ to 97.3℃ (52.4% decrease). The cylinder moves to the final position of ($x = -9.7, y = -13.5$) mm.

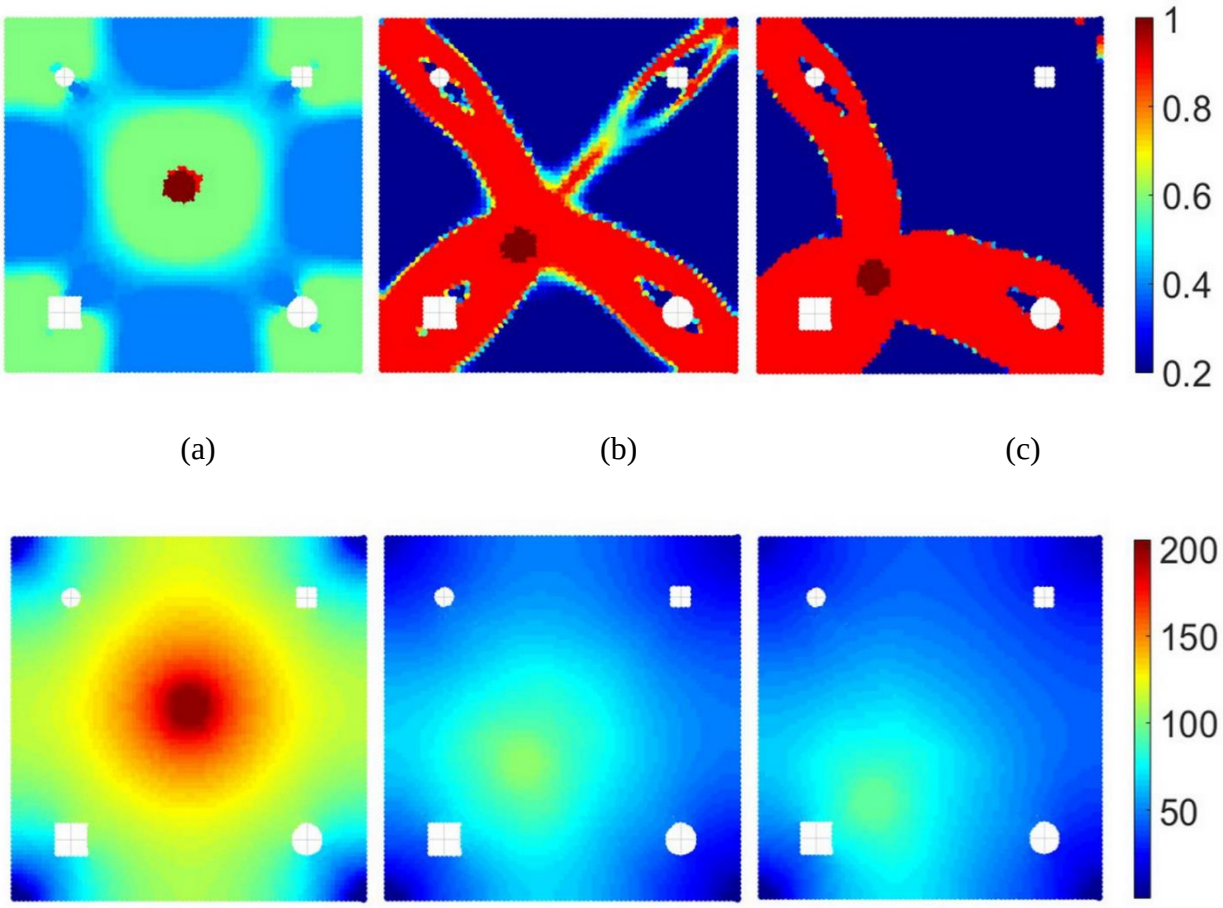

Figure 4.39: Optimization Result with Moveing Heat Flux Boundary. (a)-(c) Relative Density Distribution at Iteration 1, 10 and 58, and (d)-(f) Corresponding Temperature Distribution.

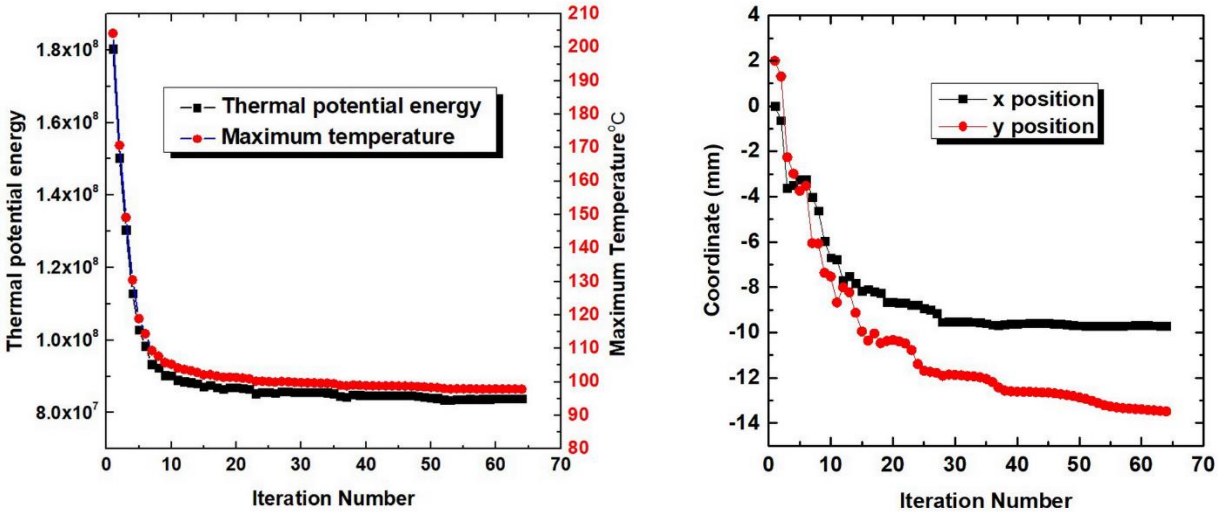

(a) (b)

Figure 4.40: Convergence History of the Optimization: (a) Optimal History of the Objective Function and Maximum Temperature of the Design Domain and (b) Position of the Movable Boundary.

For comparison, an alternative problem is studied in which the cylinder position is fixed instead. Figure 4.41 gives the optimization result, where the lattice materials nearly evenly distribute along the four paths between the corners and the cylinder. Figure 4.41(c) presents the convergence history of the objective function and the maximum temperature. The objective function decreases from 1.8×10^8 W · K to 9.5×10^7 W · K (47.6% decrease) and the maximum temperature reduces from 204.2 ℃ to 108.9 ℃ (46.7% decrease). Compared to the results obtained from the concurrent optimization, the objective function value is 6.11% higher, while the maximum temperature is 11.5 ℃ larger. It implies that the concurrent method can effectively improve the result optimality compared to the LSTO alone.

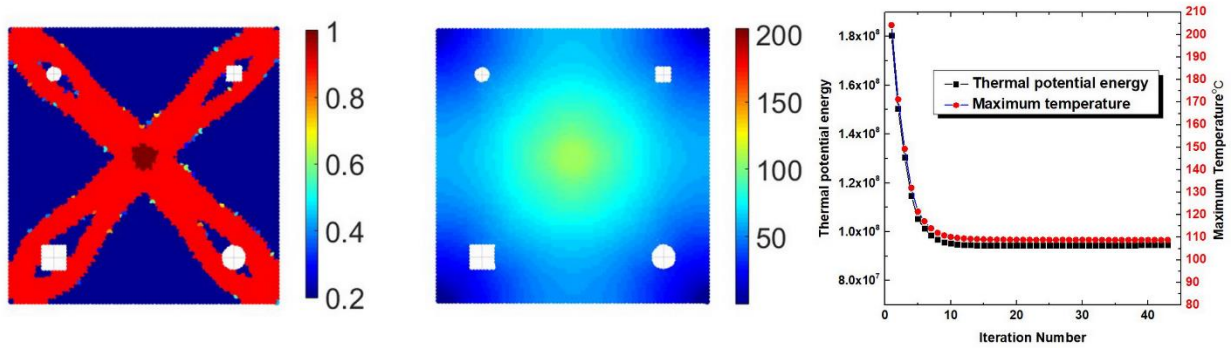

(a) (b) (c)

Figure 4.41: Optimization Result with Moveing Heat Flux Boundary.(a) Optimal Density Distribution; (b) Temperature Distribution (c) Convergence History.

To verify the accuracy of the homogenized FEA model and IB method, we conduct full scale simulation of the optimized models obtained from both the concurrent optimization and the LSTO. Figure 4.42 illustrates the temperature field of the full-scale simulation. The maximum temperature of the concurrently optimized model obtained through full scale simulation is 97.0℃, which is 0.31% smaller than that obtained from homogenization model combined with the IB method. The difference in maximum temperature of the LSTO model between full scale simulation and homogenized model is about 0.5%. The small error proves the accuracy of the IB method and the homogenized FEA model.

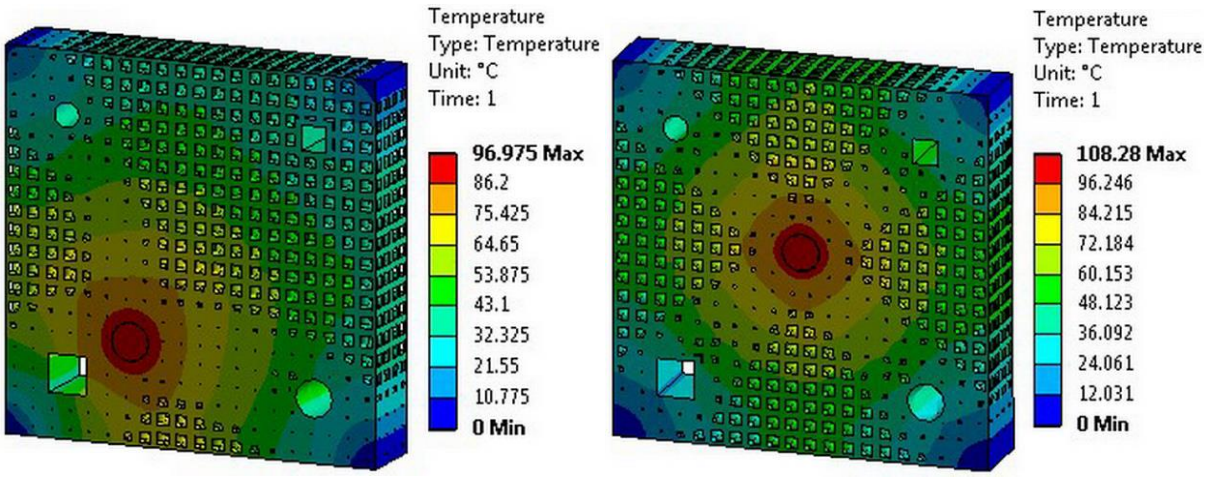

(a) (b)

Figure 4.42: Full Scale Simulation for the Concurrent Design and Fixed Design: (a) Concurrent Design; (b) Fixed Design.

One important aspect of concurrent optimization is the dependency of initial conditions. To examine this dependency, a numerical experiment is performed to investigate the influence of the initial position of the movable feature on the final design. Figure 4.43 illustrates the CAD model of the experiment. The boundary conditions and material property of the base plate are the same. The cylinder applied heat flux surface condition is initially placed at four different positions: #1 (x=2, y=-10) mm, #2 (x=-5, y=12) mm, #3 (x=-11, y=-2) mm, and #4 (x=11, y=3) mm. Other basic settings, such as relative density bond and volume fraction of the structure, remain the same.

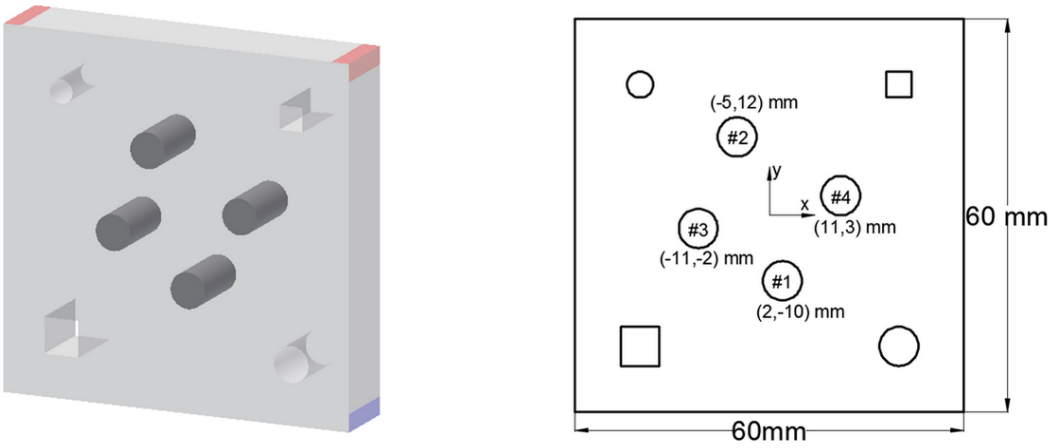

Figure 4.43: Optimization Problem Involving Solid Cylinder with Different Initial Positions.

The optimization results of this example are presented in Figure 4.44, including the initial density profile, optimal density profile and the temperature distribution of the final design. As illustrated in the figure, when the cylinder is randomly distributed in the base plate, it tends to move towards the nearest corner of the plate. The density distribution of the background lattice structure depends strongly on the final position of the cylinder, in which the high-density paths are formed to efficiently conduct the heat from the heat source to the lower temperature corner. More details about the optimization results are tabulated in Table 4.3. It can be seen that the #1 cylinder shows best performance compared with the other three cases. The reason is that the cylinder is positioned at the lower right corner, where temperature is smaller than the two upper corners, while the cylindrically void feature allow better heat conduction. The #4 cylinder exhibits the worst performance, because the temperature of the nearest corner is higher than the bottom two corners. The other two cases show similar evolution, in which the cylinder moves to the nearest corner and high-density path is generated for efficient heat conduction. Based on the investigation above, it is found that the optimization results have strong dependency on initial conditions. This implies

that the movable features tend to be positioned at a local optimal position and the density distribution of the base plate is determined by the cylinder location.

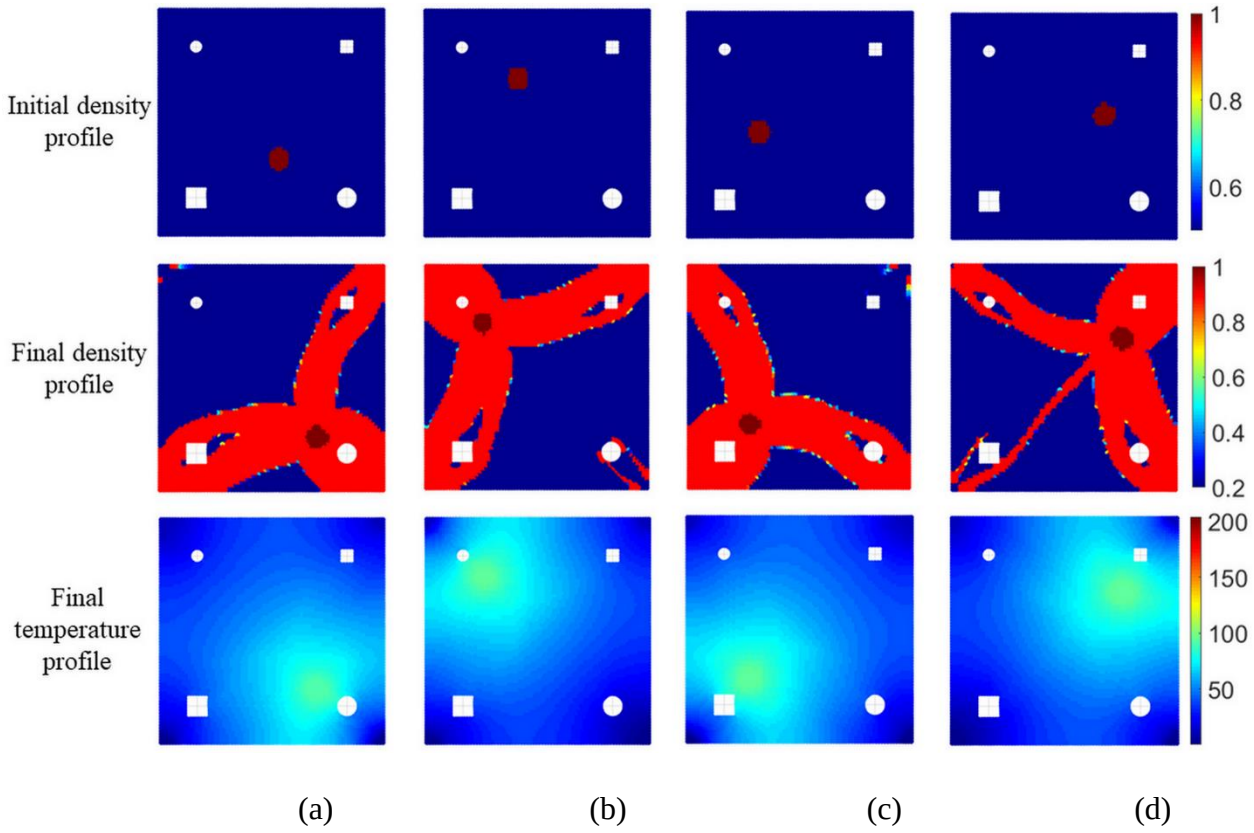

Figure 4.44: Optimization Result of Moving Heat Flux with Different Initial Positions. (a) #1 Cylinder (b) #2 Cylinder (c) #3 Cylinder and (d) #4 Cylinder.

Table 4.3: Comparison of the Optimization Results for Cylinder Subjected to Heat Flux with Different Initial Positions.

	#1	#2	#3	#4
Initial position (mm)	(2,-10)	(-5,12)	(-11,-2)	(11,3)
Final position (mm)	(12.1,-15.8)	(-14.6,14.6)	(-13.4,-12.9)	(15.7,10.4)
Objective function change ($W \cdot K$)	$1.68 \times 10^8 \sim 7.74 \times 10^7$ (↓53.9%)	$1.68 \times 10^8 \sim 7.76 \times 10^7$ (↓53.8%)	$1.70 \times 10^8 \sim 7.96 \times 10^7$ (↓53.2%)	$1.67 \times 10^8 \sim 7.88 \times 10^7$ (↓52.8%)
Maximum Temperature change from homogenization (℃)	197.8℃~**92.8** ℃ (↓53.1%)	199.0℃~**95.5**℃ (↓52.0%)	199.7℃~**96.2** ℃ (↓52.0%)	197.7℃~**96.9** ℃ (↓51.0%)
Maximum temperature from simulation (℃)	93.8℃	94.7℃	96.7℃	97.9℃

Full scale simulations are carried out to examine the accuracy of the homogenized model. Figure 4.45 illustrates the temperature distribution while the maximum temperatures are tabulated in table 1. Comparing with the prediction from homogenization, the variation of the maximum temperature between full scale simulation and homogenized model is much smaller (i.e. around 1%). This demonstrates that homogenization can be efficiently used for the representation of variable density lattice structure including movable feature.

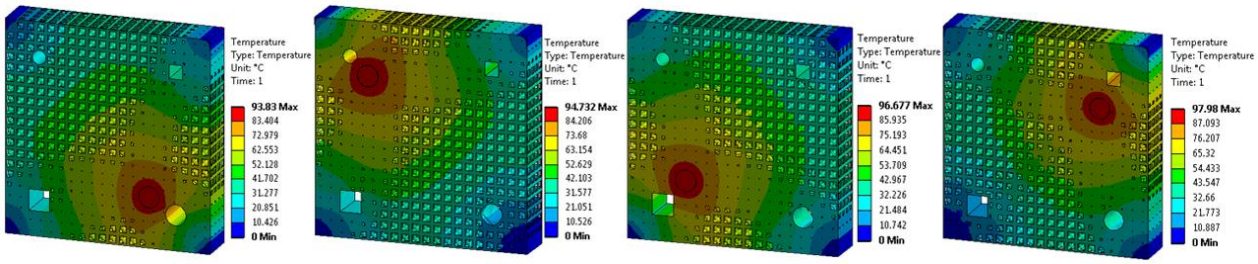

(a) (b) (c) (d)

Figure 4.45: Full Scale Simulation for Different Initial Positions of the Cylinder with Heat Flux. (a) Cylinder #1, (b) Cylinder #2 (c) Cylinder #3 and (c) Cylinder #4.

4.3.2.3 Heat Generation Problem

The second example considers the movable feature with heat generation volume condition. As demonstrated in Figure 4.46, a cross feature is placed at the center of the base plate, and a heat generation rate of $0.2\ \mathrm{W/mm^3}$ is imposed on it. The cross feature has the initial position of ($x = 0$, $y = 0$) mm and , $\theta = 0$ rad , and it has the design freedom of planar movement and roration. Hence there are three geometric design variables for the cross, which include x coordinate, y coordinate, and angle θ of the cross. The other aspects of the problem setup are the same as the previous example.

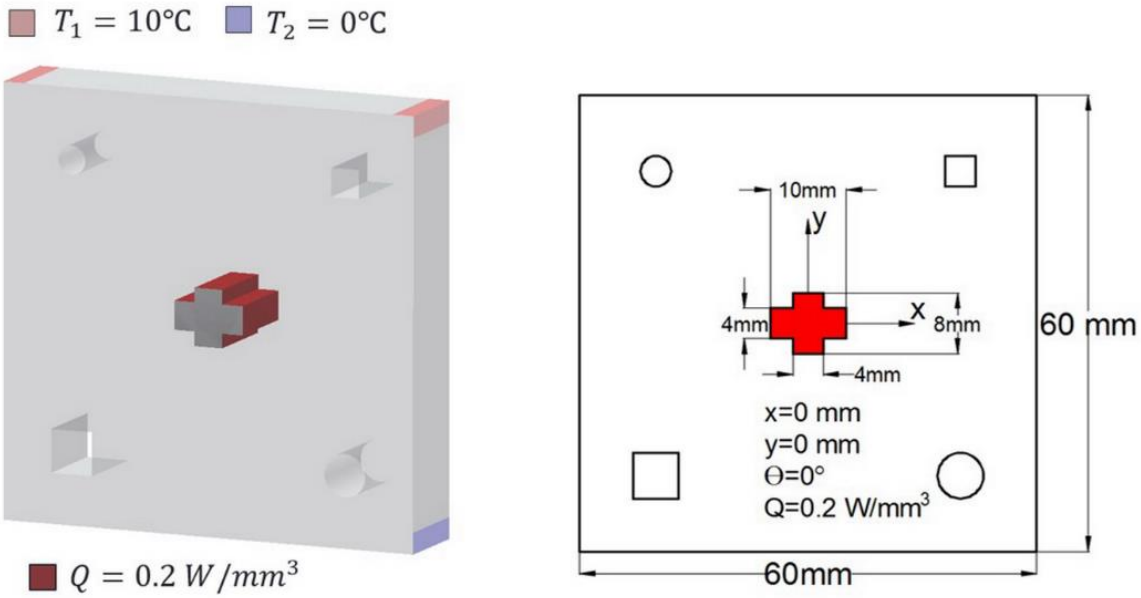

Figure 4.46: Optimization Problem Involving a Cross with Heat Generation Boundary Condition.

Figure 4.47 presents some intermediate results and the final design. The trajectory of the cross feature is similar to the last example. The cross moves towards the lower left corner and rotates to allow the heat to efficiently conduct to the four corners. The difference is that the high-density path connecting the upper right corner is not as thick as the other three paths, as the cross is the farthest away from it. Figure 4.48 shows the convergence history of the objective function, maximum temperature, and position of the cross feature. The final position of the cross is ($x = -5.6, y = -10.7$) mm and $\theta = 0.34$ rad. The objective function reduces from 2.8×10^8 W · K to 1.2×10^8 W · K (56.9% decrease) and the maximum temperature decreases from 246.1 ℃ to 119.0 ℃ (51.6% decrease).

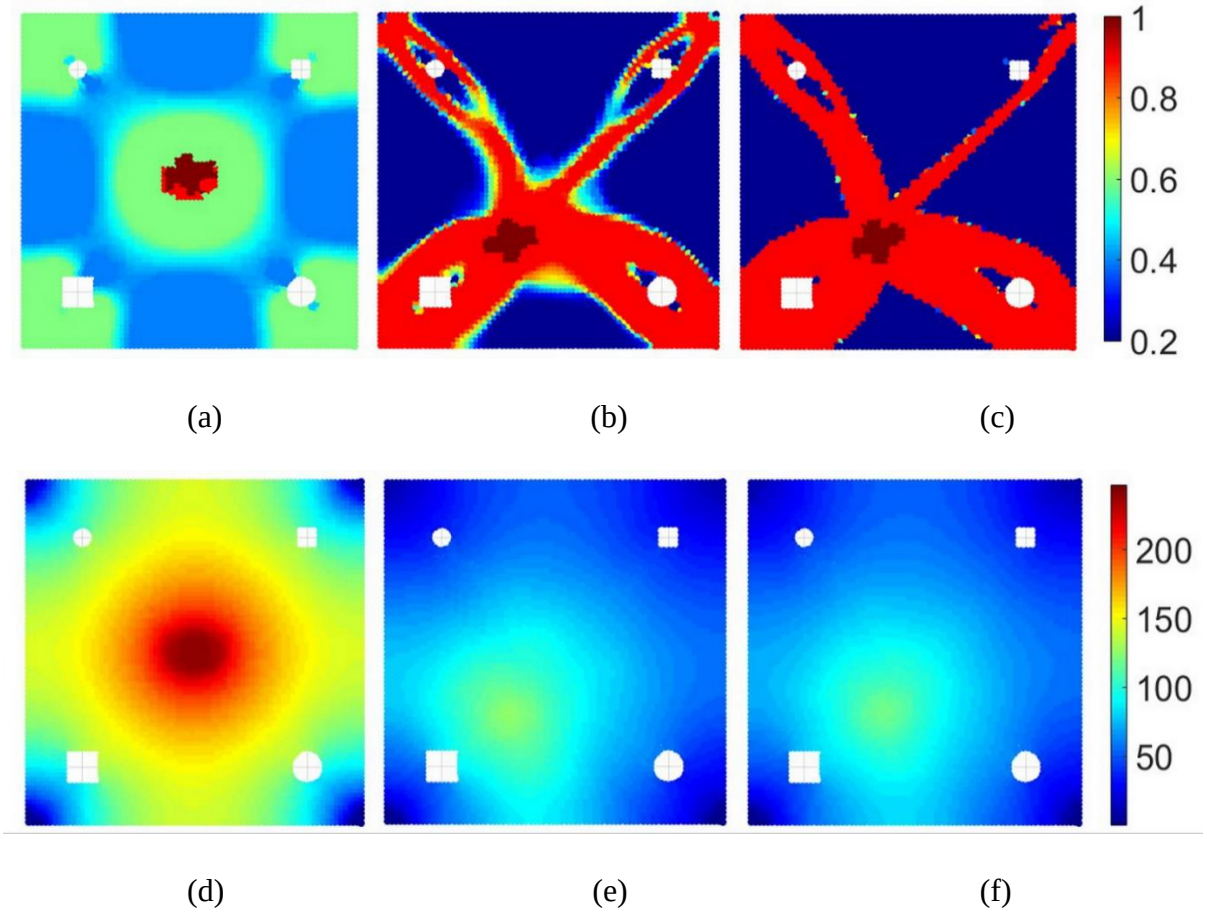

Figure 4.47: Optimization Result with Moving Heat Generation: (a)-(c) Density Distribution of the Design Domain at Iteration 1, 10 and 73; (d)-(f) Corresponding Temperature Distribution of the Design Domain.

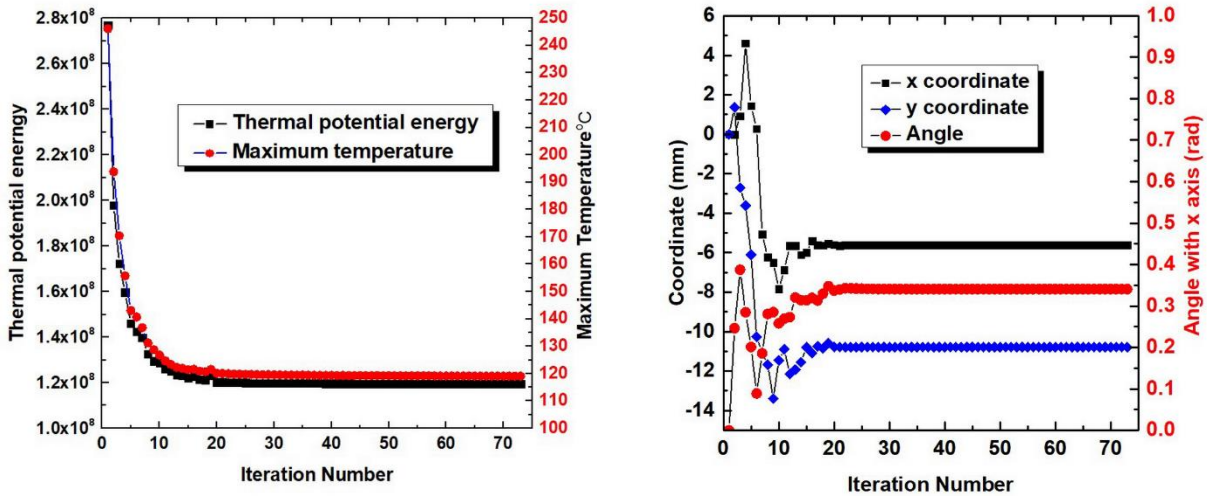

(a) (b)

Figure 4.48: Convergence History of the Optimization: (a) Optimal History of the Objective Function and Maximum Temperature of the Design Domain and (b) Position of the Movable Boundary.

An optimization process with the fixed cross position is conducted and the corresponding result is given in Figure 4.49. Differences can be clearly identified that materials are more evenly distributed along the four conduction paths while the two connecting the two bottom corners are slightly thicker because of the lower tempature at the bottom corners. As illustrated in Figure 4.49(c), the objective function converges from 2.8×10^8 W · K to 1.4×10^8 W · K (50.8% decrease) and the maximum temperature reduces from 246.1 ℃ to 131.0 ℃ (46.7% decrease). Comparing with the fixed design, the concurrent optimization result is 6.1% better in thermal potential energy, while the highest temperature drops 11.9 ℃. This demonstrates the significant advantage of the proposed concurrent strategy.

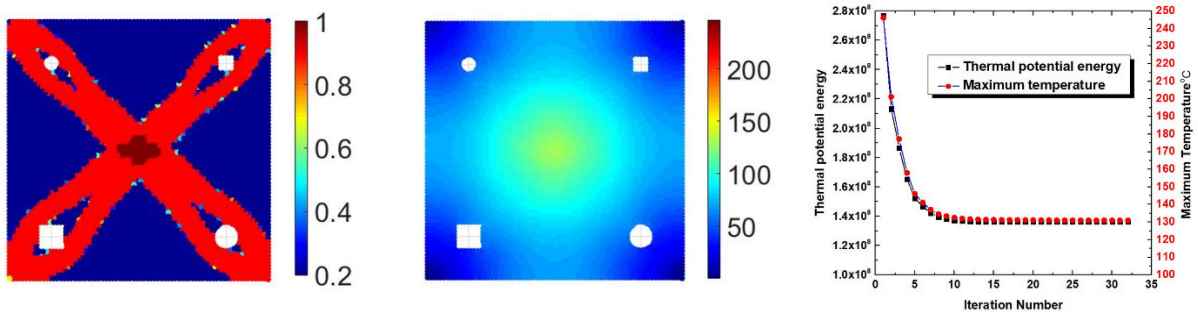

(a) (b) (c)

Figure 4.49: Optimization Result with Fixed Heat Generation Boundary: (a) Optimal Density Distribution; (b) Temperature Distribution And (c) Convergence History.

Again, full scale simulation is performed to verify the accuracy of the homogenization-based simulation. Figure 4.50 shows the full-scale simulation results of both the concurrent design and the design with fixed cross feature position. It can be seen that the highest temperature agrees well in both cases and there are only small differences of 1.2% for the concurrent design and 0.25% for the fixed design.

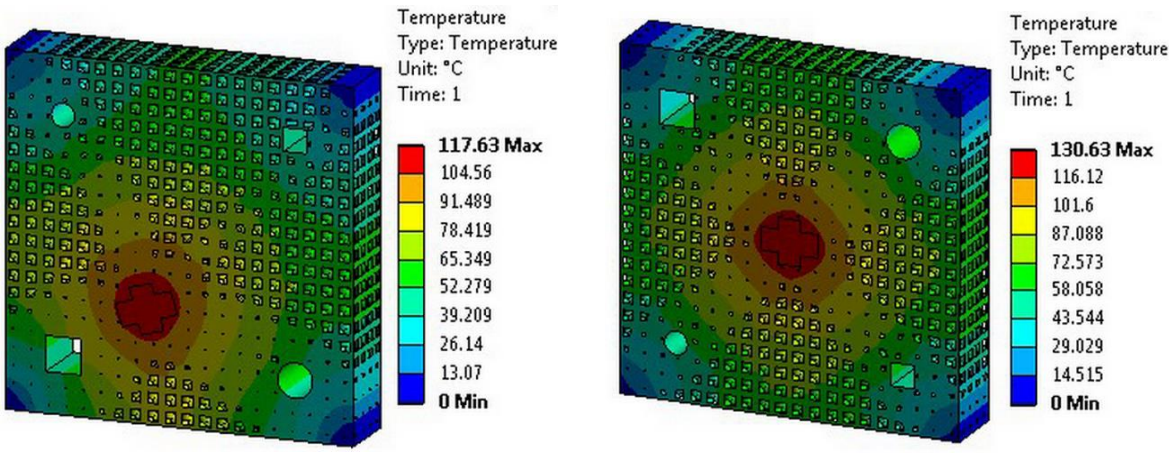

(a) (b)

Figure 4.50: Full-scale Simulation for the Concurrent Design and Fixed Design: (a) Concurrent Design and (b) Fixed Design.

4.3.2.4 Cooling Channel Design Example

In this case, the proposed methodology is employed to optimize the lattice density distribution and at the same time, find the optimal layout of the cooling channels in a three-dimensional setting. Figure 4.51 presents the CAD model, boundary conditions and initial layout of the cooling channels. As illustrated in the figure, the cooling channels are initially placed in two parallel next to the key-hole shaped heat source at the center of the design domain (shown red in color). A constant heat flux of $0.5\,\mathrm{W/mm^2}$ is applied to the surface of the heat source. A temperature of $22\,℃$ is applied to the six surfaces of the rectangle domain. A constant heat convective rate of $1\,\mathrm{W/mm^2}$ is applied to the cooling channel surface and the coolant temperature is assumed to be $10\,℃$. Note that the temperature of the coolant will increase as the fluid flow passes through the channels due to the heat from the cooling target. In this work, to simplify the

calculation of the cooling processes, we assume the coolant temperature is a constant along the channels. For more accurate prediction, heat transfer in the channels will need to be taken into account. The vertical channel segments illustrated in Figure 4.51 are numbered from 1 to 4 as shown in the right panel of the figure. In the optimization, a constraint of distance from the channels to surface of the heat source is used to prevent the cooling channels from moving out of the design domain. Considering practical application, the inlet and outlet channel segments are free to translate and rotate but the angles between adjacent segments are maintained, in order to ensure the flow can be easily pumped into and out of the channel.

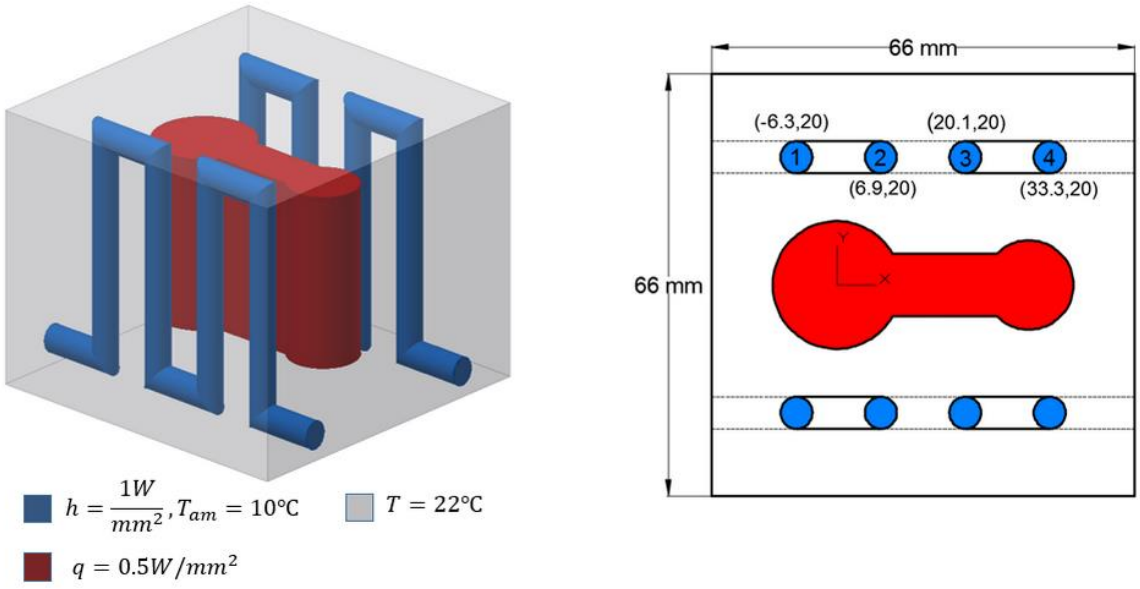

Figure 4.51: Optimization Problem Involving Cooling Channels with Heat Convection Boundary.

Due to the geometric symmetry, only half of the design domain is considered in the numerical analysis. The heat flux and temperature boundary conditions are explicitly applied to

the finite element model, while the heat convection boundary condition is implicitly applied to the cooling channel surfaces using the IB method. Figure 4.52 illustrates the mesh information and boundary conditions of the model. A 103,923 tetrahedral 10-node element mesh is employed in the simulation to solve the temperature field.

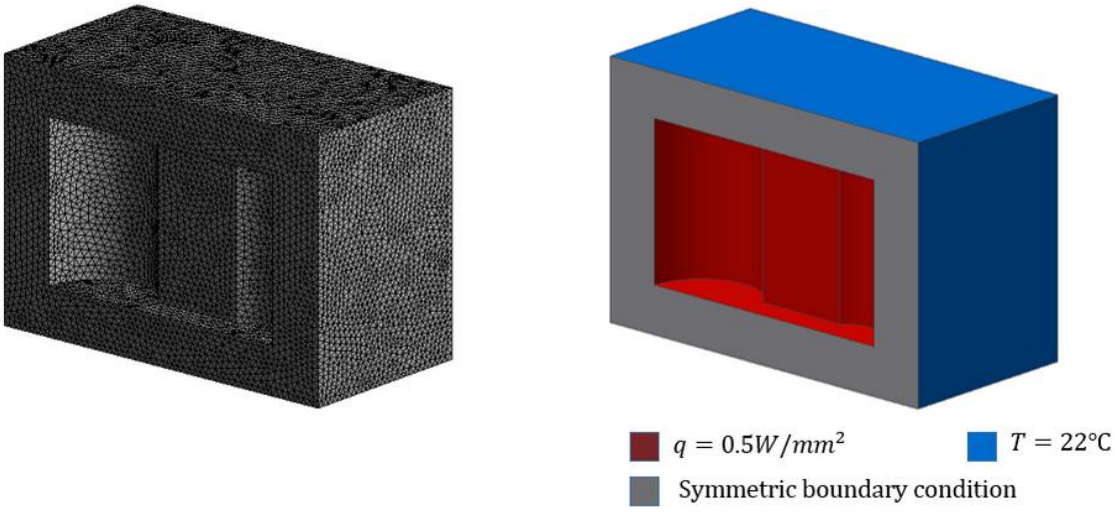

Figure 4.52: Model of Cooling Channel Problem for Optimization: (a) Mesh Model Including 103923 Ten-Node Tetrahedral Elements; (b) Explicit Boundary Condition for the Design Domain Including the Heat Flux at the Inner Surface and The Temperature at the Outer Surface.

Figure 4.53 provides the optimization results including the lattice density distribution, the temperature field and the convergence history. As shown in the figure, the material distribution exhibits the expected trend that high densities appear near the heat source, while lower densities are at the areas far from the heat source. This effectively enhances the structural heat transfer effect. The evolution of the temperature field further proves this conclusion, i.e., the temperature

field of the final design is more uniform and evidently lower than that at the first iteration. As can be seen from the convergence history, the objective function of the structure decreases from 1.0×10^9 W · K to 2.2×10^8 W · K (78.0%decrease) after 41 iterations, while the maximum temperature decreases from 184.1 ℃ to 50.9 ℃ (72.4% decrease).

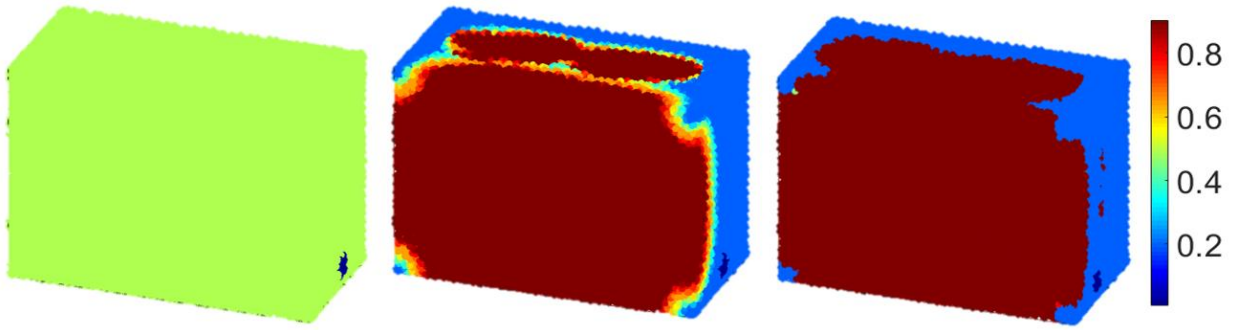

(a) (b) (c)

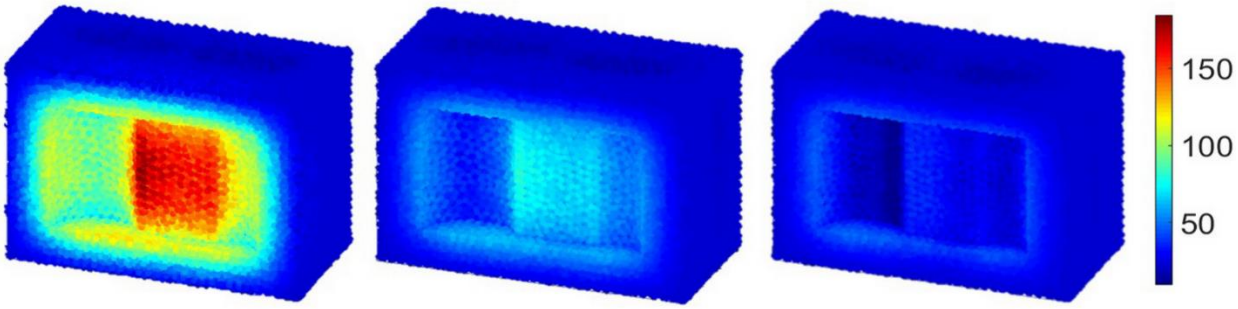

(d) (e) (f)

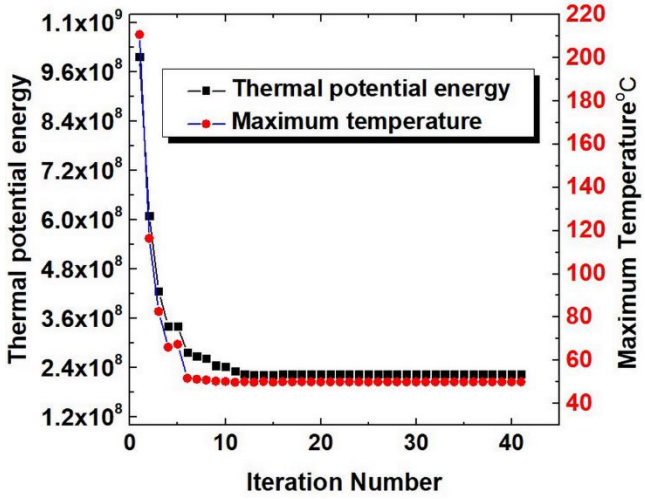

(g)

Figure 4.53: Optimization Result of Cooling Channel Problem. (a)-(c) Density Distribution of the Design Domain at Iteration (1), (3) and (41); (d)-(f) Corresponding Temperature Distribution at Iteration (1), (3) and (41); (g) Convergence History.

The detailed convergence history is given in Figure 4.54 showing the evolution of the cooling channel positions. Here the cross-sectional view from the top is provided. In this view, the solid lines represent the cooling channels near the upper surface, and the dash line indicates the cooling channels near the bottom. Figure 4.54 (a)-(f) illustrates the layout of the cooling channels at different iterations. The exact positions of each pipe are presented in the last figure. It can be seen that the cooling channels move towards the heat source and distributed conformally to the contour of the heat flux boundary. This leads to a type of conformal cooling arrangement and promotes the heat transfer between the heat source and the cooling channels.

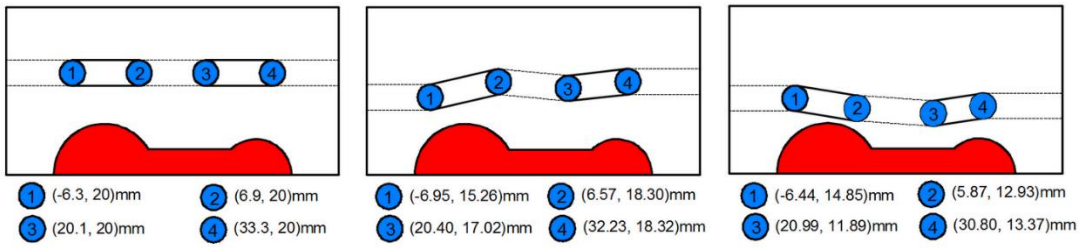

(a) (b) (c)

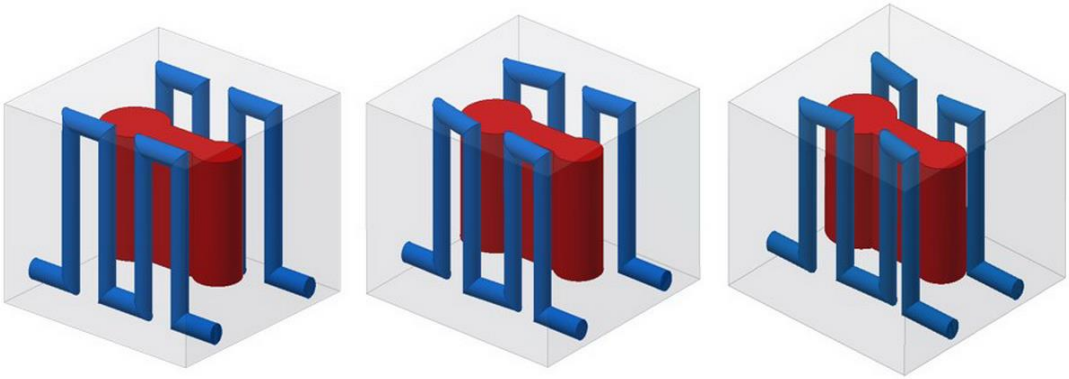

(d) (e) (f)

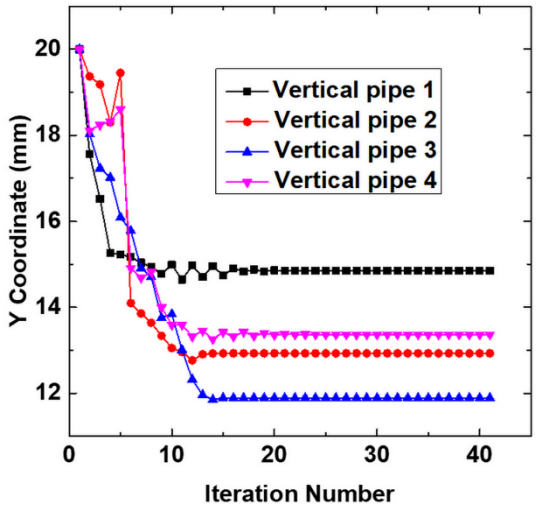

(g)

Figure 4.54: Position of Cooling Channels at Different Iterations: (a)-(c) Is the Position at Iteration 1, 3 and 41; (d)-(f) Is the Corresponding Position in 3D; (g) Convergence History of the Y Coordinate of the Vertical Cooling Channels.

For the purpose of comparison, the optimization with fixed cooling channels is carried out. Figure 4.55 represents the corresponding optimization results. It is seen that the objective function converges to 4.1×10^8 W · K while the maximum temperature decreases to 75.5 ℃. Compared with the concurrent design, the objective function is 1.8 times larger while the maximum temperature is 25.4 ℃ higher in the fixed cooling channel optimization. This indicates that the concurrent scheme for the cooling system design is much more efficient than employing only LSTO.

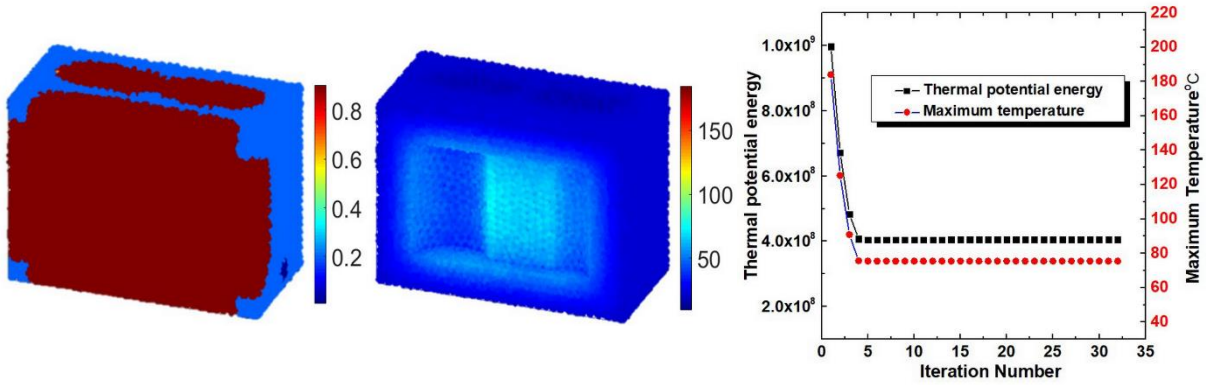

(a) (b) (c)

Figure 4.55: Optimization Results of the Structure Fixed Cooling Channels: (a) Optimal Density Distribution of the Structure; (b) Temperature Field of the Structure and (c) Iteration History of the Objective Function and Maximum Temperature of the Design Domain.

For the purpose of examination, full scale simulations are carried out for the concurrent LSTO design, fixed LSTO design, and also the total solid design. The number of elements used in the full scale FEA is 1,145,509 for the concurrent LSTO design, 1,177,279 for the fixed LSTO

design, and 375,087 for the full solid design, respectively, all of which are much larger that used in the optimization itself (103,923 elements), which is based on the homogenized model with the IB method. Figure 4.56 presents the temperature fields of the simulations using the same legend. As illustrated in the figure, the maximum temperature obtained via concurrent optimization is much smaller than the other two, i.e., 25.6 ℃ lower than the fixed LSTO design and 22.8 ℃ lower than the pure solid design. This proves that the proposed concurrent methodology can significantly enhance the thermal performance and reduce the maximum temperature of the structure with less material usage. Table 4.4 tabulates volume fraction of the structure, the maximum temperature obtained by full scale simulation and homogenization, and also the number of elements used in the simulation. Note that the maximum temperature obtained from the homogenized model is only 1.4 ℃ lower than the full scale simulation for concurrent LSTO and 2.4 ℃ lower than full scale simulation for fixed LSTO. Such a small difference further demonstrates the accuracy of the homogenized model for variable-density lattice structure, and also shows that the IB method can be efficiently used to formulate the moving features with design-dependent boundary.

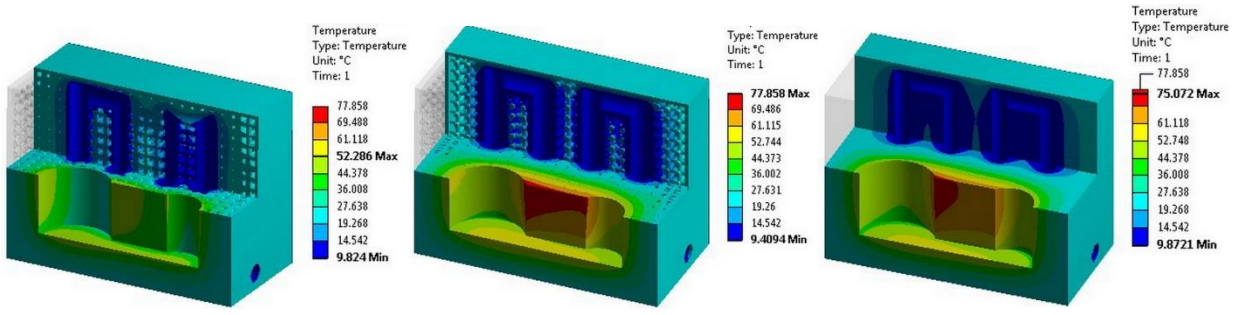

(a) (b) (c)

Figure 4.56: Temperature Field of Full-scale Simulation for: (a) Concurrent Optimization; (b) LSTO Result with Fixed Cooling Channel Layout; (c) Solid Design without Optimization.

Table 4.4: Comparison of Maximum Temperature of Three Designs.

Design	Concurrent LSTO design	Fixed LSTO design	Full solid design
Numerber of element used for simulation	1,145,509	1,177,279	375,087
Overall volume fraction	0.5	0.5	1.0
Maximum temperature from simulation (℃)	52.286	77.858	75.858
Maximum temperature from homogenization (℃)	50.86	75.46	-

To demonstrate the manufacturability of the design, we printed out the cooling channel design using metal additive manufacturing by EOS M290 DMLS system in Ti6Al4V. As shown in Figure 4.57, the optimized design can be printed without support structure for both the variable density lattice layout and the cooling channels.

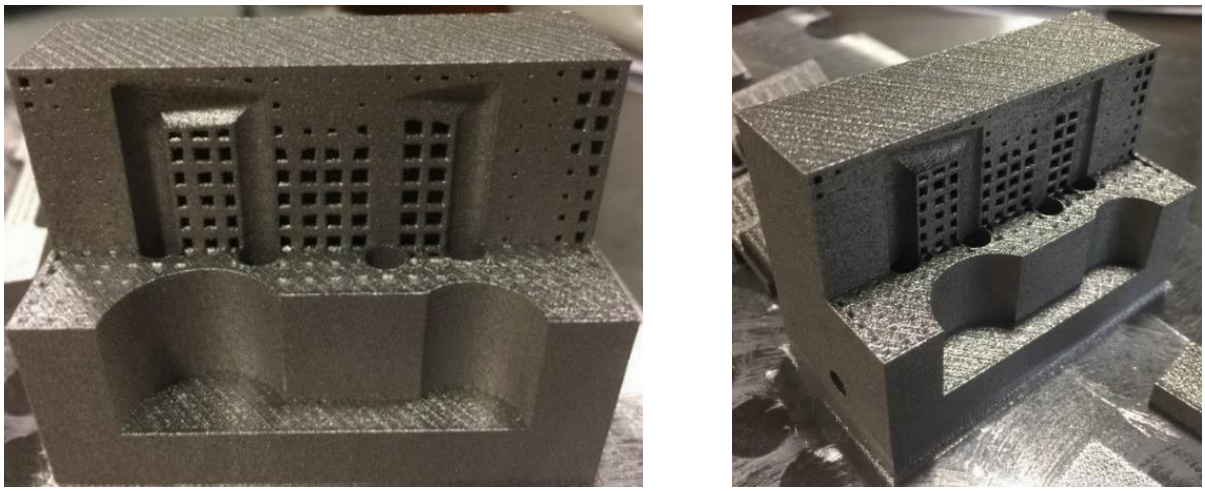

Figure 4.57: Photos of the Optimal Cooling Channel Design Printed out in Ti6Al4V Using the EOS M290 DMLS System.

4.3.3 Summary

A novel methodology is proposed to optimize the density distribution of the lattice infill and the position of the movable features with design-dependent boundary conditions simultaneously. Asymptotic homogenization is employed to obtain the effective thermal conductivity of the lattice structure in terms of relative density within the whole density range. Specficially, the R-functions are used to represent the movable features and optimization based on the level set method is embedded into the lattice topology optimization procedure, leading to a concurrent optimization framework. Moreover, an IB method is proposed to implicitly represent the boundary conditions for both surface and volume boundary and detailed simulations are provided to demonstrate the efficiency of the method. Several numerical examples were studied to validate the proposed optimization framework. By comparing with the LSTO method, it is found

that the concurrent optimization method can significantly improve the performance of the structure. Full scale simulation on the variable density lattice structure design is carried out and the comparison with homogenized model implies that the proposed method using IB method and AH method can provide accurate result. In particular, we further applied the proposed algorithm to design the cooling channel, which significantly decreases the maximum termperature of the structure, even compared with fully solid design. This implies that the proposed methodology can efficiently applied for the optimal design with enhanced performance.

In this work, we mainly focus on the thermal conductivity of lattice structure with movable features. Actually, lattice structure has great potential for heat transfer, such as natural convection and force convection. Our next step work will try to exploit this potential and intend to promote the variable density lattice structure for the design with superior thermal performance.

5.0 Support Structure Design for Residual Stress Induced Build Failure

5.1 Introduction

After several decades, powder-bed metal additive manufacturing (AM) has been among the most popular AM techniques to fabricate functional end-use component for various applications, such as aerospace, biomedical implant, mold manufacturing, etc. However, a serious weakness that prevents it from broad application is the residual stress inherent in the melting and solidification process [139-141]. In powder-bed AM, the material in the build is melted and cooled several times, and stress is accumulated due to inconsistent level of heating [142]. The residual stress leads to severe problem because it can cause warpage, cracks, and delamination during processing, which may block the recoater blade and result in build failure. Figure 5.1(a) illustrates such example of a failed build. The powder spreading is stopped as the built part delaminates from the building tray and deforms so significantly that it stops the powder recoater blade from moving. Such a build failure is very common in practice, which leads to a waste of manufacturing time and material consumption.

Another challenge of the residual stress is the large deformation after the part is removed from the build tray. Sometimes the part may not exhibit deformation during the printing processes, however, once it is cut from the substrate, residual stress is relaxed and deforms the component. This results in limited load resistance, dimensional inaccuracy, and reduction of the fatigue performance compared with the conventional bulk material [143, 144]. As illustrated in Figure 5.1(b), an implant manufactured using Direct Metal Laser Sintering (DMLS) in Ti6Al4V shows undesirable deformation after removal from the build tray. For component with overhang or

protruding features, refer to Fig. 1(c), the problem is even more challenging since residual stress tends to cause distortion and leads to severe warpage and damage at those areas.

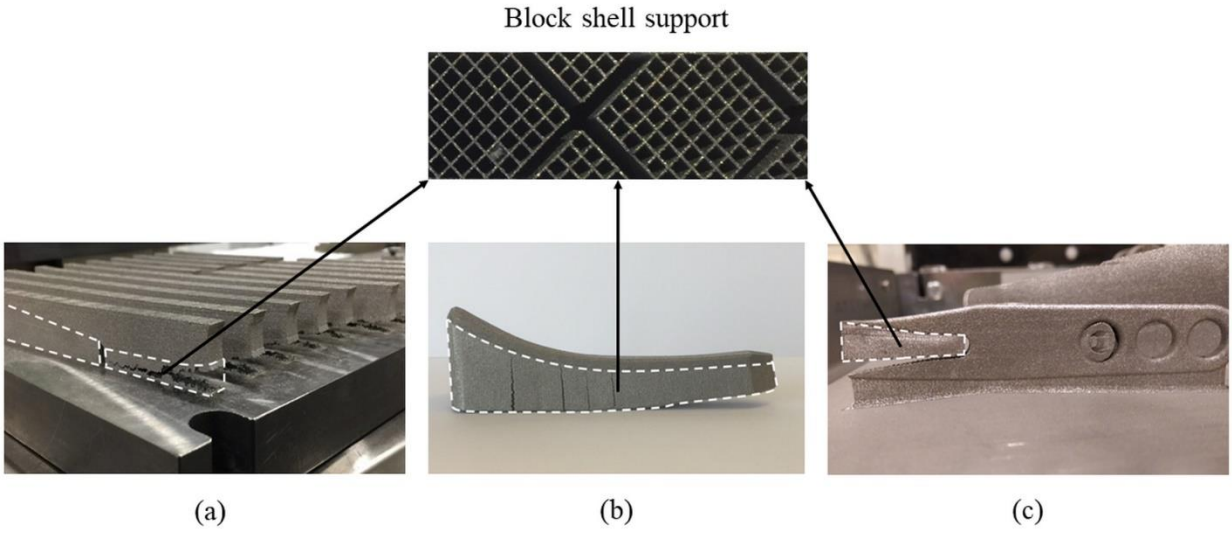

Figure 5.1: Residual Stress and Large Deformation of Metal AM: (a) Bulk Block with Support Structure Before Cutting From the Building Chamber; (b) Implant with Support Structure after Removal from the Chamber; (c) Component with Protruding Feature Deformed During the Manufacturing.

The aim of this work is to experimentally explore the feasibility of a support structure optimization framework for part-scale applications, in order to address the residual stress introduced build failure and guarantee the manufacturability. Instead of conducting detailed thermomechanical analysis, a modified inherent strain method [88, 145] is employed to calculate residual stress and simplify the computationally expensive process into a single-step structural analysis. This significantly reduces the computational cost from hours to minutes or seconds and makes it possible to use physics-based optimization for support structure design to reduce

maximum residual stress. The simulation is based on the hypothesis that the component is completely manufactured without residual stresses release due to cracks growth and delamination. With the progress of the layer-wised manufacturing [146, 147], more stresses accumulate in the component and thus the maximum residual stress obtained from the as-built component is larger than any intermediate states. This ensures the effectiveness of the optimization for the general build failure illustrated in Figure 5.1. To circumvent the error-prone mesh generation process, voxel-based mesh generation [148-150]is employed to discretize the domain of built part and support structure while a fictitious domain method (i.e. finite cell method) is employed to implement inherent strain method for residual stress calculation. In addition, a build orientation optimization method coupled with the LSTO method [108, 111, 135, 151]is used to minimize volume of support structure and maximum residual stress, in order to systematically address the residual stress induced build failure.

The remaining content of this Chapter is organized as follows. In Section 5.2, a voxel-based Cartesian mesh generation for a part and its support structures are introduced. Section 5.3 give a brief introduction about the inherent strain method for fast process modeling of residual stresses distribution. Section 5.4 covers the build orientation optimization for support volume minimization and maximum residual stress reduction. Section 5.5 describes the support structure optimization by using the LSTO method.

5.2 Voxel-Based Cartesian Mesh Generation for Parts and Support Structures

One key step of minimization for support volume and simulation-based orientation optimization is the mesh generation. Especially when the bulk component is randomly rotated in

the manufacturing space, the method that can rapidly generate mesh for both the component and its support structure along build direction is necessary. In general, conformal mesh is employed in finite element analysis (FEA) to provide accurate description. This is easy to achieve for component with simple geometry, while for structures of highly complex geometry (i.e. aerospace component for metal AM shown in Figure 5.2), severe problems are encountered for conformal mesh generation [152]. It is because the translation from computer-aided design (CAD) model to finite element (FE) discretization is extremely computational expensive, and the generation of the conformal mesh is hardly automated and error-prone, which normally requires extra effort for trial-and-error by the users [153]. On the other hand, the generation of support structure for complex geometry based on CAD model is also time-consuming, due to the construction of support structure using thin wall features [150, 154] or lattice structures [155-157]. The mesh generation for these support structure can also lead to high computational cost, making it impractical to minimize residual stress and at the same time to minimize support volume for build orientation optimization. To circumvent these problems, a voxel-based methodology is employed and improved to automatically generate layerwise Cartesian mesh and support structure along the build direction, see the results in Figure 5.2(c). Note that uniform voxel-based mesh is generated in this work, which may lead to large number of elements for FEA. To ensure the efficiency of the analysis, the selection of element size is based on the convergence study of h-version finite cell method (FCM) in [158].

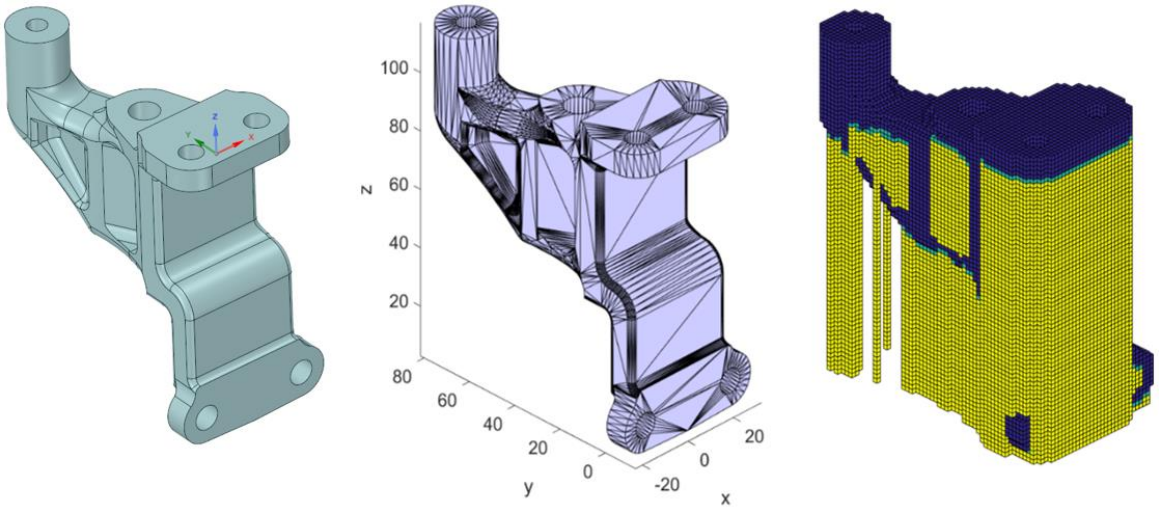

(a) (b) (c)

Figure 5.2: Component for Aerospace: (a) CAD Model; (b) STL File; (c) Voxel-Based Mesh and Support Generation.

The voxel-based support generation was first proposed by Paul et al. [148] to minimize support volume and reduce form errors in the AM process. Das et al. [149] further extended this approach to minimize support structure volume and support contact area, and at the same time, maximize support structure removal to satisfy all the GD&T callouts. The voxel-based approach converts Stereolithography (STL) file into voxel discretization using ray tracing methods [159, 160], and add support voxel based on the overhang facets detection. Although the facet overhang detection in Ref. [149] can reduce the support volume compared with the method in [148], it may lead to underestimation of the volume in the overhang structures that need to be supported. An overhang benchmark is designed to illustrate the performance of these two previous methods. As illustrated in Figure 5.3, there are four different overhang structures in the benchmark.

- Case 1. A horizontal overhang facet connected with two facets that satisfy the overhang angle. Support structure only needs to add under the horizontal facets.
- Case 2. A concave feature consisted of two facets that satisfy the overhang angle (i.e. 45° along the build direction) requirement. No support structure is needed for this feature.
- Case 3. A convex feature consisted of two facets that satisfies the overhang requirement but needs support structure added along the overhang edge.
- Case 4. A convex feature consisted of four facets that satisfies the overhang requirement but needs support structure added to the protruding point overhang.

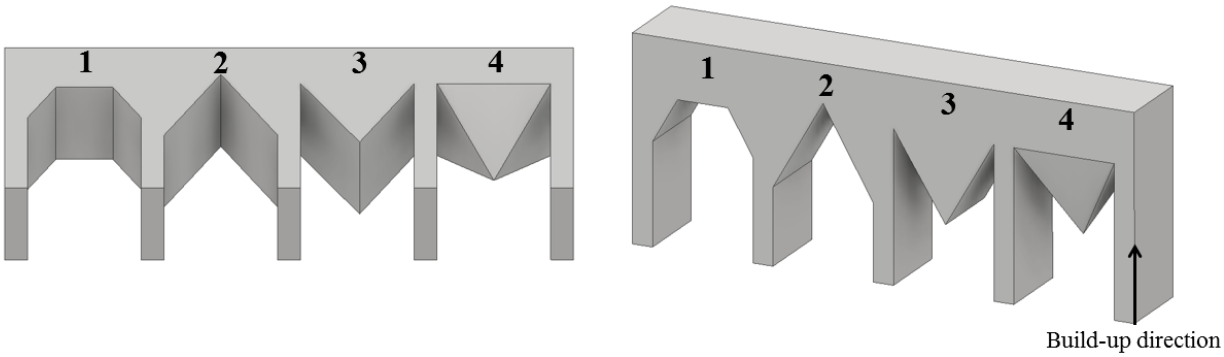

(a) (b)

Figure 5.3: Benchmark of the Overhang for Voxel-Based Detection, (a) Angled Bottom View; (b) Home View.

Using the method in [148], the overhang detections for the benchmark are highlighted in Figure 5.4(a) while the voxel-based support generation is illustrated in Figure 5.4(b). As can be seen, this method tends to support all the undercut discussed in Cases 1-4 and leads to an

overestimation for the support structure calculation, making it difficult to remove support structure for metal AM.

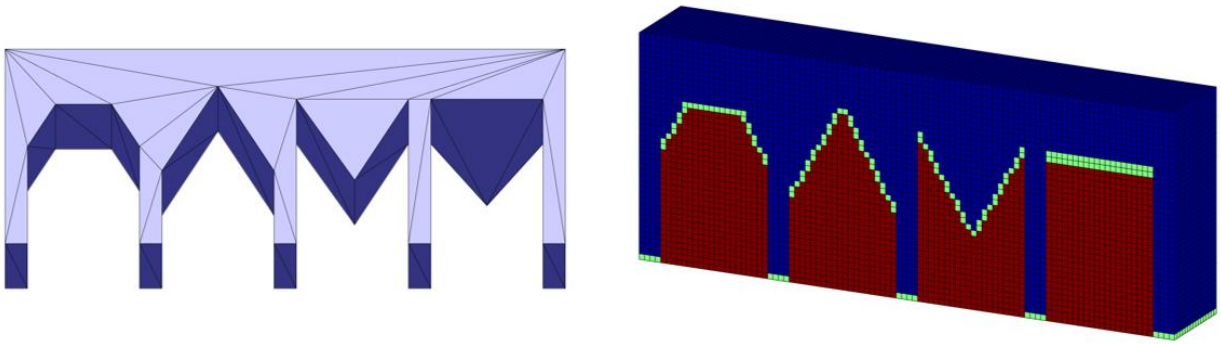

(a) (b)

Figure 5.4: Overhang Detection in [148] and Its Voxel-Based Support Generation for Benchmark: (a) Overhang Detection; (b) Voxel-Based Support Generation and Mesh Generation.

The overhang detection, voxel-based support generation according to the work of [149] are illustrated in Figure 5.5. As shown in the figure, when only the facet overhangs are detected, support structure described in Cases 2, 3 and 4 is removed from the support voxel compared with the result in Figure 5.4(b). For edge overhang and point overhang discussed in Cases 3 and 4, the support generated by this method is obviously an underestimation, because the floating structures in those two cases can lead to failure of an AM build.

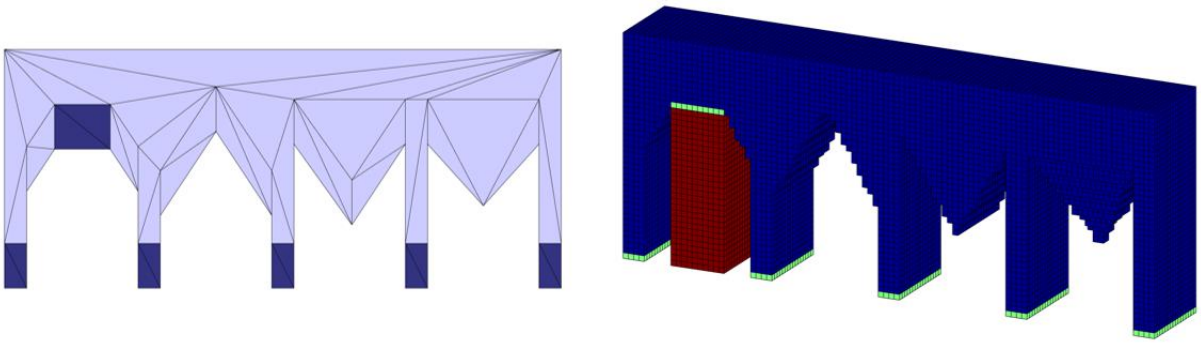

(a) (b)

Figure 5.5: Overhang Detection in [149] and Its Voxel-Based Support Generation for Benchmark. (a) Overhang Detection; (b) Voxel-Based Support Generation and Mesh Generation.

To address the issues of overhang detection in those previous voxel-based methods [148, 149], similar to the work of [155], the overhangs are divided into three categories: Facet overhang, edge overhang and point overhang, whose definition are given below:

- **Facet overhang** is a *downward triangular facet* in STL file which included angle $\theta(\boldsymbol{n}_i^f, \boldsymbol{n}_p)$ of its normal $\boldsymbol{n}_i^f$ to the printing direction $\boldsymbol{n}_p$ is not less than a threshold value, $\pi - \theta_f$, where θ_f denotes the smallest angle of a facet that can be printed without support structure. Figure 5.6 (a) illustrates the definition of the included angle of facet about the printing direction $\boldsymbol{n}_p$, the corresponding 2D description is shown in Figure 5.6(b). It can be seen when $\theta(\boldsymbol{n}_i^f, \boldsymbol{n}_p)$ is larger than the threshold value $\pi - \theta_f$ (i.e. $\frac{3}{4}\pi$), the included angle γ between the facet and the horizontal surface (i.e. the black dash line in Figure 5.6 (b)) is smaller than a critical value θ_f (i.e. $\theta_f = \frac{\pi}{4}$), which can lead to collapse of the manufacturing. Then, the facet i is labeled as a

facet overhang and saved in set of O_f. Otherwise, the facet is grouped into self-supporting facets, which can be printed out without support structure.

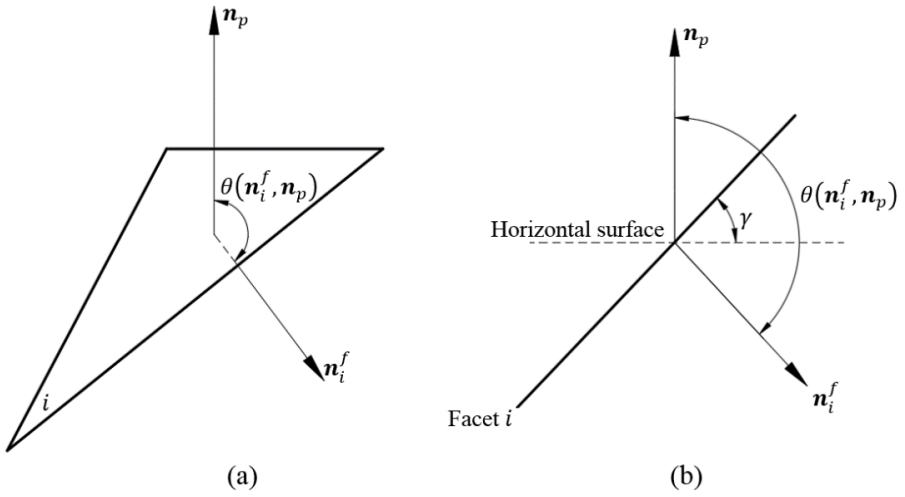

Figure 5.6: Definition of Included Angle of Facet about the Printing Direction: (a) Included Angle of Normal Of i^{th} Facet and Printing Direction, (b) 2D Description of Included Angle for Facet i.

- **Edge overhang** is a *downward convex* edges that do not belong to the facet overhang and at the same time the included angle between the normal of an edge $\boldsymbol{n}_j^e$ and the printing direction $\boldsymbol{n}_p$ is not less than a critical angle $\pi - \theta_e$, where θ_e is the threshold angle of edges that can be printed without support structures. Figure 5.7(a) illustrates the definition of the normal of edge j, which is the addition of normal $\boldsymbol{n}_{j1}^f$ and normal $\boldsymbol{n}_{j2}^f$, where $\boldsymbol{n}_{j1}^f$ and $\boldsymbol{n}_{j2}^f$ are the normal of two facets ($j1$ and $j2$) that are connected by edge j. As shown in Figure 5.7 (b), similar to the definition of facet overhang, when the included angle of edge normal $\boldsymbol{n}_j^e$ and

printing direction $\boldsymbol{n}_p$ is larger than the threshold value, $\pi - \theta_e$, the edge is labeled as an edge that needs to be further analyzed for edge overhang; otherwise, the edge is safe for printing without support structures.

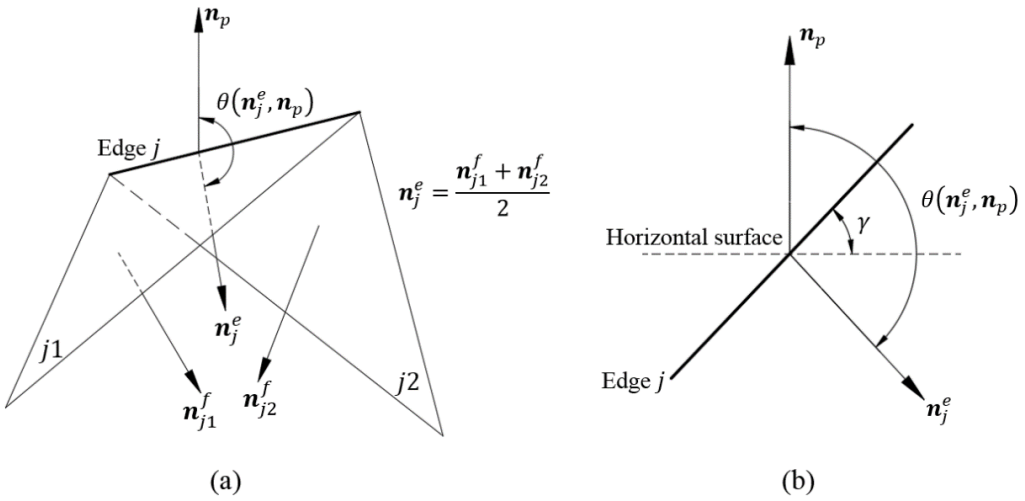

Figure 5.7: Definition of the Edge Normal: (a) Included Angle of Normal of j^{th} Edge and Printing Direction; (b) 2D Description of Included Angle for Edge *j*.

In the work of [155], the definition of the edge normal is the average of the normal of its two incident facets. However, it is found that this definition may include some edges that satisfy the manufacturing requirement. As discussed in the four cases of benchmark, although the included angle of the edges in Case 2 and Case 3 are same, Case 2 does not need support structure while Case 3 requires support structure. To address this issue, an additional variable α_j for edge j is introduced and a constraint is added to distinguish edges in Case 2 and Case 3. The definition of introduced angle α_j is given in Figure 5.8 and can be calculated using $\alpha_j = \theta(\boldsymbol{n}_{j1}^f, \boldsymbol{n}_{j2}^{j1})$, where $\boldsymbol{n}_{j1}^f$ represents normal of facet $j1$ for edge j, $\boldsymbol{n}_{j2}^{j1}$ is a vector which tail is the point of facet $j1$ that is not on edge j and the head is the remaining point of facet $j2$, refer

to Figure 5.8 (a). It can be seen when $\alpha_j \geq \frac{\pi}{2}$, the edge is a convex structure, while when $\alpha_j < \frac{\pi}{2}$, the edge is a concave structure. Thus, the additional constraint of $\alpha_j \geq \frac{\pi}{2}$ is added to ensure only the downward convex edge is identified in the edge overhang detection.

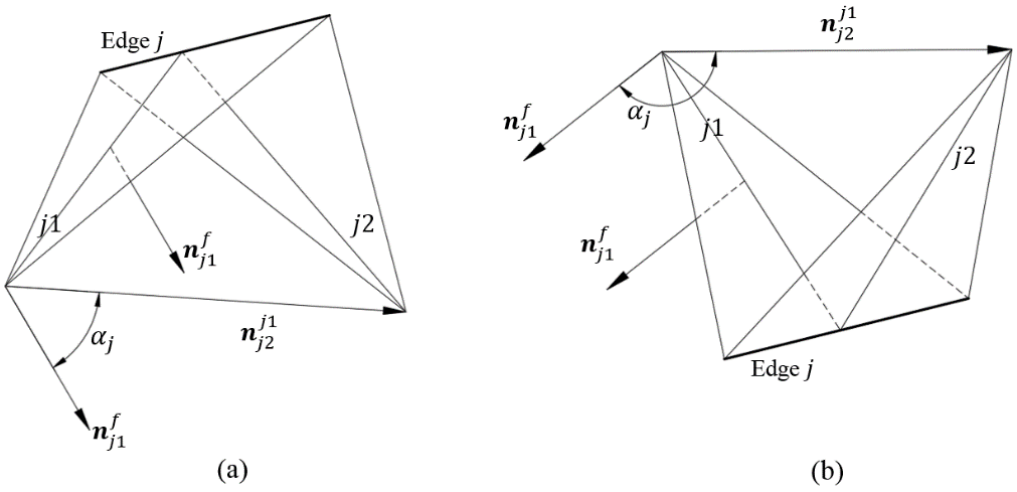

Figure 5.8: Edge with the Same Normal but Different Support Requirement: (a) Downward Concave Edge without Requirement of Support Structure (b) Downward Convex Edge Needs to be Supported.

- **Point overhang** is a point on the downward facet that is lower than its neighbor points and at the same time belongs neither to the facet overhang group nor to the edge overhang.

Once the overhang facets, edges and points are detected based on the three schemes, the ray tracing method [159, 160] is employed to generation voxels for the bulk component and its support structures. By using the new detection methodology, the overhang detection and voxel-based support and mesh generation are given in Figure 5.9(a) and (b), respectively. It can be seen both the downward convex edge overhang and point overhang are identified and the corresponding

support voxel is added in the voxel design. Comparing with the previous method, the new methodology can provide more accurate support volume calculation and voxel mesh generation for the analysis.

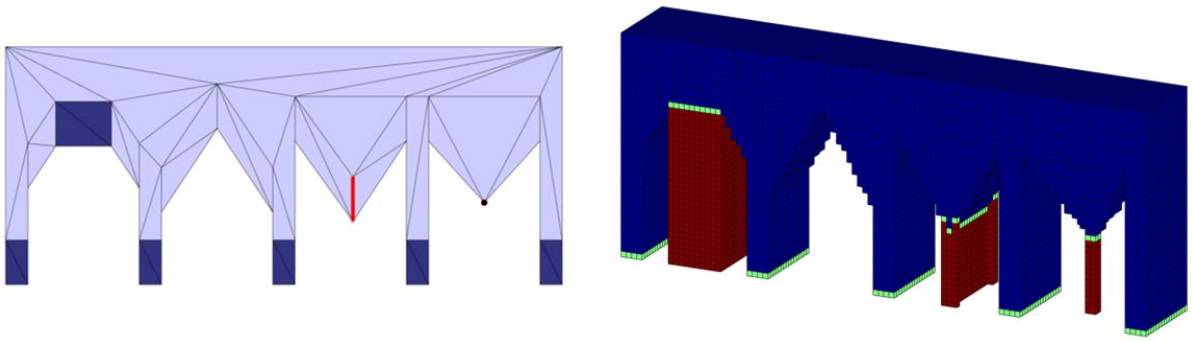

(a) (b)

Figure 5.9: New Overhang Detection and Voxel-Based Support Generation for Benchmark: (a) Overhang Detection; (b) Voxel-Based Support and Mesh Generation.

It is noted that the software code for overhang detection and voxel mesh generation for both solid part and support structures is developed and implemented in MATLAB 2016a. There are three main functions for the implementation. First, a function is developed to read STL file and detect overhang faces, edges and points based on the norms of triangle facets of a given STL file. Second, a function of ray tracing method is developed to covert the STL file to voxel representation, in which the voxels corresponding to the detected overhang features are labeled (e.g. the yellow voxels in Figure 5.9) for support generation. Third, based on the labeled voxels, a function is developed to generate support voxels and combine with part voxels obtained from previous function to form Cartesian mesh for FCM analysis.

5.3 Voxel-Based Fast Process Modeling for Calculation of Maximum Stress

5.3.1 Mechanical Properties of Lattice Structure: Elasticity and Plasticity

In this work, lattice structure is used as the support material to dissipate heat and provide strength to anchor the bulk component to the substrate. Comparing with the block shell support structure widely used for metal AM, refer to Figure 5.10(a), the prominent characterization of lattice structure is its open-cell and self-support nature. This makes it an ideal material for support structure, since it can be printed out without support structure and also allows the trapped powder to be easily removed. Although lattice structure is an efficient material for support structure, it is computationally expensive to explicitly perform full-scale simulation to model the microstructural feature of lattice structure for metal AM. The major challenge is the mesh generation and considerably computational cost for detailed simulation on the microstructure of lattice materials.

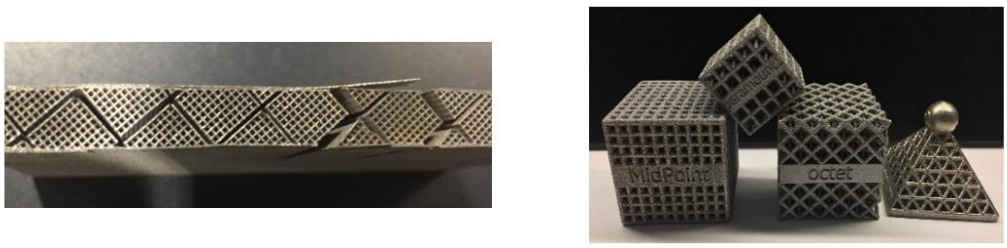

(a) (b)

Figure 5.10: Structure for Support Structure: (a) Block Shell Support Structure; (b) Lattice Structure.

To avoid time-consuming computation for lattice structure, asymptotic homogenization (AH) [94, 161] method is employed to compute the effective elastic properties of lattice structure, while a multiscale model [162] is proposed to capture the anisotropy. By performing analysis on representative volume element (RVE) of lattice structure, a homogenized model is developed to treat lattice material as continuum material with equivalent properties. This simplifies the analysis concerning microstructural feature of lattice structure to analysis based on the homogenized model. Thus, full-scale simulation on lattice structure is circumvented by utilizing equivalent properties obtained from homogenized model to the elements in the support design domain. This makes it possible to conduct optimization to iteratively find the optimal orientation to minimize maximum residual stress. Appendix A details the AH method used to compute both effective elastic properties and yield strength of lattice material based on the analysis on RVE model. Detailed information on the AH method can be found in Refs. [94, 151, 162].

In this work, to study the influence of microstructure of lattice materials on residual stress of the AM component, three different types of lattice structure are studied. As shown in Figure 5.11, the three lattice structures are cubic, cross, and diagonal. The major difference of these three lattice structures is that the “cross” lattice added crossing ligaments to the faces of the “cubic” lattice, while the “diagonal” lattice adds crossing ligaments to the diagonals of the “cubic” lattice. We would like to investigate the influence of the distribution of ligaments on the stress distribution. Figure 5.11 (d) illustrates support structure design for the overhang benchmark mentioned in Section 2 using cubic lattice structure.

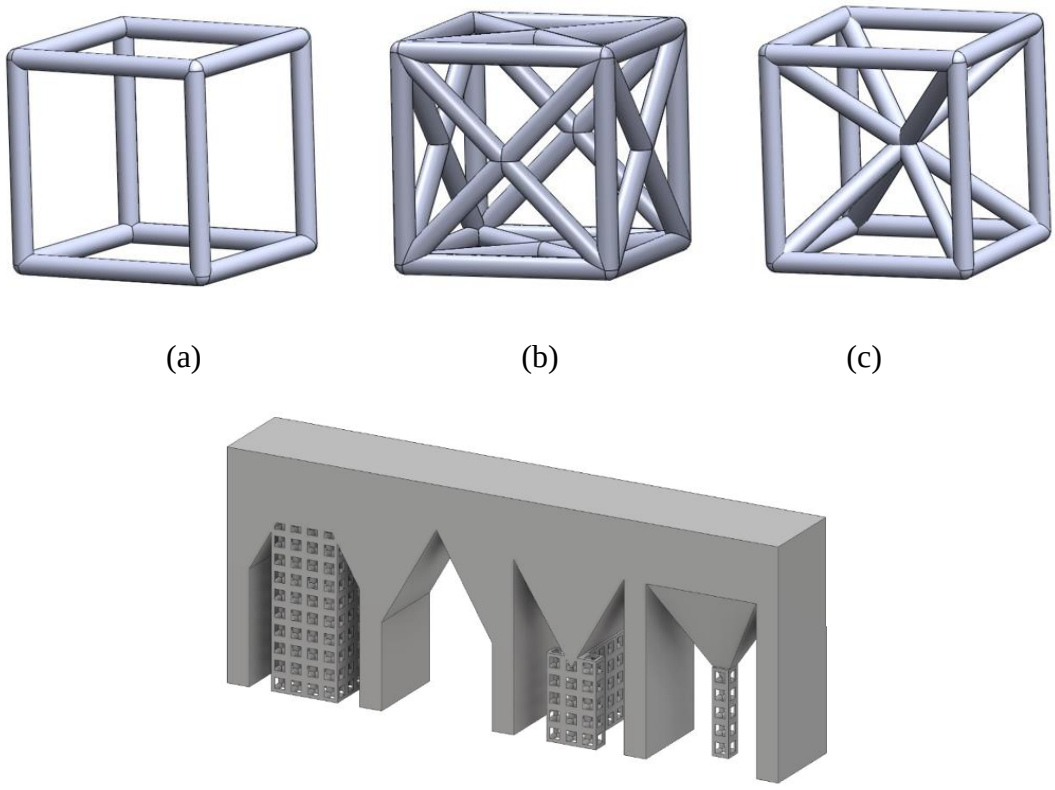

(a) (b) (c)

(d)

Figure 5.11: Lattice Structure Used for Support Design: (a) Cubic, (b) Cross, (c) Diagonal, and (d) Support Structure Design for Overhang Benchmark.

5.3.2 Inherent Strain Method for Fast Prediction Of Residual Stress

Powder-bed metal AM is a process to selectively melt metal powder in a layer-by-layer fashion according to the contour of the sliced CAD model. Once one layer of powder is melted and solidified, a fresh layer of powder is spread by a roller while the melting and solidification process is repeated until the entire part is successfully manufactured. Although metal AM technique has the ability to fabricate parts with complex geometry, residual stress induced failure

is a severe issue for this advanced technology. As explained in [139, 142, 163], two mechanisms introduce residual stresses into the build component at mesoscale, refer to Figure 5.12. At first, when a single layer of powder is rapidly scanned by the laser beam, a transient heat is input on the upper surface and leads to a steep temperature gradient. The heated layer tends to be freely expanded. However, due to the restriction of the surrounding area, an elastic compressive strain is introduced on the top surface. When the yield strength of the material is reached, plastic compression will occur on the top layer, as shown in Figure 5.12 (a). Second, in the cooling process of the molten top layer, the heated layer tends to shrinkage due to thermal contraction. Owing to the inhibition of the underlying material, the shrinkage is prevented, and a tensile stress is introduced on the top of the added layer, refer to Figure 5.12 (b). In the entire manufacturing process, each layer may experience several heating and cooling cycles at inconsistent level, which leads to the accumulation of the residual stresses, and thus the undesirable large deformation, cracks, delamination, etc.

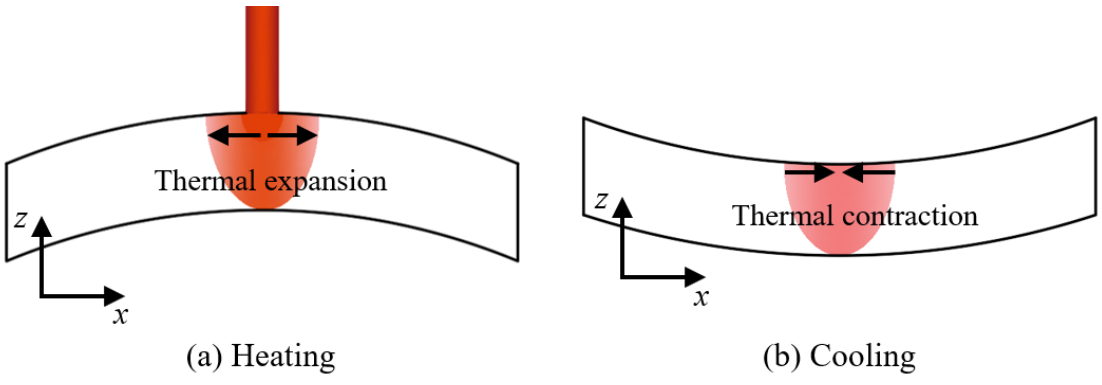

Figure 5.12: Two Mechanisms of Residual Stresses Generation at Mesoscale

However, it is challenging to perform iterative optimization for residual stress minimization due to the expensive computational cost for both mesh generation and simulation for full-scale thermomechanical process. For the former challenge, voxel-based Cartesian mesh generation proposed in Section 2 is used to circumvent the mesh generation issue. While for the second challenge, the most accurate way for residual stress estimation is to perform detailed simulation where the powder melting, and solidification process is modeled in detail based on the printing strategy. It has been proved that such high-fidelity analysis can provide accurate prediction for temperature history and deformation field [164-168]. Nevertheless, this type of simulation takes tens of hours for even a small-scale build and makes it impractical for part-scale problem. To make the proposed optimization method practical, the inherent strain method is employed in this work to efficiently simulate residual stress inherent in the DMLS process. There have been a number of published works regarding the development of this method for AM. Keller et al [169] developed a multi-scale approach to extract inherent strain tensor components and implemented the inherent strain method by pure mechanical simulation. Good agreement was observed between computed distortion and experimental measure in their work. Li et al [163] developed a multi-scale finite element model for fast prediction of distortion of parts manufactured by selective laser melting (SLM) process; however, no details were given on how to extract the inherent strain tensor in this work. Recently, Bugatti et al [170] developed a finite element AM simulation based on the inherent strain method and discussed the limitations and strengths of inherent strain method for prediction of residual deformation in metal AM through experiments. As illustrated in this work, the difference for the prediction of residual distortion between the calibrated inherent strain method and experimental measure is less than 100 μm. Liang et al [88, 171] proposed a modified inherent strain method for laser engineered net shaping (LENS) and

conducted experiments to validate the predicted residual distortion. Based on Liang et al [88, 171], a maximum of 10% error for the predicted residual distortion is observed. Setien et al [87] presented an empirical methodology to determine inherent strains and validated it using the twin-cantilever beam made in Ti6Al4V alloy. Bilal et al [145] experimentally showed that residual stresses predicted by inherent strain method agree well with the value measured by contour method. Marvin et al [172] applied X-ray diffraction to measure the residual stress for a small test samples and compared with the prediction from inherent strain method. It is found that the inherent strain method provides reliable prediction of residual stresses.

Although the inherent strain method has been employed to simulate residual stress and distortion of AM components, there are two major limitations of the existing methodology. First, the prominent feature of the inherent strain method is its replacement of the complex thermomechanical process by a pure mechanical analysis. This simplification results in lack of detailed information regarding thermomechanical history of the printing process. Second, the inherent strain method is based on the assumption of continuum description for powders in the simulation. This neglects the powder distribution and makes it impractical to simulate morphology of melting pool, evolution of microstructure, as well as the local defects (e.g. less-fusion, porosity, spatter, denudation, keyholing) for an AM part. However, the goal of this work is to develop an optimization method for build orientation to address the residual stress induced build failure at part-scale level. Hence, the limitations of inherent strain method at microscale are neglected, while the unique capability of inherent strain method for efficiently simulating residual stress for larger model is utilized to perform build orientation optimization. For detailed theory and validation for the inherent strain method, readers are referred to Refs. [88, 145, 172]. With regard to implementation of the proposed method, the fictitious domain method [173-175] (i.e. finite cell

method (FCM)) is applied to perform inherent strain method and compute residual stresses. The FCM method belongs to the fictitious domain method/immersed boundary method (IBM) and proposed by Parvizian et al [158] to avoid error-prone conformal mesh generation. It has been successfully applied to solve various problems, such as non-linear analysis [153], transport problem in porous media [176], biomechanical analysis [177, 178], etc.

5.4 Build Orientation Optimization

Build orientation plays an important role in residual stresses accumulation, since it determines the support structure generation and thus the distribution of stress and strain introduced by the manufacturing process. Consider the dogbone shown in Figure 5.13(a) as an example. The dogbone is built in three different directions (i.e. 0°, 45° and 90° by y-axis, refer to Figure 5.13 (b-d)) with support structures added to support overhanging structures, which are detected by the method proposed in Section 5.2. It can be observed that the support structures vary a lot among the three build orientations. This illustrates that as the build orientation is changed, the manufactured volume, especially the support structure volume, is changed. To examine the influences of the build orientation, fast process simulation by using the inherent strain method [88, 145, 170, 179] is performed to calculate the residual stress distributions for the three build orientations. Figure 5.13 (e-g) show the three residual stress distributions. As can be seen, the maximum normalized residual stress by Hill's stress measure of the horizontal orientation in Figure 5.13 (e) is 2.30, the maximum value of orientation 45° in Figure 5.13 (f) is 1.62, and the maximum value of orientation 90° in Figure 5.13 (g) is 1.14, in which the vertical orientation in

Figure 5.13 (g) exhibits the smallest maximum residual stress comparing with another two build orientations. This demonstrates that build orientation has significant influence on the residual stress distribution. Hence, it is possible to address the residual stress induced failure through optimization for the build orientation.

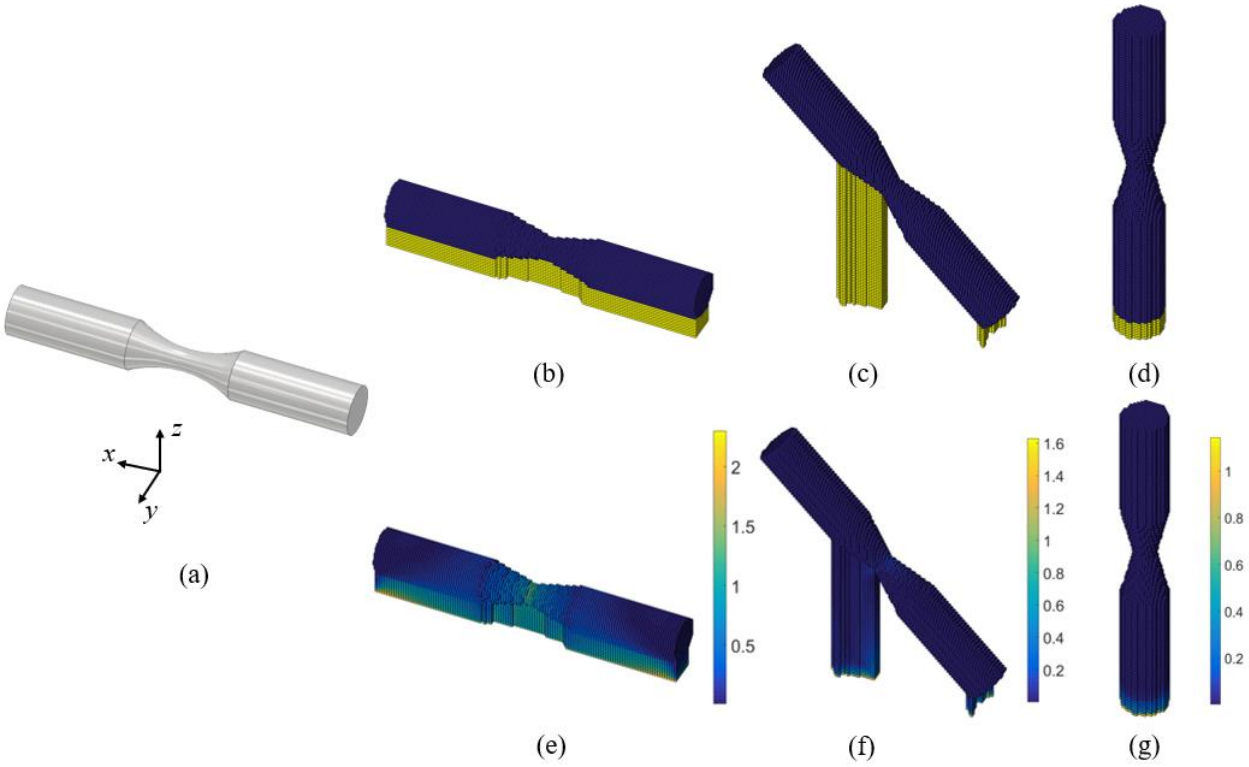

Figure 5.13: Influence of Build Orientation on a Generic Dogbone. (a) CAD Model of a Dogbone (b) Mesh of the Dogbone is Oriented 0° by Y-Axis (c) Mesh of the Dogbone is Oriented 45° By Y-Axis (d) Mesh of The Dogbone is Oriented 90° by Y-Axis; (e) Normalized Residual Stress Distribution of 0° Orientation (f) Normalized Residual Stress Distribution of 45° Orientation (g) Normalized Residual Stress Distribution of 90° Orientation.

5.4.1 Optimization Model for Minimizing Support Structure Volume and Residual Stress

In the Sections 5.2 and 5.3.2 , the methodology for calculating support structure volume and residual stress have been explained. Open-cell lattice structure is used as the support structure to anchor the solid component to build tray. When the volume fraction of the support structure is set to a constant value (e.g. $V = 0.3$) to ensure manufacturability, both the volume of support structure and stress distribution are assumed to be solely determined by the build orientation. This makes it possible to minimize the volume of support structure while reducing maximum residual stress simultaneously. However, these two objectives may conflict with each other. A build orientation optimized for support volume may lead to a reduction of support volume but result in an increase of maximum residual stress. To address the conflict between these two objectives, a multi-objective optimization model is proposed here to optimize the build orientation in order to minimize the maximum residual stress along with the total volume of the support structure by a weighting function. Hence the maximum stress and the volume of support structure are combined using a linear function to form a single weighted aggregate optimization. The definition is given as follows:

$$F(\theta, \phi) = w\lambda V_s(\theta, \phi) + (1 - w)\bar{\sigma}^H_{max}(\theta, \phi) \tag{5.1}$$

$$\begin{gathered} s.t.\ \ \mathbf{KU} = \mathbf{F}^{in} \\ -\pi \leq \theta < \pi \\ -\pi \leq \phi < \pi \end{gathered} \tag{5.2}$$

where θ and ϕ are the angles by which the part is rotated about x and y axis, respectively, and $F(\theta, \phi)$ represents the combined objective function; V_s is the volume of support structure calculated from support voxel; $\bar{\sigma}^H_{max}$ denotes the normalized maximum residual stress in the

domain including both the support structure and bulk component. w is the weighting value used to provide the flexibility to vary the contribution of the different objectives to the combined objective function. λ represents the scaling factor used to ensure that the support volume is within the same order of magnitude as the maximum stress. The two inequalities in Eq. (5.2) impose the constraints of the rotation angle about the x and y axes. Note that z axis is assumed to be the printing direction.

Since the explicit mathematical model between the objective function in Eq. (5.1) and design variables are difficult to obtain, the heuristic optimization method named particle swarm optimization (PSO) [180] is employed to find the optimal solution. For multi-objective optimization problem, due to the conflict among competitive objectives, there exists more than one optimal solutions, which are referred as Pareto Optimal solutions [181]. The solutions within the Pareto Optimal solutions are considered equally optimal. Particularly in this work, the solutions with minimum height are selected as the optimal design since the manufacturing time is determined by the height of the part. The lower the part, the less the time it takes to print.

5.4.2 Numerical Examples and Experimental Validation

For validation purpose, a realistic industrial component is used to investigate the performance of the proposed orientation optimization framework. The aims of the investigation include studying the effects of: 1) three overhang strategies on the minimum support volume calculation, 2) different types of lattice structures on the minimization of maximum residual stress, and 3) multiple objective optimization on the final design. To examine the performance of the optimal design for stress minimization, the designed component is printed out by the EOS M290

DMLS system in Ti6Al4V and compared with the non-optimal design and default design provided by the Magics software widely used for inserting supports into a build prior to printing.

The material properties of Ti6Al4V is used in the analysis include Young's modulus ($E = 110\ \text{GPa}$), Poisson's ratio ($\nu = 0.3$), and yield strength ($\sigma_y^* = 1{,}060\ \text{MPa}$). Without losing generality, the stresses illustrated below are normalized by the material's yield strength. When the local normalized stress is larger than 1, the material is undergoing plastic deformation; when the stress is smaller than 1, the stress state is elastic. The new overhang detection algorithm proposed in Section 2 is applied to compute the support volume. The inherent strain method, coupled with homogenized model of the lattice structure (introduced in Section 3), is employed to compute residual stress of the support domain and bulk component domain very efficiently. To ensure manufacturability of the support design, the volume fraction of the support structure is set to be $V = 0.3$, and the lowest point of the component to the build tray is 7 mm for the purpose of component post-removal. Particle swarm optimization (PSO) method is applied to solve the optimization problem in Eq. (1-2) [180]. The optimization is terminated when the change of the objective function within five successive iterations is smaller than 1×10^{-3} while the minimum iteration number constraint (i.e. 10 iterations at least) is satisfied. The FCM method for executing the inherent strain method and multi-objective PSO method are implemented using MATLAB 2016a. Generation of the lattice structure support is conducted by an in-house software code based on the application programming interface (API) of Autodesk Inventor Professional 2018. The computer with configuration of 7-core Intel(R) Xeon(R) CPU E5-2687 v3 @ 3.10 GHz is used for the mesh generation, FCM analysis, and optimization. Without specific notation, the computational cost discussed in the following section is calculated in this computer.

5.4.2.1 Minimization of the Support Volume Based on the Proposed Overhang Detection

In this case, a realistic industrial component is taken as the objective to compare with the three overhang detection methods described in Section 5.2. Figure 5.14 illustrates the CAD model and STL file of the bearing bracket used for the investigation. As shown in the figure, the bracket has two major features: One is the cylinder, which has an inner diameter of 18 mm and external diameter of 30 mm; the other is the base plate including two bolt holes used to fix the whole structure, whose dimension is $48 \times 36 \times 8$ mm^3. The two features are connected by a rib structure with a constant thickness of 8 mm. Due to its complexity, it is difficult to empirically determine the optimal orientation of the component to minimize support volume and maximum residual stress simultaneously. This case mainly focuses on the minimization of support volume and w in Eq. (5.1) is equal to 1. Hence, the optimization problem becomes a single support volume optimization for finding the optimal build orientation. Considering the symmetry of the component along the $x - z$ plane, the ranges of the rotation of the part are $\theta \in [-\pi, \pi]$ and $\phi \in [0, \pi]$, respectively. In the optimization, 32 points are being uniformly distributed in the design domain as the initial particles for the PSO method. The three overhang detection schemes introduced in Section 5.2 are employed here for comparison purpose.

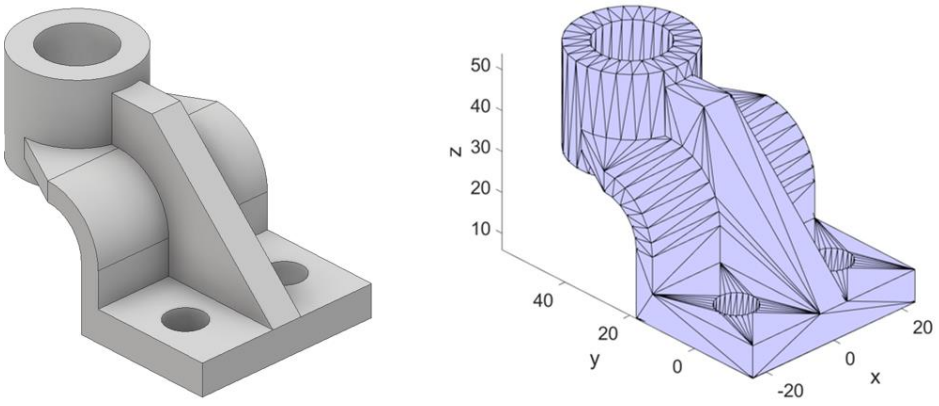

(a) (b)

Figure 5.14: Bearing Bracket for Investigation of the Optimization Framework. (a) CAD Model (b) STL File.

Figure 5.15 illustrates the initial state of the particles for the PSO method, the convergence history of the best position and the optimal support design with the build tray. The black dots given in the contour plot of Figure 5.15 (a) and the surface plot of Figure 5.15 (b) are the orientations of the particles. As shown in Figure 5.15 (a) and (b), there exists many local optima in the searching space according to the initial particles. By moving these particles using the PSO method, the objective function goes from 4.511×10^4 mm^3 to a converged value of 4.132×10^4 mm^3, or a decrease of 8.4%. The optimal orientation of minimum support volume is given in Figure 5.15 (d), in which the orientation is $(\theta, \varphi) = (\pi, \frac{\pi}{2})$.

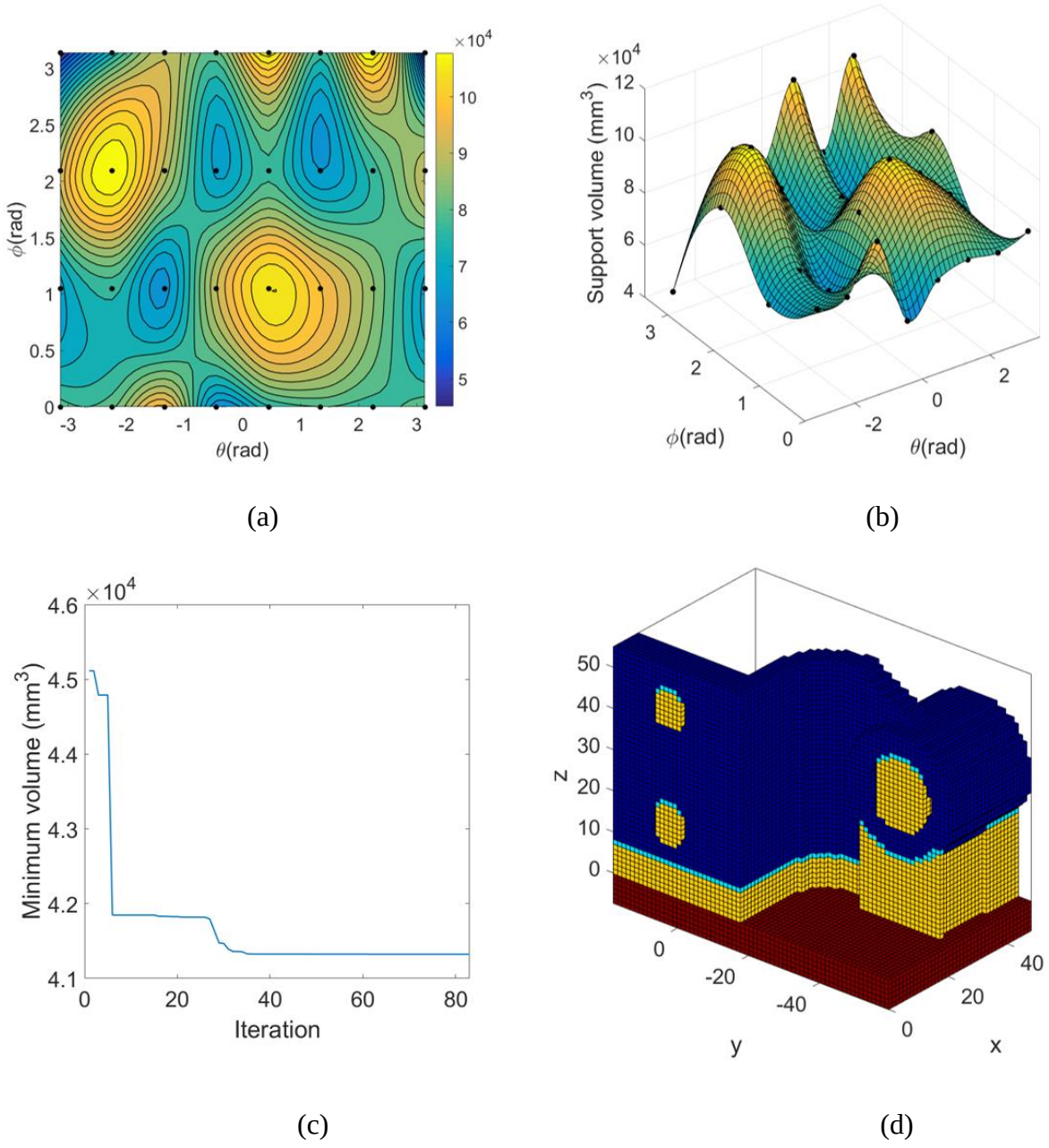

Figure 5.15: Result of Support Volume Minimization Using the Method in [148]. (a) Contour Plot of the Support Volume at Initial State (b) Surface Plot of the Support Volume at Initial State (c) Convergence History of Best Objective Function at Each Iteration (d) Optimal Support Design.

The results based on the facet overhang detection proposed in [149] are shown in Figure 5.16 including contour plot and surface plot of initial state of the support volume. For comparison purpose, the initial orientations of the particles are identical to the previous one. As can be seen, due to the change of the overhang detection, the initial distribution of the support volume in Figure 5.16(a) and (b) is different from the previous one. After 40 iterations, the support volume is reduced to zero and the orientation coordinates are (θ, ϕ)=(0.7192, 2.7842). As shown in Figure 5.16 (d), since at the optimal orientation, no facet overhang is detected, and the bulk component is suspended on the build tray, which is not feasible. This shows that the single facet overhang detection strategy cannot guarantee successful support generation.

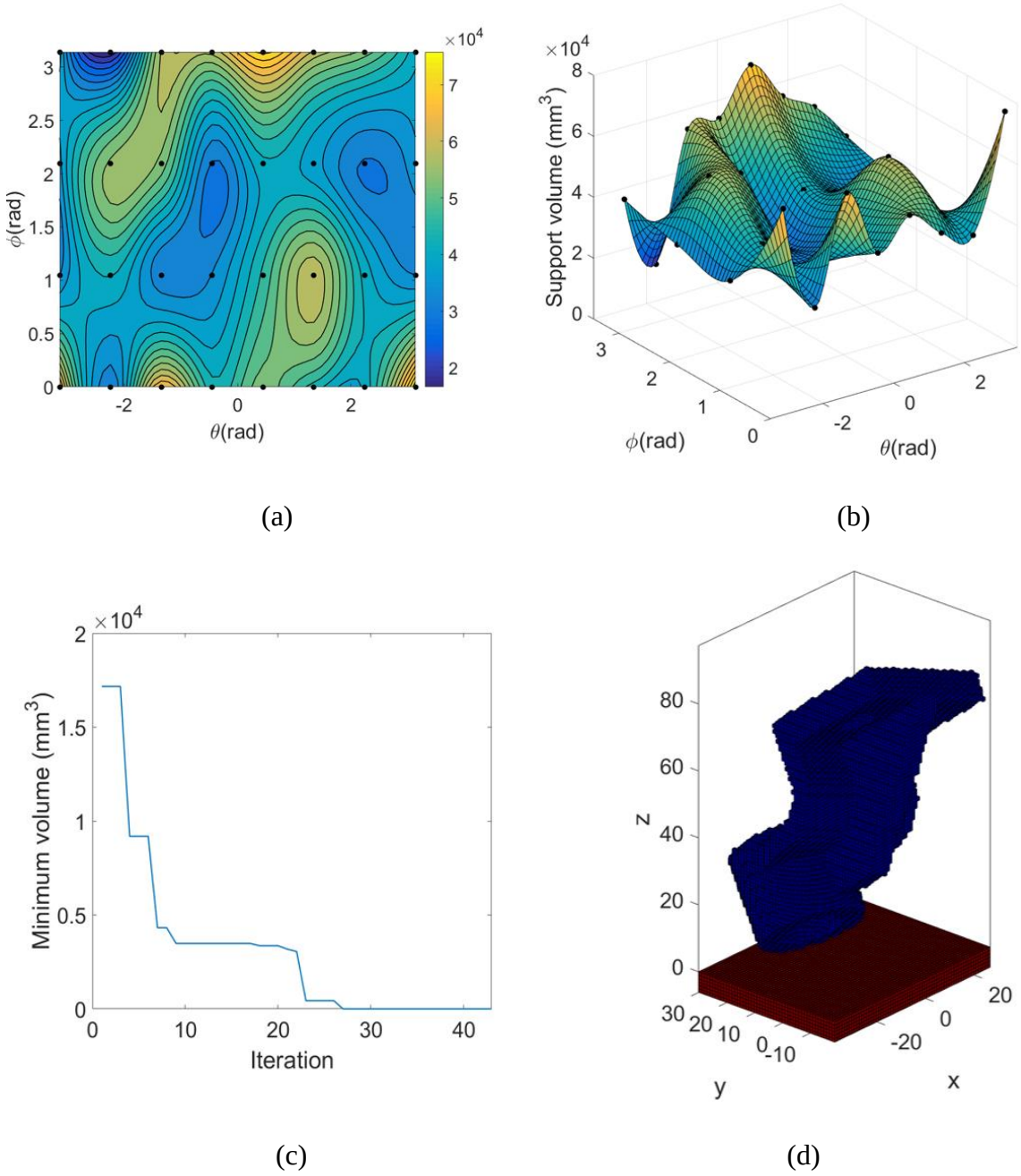

Figure 5.16: Result of Support Volume Minimization Using the Method in [149]. (a) Contour Plot of the Support Volume at Initial State (b) Surface Plot of the Support Volume at Initial State (c) Convergence History of Best Objective Function at each Iteration (d) Optimal Support Design.

The optimization result using the overhang detection proposed in this work is given in Figure 5.17. Comparing with the other two methods, the initial contour plot and surface plot are similar to the results shown in Figure 5.16(a), but the optimal result is much different due to the detection of edge and point overhang. The minimum support volume of the particles converges from 2.104×10^4 mm^3 to 6.988×10^3 mm^3, or a decrease of 66.8%, and the optimal orientation is $(\theta, \phi) = (-2.356,\ 3.130)$. The optimal orientation obtained by the proposed methodology is different from the previous methods.

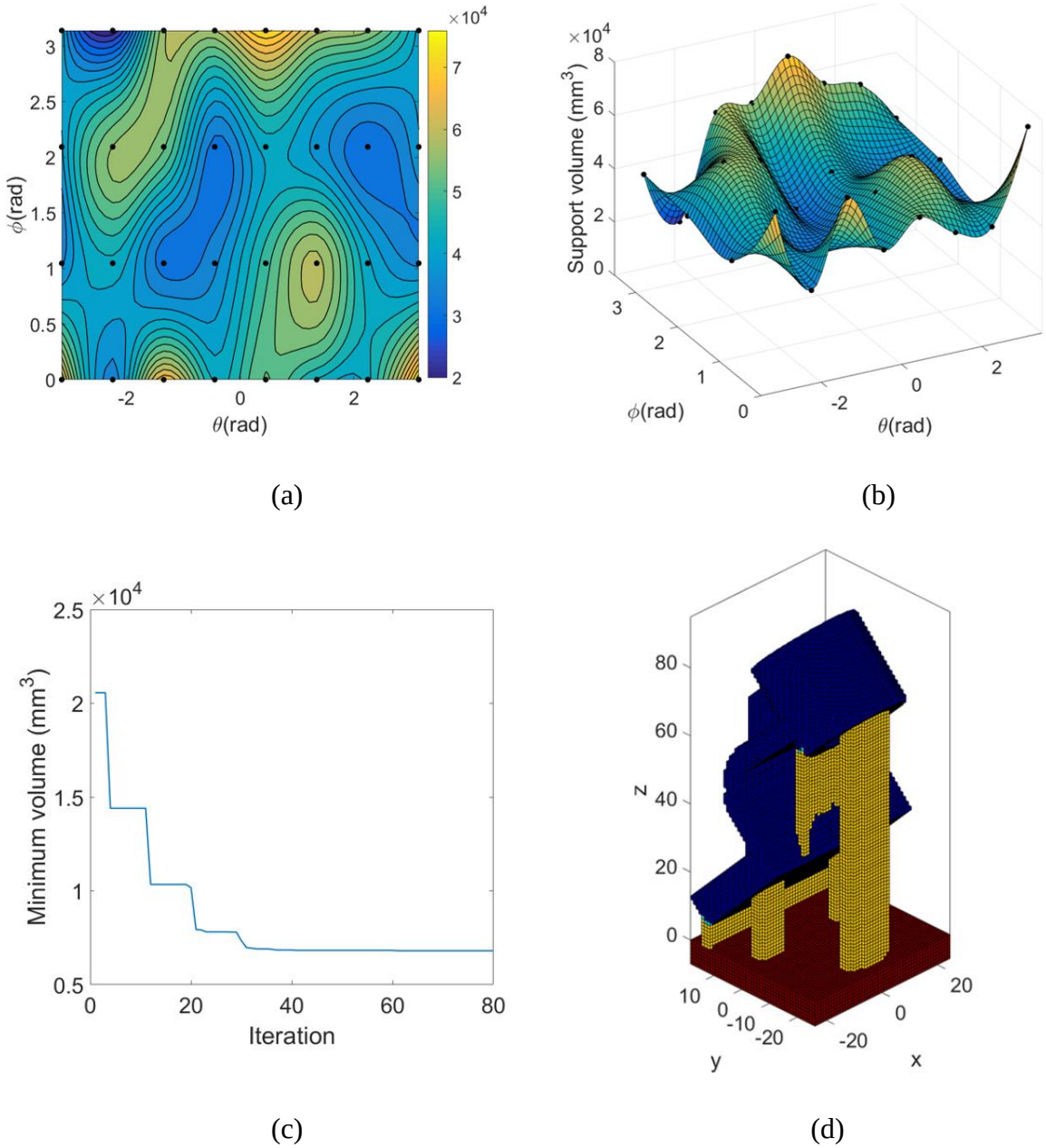

Figure 5.17: Result of Support Volume Minimization Using the New Method. (a) Contour Plot of the Support Volume at Initial State (b) Surface Plot of the Support Volume at Initial State (c) Convergence History of Best Objective Function at each Iteration (d) Optimal Support Design.

The mesh generation was performed on the computer with 7-core CPU. The computation cost of voxel mesh generation, overhang detection and volume calculation for the bearing bracket using the in-house MATLAB code was 0.5644 seconds per orientation, which equates to 24.08 mins in total for 80 iterations shown in Fig. 18. For comparison purpose, the bearing bracket was meshed by body fit mesh of the same element size (e.g. 1 mm) and the same number of computer cores using ANSYS v18.2. The computation cost was 6 s and so is 11 times longer than the proposed voxel mesh generation. This implies that the proposed voxel-based support structure detection and mesh generation is much faster than the body-fit mesh method and makes it desirable for support volume calculation and mesh generation for iterative optimization.

5.4.2.2 Study of the Design with Different Lattice Structure

In this sub-section, the single objective of minimizing maximum residual stress is performed based on different types of lattice structures given in Figure 5.10. The bearing bracket used in the previous case is utilized to compare the influence of microstructure of lattice structure on the optimal orientation for minimization of maximum stress. Note that the volume fraction of lattice structure is set to be $V^* = 0.3$ to ensure manufacturability. In the optimization, there are 18 particles uniformly distributed in the design domain (i.e. 6 points for $\theta \in [-\pi, \pi]$, and 3 points for $\phi \in [0, \pi]$). The goal of the optimization is to minimize the maximum residual stress through the adjustment of build orientation on the build tray. For comparison purpose, the stress distributions of bearing bracket with the support structure consisting of the three lattice structures at default position are illustrated in Figure 5.18(a-c). It can be seen that although the stress distributions are different, the larger stresses are mainly distributed at the bottom surface of support structure along the build tray, where most cracks are typically formed in the AM process. The maximum normalized residual stresses for three lattice structures are much higher than the yield strength of

unity (i.e. 1.71, 1.85 and 2.02, respectively). This can lead to severe delamination and warpage during the printing process.

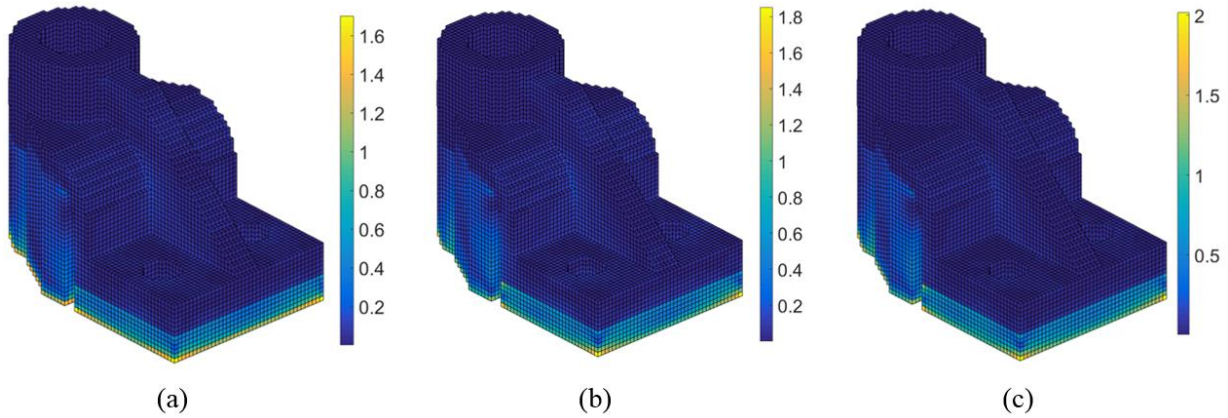

Figure 5.18: Normalized Stress Distribution of Bearing Bracket with Support Structure Consisting of Different Lattice Structure. (a) Cubic Lattice Structure,$\bar{\sigma}^{H}_{max} = 1.71$, (b) Diagonal Lattice Structure, $\bar{\sigma}^{H}_{max} = 1.85$ (c) Cross Lattice Structure, $\bar{\sigma}^{H}_{max} = 2.02$.

To examine the efficiency of the inherent strain method, the three designs with lattice structure as their support, as well as the design with default support structure provided by the Magics software are printed out for deformation observation. Figure 5.19 illustrates the CAD models of the four designs. It is noted that the design of support structure from the Magics software is the default setting with a volume fraction of 0.4.

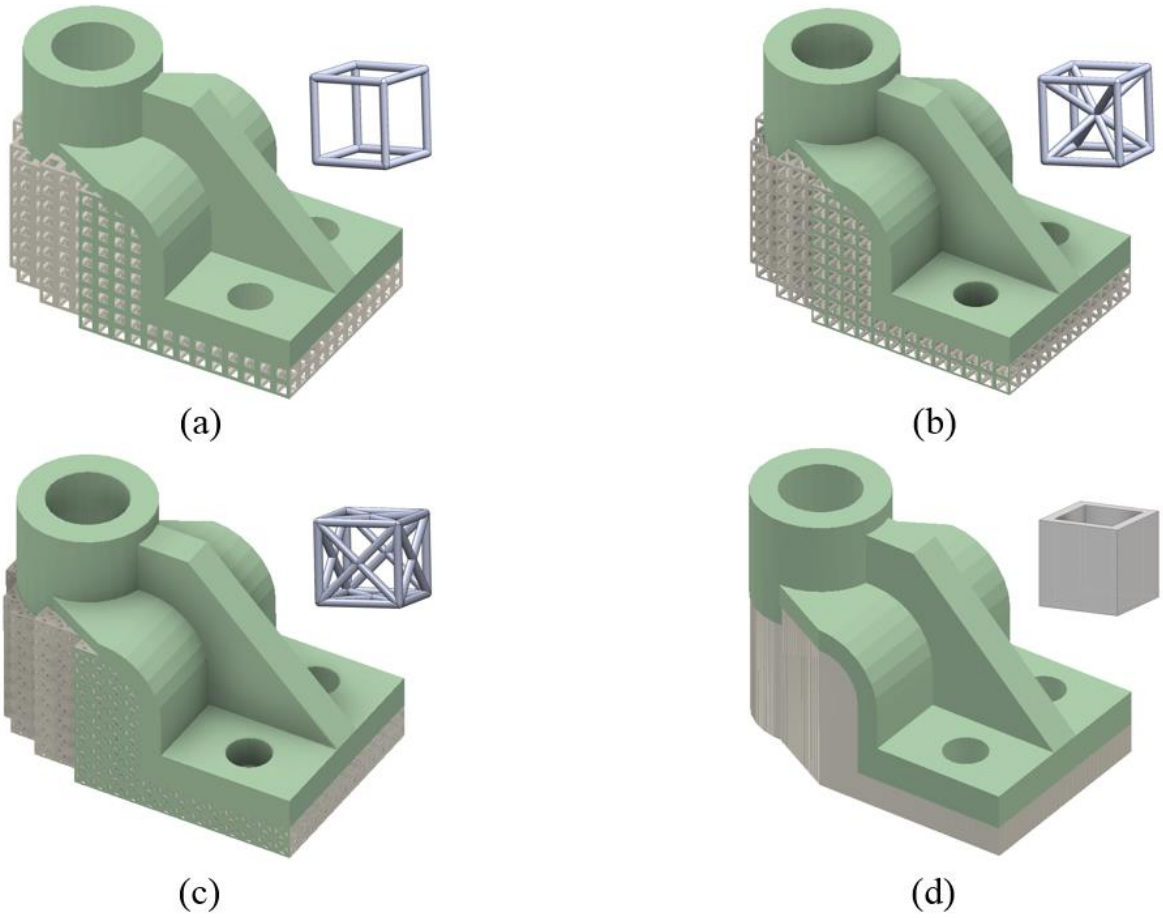

Figure 5.19: CAD Model of the Bearing Bracket with Support Structures for Printing Test: (a) Design of Cubic Lattice Support Structure (b) Design of Diagonal Lattice Support Structure (c) Design of Cross Lattice Support Structure (d) Design of Shell Wall Support Structure From Magic Software.

For validation purpose, the four designs in Fig. 20 were printed out and the samples are illustrated in Fig. 21. As shown in the figure, although the bearing brackets were "successfully" manufactured using powder-bed metal AM, cracks and large deformation are observed and highlighted by red box. Compared with the default support structure design from the Magics software, the designs with lattice structure support exhibit better performance for the deformation control. For instance, the support from the Magics software detaches from the build tray and has

severe cracks and delamination for the manufactured part, see Figure 5.20(b), while the design with lattice structure support shows relatively small deformation. On the other hand, although lattice support structure can significantly reduce the deformation of the part, warpages are observed at the bottom surface of the bracket around the corners of the horizontal plate. It is consistent with the stress distribution in Figure 5.18, where the maximum stress emerges near the corners of the bottom surface. This demonstrates that the proposed fast process modeling framework can provide good guidance to possible build failure for the laser powder-bed AM process.

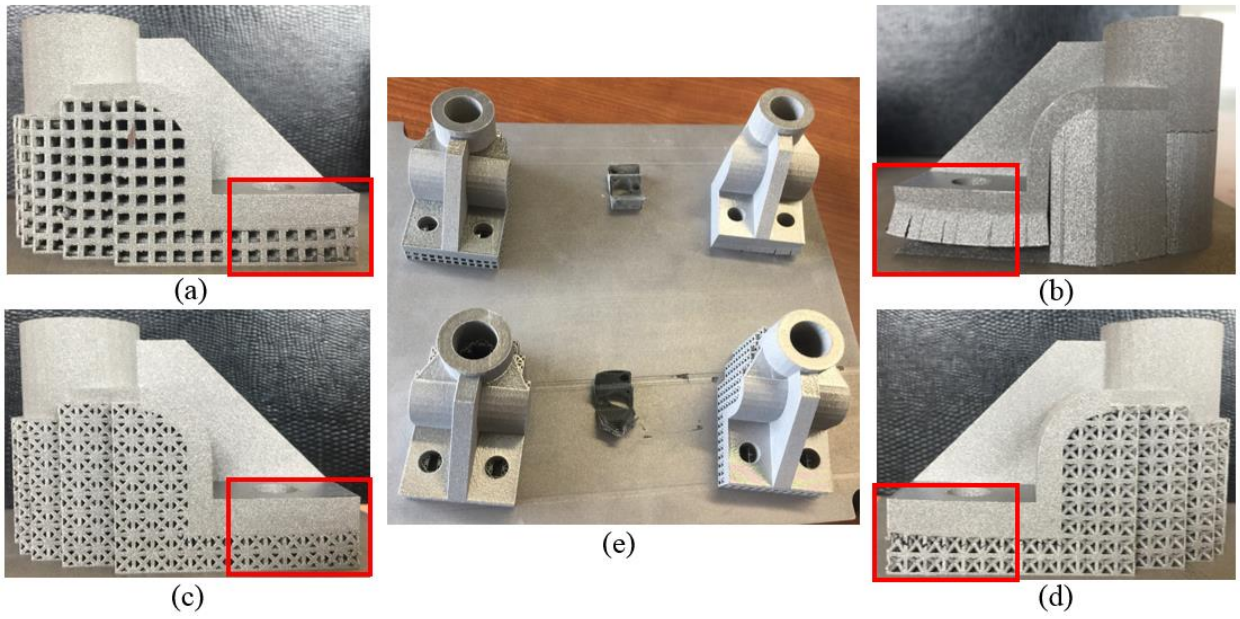

Figure 5.20: Printed Samples in Default Orientation with Different Support Structures: (a) Side View of the Bearing Bracket with Cubic Lattice Support Structure, (b) Side View of the Bearing Bracket with Shell Wall Support Structure, (c) Side View of the Bearing Bracket with Cross Lattice Support Structure (d) Side View of the Bearing Bracket with Diagonal Lattice Support Structure, (e) Front View of the Printed Bearing Bracket. Note that Cracks are Highlighted by Red Box in Figure (a-d).

The following task is to apply the proposed method to find an optimal orientation for the bearing bracket based on different lattice structure supports. The first test is the cubic lattice structure, whose geometry is given in Figure 5.10 (a). The material properties obtained from the homogenized model for elasticity and multiscale model for plasticity are applied to the support voxels in the analysis to calculate the maximum residual stress. The initial distribution of the maximum residual stress is plotted in Figure 5.21(a) and Figure 5.21 (b), respectively. It can be observed that the distribution is much difference from the support volume distribution given in Figure 5.17(a). This implies that there is a trade-off between support volume minimization and maximum residual stress minimization. Figure 5.21 (c) presents the convergence history of the optimization. The minimum value of the maximum normalized stress converges from 1.56 to 1.06 after 54 iterations with a reduction of 32.1%, while the bearing bracket is orientated at (θ,ϕ)=(-2.359, 0.08). The corresponding support volume in this orientation is 1.0212×10^4 mm^4, which is 3.224×10^3 mm^4 larger than the result of support volume optimization. The voxel-based mesh and the normalized stress distribution of the optimal design are given Figure 5.21 (d) and (e), respectively, while the realization of the support structure using cubic lattice structure is provided in Figure 5.21 (f) including the bottom view of the support. Compared with the optimal support volume in Figure 5.17(d), the cylindrical feature is rotated to the downward direction of the building direction and the part deviates a little along the build direction (i.e. $\varphi = 0.08$). The bottom view also illustrates this observation. Another interesting observation is that the optimization tends to orient the part with edge overhangs. This implies that edge overhang for cubic lattice structure may have smaller residual stress.

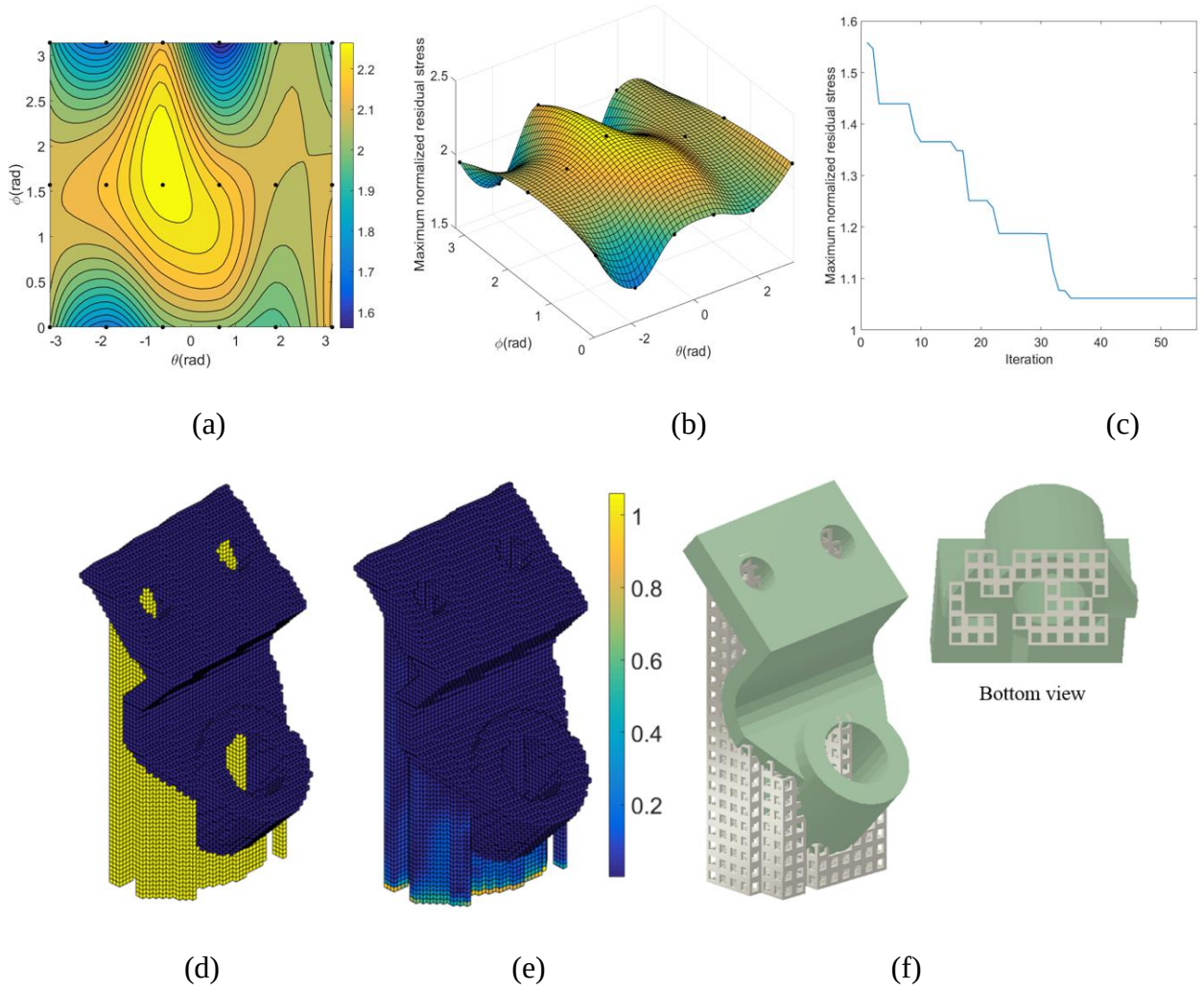

Figure 5.21: Orientation Optimization of Maximum Residual Stress Minimization for Bearing Bracket with Cubic Lattice Structure Support: (a) Contour Plot of the Initially Maximum Normalized Stress Distribution; (b) Surface Plot of the Initially Maximum Normalized Stress Distribution; (c) Convergence History of the Objective Function; (d) And (e) Optimal Orientation and the Corresponding Normalized Stress Distribution; (f) Optimal Orientation Design Reconstructed by Cubic Lattice Structure.

The second test lattice structure is the diagonal lattice structure, whose geometry is given in Figure 5.10(b). The optimization results for support structure consisting of diagonal lattice structure are illustrated in Figure 5.22. Due to the change of the lattice geometry, the initially

maximum residual stress distribution in Figure 5.22 (a) and (b) is different from the case of cubic lattice structure in Figure 5.22 (a) and (b), but the regions are much similar. The convergence history of the best objective function in each iteration is shown in Figure 5.22 (c). After 50 iterations, the best maximum normalized residual stress is reduced from 1.24 to 0.93, which is below the yield strength and a reduction of 25% after optimization. The bearing bracket is oriented in the direction (θ, ϕ)=(-2.343, 0.004) and the support volume is 3.288×10^4 mm^3. Due to the existence of the internal ligaments in the diagonal lattice structure, the optimal orientation and support volume are different from cubic lattice structure. The voxel-based mesh, normalized stress distribution and reconstruction for support structure design by diagonal lattice structure are given in Figure 5.22 (d-f), respectively. From the bottom view of reconstruction, the part is more straightforward compared with the cubic design (i.e. $\varphi = 0.004$).

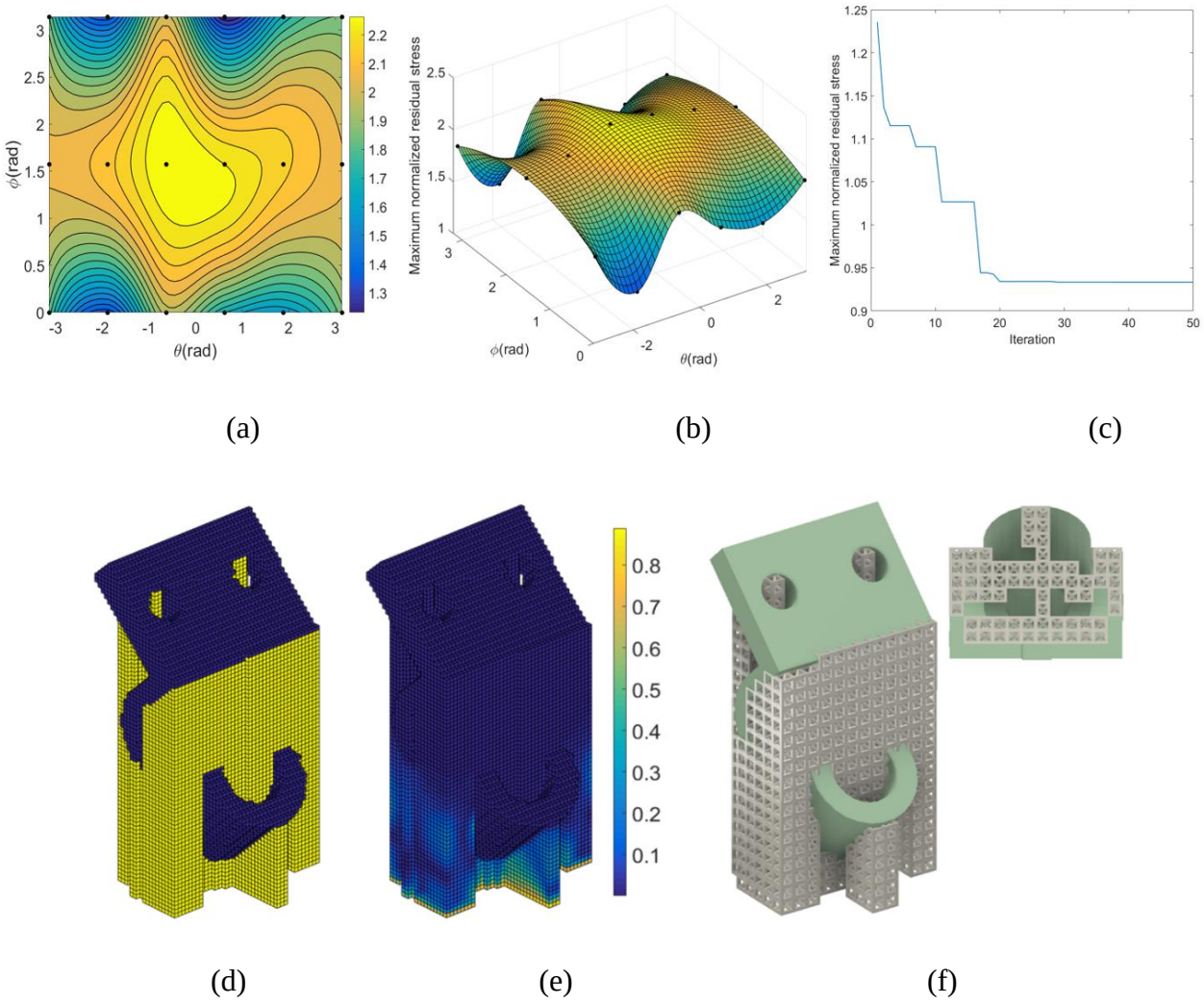

Figure 5.22: Orientation Optimization of Maximum Residual Stress Minimization for Bearing Bracket with Diagonal Lattice Structure Support: (a) Contour Plot of the Initially Maximum Normalized Stress Distribution; (b) Surface Plot of the Initially Maximum Normalized Stress Distribution; (c) Convergence History of the Objective Function; (d) and (e) Optimal Orientation and the Corresponding Normalized Stress Distribution; (f) Optimal Orientation Design Reconstructed by Diagonal Lattice Structure.

Again, the stress optimization is conducted on the build with support structure consisted of the cross-lattice structure. Compared with cubic lattice structure, twelve ligaments are added to the six faces of the cubic lattice structure, refer to Figure 5.10(c). The optimization results are

illustrated in Figure 5.23. The objective function converges from 1.48 to 1.16 after 37 iterations and the bracket is oriented in the direction (θ, ϕ)=(2.348, 0). The support volume at the optimal orientation is 3.007×10^4 mm^3. For comparison purpose, the optimization results of the three lattice structures are tabulated in Table 5.1. Based on the comparison, it can be concluded that the geometry of the lattice structure has a significant influence on the stress optimization, in which the diagonal lattice structure exhibits the best performance among the three lattice structures. By rotating the component, the maximum residual stress can be considerably reduced, but cannot guarantee the magnitude of the maximum stress is less than the yield strength. Moreover, the computational cost per orientation and the total cost are also tabulated in Table 5.1. It can be observed that the simulation time per orientation is 20.9 s while the total optimization cost varies with the change of lattice structure. Differentiating from the support volume minimization, stress analysis is much more time-consuming than the volume calculation due to the process of FCM analysis for residual stresses. The general computation cost of build orientation for bearing bracket is 3-5 hours using the in-house code. The computation cost should be acceptable to practicing designers and operators as typical complex parts take days to build by powder-bed process. To further accelerate the optimization, potential improvement can be achieved in the future by implementing the proposed method using a GPU-based platform.

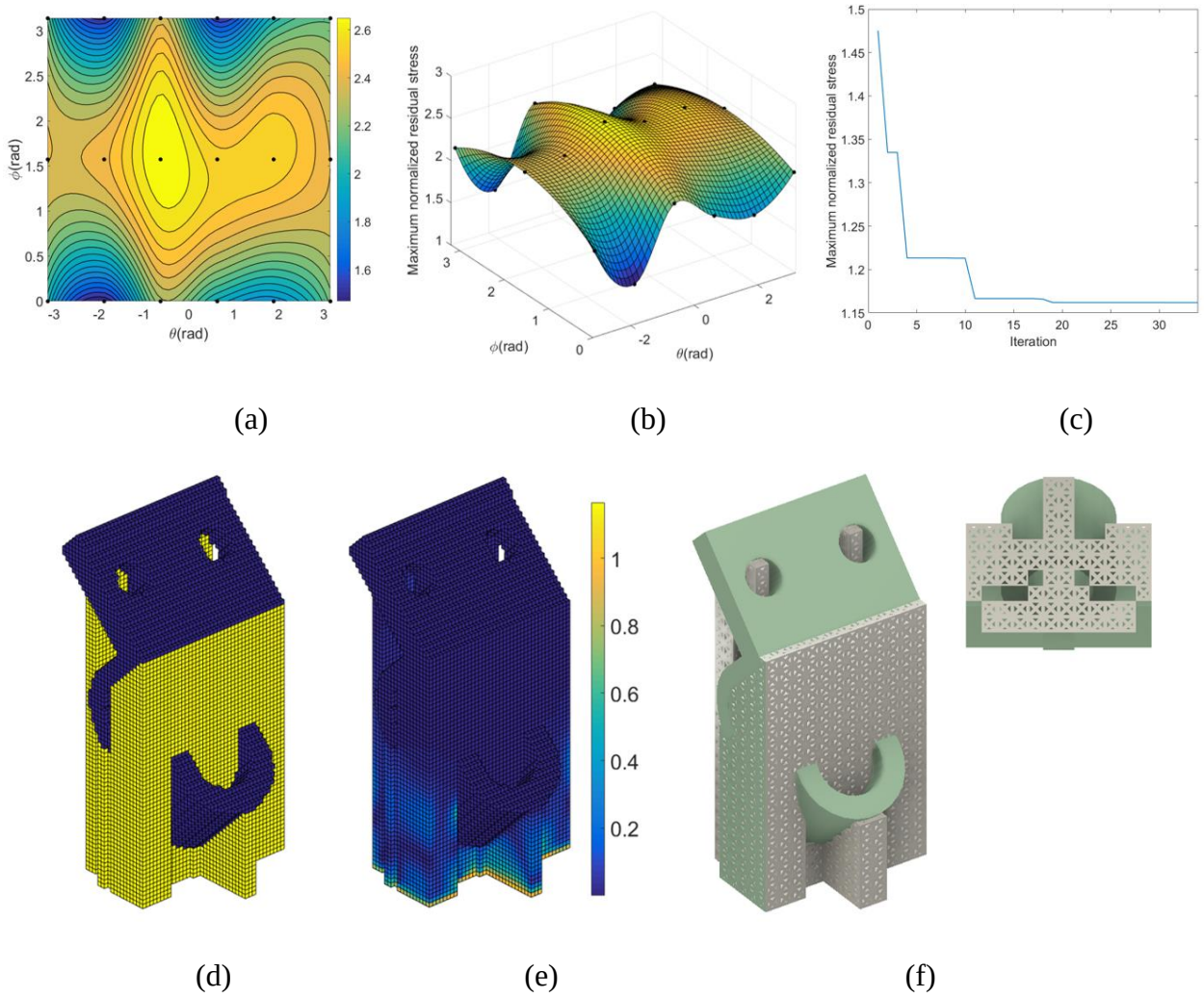

Figure 5.23: Orientation Optimization of Maximum Residual Stress Minimization for Bearing Bracket with Cross Lattice Structure Support. (a) Contour Plot of the Initially Maximum Stress Distribution; (b) Surface Plot of the Initially Maximum Stress Distribution; (c) Convergence History of the Objective Function; (d) and (e) Optimal Orientation and the Corresponding Normalized Stress Distribution; (f) Optimal Orientation Design Reconstructed by Cross Lattice Structure.

Table 5.1: Comparison of the Optimization Results of the Three Lattice Structure Types

	Cubic	Diagonal	Cross
Initially smallest maximum normalized stress	1.56	1.24	1.48
Optimized maximum normalized stress	1.06	0.93	1.16
Optimal orientation (ϕ, φ)	(-2.359, 0.08)	(-2.343, 0.004)	(2.348, 0)
Support volume of optimal orientation (mm^3)	1.0212×10^4	3.288×10^4	3.007×10^4
Total Iteration	54	50	37
Average computational cost per orientation (seconds)	20.9		
Total computational cost (hours)	5.62	5.21	3.85

To examine the performance of the proposed methodology, the three designs shown in Figure 5.21(f), Figure 5.22(f) and Figure 5.23(f) are printed out in Ti6Al4V using the EOS DMLS system. Compared with the samples shown in Figure 5.20, it can be observed in Figure 5.24 that all the three designs are successfully printed out without obvious deformation. This implies that although the maximum residual stress is larger than yield strength for cubic and cross lattice supports, the components can still be printed out successfully without obvious cracks. The photos also prove that the overhang detection and support structure generation are efficient for a given component.

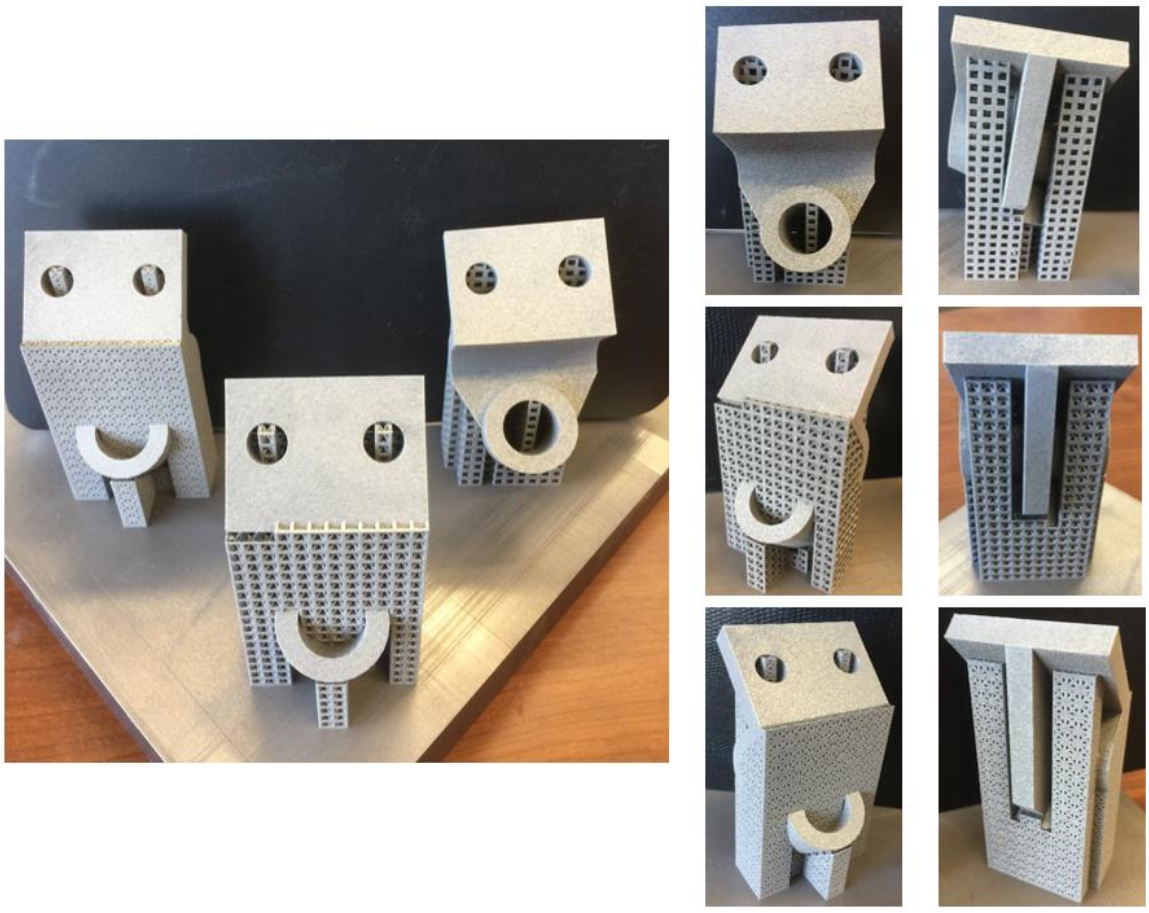

Figure 5.24: Photos of the printed-out bearing bracket with support structure consisted of three lattice structures.

5.4.2.3 Study of Multi-objective Optimization

In the previous two sections, a single objective function was developed to find a build orientation to minimize support volume or maximum residual stress. Minimizing both the support volume and maximum residual stress simultaneously may be more important for practical

applications, since support structure as a sacrificial structure is removed after the manufacturing. To compare with the previous results, the same bearing bracket is employed, and different weight factor, such as 0, 0.2, 0.4, 0.6, 0.8 and 1.0, in Eq. (5.1) is investigated. Note that diagonal lattice structure is used as the support material due to its good performance for stress minimization, and the volume fraction is set to be 0.3. There are eighteen particles initially distributed in the design domain. The PSO method [180] is employed to conduct the optimization to minimize the two objectives together.

The convergence history of the simultaneous optimization of support volume and maximum residual stress for different weight factors are illustrated in Figure 5.25. Table 5.2 tabulates the corresponding optimal values of the objectives and design variables. Both of the two objectives oscillate remarkably in the first 30 iterations and then converge to the optimal results. By comparing the two objectives with respect to a weight factor, it can be observed that as the weight factor is increased from 0 to 1, the maximum normalized residual stress increases from 0.9334 to 1.31, while the minimum support volume decreases from $3.29 \times 10^4 \text{mm}^3$ to $6.83 \times 10^3\ \text{mm}^3$. Especially, when $w = 0.4$ and $w = 0.6$, the support volume is on the same order as the minimum value, while the maximum residual stress is in the safe zone (i.e. less than yield strength). This implies that it is possible to orient a given component with prescribed lattice support to minimize the support volume, and at the same time ensure its manufacturability by minimizing the maximum residual stress below the material's yield strength.

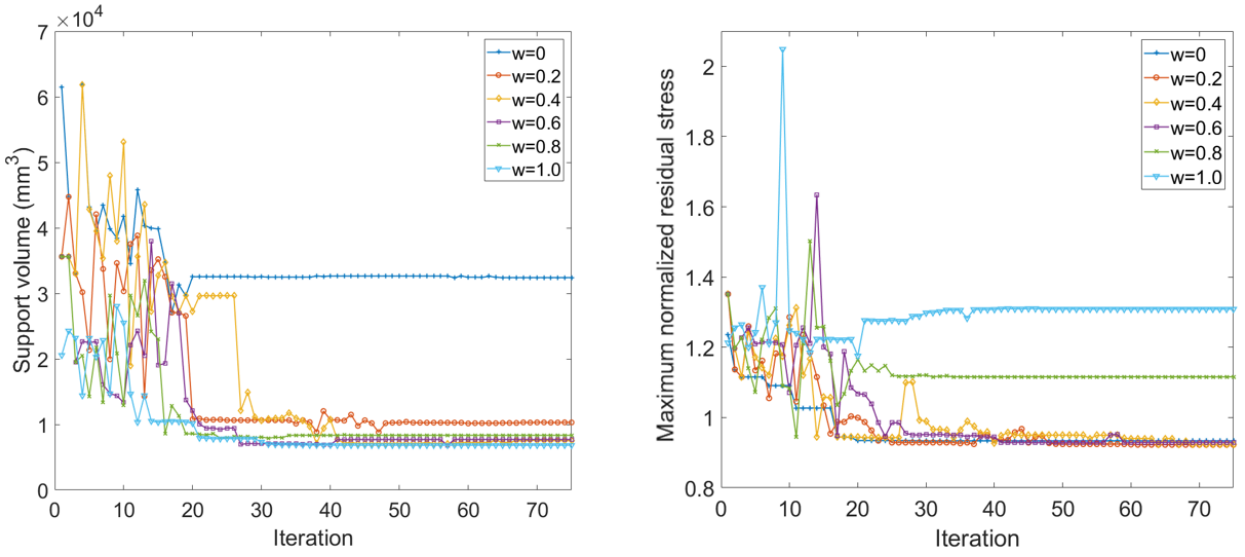

(a) (b)

Figure 5.25: Multi-Objective Optimization Results for Bearing Bracket by Considering both the Minimum Of Support Volume and the Maximum Residual Stress with Different Weight Factors. (a) Results of Support Volume; (b) Result of Maximum Normalized Residual Stress.

Table 5.2: Comparison of the Optimal Results for Different Weight Factors

	$w = 0$	$w = 0.2$	$w = 0.4$	$w = 0.6$	$w = 0.8$	$w = 1.0$
Optimal support volume (mm^3)	3.29×10^4	1.03×10^4	7.51×10^3	7.70×10^3	8.45×10^3	6.83×10^3
Maximum normalized residual stress	0.9334	0.9504	0.9546	0.9450	1.11	1.31
Optimal Orientation	$\theta = -2.343$ $\varphi = 0.004$	$\theta = -2.352$ $\varphi = 0.151$	$\theta = -2.372$ $\varphi = 0.187$	$\theta = 0.771,$ $\varphi = 2.954$	$\theta = -2.365$ $\varphi = 2.975$	$\theta = -2.356$ $\varphi = 3.130$

Figure 5.26 illustrates the build orientation of the bearing bracket after optimization using different weight factors. As the weight factor is increased from 0 to 1, and the weight of the stress objective becomes less important, the cylindrical feature is gradually rotated upward to achieve the minimum support volume. It is also proved that the orientation of the component plays an important role in the build of the component, especially the manufacturability for metal AM components. Figure 5.27 illustrates the normalized stress distribution with respect to the six build orientations shown in Figure 5.26. It can be observed that, when $w \leq 0.6$, the maximum normalized residual stress of the four optimal orientations is at the same level (e.g. 0.93~0.95), while for $w > 0.6$, the maximum normalized stress is larger than the yield strength (e.g. 1.1~1.3) and larger stresses are mainly distributed in the support structures under the edge overhang.

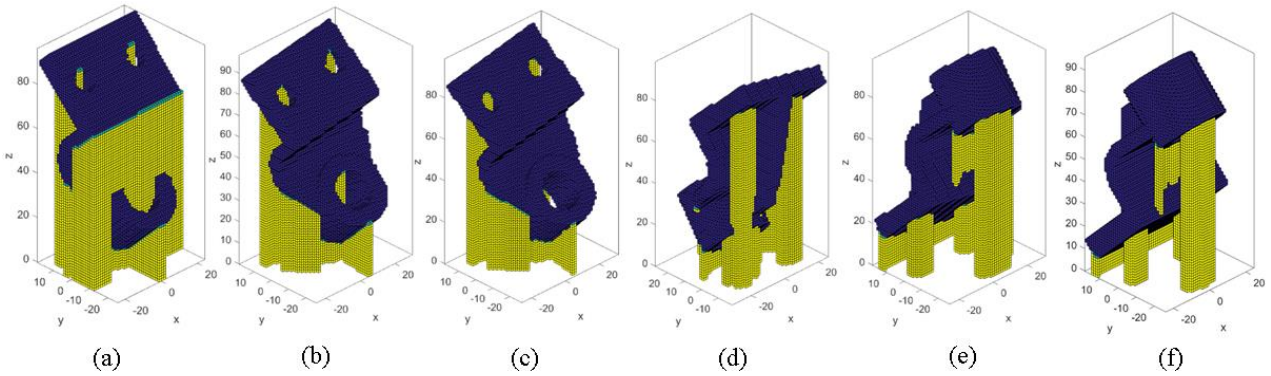

Figure 5.26: Optimal Results for Bear Bracket with Different Weight Factor. (a) Voxel-Based Design for $w = 0$; (b) Voxel-Based Design for $w = 0.2$; (c) Voxel-Based Design for $w = 0.4$; (d) Voxel-Based Design for $w = 0.6$; (e) Voxel-Based Design for $w = 0.8$; (f) Voxel-Based Design for $w = 1.0$.

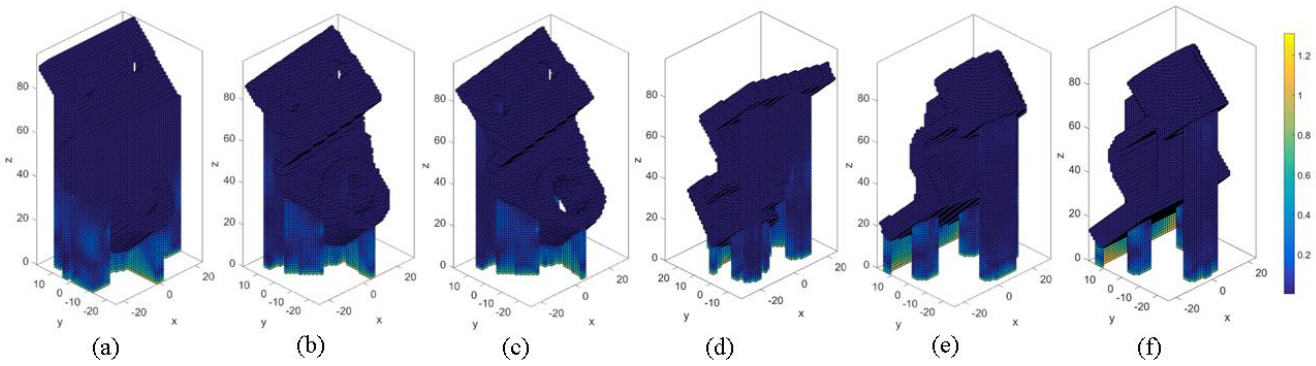

Figure 5.27: Normalized Residual Stress Results for Bear Bracket with Different Weight Factor. (a) Voxel-Based Design for $w = 0$; (b) Voxel-Based Design for $w = 0.2$; (c) Voxel-Based Design for $w = 0.4$; (d) Voxel-Based Design for $w = 0.6$; (e) Voxel-Based Design for $w = 0.8$; (f) Voxel-Based Design for $w = 1.0$.

5.4.3 Summary

In this work, a novel multi-objective optimization framework is proposed to automatically determine the optimal build orientation for complex components to minimize the support volume and maximum residual stress. First, a voxel-based methodology is employed to generate efficient Cartesian mesh for both bulk component and its support structure for FEA. Differentiating from previous works, a new overhang categorization scheme is developed to divide overhang voxels into three groups: Facet overhang, edge overhang, and point overhang. A benchmark is designed to illustrate the efficiency of the new voxel-based support generation method. Instead of using the default support structure from the Magics software, cubic lattice structures, such as simple cubic lattice structure, diagonal lattice structure and cross lattice structure, are used to investigate the influence of the lattice structure type on the orientation optimization. Due to its self-supporting and open-cell nature, lattice structure is an ideal structure for support structure design. The AH method and a multiscale model are employed to compute both the effective elastic and plastic

properties. This avoids expensive computational cost to implementation of lattice structure for FEA. Second, the inherent strain method is used to efficiently perform analysis to compute the residual stress for the component printed by powder-bed metal AM. To avoid the mesh generation in the optimization iterations, the voxel-based Cartesian mesh is used to discretize the design domain of a given component and solve the problem. The fictitious domain method (i.e. finite cell method) is used to conduct the analysis. Finally, a multi-objective optimization framework is proposed to find the optimal build orientation for a component with minimum support volume and/or maximum residual stress. Several numerical examples are studied to examine the performance of the optimization. First, we compare the new method with previous methods for support volume minimization. Second, the single objective of minimizing the maximum residual stress is performed for the realistic component with three different types of lattice structures. It is found that the geometry of lattice structure plays an important role in the optimal orientation for stress minimization. The diagonal lattice structure exhibits the best performance among the lattices that also include simple cubic lattice structure and cross lattice structure. In particular, the three designs are successfully printed out, which further demonstrate the efficiency of the proposed method. Third, multi-objective optimization for support volume and weight is conducted to the same component. It is observed that it is possible to achieve minimization of support volume while limiting the maximum residual stress under yield strength by selecting appropriate lattice structure.

5.5 Support Structure Optimization

5.5.1 Problem Formulation

The mathematical problem of optimizing the design of support structure for metal AM is described below. As shown in Figure 5.28, suppose an AM part were to be built on a build tray with support structure underneath the long overhang. The entire domain can be divided into three sub domains: Build tray Ω_t, support structure Ω_s, and bulk component Ω_c. The bulk component is anchored onto the build tray by support structure. The goal of the optimization is to design the material distribution in support structure domain Ω_s to prevent residual stress induced build failure. Support structure has been widely used in metal AM techniques to provide mechanical fixture and heat dissipation to ensure manufacturability and is removed as sacrificial materials once AM builds are completed. Hence a reasonable objective for support design optimization is to minimize the overall mass of sacrificial support structure while constraining the maximum stress in domain Ω_s and Ω_c under the allowable stress. Note that the mass of the support domain will not completely vanish after optimization using the proposed objective. This is because the support domain connects the bulk component a build tray, and the bulk component is subjected to body loading of inherent strains, which remain unchanged during optimization. Hence the material distribution would tend to decrease from very high density near the bulk component toward lower density away from it. To reduce computation time in this optimization problem, we only consider the residual stress distribution after the entire part is done printing. The optimization is performed to iteratively update the density distribution in the support domain Ω_s until the stress constraint in domain $\Omega_s + \Omega_c$ is satisfied.

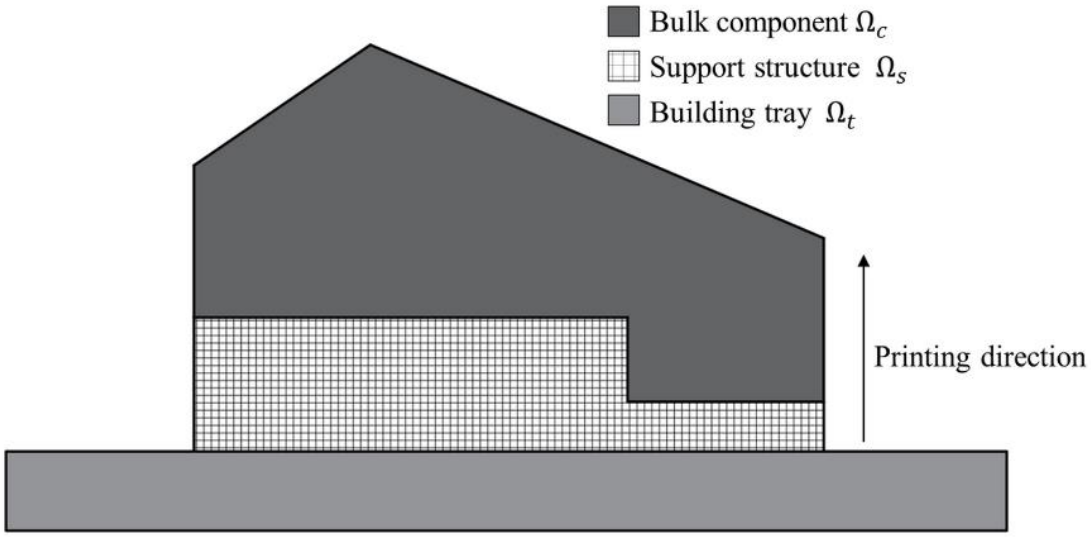

Figure 5.28: Domain of an AM Build

Based on the above discussion, the optimization problem for support structure design can be expressed mathematically as:

$$minimize \quad m(\boldsymbol{\rho}) = \sum_{e=1}^{N} \rho_e v_e \tag{5.3}$$

$$w.r.t \qquad \rho_e$$

$$such\ that \begin{cases} \mathbf{KU} = \mathbf{F}^{in} \\ \overline{\boldsymbol{C}} = \overline{\boldsymbol{C}}(\boldsymbol{\rho}) \\ \sigma_{max}^{H}(\boldsymbol{\rho}) \leq 1, \\ \underline{\rho} \leq \rho_e \leq \overline{\rho}, \quad e = 1, \dots, N \end{cases} \tag{5.4}$$

where $m(\boldsymbol{\rho})$ is the objective function of the optimization problem and represents the total mass of the support structure. **K**, **U** and $\mathbf{F}^{in}$ in the equilibrium equation denote the stiffness matrix, global displacement and prescribed loading, respectively. ρ_e is the relative density of element e, and v_e is the corresponding elemental volume. The design variable ρ_e is limited by the upper bound $\overline{\rho}$

and lower bound $\underline{\rho}$. $\overline{\boldsymbol{C}} = \overline{\boldsymbol{C}}(\boldsymbol{\rho})$ represents elastic model of the support structure. σ_{max}^{H} denotes the maximum stress of the entire domain, and N is the number of elements in the support domain. It is noted that the stress measure in this work is modified Hill's criterion [182]. Without losing the generality, the stress illustrated below is normalized by material's yield strength, which means that when the value of stress is larger than 1, plastic deformation occurs in the material while when the stress is smaller than 1, the stress state is elastic. To solve the optimization problem in Eq. (5.3)-(5.4), the P-norm stress [43, 44, 183, 184] is applied for the maximum residual stress constrain, the sensitivity analysis is performed for both objective function and its constrains, and the Method of Moving Asymptotes (MMA) [118, 123] is employed to obtain the optimal design.

5.5.2 Sensitivity Analysis

The optimization problem for designing support structure proposed in Eq. (5.3)-(5.4) is solved by the Method of Moving Asymptotes (MMA) proposed by Svanberg [124], in which the first order derivative of the objective function and constraints are required. The following gives the sensitivity analysis of objective function and stress constraints. The first derivative of the objective function is

$$\frac{\partial m(\boldsymbol{\rho})}{\partial \rho_e} = v_e \tag{5.5}$$

The first order derivative of stress constraint to relative density in Eq. (5.4) is

$$\frac{\partial \sigma^{PN}}{\partial \rho_e} = \sum\nolimits_{e=1}^{N} \frac{\partial \sigma^{PN}}{\partial \bar{\sigma}_e^H} \frac{\partial \bar{\sigma}_e^H}{\partial \rho_e} \tag{5.6}$$

The first term in the right-hand side of Eq. (5.6) can be calculated based on the *P*-norm proposed in [183] as:

$$\frac{\partial \sigma^{PN}}{\partial \bar{\sigma}_e^H} = \left(\sum\nolimits_{e=1}^{N} (\bar{\sigma}_e^H)^P\right)^{\left(\frac{1}{P}-1\right)} (\bar{\sigma}_e^H)^{(P-1)} \tag{5.7}$$

The second derivative in the right-hand side of Eq. (5.6) can be calculated as:

$$\begin{aligned}\frac{\partial \bar{\sigma}_e^H}{\partial \rho_e} &= \frac{\partial\left\{\left[\left(\bar{\boldsymbol{\varepsilon}}-\epsilon\boldsymbol{\varepsilon}^{in}\right)^T \mathbb{R}\left(\bar{\boldsymbol{\varepsilon}}-\epsilon\boldsymbol{\varepsilon}^{in}\right)\right]^{\frac{1}{2}}\right\}}{\partial \rho_e} = \frac{1}{2}\left[\left(\bar{\boldsymbol{\varepsilon}}-\epsilon\boldsymbol{\varepsilon}^{in}\right)^T \mathbb{R}\left(\bar{\boldsymbol{\varepsilon}}-\epsilon\boldsymbol{\varepsilon}^{in}\right)\right]^{-\frac{1}{2}} \frac{\partial\left[\left(\bar{\boldsymbol{\varepsilon}}-\epsilon\boldsymbol{\varepsilon}^{in}\right)^T \mathbb{R}\left(\bar{\boldsymbol{\varepsilon}}-\epsilon\boldsymbol{\varepsilon}^{in}\right)\right]}{\partial \rho_e} \\ &= \frac{1}{2\bar{\sigma}_e^H}\left(2\left(\bar{\boldsymbol{\varepsilon}}-\epsilon\boldsymbol{\varepsilon}^{in}\right)^T \mathbb{R}\frac{\partial\left(\bar{\boldsymbol{\varepsilon}}-\epsilon\boldsymbol{\varepsilon}^{in}\right)}{\partial \rho_e} + \left(\bar{\boldsymbol{\varepsilon}}-\epsilon\boldsymbol{\varepsilon}^{in}\right)^T \frac{\partial \mathbb{R}}{\partial \rho_e}\left(\bar{\boldsymbol{\varepsilon}}-\epsilon\boldsymbol{\varepsilon}^{in}\right)\right)\end{aligned} \tag{5.8}$$

where $\mathbb{R}$ is the tensor used to formulate yield strength of lattice structure by using the constitutive model and the yield strength tensor, which can be formulated as $\mathbb{R} = \bar{\boldsymbol{C}}^{\boldsymbol{T}}\mathbb{M}\bar{\boldsymbol{C}}$ and $\mathbb{M}$ represents the plastic constants matrix, and $\bar{\boldsymbol{C}}$ denotes the constitutive model. More details about these two matrixes refer to [162]. Since the macroscopic strain $\bar{\boldsymbol{\varepsilon}}$ can be expressed as $\bar{\boldsymbol{\varepsilon}} = \boldsymbol{B}\mathbf{U}$, where $\boldsymbol{B}$ denotes the strain-displacement matrix while $\mathbf{U}$ is the displacement vector. Thus, the first term in Eq. (A8) can be expressed as:

$$\begin{aligned}2\left(\bar{\boldsymbol{\varepsilon}}-\epsilon\boldsymbol{\varepsilon}^{in}\right)^T \mathbb{R}\frac{\partial\left(\bar{\boldsymbol{\varepsilon}}-\epsilon\boldsymbol{\varepsilon}^{in}\right)}{\partial \rho_e} &= 2\left(\bar{\boldsymbol{\varepsilon}}-\epsilon\boldsymbol{\varepsilon}^{in}\right)^T \mathbb{R}\left(\frac{\partial(\boldsymbol{BU})}{\partial \rho_e} - \frac{\partial \epsilon}{\partial \rho_e}\boldsymbol{\varepsilon}^{in}\right) \\ &= 2\left(\bar{\boldsymbol{\varepsilon}}-\epsilon\boldsymbol{\varepsilon}^{in}\right)^T \mathbb{R}\left(\boldsymbol{B}\frac{\partial \boldsymbol{U}}{\partial \rho_e} - \frac{\partial \epsilon}{\partial \rho_e}\boldsymbol{\varepsilon}^{in}\right)\end{aligned} \tag{5.9}$$

While the second term can be expressed as:

$$\left(\bar{\boldsymbol{\varepsilon}}-\epsilon\boldsymbol{\varepsilon}^{in}\right)^T \frac{\partial \mathbb{R}}{\partial \rho_e}\left(\bar{\boldsymbol{\varepsilon}}-\epsilon\boldsymbol{\varepsilon}^{in}\right) = \left(\bar{\boldsymbol{\varepsilon}}-\epsilon\boldsymbol{\varepsilon}^{in}\right)^T \left(2\bar{\boldsymbol{C}}^{\boldsymbol{T}}\mathbb{M}\frac{\partial \bar{\boldsymbol{C}}}{\partial \rho_e} + \bar{\boldsymbol{C}}^{\boldsymbol{T}}\frac{\partial \mathbb{M}}{\partial \rho_e}\bar{\boldsymbol{C}}\right)\left(\bar{\boldsymbol{\varepsilon}}-\epsilon\boldsymbol{\varepsilon}^{in}\right) \tag{5.10}$$

Substituting Eq. (5.9) and Eq. (5.10) into Eq. (5.8) yields

$$\frac{\partial \bar{\sigma}_e^H}{\partial \rho_e} = \frac{1}{2\bar{\sigma}_e^H}\Bigg(2\left(\bar{\boldsymbol{\varepsilon}} - \epsilon\boldsymbol{\varepsilon}^{in}\right)^T \mathbb{R}\left(\boldsymbol{B}\frac{\partial \boldsymbol{U}}{\partial \rho_e} - \frac{\partial \epsilon}{\partial \rho_e}\boldsymbol{\varepsilon}^{in}\right) + \left(\bar{\boldsymbol{\varepsilon}} - \epsilon\boldsymbol{\varepsilon}^{in}\right)^T \left(2\bar{\boldsymbol{C}}^{\boldsymbol{T}}\mathbb{M}\frac{\partial \bar{\boldsymbol{C}}}{\partial \rho_e} + \bar{\boldsymbol{C}}^{\boldsymbol{T}}\frac{\partial \mathbb{M}}{\partial \rho_e}\bar{\boldsymbol{C}}\right)\left(\bar{\boldsymbol{\varepsilon}} - \epsilon\boldsymbol{\varepsilon}^{in}\right)\Bigg) \tag{5.11}$$

Substituting Eq. (5.7) and Eq. (5.11) into Eq. (5.6), the sensitivity of the *P*-norm stress can be computed as:

$$\begin{aligned}\frac{\partial \sigma^{PN}}{\partial \rho_e} &= \sum_{e=1}^N \Bigg\{\left(\sum_{e=1}^N (\bar{\sigma}_e^H)^P\right)^{\left(\frac{1}{P}-1\right)} (\bar{\sigma}_e^H)^{(P-1)} \Bigg[\frac{1}{2\bar{\sigma}_e^H}\Bigg(2\left(\bar{\boldsymbol{\varepsilon}} - \epsilon\boldsymbol{\varepsilon}^{in}\right)^T \mathbb{R}\left(\boldsymbol{B}\frac{\partial \mathbf{U}}{\partial \rho_e} - \frac{\partial \epsilon}{\partial \rho_e}\boldsymbol{\varepsilon}^{in}\right) + \left(\bar{\boldsymbol{\varepsilon}} - \epsilon\boldsymbol{\varepsilon}^{in}\right)^T \left(2\bar{\boldsymbol{C}}^{\boldsymbol{T}}\mathbb{M}\frac{\partial \bar{\boldsymbol{C}}}{\partial \rho_e} + \bar{\boldsymbol{C}}^{\boldsymbol{T}}\frac{\partial \mathbb{M}}{\partial \rho_e}\bar{\boldsymbol{C}}\right)\left(\bar{\boldsymbol{\varepsilon}} - \epsilon\boldsymbol{\varepsilon}^{in}\right)\Bigg)\Bigg]\Bigg\} \\ &= \sum_{e=1}^N \left[\left(\sum_{e=1}^N (\bar{\sigma}_e^H)^P\right)^{\left(\frac{1}{P}-1\right)} (\bar{\sigma}_e^H)^{(P-2)}\left(\bar{\boldsymbol{\varepsilon}} - \epsilon\boldsymbol{\varepsilon}^{in}\right)^T \mathbb{R}\left(\boldsymbol{B}\frac{\partial \mathbf{U}}{\partial \rho_e} - \frac{\partial \epsilon}{\partial \rho_e}\boldsymbol{\varepsilon}^{in}\right)\right] \\ &+ \frac{1}{2}\sum_{e=1}^N \left[\left(\sum_{e=1}^N (\bar{\sigma}_e^H)^P\right)^{\left(\frac{1}{P}-1\right)} (\bar{\sigma}_e^H)^{(P-2)}\left(\bar{\boldsymbol{\varepsilon}} - \epsilon\boldsymbol{\varepsilon}^{in}\right)^T \left(2\bar{\boldsymbol{C}}^{\boldsymbol{T}}\mathbb{M}\frac{\partial \bar{\boldsymbol{C}}}{\partial \rho_e} + \bar{\boldsymbol{C}}^{\boldsymbol{T}}\frac{\partial \mathbb{M}}{\partial \rho_e}\bar{\boldsymbol{C}}\right)\left(\bar{\boldsymbol{\varepsilon}} - \epsilon\boldsymbol{\varepsilon}^{in}\right)\right]\end{aligned} \tag{5.12}$$

Based on the equilibrium equation, the derivative of $\frac{\partial \mathbf{U}}{\partial \rho_e}$ can be calculated using the equilibrium equation as:

$$\frac{\partial \mathbf{U}}{\partial \rho_e} = \mathbf{K}^{-1}\frac{\partial \mathbf{F}^{in}}{\partial \rho_e} - \mathbf{K}^{-1}\frac{\partial \mathbf{K}}{\partial \rho_e}\mathbf{U} \tag{5.13}$$

Substituting Eq. (5.13) into the first term of Eq. (5.12), one can obtain

$$\begin{aligned}\frac{\partial \sigma^{PN}}{\partial \rho_e} &= \sum_{e=1}^N \left[\left(\sum_{e=1}^N (\bar{\sigma}_e^H)^P\right)^{\left(\frac{1}{P}-1\right)} (\bar{\sigma}_e^H)^{(P-2)}\left(\bar{\boldsymbol{\varepsilon}} - \epsilon\boldsymbol{\varepsilon}^{in}\right)^T \mathbb{R}\left(\boldsymbol{B}\mathbf{K}^{-1}\left(\frac{\partial \mathbf{F}^{in}}{\partial \rho_e} - \frac{\partial \mathbf{K}}{\partial \rho_e}\mathbf{U}\right) - \frac{\partial \epsilon}{\partial \rho_e}\boldsymbol{\varepsilon}^{in}\right)\right] + \frac{1}{2}\sum_{e=1}^N \left[\left(\sum_{e=1}^N (\bar{\sigma}_e^H)^P\right)^{\left(\frac{1}{P}-1\right)} (\bar{\sigma}_e^H)^{(P-2)}\left(\bar{\boldsymbol{\varepsilon}} - \epsilon\boldsymbol{\varepsilon}^{in}\right)^T \left(2\bar{\boldsymbol{C}}^{\boldsymbol{T}}\mathbb{M}\frac{\partial \bar{\boldsymbol{C}}}{\partial \rho_e} + \bar{\boldsymbol{C}}^{\boldsymbol{T}}\frac{\partial \mathbb{M}}{\partial \rho_e}\bar{\boldsymbol{C}}\right)\left(\bar{\boldsymbol{\varepsilon}} - \epsilon\boldsymbol{\varepsilon}^{in}\right)\right]\end{aligned} \tag{5.14}$$

An adjoint variable $\boldsymbol{\lambda}$ is introduced to solve the sensitivity of the first term, and its definition is

$$\boldsymbol{\lambda}^{\boldsymbol{T}} = \sum_{e=1}^{N}\left(\sum_{e=1}^{N}(\bar{\sigma}_e^H)^P\right)^{\left(\frac{1}{P}-1\right)}(\bar{\sigma}_e^H)^{(P-2)}\left(\bar{\boldsymbol{\varepsilon}} - \epsilon\boldsymbol{\varepsilon}^{in}\right)^T \mathbb{R}\boldsymbol{B}\mathbf{K}^{-1} \tag{5.15}$$

The adjoint variable $\boldsymbol{\lambda}$ can thus be computed by solving the following adjoint equation

$$\mathbf{K}\boldsymbol{\lambda} = \sum_{e=1}^{N}\left(\sum_{e=1}^{N}(\bar{\sigma}_e^H)^P\right)^{\left(\frac{1}{P}-1\right)}(\bar{\sigma}_e^H)^{(P-2)}\mathbb{R}\boldsymbol{B}\left(\bar{\boldsymbol{\varepsilon}} - \epsilon\boldsymbol{\varepsilon}^{in}\right) \tag{5.16}$$

Once the adjoint variable is obtained, the sensitivity of the *P*-norm stress constraint in Eq. (5.14) yields

$$\begin{aligned}\frac{\partial\sigma^{PN}}{\partial\rho_e} = \boldsymbol{\lambda}^{\boldsymbol{T}}\left(\frac{\partial\mathbf{F}^{in}}{\partial\rho_e} - \frac{\partial\mathbf{K}}{\partial\rho_e}\mathbf{U}\right) - \sum_{e=1}^{N}\Bigg[\left(\sum_{e=1}^{N}(\bar{\sigma}_e^H)^P\right)^{\left(\frac{1}{P}-1\right)}(\bar{\sigma}_e^H)^{(P-2)}\Big(\bar{\boldsymbol{\varepsilon}} - \\ \epsilon\boldsymbol{\varepsilon}^{in}\Big)^T\mathbb{R}\frac{\partial\epsilon}{\partial\rho_e}\boldsymbol{\varepsilon}^{in}\Bigg] + \frac{1}{2}\sum_{e=1}^{N}\Bigg[\left(\sum_{e=1}^{N}(\bar{\sigma}_e^H)^P\right)^{\left(\frac{1}{P}-1\right)}(\bar{\sigma}_e^H)^{(P-2)}\left(\bar{\boldsymbol{\varepsilon}} - \epsilon\boldsymbol{\varepsilon}^{in}\right)^T\left(2\overline{\boldsymbol{C}}^{\boldsymbol{T}}\mathbb{M}\frac{\partial\overline{\boldsymbol{C}}}{\partial\rho_e} + \\ \overline{\boldsymbol{C}}^{\boldsymbol{T}}\frac{\partial\mathbb{M}}{\partial\rho_e}\overline{\boldsymbol{C}}\right)\left(\bar{\boldsymbol{\varepsilon}} - \epsilon\boldsymbol{\varepsilon}^{in}\right)\Bigg]\end{aligned} \tag{5.17}$$

The sensitivities in Eqs. (5.5) and (5.17) are implemented in the MMA method and are used for the lattice structure topology optimization for support structure design.

5.5.3 Lattice Structure Topology Optimization for Support Structure Design

Another barrier concerning the support design optimization problem stated in Eqs. (5.3)-(5.4) is that designs obtained by conventional topology optimization (TO) may include a large number of long overhangs and closed-void structures [185], which lead to manufacturability issues and trapped powders. To address these issues, graded lattice structure topology optimization (LSTO) is employed to design the support structure instead of conventional TO. The key feature of lattice structure is its self-supporting and open-celled nature when the bridge span and strut size

are chosen appropriately for the AM process and material of interest. This makes lattice structure ideal for support structure design, since it can be printed out without support structure while the trapped powder can be easily removed. The LSTO method utilizes homogenized model to gain efficiency and has been applied to determine the layout of graded lattice structure for various problems, such as minimum compliance [135, 186], natural frequency [136], and heat conduction [108, 187]. In this work, the LSTO method with the objective of mass minimization under maximum stress constraint is employed for support structure design. As shown in Figure 5.29, for a given component shown in Figure 5.29(a), an overhang detection method [148, 149] is first applied to obtain support structure domain Ω_s for optimization. Instead of infilling support structure domain with block shell support, variable-density lattice structure (see Figure 5.29(b)) obtained from LSTO is used to provide mechanical fixture, dissipate heat, as well as guarantee the manufacturability. The details of the constrained stress optimization algorithm under the LSTO framework can be found in Ref. [182, 188] for interested readers. With regard the overhang detection, this work categorizes overhang features into three groups: facet overhang, edge overhang and point overhang, to ensure accuracy of formation for support structure domain. For instance, in Figure 5.29 (d), the overhang edges on the bottom surface of the oriented component are automatically detected, and the corresponding lattice structure supports are generated after optimization.

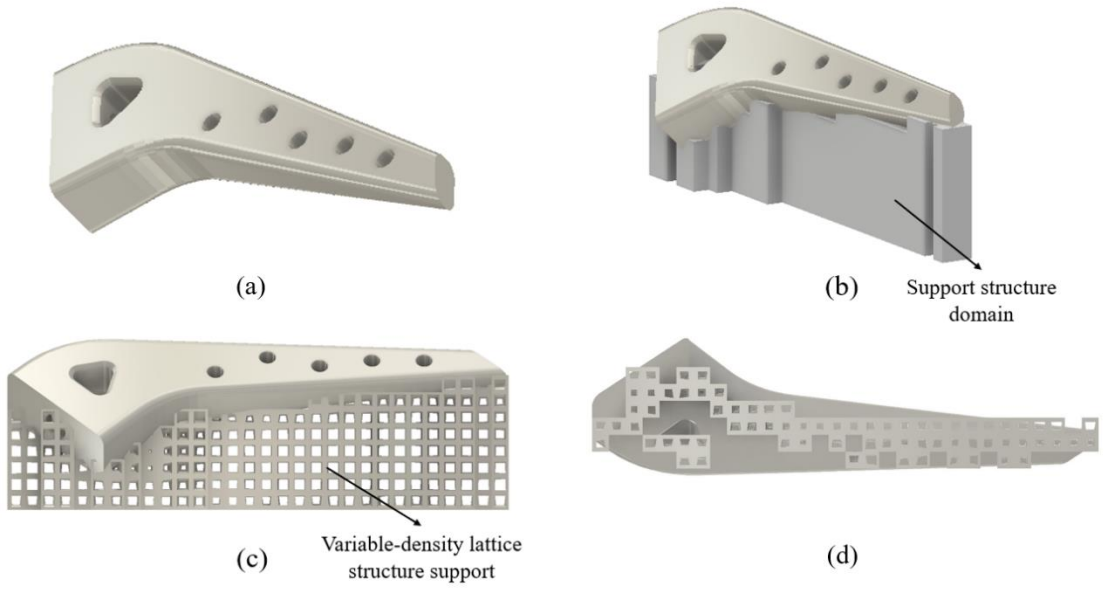

Figure 5.29: Support Structure Design by the LSTO Method: (a) Component, (b) Component with Bulk Support, and (c) Component with Optimized Variable-Density Lattice Structure Support, (d) Bottom View of the Optimized Support Structure for the Component.

5.5.4 Finite Cell Method for Modified Inherent Strain Method

The unique feature of AM technology is its ability to manufacture geometrically complex components naturally with no additional tooling required. Nevertheless, mesh generation for such complex component and its support structure and build tray is computationally expensive and often error-prone. To simplify the mesh generation for complex geometry, the finite cell method (FCM) is employed to perform inherent strain-based analysis to obtain residual stress distribution for an AM build. The FCM, as a type of fictitious domain method, was first proposed by Parvizian et al. [158] in 2007. The underlying principle of FCM [158, 177, 189] is to immerse the material domain of interest into a larger one, and a favorable Cartesian grid can thus be generated to avoid time-

consuming and error-prone mesh generation. It has been successfully applied to solve a wide-range of problems, such as non-linear analysis [153], transport problem in porous media [176], biomechanical analysis [177, 178], etc.

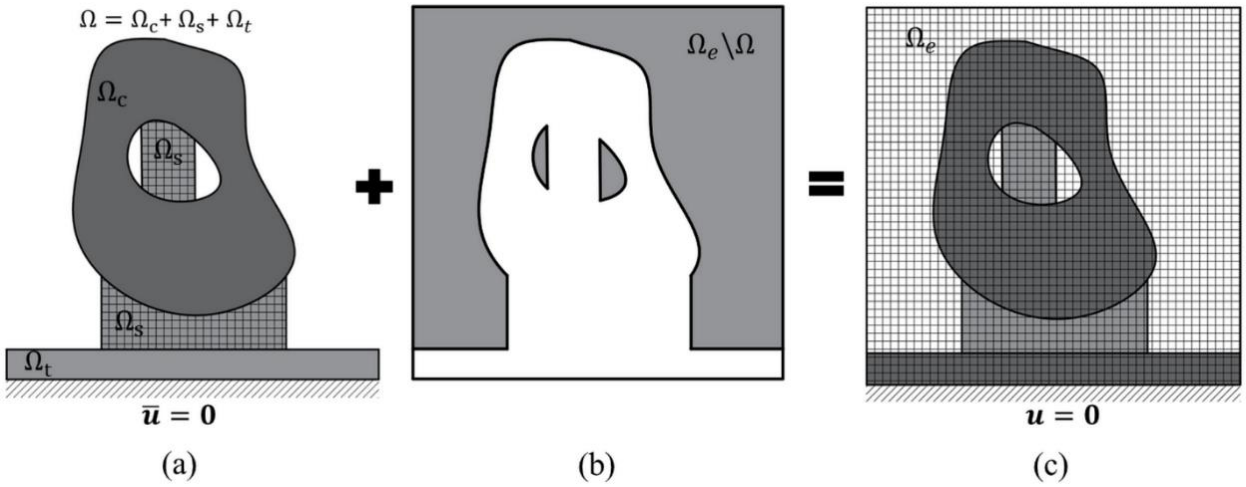

Figure 5.30: The Domain Ω in Powder-Bed AM is Embedded in a Voxel-Based Domain Ω_e: (a) Domain of Printed Component, Which is the Combination by Three Subdomains: Bulk Component Domain Ω_c, Support Structure Domain Ω_s, and Build Tray Domain Ω_t; (b) Fictitious Domain, and (c) Embedding Domain Ω_e.

In the context of inherent strain analysis of an AM build, the domain of the build shown in Figure 5.30 is embedded into a larger domain based on FCM, and its boundary conditions are depicted in Figure 5.30(c). The domain of computation Ω is the combination of three subdomains: Bulk component domain Ω_c, support structure domain Ω_s, and build tray domain Ω_t, and $\Omega = \Omega_c + \Omega_s + \Omega_t$. The physical domain Ω is embedded in a fictitious domain Ω_e with the boundary of $\partial\Omega_e$. The embedded boundary of Ω within Ω_e can be described as $\Gamma = \partial\Omega(\partial\Omega \cap \partial\Omega_e)$. For metal AM process, the bottom of build tray is fixed in place, and hence, the Dirichlet boundary

$\bar{\boldsymbol{u}} = 0$ in domain Ω is directly extended to the embedded domain Ω_e. In the implementation, elements in the fictitious domain $\Omega_e \backslash \Omega$ is treated as a virtual material, whose elastic constants are set to small values to ensure robustness of the calculation, while for elements within the component domain Ω_c and support structure domain, inherent strain vector is assigned as a body force in the analysis. It is noted that voxelization method proposed in Ref. [148] is employed to discretize the domains and generate the desired Cartesian mesh for FCM analysis.

Once the optimization based on FCM method is finished and the relative density is obtained, lattice reconstruction is performed to convert the density profile obtained from optimization into graded lattice structures. Figure 5.31 illustrates the reconstruction process for the support structure design. As can be seen in Figure 5.31 (b), for a given component, the voxel-based mesh is used to discretize the part and its support structure. The optimization problem proposed in Eqs. (5.3)-(5.4) is solved by the method of moving asymptotes (MMA) [118] in order to optimize the relative density distribution in the support domain, refer to Figure 5.31 (c). After optimization, the relative density of the support structure is converted into variable-density lattice structure and combined with the solid component, which is then realized by AM.

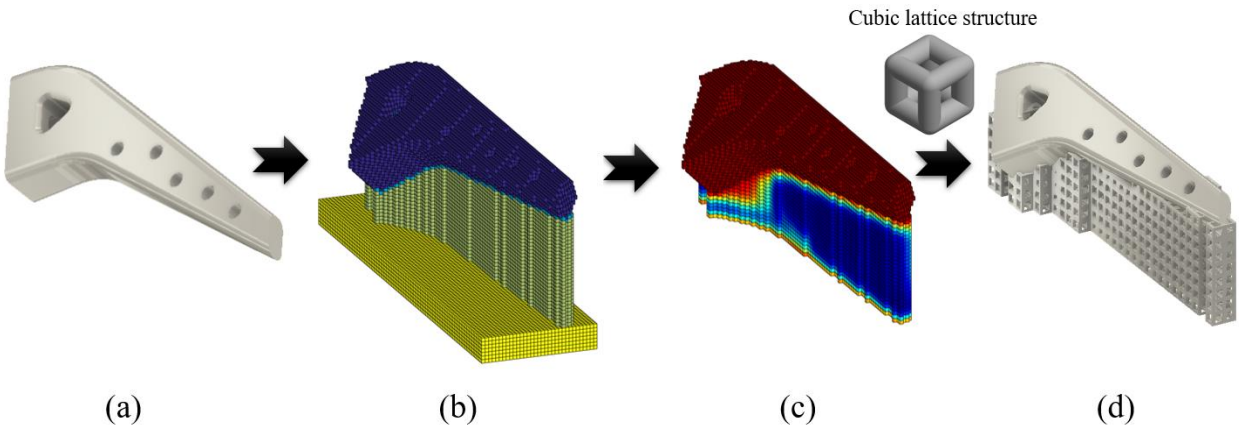

Figure 5.31: Reconstruction Process for a Practical Component. (a) Component for AM (b) Voxel-Based Mesh for FCM Analysis (c) Optimal Density Profile of Support Domain (d) CAD Model of Component and Optimal Lattice Support.

5.5.5 Numerical Example and Experimental Validation

The material of interest in this work is Ti6Al4V, which has a Young's modulus of 110 GPa, Poisson's ratio of 0.3, and yield strength of 1160 MPa. As mentioned in Section 2.4, residual stresses described in the following work is normalized by yield strength in order to make it generic for different materials. The inherent strain vector of Ti6Al4V used in this work is (-0.012, -0.012, 0.01), which is extracted by an inhouse code of multiscale modeling for powder-bed metal AM following the works of [87, 88, 169, 190]. Cubic lattice structure, as shown in Figure 5.31, is used as the support material to anchor the solid component to the build tray. The homogenized elastic and yield models for the cubic lattice structure obtained in [191] are used to effectively describe its properties as a function of relative density in the support domain Ω_s. The relative density range of the support structure is set to be $\underline{\rho} = 0.2$ and $\bar{\rho} = 0.95$. The optimization is stopped when the change of volume fraction of the support structure within three successive iterations is smaller than

10^{-3}, while the stress constraint is satisfied. The voxel-based finite element analysis is implemented using Matlab R2016a.

5.5.5.1 Double Cantilever Beam Example

The first example is a classical double cantilever beam widely used as a benchmark to examine the accuracy of metal AM process simulation. Here, the model is applied to investigate the performance of the proposed method for support structure optimization. The CAD model and voxel-based mesh for the double cantilever beam are illustrated in Figure 5.32. The design domain for the support structure is below the overhanging beams. As illustrated in the figure, the dimension of the double cantilever beam is $80 \times 40 \times 20\ mm^3$. The support domain for the double cantilever beam is two blocks of $36 \times 32 \times 15\ mm^3$. The aim of the optimization is to minimize support volume and at the same time restrict the maximum residual stress in the domain $\Omega_s + \Omega_c$ under the allowable stress. A mesh of element size of 1 mm or of 49,600 eight-node hexahedra elements is applied to discretize the entire domain and solve the optimization problem. As illustrated in Figure 5.32(b), the voxels of yellow color are for the support domain, blue ones for the solid component, and red for the substrate. Note that in the simulation of residual stresses, a fixed boundary condition is subjected to the bottom of the substrate while inherent strain is assigned on the both solid component and support structure. The thickness of the substrate is set to be 8 mm in the simulation to ensure the deformation of the bottom of the printed part and its support structure. For simplicity, only the results in the domains of support structure Ω_s and the bulk component domain Ω_c are shown in the following work. The relative density of each element in the support domain is initially set to 0.9, while the elements in component domain and substrate domain remain solid ($\rho = 1$) during the optimization.

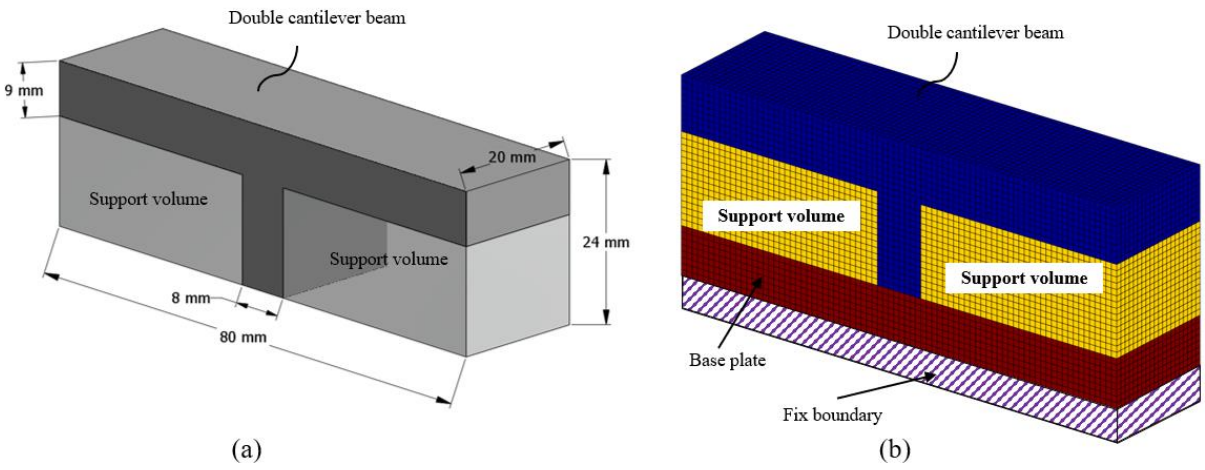

Figure 5.32: CAD Model and Mesh Model of Double Cantilever Beam Used for Validation. (a) CAD Model of the Beam (b) Voxel-Based Mesh Model.

The optimization results are presented in Figure 5.33 including the optimal density distribution, stress distribution, and also the convergence history of the objective function and maximum residual stress. As can be seen in Figure 5.33(c), the volume fraction of the support domain changes from 0.9 to 0.412 after 53 iterations (a 54.2% decrease), while the normalized maximum residual stress is decreased from 1.1 to 0.99, where unity indicates yielding. For the optimization results, the higher densities are mainly distributed around the upper corners of the beam, while lower densities are found far away from the center pillar. A number of intermediate densities (i.e. the yellow color area) exist in support domain between the high-density region and low-density region. The corresponding stress after the optimization is given in Figure 5.33 (b). It can be observed that most of the stresses within the support domain are smaller than 0.8. The larger stresses are distributed at the bottom surface of the center pillar, where the relative densities remain solid during optimization. The maximum stress of the domain $\Omega_s + \Omega_c$ are smaller than yield strength, which theoretically ensures manufacturability of the build.

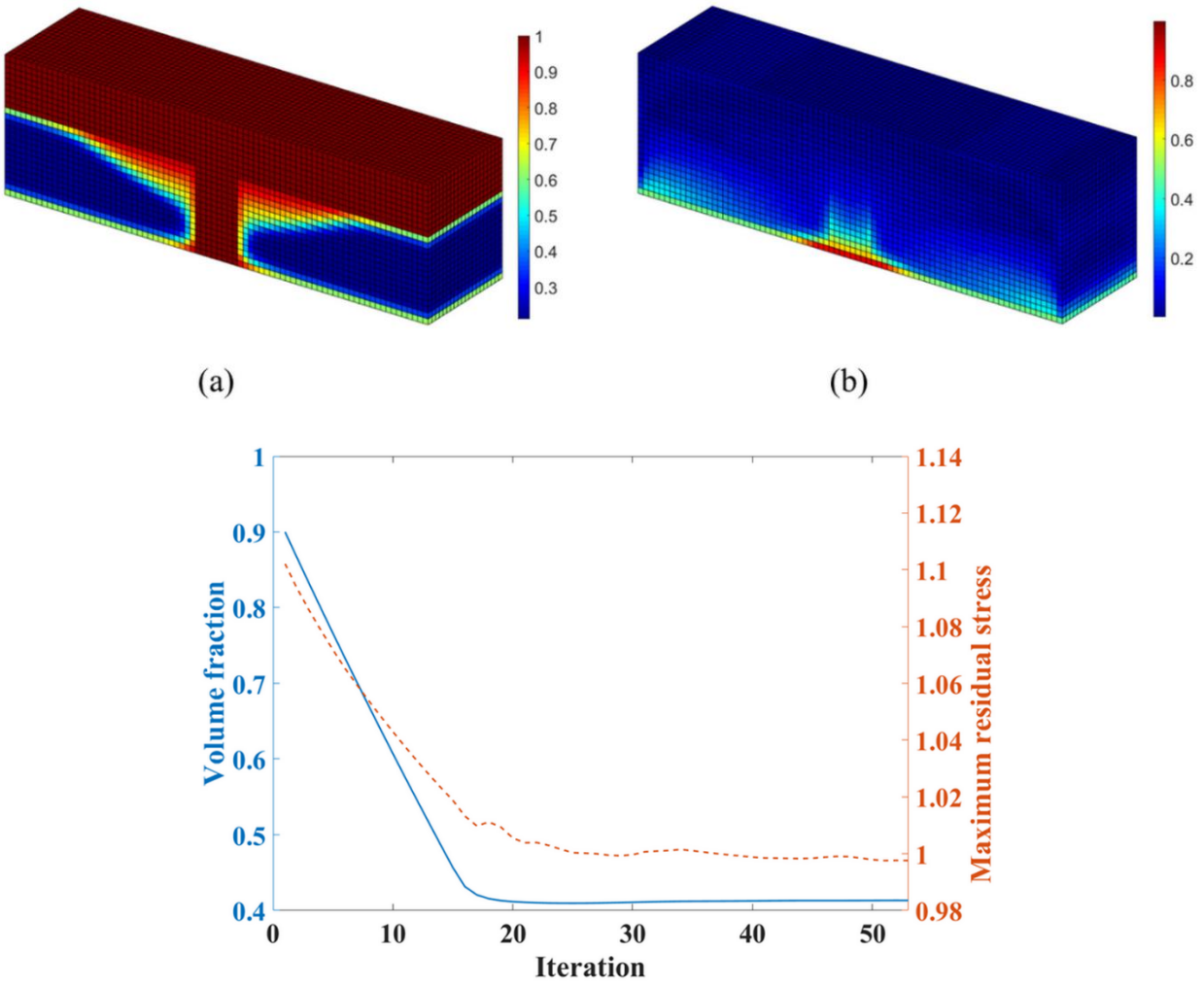

Figure 5.33: Optimization Results of the Double Cantilever Beam: (a) Optimal Density Distribution (b) Optimal Stress Distribution (c) Convergence History.

For comparison purpose, the simulation is performed on uniform lattice structure of the same volume fraction or 0.412. The results are presented in Figure 5.34. Compared with the optimal design, the maximum stress of the uniform design is 1.09, which is larger than yield

strength. The largest stresses are observed at the four bottom corners of the beam and the bottom surface of the center pillar.

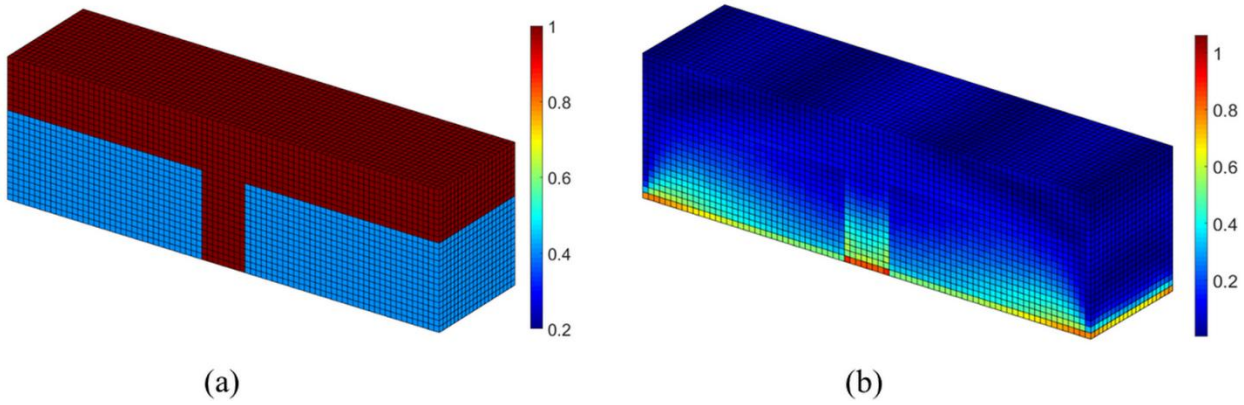

Figure 5.34: Simulation Result of the Design with Uniform Lattice Structure: (a) Density Distribution (b) Stress Distribution.

To quantify performance of the optimal design, the double cantilever beams with four different support structures are designed and printed out for deformation measurement and comparison. Figure 5.35 illustrates the four different designs: i) Block shell support from Materialize Magics software (widely used in metal AM), ii) optimal variable-density lattice structure support, iii) uniform lattice structure support, and iv) tooth support. The volume fraction of the block shell support is 0.45, while the volume fraction of tooth support is 0.5.

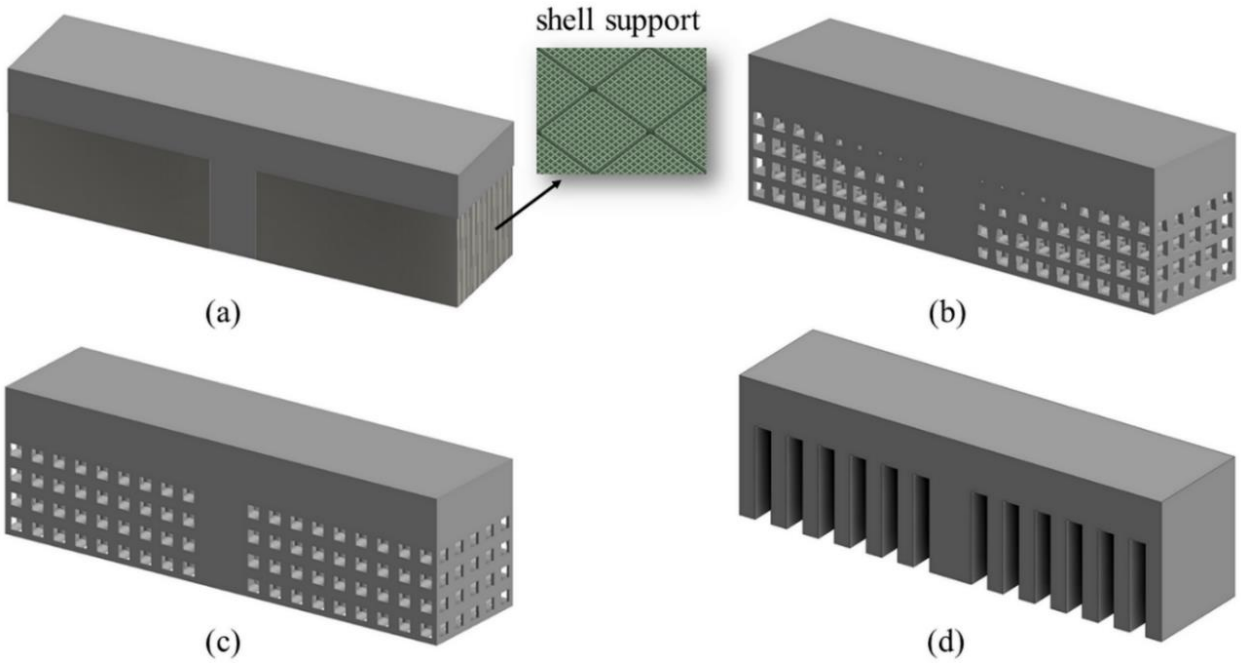

Figure 5.35: Four Different Support Structure Designs for Double Cantilever Beam for Comparison Purpose: (a) Shell Support From Magic Software (b) Optimally Variable-Density Lattice Structure Support (c) Uniform Lattice Structure Support, and (d) Tooth Support.

The four designs were printed out in Ti6Al4V on the same substrate and the photos are shown in Figure 5.36. Due to cracking between support structure and build tray of the block shell style support, the beam is warped upward, which stops the powder recoater blade and results in a failed build. This demonstrates that the residual stress inherent in the manufacturing process can lead to severe issue. One failed component can ruin the whole build and cause significant loss in time and costs. The failure not only lengths production of the component (i.e. designer needs to redesign the part), but also leads to a waste of material and time.

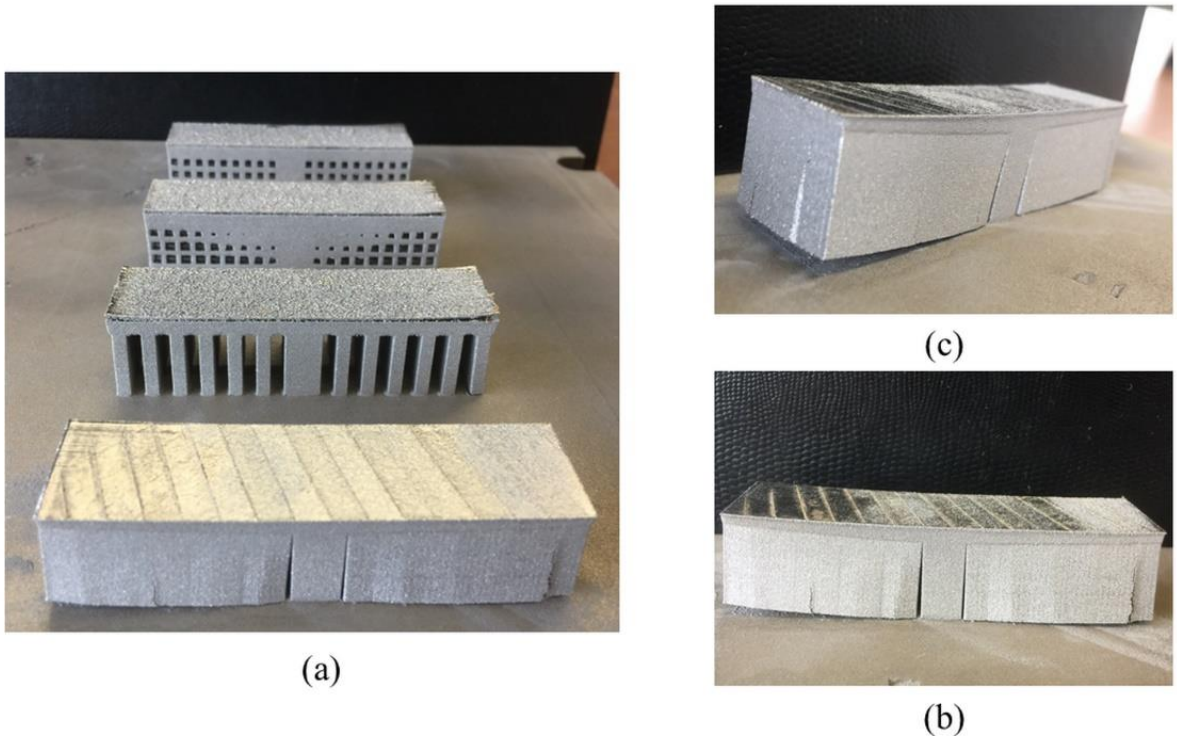

Figure 5.36: Failed Samples of the Double Cantilever Beams Printed out for Validation: (a) Failed Manufacturing due to Large Deformation Formed by Cracks Between Shell Supports from Magic Software And Build Tray. (b) and (c) Side View of the Cracks for the First Design.

To avoid build failure, the block shell support design was removed from the build and the remaining three beams were printed together in Ti6Al4V by the EOS DMLS. As shown in Figure 5.37, although cracks are observed for the tooth support design, the build for the three beams were successful. Compared to the block shell support and tooth support, both the uniform lattice structure design and optimal lattice structure design were manufactured without observed cracking. This implies that the open-cell lattice structure can relieve residual stress effectively and can be used for support structure design for metal AM.

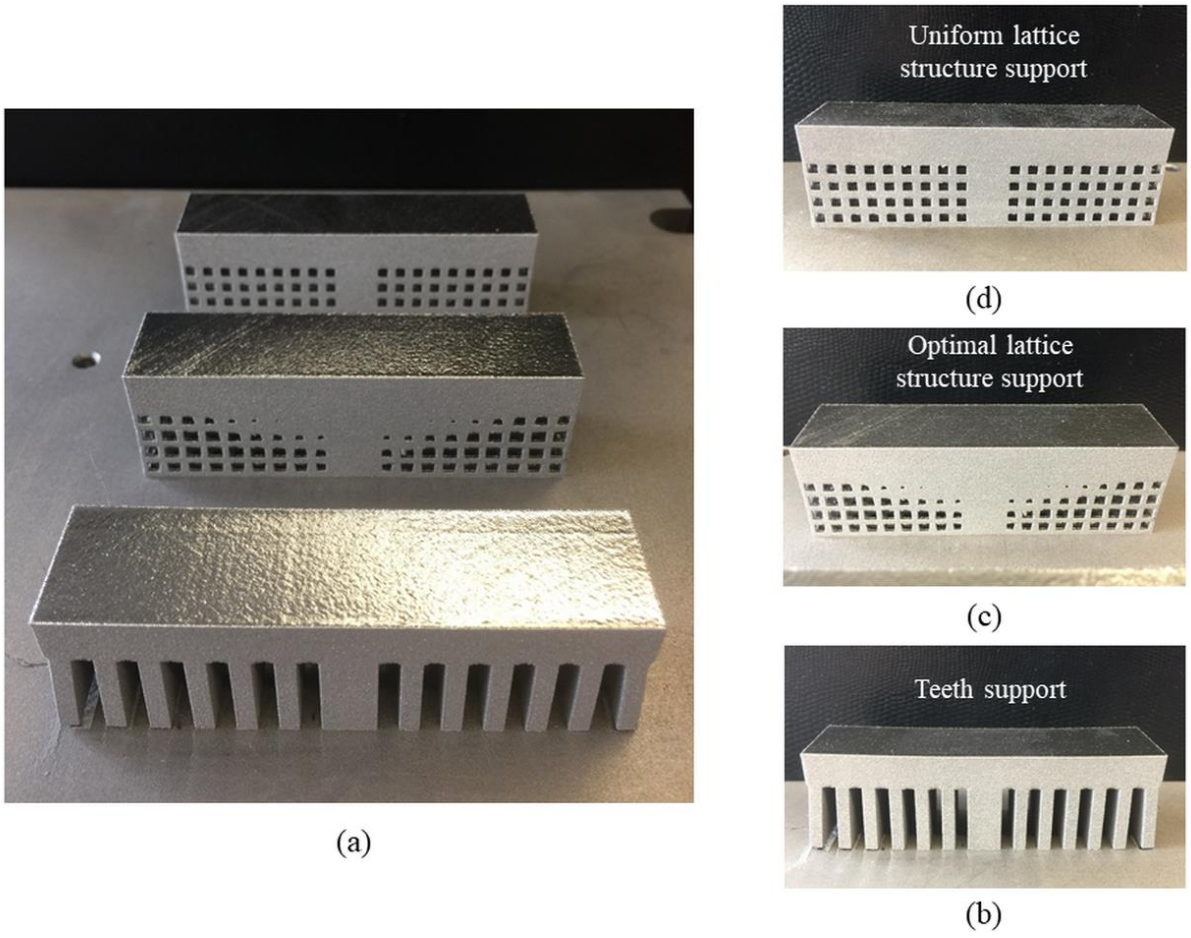

Figure 5.37: Second Build For Samples of the Double Cantilever Beam Printed out by EOS DMLA in Ti6Al4V: (a) Photos of the Three Printed out Beams for Validation; (b) Photo of the Beam with Teeth Support (c) Photo of the Beam with Optimal Lattice Structure Support (d) Photo of the Beam with Uniform Lattice Structure Support.

In order to validate the effectiveness of the proposed method, one cantilever beam on either side was created by separating each from the support structure using a wire-cut EDM machine. The beams deflected upward as a result of stress relief from the cutting. A 3D scanning device Faro Laser ScanArm V3 (FARO Technologies) with an accuracy of 0.065 mm was employed to experimentally measure the deformation. Following scanning, the Geomagic software was used to

process the data from the scan. The experimental apparatus, machined beams, and experimental results are shown in Figure 5.38, respectively. The optimized beam exhibits the smallest deformation compared to the other two designs. The maximum deformation of the beam with the optimized support is 0.45 mm, while the other two structures have deflections larger than 1 mm. This demonstrates that the proposed method can significantly reduce the residual stresses inherent in the AM process. The method not only ensures manufacturability of the design (i.e. comparing with the block style support in Figure 5.35), but also considerably enhances the quality of the bulk component (i.e. smaller deformation).

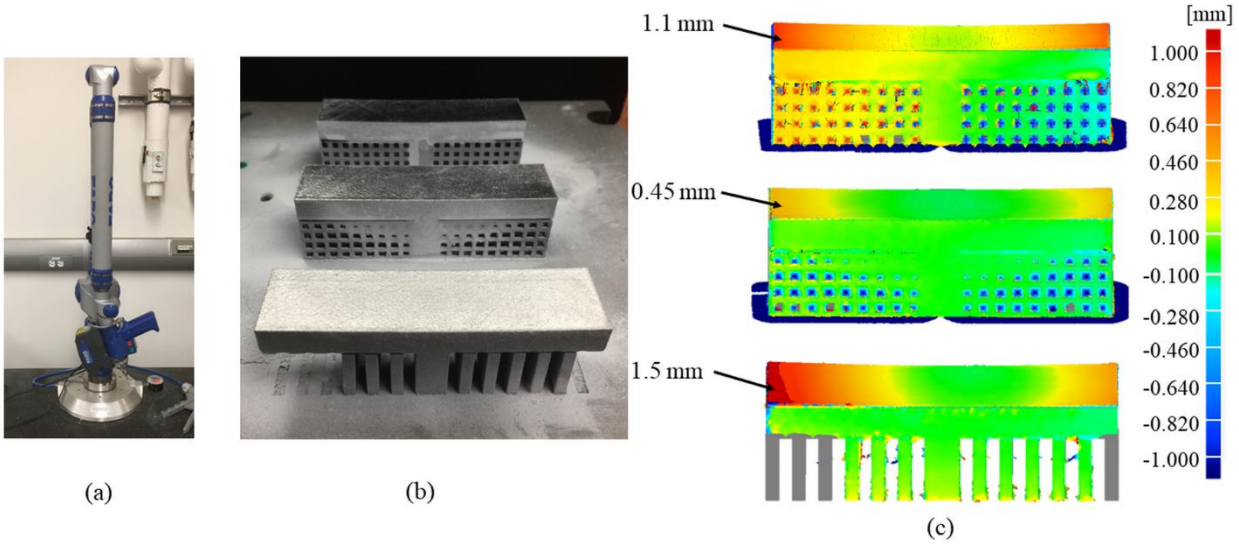

Figure 5.38: Experimental Measurement for the Distortion of the Beams after Cut by Electronic Beam Machining (EBM): (a) 3D Laser Scanning Device Faro Laser Scanarm V3 Made by FARO Technologies (b) Photos of Three Beams after Cut by EBM (c) Deformation Obtained by 3D Scanning.

To further examine the performance of the optimized design, full-scale simulations by inherent strain method are performed on the three designs shown in Figure 5.38. The commercialized software Simufact from MSC Inc is employed to simulate the residual distortion and residual stresses for comparison purpose. As shown in Figure 5.39, a substrate of dimension $250 \times 250 \times 30\ mm^3$ is added under beneath the beams while a fixed boundary condition is subjected to the bottom surface of the substrate. A voxel-based mesh of element size of 0.4 mm is applied to discretize the three beams, refer to Figure 5.39 (b).

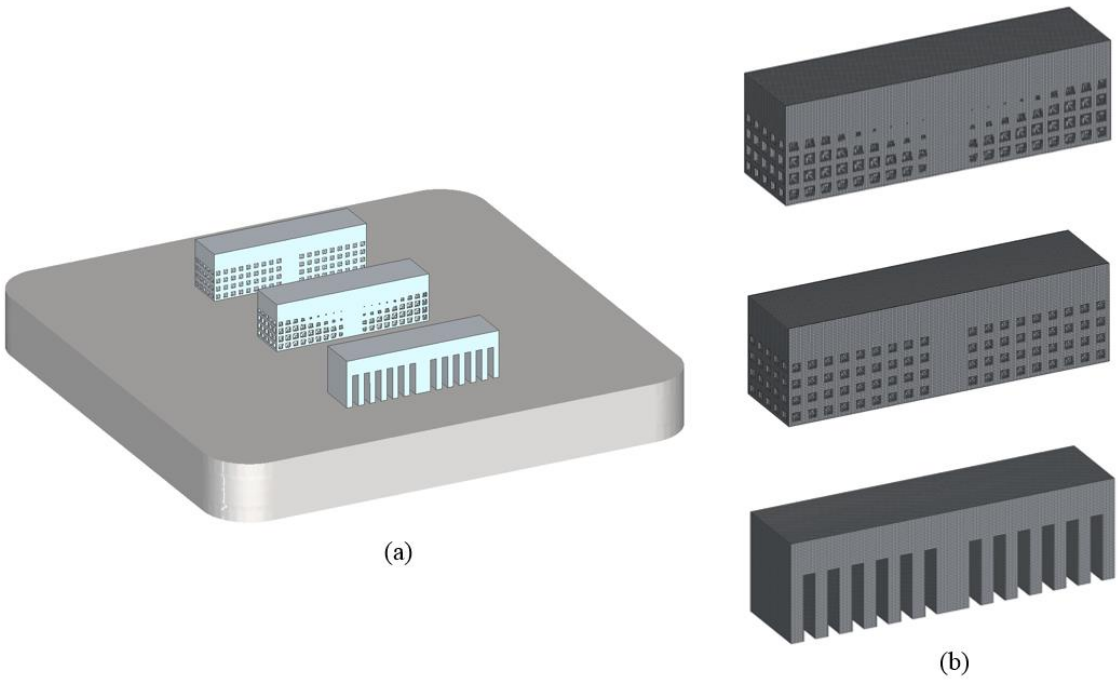

Figure 5.39: CAD Model and Mesh for Full-scale Simulation: (a) Distribution of the Beams on the Substrate (b) Voxel Mesh for the Full-scale Simulation.

The simulation results including residual distortions and residual stresses before cutting and after cutting are illustrated in Figure 5.40. It can be observed from Figure 5.40 that larger distortion mainly concentrates on the bottom boundary edge of the beams. The optimal design exhibits smallest deformation (i.e. the maximum distortion is $u_{max} = 0.26\,\text{mm}$) while teeth support design shows largest distortion (i.e. the maximum distortion is $u_{max} = 0.54\,\text{mm}$). This is consistent with the observation in Figure 5.38 (d). The residual stress distributions before cutting are given in Figure 5.40 (b). As can be seen, both the uniform lattice structure support design and optimal lattice structure support design show relative smaller residual stresses than the teeth support design, in which high stresses distribute at the bottom corners of the teeth supports. The cracks grow from these corners and leads to delamination in the manufactured beam, refer to Figure 5.38. Moreover, the employment of lattice structure for support design results in the dispersion of the stress concentration. This avoids the local accumulation of the residual stresses and thus prevents the growth of cracks.

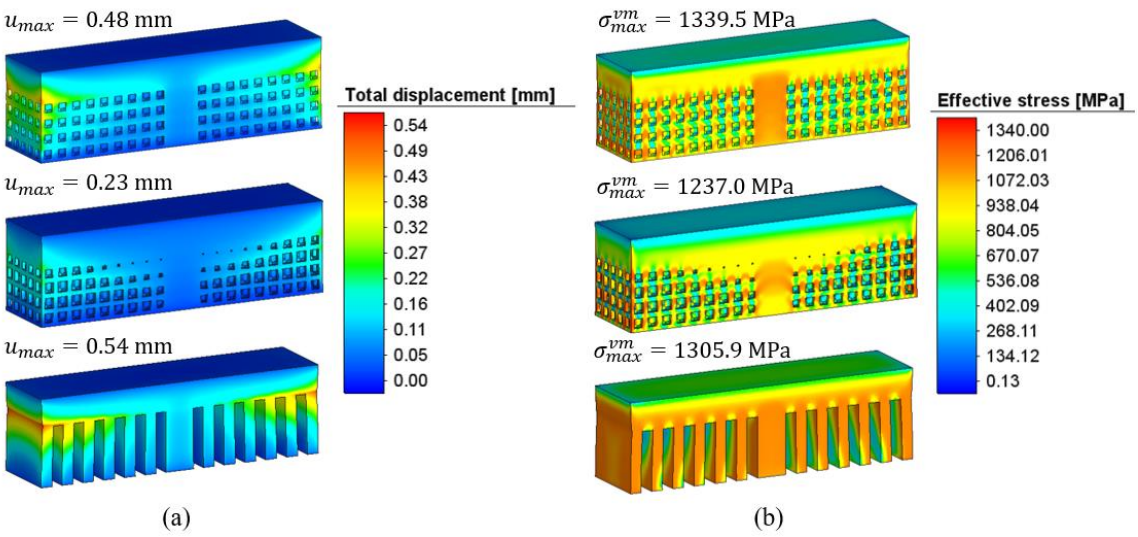

Figure 5.40: Full-scale Simulation Results of the Beams Before Cutting: (a) Displacement Distribution of the Three Beams (b) Residual Stress Distribution of the Beams.

The simulation results after cutting are presented in Figure 5.41 including both the displacement distribution and residual stress distribution. For comparison purpose, the legend of the total displacement in Figure 5.41(a) is same as the experiment measurement. Limited by the Simufact Additive 4.0, only one side of the double cantilever beam is separated from the support structure. Compared to experiment measurement shown in Figure 5.38(c), the displacement obtained from full-scale simulation is a little larger. For instance, the maximum displacement of the optimal design is 0.67 mm, or 0.22 mm larger than the experimental measurement. The uniform lattice structure design is 1.26 mm while the teeth support design is 1.67 mm. The ratio relation among the maximum distortions for the three beams are similar to the experimental measurement. The residual stress distribution of the three designs are shown in Figure 5.41. It can be found that the residual stresses in the beam are significantly reduced after stresses are released from support structure.

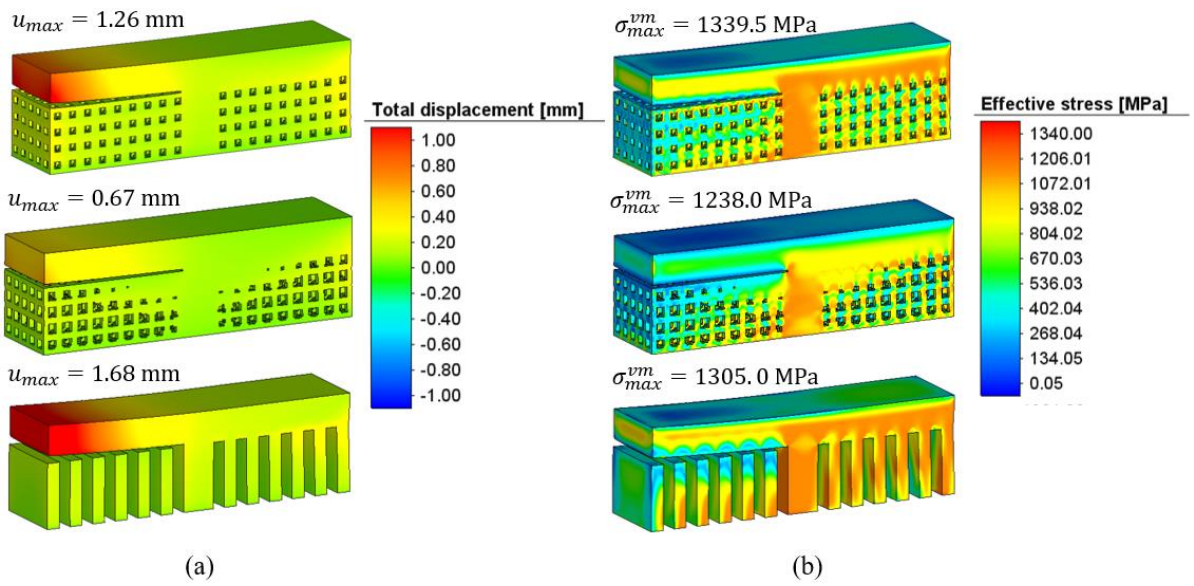

Figure 5.41: Full-scale Simulation Results of the Beams after Cutting: (a) Displacement Distribution; (b) Residual Stress Distribution

5.5.5.2 Hip Implant Example

The second case is a typical hip implant used for bone replacement. The CAD model and dimension of the hip implant is shown in Figure 5.39(a). The envelope box of the implant is $120 \times 35 \times 16$ mm^3. There are several bolt holes along the length of the implant used to fix the implant to human bone. The hip implant with the block style support structure was printed using the EOS M290 DMLS system in Ti6Al4V. However, as shown in Figure 5.39(c) and (d), cracks and delamination from the build tray occurred during the AM process due to residual stress within the support structure and solid component. The cracking and delamination occurred certainly caused larger deformation of the build than otherwise, but they were not severe enough to cause a build failure. Another issue observed from this build is that the block shell style support structure trapped most of the powders since it is a closed-cell lattice structure. The trapped powders are difficult to remove post-build and lead to almost 100% waste of material in the support domain.

On the other hand, for open-celled lattice structure, the trapped powder can be easily removed and recycled for the next build, which results in much material and cost savings.

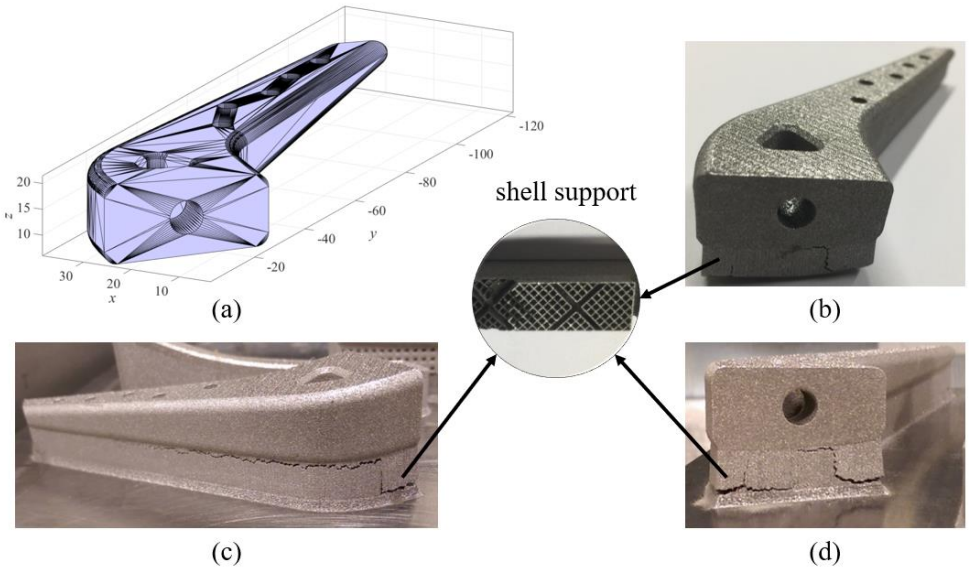

Figure 5.42: CAD Model of Implant and Its Manufacturing in Ti6Al4V by EOS DMLS with Shell Support: (a) CAD Model, (b) Printed Implant after Cutting off from Build Tray, (c) Left View of Implant Before Cutting from the Substrate, and (d) Front View of Implant before Cutting from Build Tray.

In this case, the proposed methodology is employed to optimize the support structure for the hip implant to ensure a successful build. In particular, we will use the optimization algorithm for the implant built in three different orientations, since different build orientations may lead to less support region and thus less effort for post-machining. As shown in Figure 5.43, the implant is rotated about the *y*-axis by angles of 0°, 45°, and 90°, respectively, and is voxelized for both the part and its relevant support generated by the overhang detection proposed in Section 5.2. A uniform voxel-based mesh consisting of element size of 1 mm is employed to discretize the entire

domain including solid component, support structure and build tray. The thickness of the build tray here is same as the former case and the value is 8 mm while the width and length of the base plate are determined by the bounding box of the part. The numbers of eight-node hexahedral elements used for the simulations are 97329 for orientation of 0°, 93778 for 45°, and 75607 for 90°, respectively, refer to Figure 5.43 (c), (f) and (i). In the simulation for residual stresses, the bottom surface of the base plate is fixed, and the inherent strains are assigned to both the support structure domain Ω_s and bulk component domain Ω_c. The highlighted region in Figure 5.43 (a), (d) and (g) are the detected overhangs, while the yellow voxels in Figure 5.43 (b), (e) and (h) are the corresponding detected voxels. The support volumes of these three orientations are computed by summing the number of support voxel to be: 1.602×10^4 mm^3, 1.064×10^4 mm^3 and 2.523×10^4 mm^3, respectively. It can be seen when the implant is rotated by an angle of 45°, the support volume is decreased by 5.38×10^3 mm^3 or 33.6% of the 0° angle case and by 1.459×10^4 mm^3 or 57.62% of the 90° case. This is because for angle 45°, the major detected overhangs are edge overhangs, and most of the facets at that angle satisfy the critical overhang requirement (i.e. the included angle by building direction is larger than 45°). This implies that the build orientation plays an important role in the design of support structure. Note that the figures of results in the following content only contain the distribution (i.e. residual stress distribution and relative density distribution) in domain $\Omega_s + \Omega_c$ for simplicity.

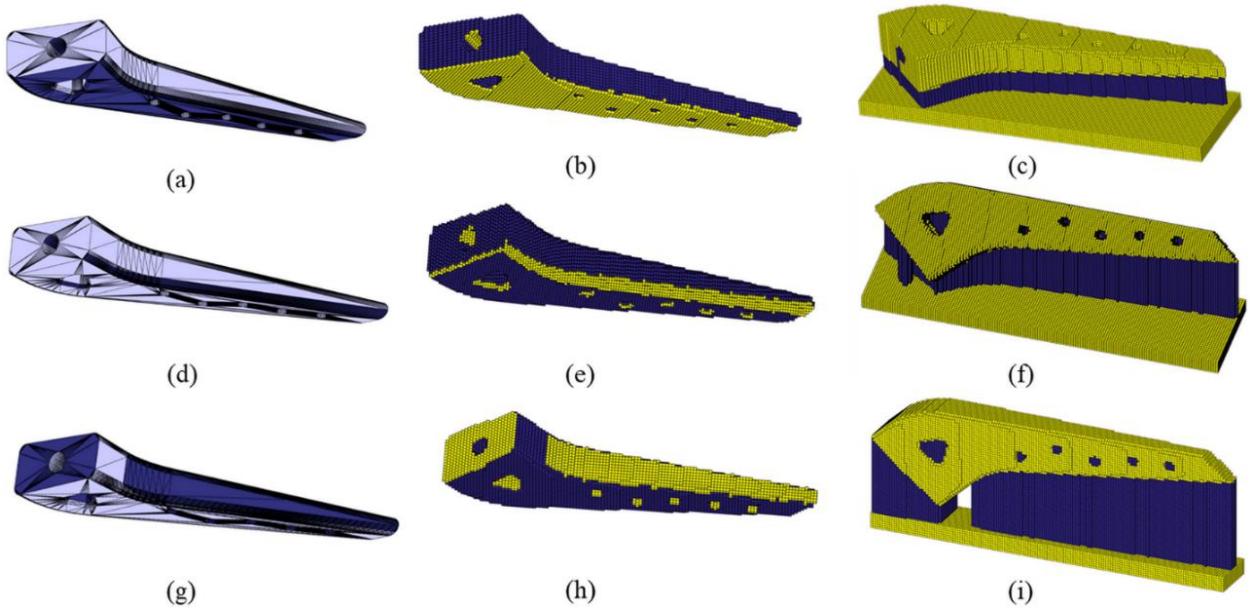

Figure 5.43: Hip Implant of Different Orientations: (a-c) STL File, Voxelized Part and Cartesian Mesh for Implant Rotated by Angle of 0°; (d-f) STL File, Voxelized Part and Cartesian Mesh for Implant Rotated by Angle of 45°; (g-i) STL File, Voxelized Part and Cartesian Mesh for Implant Rotated by Angle of 90°.

Table 5.3: Initial State of the Optimization

	Orientation 0°	Orientation 45°	Orientation 90°
Support volume (mm^3)	1.602×10^4	1.064×10^4	2.523×10^4
Maximum residual stress	3.1	2.42	2.12

The orientation of the component can also influence the stress distribution, especially the location of the stress concentration and maximum residual stress. As shown in Figure 5.44, when

the volume fraction of the support structure is set to 0.9, the large stresses mainly distribute at the interface between support structure and substrate, e.g., at the lower left and right corners of the three designs. These are the areas where cracking initiate and grow. Table 1.1 tabulates the support volume and maximum residual stress for the three cases. It can be seen that the part with no rotation (angle of 0°) has the largest maximum stress, while the case with rotation angle of 90^{o} case has the smallest value. This indicates that the orientation also has great influence on the stress distribution and magnitude of the maximum stress. The aim of this example is to explore the performance of the proposed methodology for the implant with different orientations.

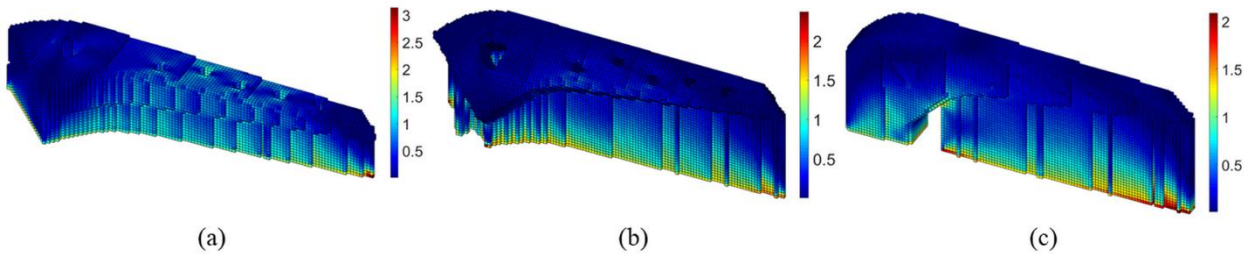

Figure 5.44: Stress Distribution of Hip Implant with Volume Fraction of 0.9: (a) Oriented by Angle of 0°, (b) Oriented by Angle of 45° and (c) Oriented by Angle of 90°.

The optimization results including the stress profile, and relative density profile are given in Figure 5.45. Table 5.4 tabulates the corresponding optimization results. For the 0° angle case, the volume fraction of the support structure converges from 0.9 to 0.41 after 60 iterations, and the maximum residual stress is decreased to 0.82 from 3.1. For the 45° angle case, the volume fraction of the support structure is reduced to 0.36, and the maximum residual stress is decreased to 0.91 after 73 iterations. In 64 iterations, the volume fraction for the final case of 90^{o} angle converges to

0.46, and the maximum stress is decreased to 0.81. The maximum residual stresses in these three cases are optimized to below the yield strength and thus satisfy the imposed constraints after optimization.

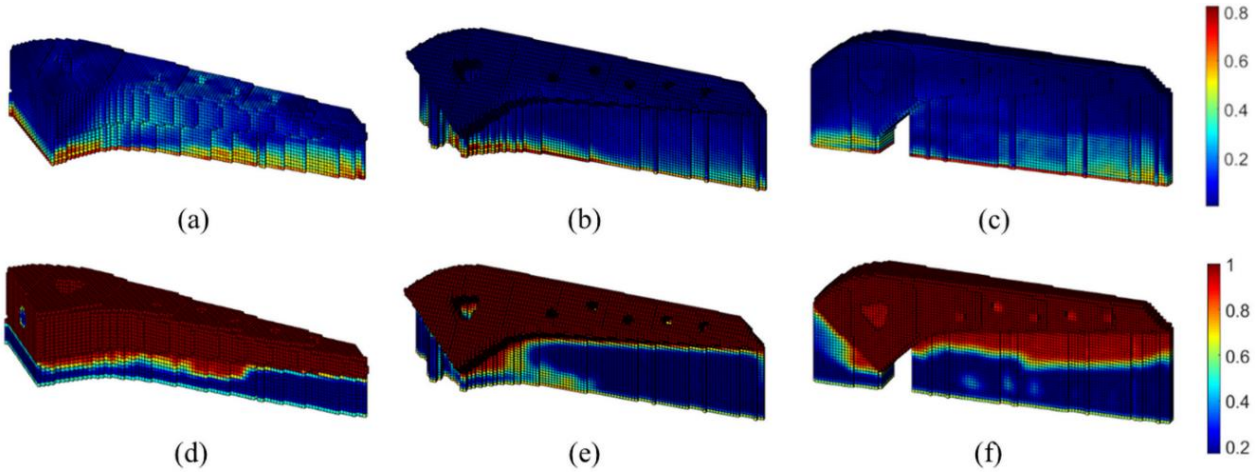

Figure 5.45: Optimization Results of the Three Orientations for Hip Implant: (a-c) Stress Distribution of the Implant Rotated by Angle of 0°, 45° and 90°; (d-f) Optimal Density Distribution of the Implant Rotated by Angle of 0°, 45° and 90°.

Table 5.4: Optimization Results of Hip Implant Oriented by Different Degrees

	Orientation 0°	Orientation 45°	Orientation 90°
Volume fraction	0.41	0.36	0.46
Maximum residual stress	0.82	0.91	0.81

The optimized densities shown in Figure 5.45(d-f) are used to reconstruct the corresponding variable-density lattice structures as illustrated in Figure 5.46 in two different views. The contact areas between the component surface and support structure vary significantly as the implant is rotated at various angles. The angle of 45° exhibits the smallest contact area, which is consistent with the support volume calculated given in Table 5.3. The contact areas influence the cost of post-machining. Thus, among these three support designs, the orientation of 45° may require lower cost for post-machining.

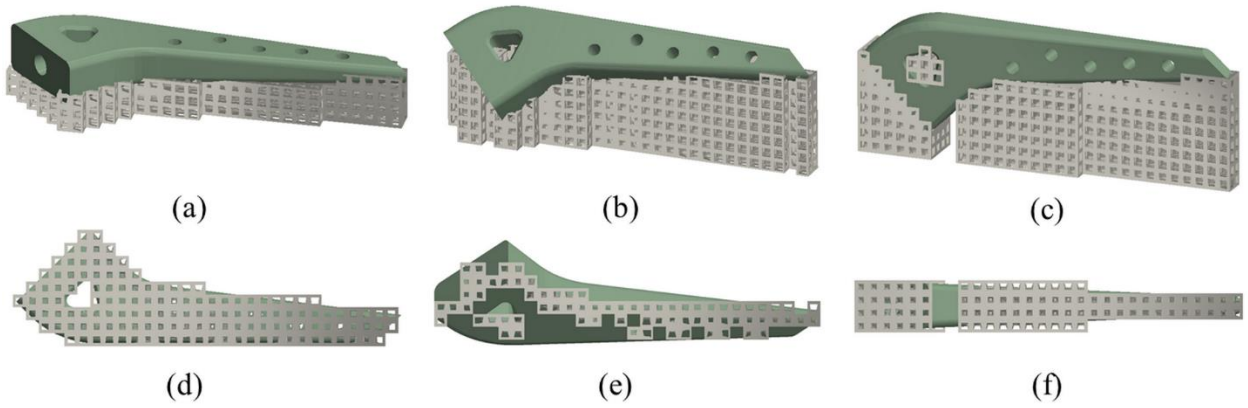

Figure 5.46: Reconstruction of the Optimal Support Structure Design Using Variable-Density Lattice Structure (a-c) Home-View of the Implant Rotated by Angle of 0°, 45°and 90°; (d-f) Bottom View Three Support Structure Designs.

For validation purpose, the three support structure designs for hip implant are printed out in Ti6Al4V and the photos are shown in Figure 5.47. Compared with the un-optimized design shown in Figure 5.42, the designs are successfully printed without obvious cracks. This demonstrates the effectiveness of the proposed methodology in reducing the residual stresses in an

AM build. It also implies that the optimization framework can be efficiently employed for components with predefined orientations.

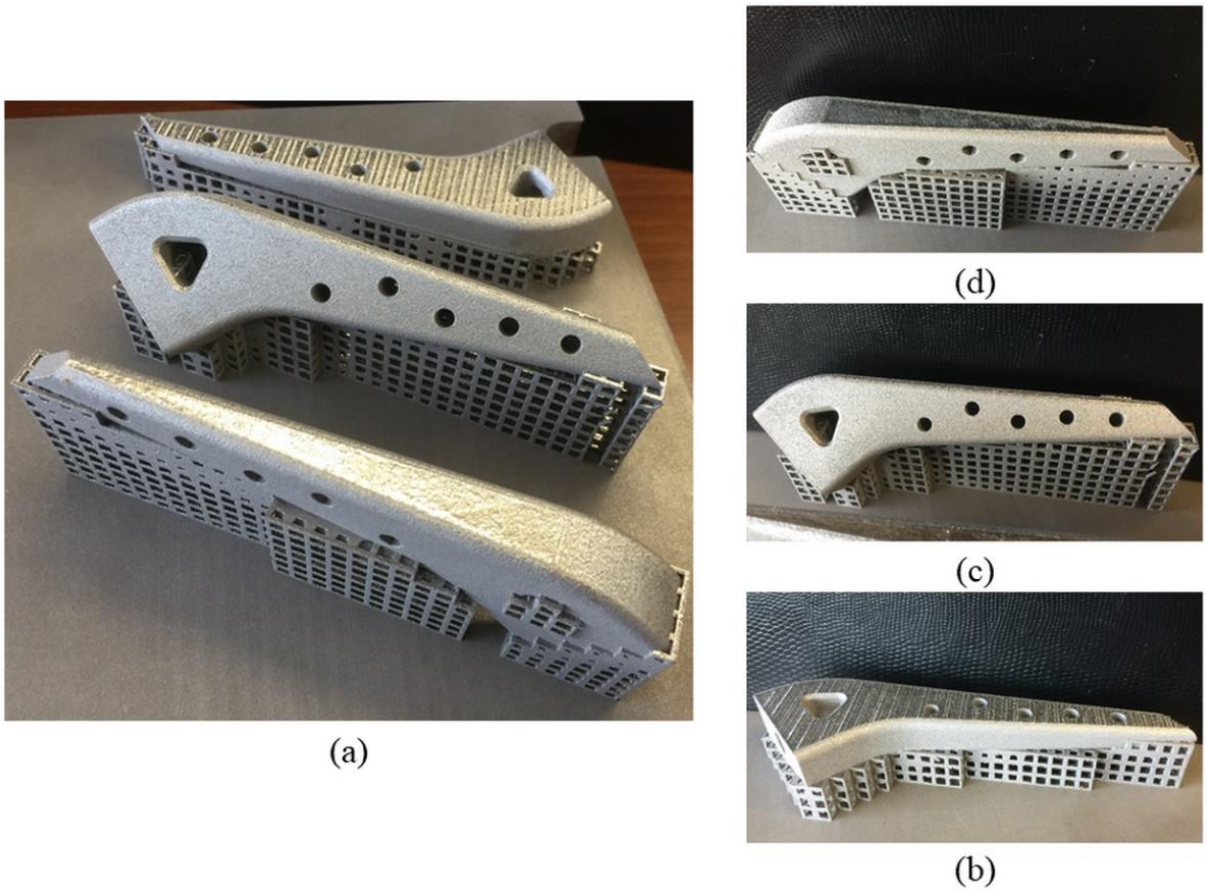

Figure 5.47: Photos of the (a) Printed Implants at Three Different Orientations with Optimized Graded Lattice Supports, (b) Implant Rotated by Angle of 0° with Its Optimized Support, (c) Implant Rotated by Angle of 45° with Its Optimized Support, and (d) Implant Rotated by Angle Of 90° with Its Optimized Support. Note that There is No Obvious Cracking in All the Designs.

5.5.6 Summary

The aim of this work is to experimentally examine the feasibility of part-scale optimization framework for support structure design, in order to address residual stress induced build failure in metal AM. The inherent strain method is employed to efficiently predict residual stress introduced by the powder melting and solidification process. The complex thermomechanical process, which normally requires very high computational cost, is simplified into a single-step static equilibrium analysis. This makes it possible to conduct optimization to iteratively solve the design problem involving residual stress. For the support structure, lattice structure is used as the support material due to its self-supporting and open-celled nature. The graded lattice structure topology optimization framework is proposed to iteratively minimize the sacrificial support structure under the maximum residual stress constraint. Several numerical examples are investigated to examine the performance of the optimization method. In the first example, the classical double cantilever beam structure is used to experimentally investigate the optimal design by comparing with a typical support design, tooth support design, and uniform lattice support design (same volume fraction as optimal design). By measuring the deformation after the beams are created by cutting, it is found that the optimal design can ensure the manufacturability of the design and also significantly reduce the residual stress (i.e. maximum deformation is reduced from 1.5 mm and 1.1 mm to 0.45 mm). The second example presents is a hip implant which also suffers from residual stress induced cracking. In that case, three different orientations are studied using the proposed optimization method and are printed out for validation. Although it is found that the orientation of the component has a significant influence on both the stress and support volume, the proposed methodology can optimize the design of support structure. Though visual inspection, the three designs for the implants are manufactured successfully without observed cracking. This further

demonstrates the methodology can be effectively used to design industrial components for practical applications.

Note that although the proposed methodology can ensure manufacturability of AM builds, the removability of the lattice structure support by post-machining has not been considered and will be investigated in our future work. Further studies could be performed to add other constraints to the optimization algorithm by considering area of the surface that is not accessible by post-machining. Another alternative to remove support structure is by using dissolvable support [183, 192], which is a self-terminating chemical process that dissolves a thin surface layer. Hence, if the struts or walls in the lattice support are made thin enough, the support structure can be dissolved using this chemical process without any post-machining. These topics will be investigated in future in order to completely solve the build failure and post support removal for the powder-bed fusion process.

6.0 Conclusions

6.1 Main Contributions

The research in this dissertation mainly focuses on the development of design methodology to leverage the potential of AM techniques for high-value applications. The aim is to extend conventionally topology optimization to design functionally graded lattice structures and apply the proposed framework to address one of the most severe problems of current powder-bed metal AM, e.g. residual stress induced build failure. The major contributions can be summarized as follows:

(1) **A homogenization-based lattice structure topology optimization method is developed to design functionally graded lattice structures for additive manufacturing.** Conventional density-based topology optimization method aims to generate black-and-white designs through an artificial penalization to drive elemental densities to void or solid. Although such a method is efficient for various problems, the applicability for practical applications is still limited since the design is too organic to manufacture. Even by using additive manufacturing, extra efforts (e.g. support structure) needs to be added to guarantee the manufacturability. To address this issue and inspired by natural materials, the homogenization model for lattice material manufactured is introduced into the framework of topology optimization to replace the artificial penalization function, in order to design graded lattice structure with prescribed properties. Due to its self-support nature and an open-cell structure, the lattice structure is able to be produced by AM techniques without extra efforts and is thus an ideal structure for the AM process. The specific contributions are as follows:

a) **The lattice structure topology optimization (LSTO) method is proposed for minimum compliance problem.** To circumvent full-scale modeling for lattice materials in the optimization, a homogenized model is proposed to capture the effective elastic properties of lattice structures through a scaling law as a function of relative density. The representation of lattice material is described by a solid material with equivalent properties. Hence, the computationally expensive cost for the microstructure of the lattice structure is significantly reduced for an iterative optimization. The accuracy of the proposed homogenization is validated through experiments on the lattice material manufactured by various AM techniques. It is proved that the proposed homogenized model is in excellent agreement with the experimental validation. Once the homogenized model is proved, the scaling law is used as a material property in the topology optimization for the minimum compliance problem to compute the optimal density distribution for the part being optimized. Finally, a reconstruction methodology based on the application program interface of CAD software is developed to convert the density distribution from optimization into functionally graded lattice structures. It has been experimentally proved that the proposed LSTO approach can significantly increase the stiffness of the structure compared with the same weight uniform lattice structure design.

b) **The LSTO method is developed for constraint stress problem.** Although the proposed LSTO method is efficient for the minimum compliance issue, the stress concentration at the corners of the lattice structure may lead to undesirable failure. In order to ensure that the designed graded lattice structures work in a safe zone, an optimization problem of minimizing the overall weight of the structure under allowable stress constraint is proposed. Specifically, a multiscale yielding criterion is proposed to capture the yield strength of lattice materials via macroscopic stresses. At the macroscale, a modified Hill's yield criterion by considering

hydrostatic pressure is proposed to depict anisotropic yield strength of the lattice structure. While at the microscale, the yield strength of the lattice structure is treated based on the materials of interest for manufacturing. By performing a homogenized analysis on a representative volume element (RVE) model, multiscale yield strength of lattice structure with respect to relative density is obtained. Experimental validation for the proposed yield strength model is conducted on the lattice material manufactured by AM techniques. Excellent agreement between the yielding model and the experiments proves that the proposed multiscale process is efficient for the description of lattice materials. The developed multiscale yield strength model and the effective elastic model is substituted into the framework of the LSTO method and used for practical applications. By conducting experiments on the practical design, the predicted yield performance of the component agrees well with the experimental measurement. This demonstrated that the proposed multiscale yield model of the LSTO method can be efficiently used for functionally graded lattice structure design under stress constraint.

c) **A natural frequency optimization method based on the LSTO framework is proposed to separate the repeated natural frequencies and maximize the first eigenfrequency under volume fraction constraint.** The aim is to prevent failure resulted from the resonance of the component by infilling the solid component with a functionally graded lattice structure. Asymptotic homogenization (AH) method is employed to calculate the effective mechanical properties of lattice structure manufactured by metal AM (e.g. EOS direct metal laser sintering (DMLS) process). The validated AH model is implemented into the proposed natural frequency optimization method for practical designs. Both full-scale simulations and experimental studies on the designed beams have demonstrated that the proposed natural frequency optimization method

can significantly increase the eigenfrequency of the component. This indicates the robustness of the developed LSTO method for the dynamic problem.

(2) **Concurrent optimization framework development for lattice structure infill coupled with design-independent/design-dependent movable features.** Although the LSTO method is extensively studied for a various problem, movable features that are non-designable are difficult to represent by lattice structures. The aim of this work is to integrate the optimization of movable features with design-dependent/design-independent boundary conditions with the proposed LSTO method. This type of problem has practical applications, such as conformal cooling channel design. To promote the development of such a method, the commonly used concept of level set representation is introduced into the LSTO framework. First, a level-set based immersed boundary method is introduced to formulate the geometry of the non-designable features in an implicit manner. Second, a combined material interpolation is proposed to integrate the property of movable features into the LSTO method. Third, a concurrent optimization framework is proposed to optimize the lattice infill and the layout of the movable features. A full-scale simulation conducted on numerical examples has proved that the proposed method can achieve better performance than non-movable design. Especially for the cooling channel design optimization, the concurrent design can further decrease the maximum temperature of the design domain 30% more than the total solid design.

(3) Metal additive manufacturing promises to be the next-generation manufacturing technique due to its excellent performance in fabricating geometrically complex structure. However, one of the most severe problems of residual stress induced build failure prevents this technique from broad application. The aim of this work is to develop a framework to systematically

address the build failure induced by residual stress accumulated in laser melting and solidification process. The contribution of this research can be summarized in the following three aspects.

(a) **A voxel-based support structure detection and mesh generation method is proposed to automatically generate Cartesian mesh for both part and its support structure.** One of the toughest issues for overcoming the build failure problem is efficient support structure detection and mesh generation. A voxel-based method is proposed to effectively detect the overhang features for a given component of any build orientation and movement. Specifically, the overhang features of an AM part are categorized into three groups, overhang facets, overhang edge, and overhang point. Based on the categorization, a ray tracing method is proposed to label the voxels corresponding to the overhang features in the voxelized part. The voxels on support structure region are thus generated according to the labeled overhang voxels. Comparing with the existing methods for support structure generation, the proposed voxel-based method is neither overestimation nor underestimation for the detection of the support structure region. Once the voxel-based mesh is obtained, it is used for rapidly simulation for residual stress computation.

(b) **A particle-swarm based method is developed for the optimization build orientation of the component.** The build orientation plays an important role in residual stress distribution, building time and support structure volume. Generally, the engineer avoids the build failure of an AM part based on their experience for the build orientation of an AM part. However, this may not work for a complex component. A multi-objective optimization including both the maximum residual stress and support structure volume is considered in this research. There are two design variables. One is the orientation of the part along the *x*-axis, the other is the orientation along the *y*-axis. By optimizing the two design variables, the optimization aims to find the optimal build orientation with the minimum residual stress and support volume, in order to guarantee the

manufacturability of the design and at the meantime reduce the sacrificial support structure. Particularly, four different support structures including three open-cell lattice supports and one block style support are studied. Part-scale experiments have proved that the proposed method can significantly reduce the residual stress with the open-cell lattice support. The microstructure of the lattice support structure has unignorably influences on the optimal build orientation.

(c) **A support structure topology optimization based on the LSTO method is developed to minimize the overall volume of the support structure under the maximum residual stress constraint.** Although the build orientation optimization method can decrease the residual stress in the metal AM process, it is not able to guarantee that the maximum residual stress is under the allowable stress (e.g. yield strength). Hence, the design is still possible to fail in manufacturing. As mentioned in the build orientation optimization, the microstructure of the support structure can affect the residual stress distribution. The aim of this research is to optimize the microstructure distribution of the support structure, in order to completely constrain the maximum residual stress below the yield strength. For this purpose, the fast simulation method called inherent strain method is employed in the optimization while a design dependent LSTO method with stress constraint is proposed. By optimizing the density distribution of the support region, the proposed approach can remove as much 60% material from the support structure region, and at the same time minimize the maximum residual stress below the yield strength. Experiments have proved that the developed method is able to control the residual stress in an AM part and guarantee the manufacturability of the design for part-scale problem.

6.2 Future Works

Although the proposed LSTO method has been extensively studied in this dissertation for various problems ranging from static structural, dynamic, heat transfer, concurrent design with design-dependent movable features, and have been successfully applied for residual stress control for metal AM process, there is still a lot of room to further study this method. The potential future works based on the research in this dissertation are summarized as follows.

(1) **Multiscale and multilateral optimization by using the LSTO method for additive manufacturing.** Natural materials normally consist of multi-layer of hierarchical structures and multi-materials for specific functional purpose. A direct extension of the proposed method is the multiscale optimization to mimic natural materials. To develop such a method, a multiscale homogenization theory needs to be first developed to capture the effective properties of structure from different length scale. The influence of the size effect should be considered when the smallest scale approximates to the nanoscale. For multi-material optimization, a material model that can smoothly switch the materials in the optimization according to the sensitivity analysis must be developed. Computational cost may be a major bottleneck that will constrain the development of such a method. Thus, advanced program in the framework of GPU should be developed to accelerate the analysis of multiscale modeling for the optimization.

(2) **Multiphysics optimization by using the LSTO method. Most of the practical component is normally designed to work in multiphysics environment and undertake multipurpose applications.** The development of multiphysicsoptimization has significant value from both academic and engineering perspectives. However, it is not straightforward to extend the existing LSTO method to multiphysical optimization. One major obstacle needs to be circumvented is an efficient homogenized model for the description of multiphysics properties of

lattice materials. Since the LSTO method tends to design variable-density lattice structure, there is no clear boundaries for the treatment of different physics. The open-cell nature of lattice structures may promote the interaction of multiphysics process. This may lead to invalid of the homogenized model obtained from single physics. To address this issue, the effect of interaction from multiphysics should be considered in the homogenization and optimization.

(3) **Extend support structure optimization to ultimate strength and dissolvable design.** Although the combination of the build orientation optimization and support structure optimization is efficient to address the residual stress induced build failure, a new problem is introduced for the design. One of the important issues is the removal of the support structure. The proposed method tends to generate very dense lattice structure at the contact region between the support structure and solid component. This dense structure is difficult to remove in the post-process when the component is complex. To address this issue, two directions may be investigated: 1) Combine the build orientation and support optimization together to prevent the generation of support structure at the regions that are difficult to clean in the post-process; 2) design dissolvable support structures that are easy to remove by using the chemical process, such as a thin surface layer support structure. Another potential direction for this topic is to extend the yield strength constraint to ultimate strength. This will help to further reduce the sacrificial support structure and promote the development of dissolvable support.

Bibliography

[1] W. E. Frazier, "Metal additive manufacturing: a review," *Journal of Materials Engineering and Performance,* vol. 23, pp. 1917-1928, 2014.

[2] I. Gibson, D. W. Rosen, and B. Stucker, *Additive manufacturing technologies* vol. 238: Springer, 2010.

[3] K. V. Wong and A. Hernandez, "A review of additive manufacturing," *ISRN Mechanical Engineering,* vol. 2012, 2012.

[4] N. Guo and M. C. Leu, "Additive manufacturing: technology, applications and research needs," *Frontiers of Mechanical Engineering,* vol. 8, pp. 215-243, 2013.

[5] M. Fransen, "Eigenstrain reconstruction of residual stresses induced by selective laser melting," 2016.

[6] T. Wohlers and T. Gornet, "History of additive manufacturing," *Wohlers Report: Additive Manufacturing and 3D Printing State of the Industry Annual Worldwide Progress Report,* 2011.

[7] W. Gao, Y. Zhang, D. Ramanujan, K. Ramani, Y. Chen, C. B. Williams, *et al.*, "The status, challenges, and future of additive manufacturing in engineering," *Computer-Aided Design,* vol. 69, pp. 65-89, 2015.

[8] E. company. (2017). *Additive Manufacturing for Medical Devices*.

[9] A. Emelogu, M. Marufuzzaman, S. M. Thompson, N. Shamsaei, and L. Bian, "Additive manufacturing of biomedical implants: A feasibility assessment via supply-chain cost analysis," *Additive Manufacturing,* vol. 11, pp. 97-113, 2016.

[10] S. Singare, L. Yaxiong, L. Dichen, L. Bingheng, H. Sanhu, and L. Gang, "Fabrication of customised maxillo-facial prosthesis using computer-aided design and rapid prototyping techniques," *Rapid prototyping journal,* vol. 12, pp. 206-213, 2006.

[11] J. Winder, R. Cooke, J. Gray, T. Fannin, and T. Fegan, "Medical rapid prototyping and 3D CT in the manufacture of custom made cranial titanium plates," *Journal of medical engineering & technology,* vol. 23, pp. 26-28, 1999.

[12] L. Murr, S. Gaytan, F. Medina, H. Lopez, E. Martinez, B. Machado, *et al.*, "Next-generation biomedical implants using additive manufacturing of complex, cellular and functional mesh arrays," *Philosophical Transactions of the Royal Society of London A: Mathematical, Physical and Engineering Sciences,* vol. 368, pp. 1999-2032, 2010.

[13] A. L. Jardini, M. A. Larosa, R. Maciel Filho, C. A. de Carvalho Zavaglia, L. F. Bernardes, C. S. Lambert, *et al.*, "Cranial reconstruction: 3D biomodel and custom-built implant created using additive manufacturing," *Journal of Cranio-Maxillofacial Surgery,* vol. 42, pp. 1877-1884, 2014.

[14] D. W. Rosen, "Computer-aided design for additive manufacturing of cellular structures," *Computer-Aided Design and Applications,* vol. 4, pp. 585-594, 2007.

[15] M. P. Bendsøe and N. Kikuchi, "Generating optimal topologies in structural design using a homogenization method," *Computer methods in applied mechanics and engineering,* vol. 71, pp. 197-224, 1988.

[16] M. P. Bendsøe and O. Sigmund, "Material interpolation schemes in topology optimization," *Archive of applied mechanics,* vol. 69, pp. 635-654, 1999.

[17] B. A. Szost, S. Terzi, F. Martina, D. Boisselier, A. Prytuliak, T. Pirling, *et al.*, "A comparative study of additive manufacturing techniques: Residual stress and microstructural analysis of CLAD and WAAM printed Ti–6Al–4V components," *Materials & Design,* vol. 89, pp. 559-567, 2016.

[18] Y. Xie and G. Steven, "Evolutionary structural optimization for dynamic problems," *Computers & Structures,* vol. 58, pp. 1067-1073, 1996.

[19] M. Y. Wang, X. Wang, and D. Guo, "A level set method for structural topology optimization," *Computer methods in applied mechanics and engineering,* vol. 192, pp. 227-246, 2003.

[20] G. Allaire, F. Jouve, and A.-M. Toader, "Structural optimization using sensitivity analysis and a level-set method," *Journal of computational physics,* vol. 194, pp. 363-393, 2004.

[21] O. Sigmund and J. Petersson, "Numerical instabilities in topology optimization: a survey on procedures dealing with checkerboards, mesh-dependencies and local minima," *Structural optimization,* vol. 16, pp. 68-75, 1998.

[22] B. Bourdin, "Filters in topology optimization," *International Journal for Numerical Methods in Engineering,* vol. 50, pp. 2143-2158, 2001.

[23] O. Sigmund, "Morphology-based black and white filters for topology optimization," *Structural and Multidisciplinary Optimization,* vol. 33, pp. 401-424, 2007.

[24] A. Diaz and O. Sigmund, "Checkerboard patterns in layout optimization," *Structural optimization,* vol. 10, pp. 40-45, 1995.

[25] K. Matsui and K. Terada, "Continuous approximation of material distribution for topology optimization," *International Journal for Numerical Methods in Engineering,* vol. 59, pp. 1925-1944, 2004.

[26] D. Fujii and N. Kikuchi, "Improvement of numerical instabilities in topology optimization using the SLP method," *Structural and Multidisciplinary Optimization,* vol. 19, pp. 113-121, 2000.

[27] X. Huang and Y. Xie, "Convergent and mesh-independent solutions for the bi-directional evolutionary structural optimization method," *Finite Elements in Analysis and Design,* vol. 43, pp. 1039-1049, 2007.

[28] T. E. Bruns and D. A. Tortorelli, "Topology optimization of non-linear elastic structures and compliant mechanisms," *Computer Methods in Applied Mechanics and Engineering,* vol. 190, pp. 3443-3459, 2001.

[29] T. Tsai and C. Cheng, "Structural design for desired eigenfrequencies and mode shapes using topology optimization," *Structural and Multidisciplinary Optimization,* vol. 47, pp. 673-686, 2013.

[30] A. Iga, S. Nishiwaki, K. Izui, and M. Yoshimura, "Topology optimization for thermal conductors considering design-dependent effects, including heat conduction and convection," *International Journal of Heat and Mass Transfer,* vol. 52, pp. 2721-2732, 2009.

[31] T. Borrvall and J. Petersson, "Topology optimization of fluids in Stokes flow," *International journal for numerical methods in fluids,* vol. 41, pp. 77-107, 2003.

[32] J. Guedes and N. Kikuchi, "Preprocessing and postprocessing for materials based on the homogenization method with adaptive finite element methods," *Computer Methods in Applied Mechanics and Engineering,* vol. 83, pp. 143-198, 1990/10/01/ 1990.

[33] J. K. Guest, J. H. Prévost, and T. Belytschko, "Achieving minimum length scale in topology optimization using nodal design variables and projection functions," *International journal for numerical methods in engineering,* vol. 61, pp. 238-254, 2004.

[34] W. Zhang, G. Dai, F. Wang, S. Sun, and H. Bassir, "Using strain energy-based prediction of effective elastic properties in topology optimization of material microstructures," *Acta Mechanica Sinica,* vol. 23, pp. 77-89, 2007.

[35] O. Sigmund and K. Maute, "Topology optimization approaches," *Structural and Multidisciplinary Optimization,* vol. 48, pp. 1031-1055, 2013.

[36] G. Sved and Z. Ginos, "Structural optimization under multiple loading," *International Journal of Mechanical Sciences,* vol. 10, pp. 803-805, 1968.

[37] U. Kirsch, "On singular topologies in optimum structural design," *Structural and Multidisciplinary Optimization,* vol. 2, pp. 133-142, 1990.

[38] P. Duysinx and M. P. Bendsøe, "Topology optimization of continuum structures with local stress constraints," *International journal for numerical methods in engineering,* vol. 43, pp. 1453-1478, 1998.

[39] G. Cheng and X. Guo, "ε-relaxed approach in structural topology optimization," *Structural Optimization,* vol. 13, pp. 258-266, 1997.

[40] M. Bruggi, "On an alternative approach to stress constraints relaxation in topology optimization," *Structural and multidisciplinary optimization,* vol. 36, pp. 125-141, 2008.

[41] J. París, F. Navarrina, I. Colominas, and M. Casteleiro, "Topology optimization of continuum structures with local and global stress constraints," *Structural and Multidisciplinary Optimization,* vol. 39, pp. 419-437, 2009.

[42] C. Le, J. Norato, T. Bruns, C. Ha, and D. Tortorelli, "Stress-based topology optimization for continua," *Structural and Multidisciplinary Optimization,* vol. 41, pp. 605-620, 2010.

[43] E. Holmberg, B. Torstenfelt, and A. Klarbring, "Stress constrained topology optimization," *Structural and Multidisciplinary Optimization,* vol. 48, pp. 33-47, 2013.

[44] J. París, F. Navarrina, I. Colominas, and M. Casteleiro, "Block aggregation of stress constraints in topology optimization of structures," *Advances in Engineering Software,* vol. 41, pp. 433-441, 2010.

[45] E. Lee, K. A. James, and J. R. Martins, "Stress-constrained topology optimization with design-dependent loading," *Structural and Multidisciplinary Optimization,* vol. 46, pp. 647-661, 2012.

[46] M. Bruggi and P. Duysinx, "Topology optimization for minimum weight with compliance and stress constraints," *Structural and Multidisciplinary Optimization,* vol. 46, pp. 369-384, 2012.

[47] A. R. Díaaz and N. Kikuchi, "Solutions to shape and topology eigenvalue optimization problems using a homogenization method," *International Journal for Numerical Methods in Engineering,* vol. 35, pp. 1487-1502, 1992.

[48] Z.-D. Ma, N. Kikuchi, and H.-C. Cheng, "Topological design for vibrating structures," *Computer methods in applied mechanics and engineering,* vol. 121, pp. 259-280, 1995.

[49] Z.-D. Ma, H.-C. Cheng, and N. Kikuchi, "Structural design for obtaining desired eigenfrequencies by using the topology and shape optimization method," *Computing Systems in Engineering,* vol. 5, pp. 77-89, 1994.

[50] N. L. Pedersen, "Maximization of eigenvalues using topology optimization," *Structural and multidisciplinary optimization,* vol. 20, pp. 2-11, 2000.

[51] J. Du and N. Olhoff, "Topological design of vibrating structures with respect to optimum sound pressure characteristics in a surrounding acoustic medium," *Structural and Multidisciplinary Optimization,* vol. 42, pp. 43-54, 2010.

[52] J. Du and N. Olhoff, "Topological design of freely vibrating continuum structures for maximum values of simple and multiple eigenfrequencies and frequency gaps," *Structural and Multidisciplinary Optimization,* vol. 34, pp. 91-110, 2007.

[53] B. Niu, J. Yan, and G. Cheng, "Optimum structure with homogeneous optimum cellular material for maximum fundamental frequency," *Structural and Multidisciplinary Optimization,* vol. 39, pp. 115-132, 2009.

[54] X. Huang, Z. Zuo, and Y. Xie, "Evolutionary topological optimization of vibrating continuum structures for natural frequencies," *Computers & structures,* vol. 88, pp. 357-364, 2010.

[55] Z. H. Zuo, X. Huang, J. H. Rong, and Y. M. Xie, "Multi-scale design of composite materials and structures for maximum natural frequencies," *Materials & Design,* vol. 51, pp. 1023-1034, 2013.

[56] Q. Xia, T. Shi, and M. Y. Wang, "A level set based shape and topology optimization method for maximizing the simple or repeated first eigenvalue of structure vibration," *Structural and Multidisciplinary Optimization*, vol. 43, pp. 473-485, 2011.

[57] A. T. Gaynor and J. K. Guest, "Topology optimization considering overhang constraints: Eliminating sacrificial support material in additive manufacturing through design," *Structural and Multidisciplinary Optimization,* vol. 54, pp. 1157-1172, 2016.

[58] J. Wu, C. C. Wang, X. Zhang, and R. Westermann, "Self-supporting rhombic infill structures for additive manufacturing," *Computer-Aided Design*, vol. 80, pp. 32-42, 2016.

[59] X. Qian, "Undercut and overhang angle control in topology optimization: a density gradient based integral approach," *International Journal for Numerical Methods in Engineering*.

[60] Q. Li, G. P. Steven, O. M. Querin, and Y. Xie, "Shape and topology design for heat conduction by evolutionary structural optimization," *International Journal of Heat and Mass Transfer*, vol. 42, pp. 3361-3371, 1999.

[61] A. Gersborg-Hansen, M. P. Bendsøe, and O. Sigmund, "Topology optimization of heat conduction problems using the finite volume method," *Structural and multidisciplinary optimization,* vol. 31, pp. 251-259, 2006.

[62] C. Zhuang, Z. Xiong, and H. Ding, "A level set method for topology optimization of heat conduction problem under multiple load cases," *Computer methods in applied mechanics and engineering,* vol. 196, pp. 1074-1084, 2007.

[63] T. Gao, W. Zhang, J. Zhu, Y. Xu, and D. Bassir, "Topology optimization of heat conduction problem involving design-dependent heat load effect," *Finite Elements in Analysis and Design,* vol. 44, pp. 805-813, 2008.

[64] C. Zhuang, Z. Xiong, and H. Ding, "Topology optimization of multi-material for the heat conduction problem based on the level set method," *Engineering Optimization,* vol. 42, pp. 811-831, 2010.

[65] G. Marck, M. Nemer, J.-L. Harion, S. Russeil, and D. Bougeard, "Topology optimization using the SIMP method for multiobjective conductive problems," *Numerical Heat Transfer, Part B: Fundamentals,* vol. 61, pp. 439-470, 2012.

[66] C. Zhuang, Z. Xiong, and H. Ding, "Topology optimization of the transient heat conduction problem on a triangular mesh," *Numerical Heat Transfer, Part B: Fundamentals,* vol. 64, pp. 239-262, 2013.

[67] A. Takezawa, G. H. Yoon, S. H. Jeong, M. Kobashi, and M. Kitamura, "Structural topology optimization with strength and heat conduction constraints," *Computer Methods in Applied Mechanics and Engineering,* vol. 276, pp. 341-361, 2014.

[68] T. E. Bruns, "Topology optimization of convection-dominated, steady-state heat transfer problems," *International Journal of Heat and Mass Transfer,* vol. 50, pp. 2859-2873, 2007.

[69] P. Coffin and K. Maute, "Level set topology optimization of cooling and heating devices using a simplified convection model," *Structural and multidisciplinary optimization,* vol. 53, pp. 985-1003, 2016.

[70] M. Zhou, J. Alexandersen, O. Sigmund, and C. B. Pedersen, "Industrial application of topology optimization for combined conductive and convective heat transfer problems," *Structural and Multidisciplinary Optimization,* vol. 54, pp. 1045-1060, 2016.

[71] Y. Joo, I. Lee, and S. J. Kim, "Topology optimization of heat sinks in natural convection considering the effect of shape-dependent heat transfer coefficient," *International Journal of Heat and Mass Transfer,* vol. 109, pp. 123-133, 2017.

[72] K. Yaji, T. Yamada, S. Kubo, K. Izui, and S. Nishiwaki, "A topology optimization method for a coupled thermal–fluid problem using level set boundary expressions," *International Journal of Heat and Mass Transfer,* vol. 81, pp. 878-888, 2015.

[73] A. Takezawa, M. Kobashi, Y. Koizumi, and M. Kitamura, "Porous metal produced by selective laser melting with effective isotropic thermal conductivity close to the Hashin–Shtrikman bound," *International Journal of Heat and Mass Transfer,* vol. 105, pp. 564-572, 2017.

[74] T. Dbouk, "A review about the engineering design of optimal heat transfer systems using topology optimization," *Applied Thermal Engineering,* vol. 112, pp. 841-854, 2017.

[75] Q. Li, G. P. Steven, Y. Xie, and O. M. Querin, "Evolutionary topology optimization for temperature reduction of heat conducting fields," *International Journal of Heat and Mass Transfer,* vol. 47, pp. 5071-5083, 2004.

[76] S. Torquato, S. Hyun, and A. Donev, "Multifunctional composites: optimizing microstructures for simultaneous transport of heat and electricity," *Physical review letters,* vol. 89, p. 266601, 2002.

[77] T. Matsumori, T. Kondoh, A. Kawamoto, and T. Nomura, "Topology optimization for fluid–thermal interaction problems under constant input power," *Structural and Multidisciplinary Optimization,* vol. 47, pp. 571-581, 2013.

[78] S. N. Laboratories. (2015). *Albany*. Available: https://github.com/gahansen/Albany

[79] S. N. Laboratories. (2015). *Trilinos*. Available: https://trilinos.org/

[80] T. Zegard and G. H. Paulino, "Bridging topology optimization and additive manufacturing," *Structural and Multidisciplinary Optimization,* pp. 1-18, 2015.

[81] W. Gao, Y. Zhang, D. Ramanujan, K. Ramani, Y. Chen, C. B. Williams, *et al.*, "The status, challenges, and future of additive manufacturing in engineering," *Computer-Aided Design,* 2015.

[82] T. Borrvall and J. Petersson, "Topology optimization using regularized intermediate density control," *Computer Methods in Applied Mechanics and Engineering,* vol. 190, pp. 4911-4928, 2001.

[83] U. G. Wegst, H. Bai, E. Saiz, A. P. Tomsia, and R. O. Ritchie, "Bioinspired structural materials," *Nature materials,* vol. 14, pp. 23-36, 2015.

[84] L. Zhang and W. Yu, "Variational asymptotic homogenization of elastoplastic composites," *Composite Structures,* vol. 133, pp. 947-958, 2015.

[85] Y. Cai, L. Xu, and G. Cheng, "Novel numerical implementation of asymptotic homogenization method for periodic plate structures," *International Journal of Solids and Structures,* vol. 51, pp. 284-292, 2014/01/01/ 2014.

[86] A. L. Kalamkarov, I. V. Andrianov, and V. V. Danishevsâ, "Asymptotic homogenization of composite materials and structures," *Applied Mechanics Reviews,* vol. 62, p. 030802, 2009.

[87] I. Setien, M. Chiumenti, S. van der Veen, M. San Sebastian, F. Garciandía, and A. Echeverría, "Empirical methodology to determine inherent strains in additive manufacturing," *Computers & Mathematics with Applications,* 2018.

[88] X. Liang, L. Cheng, Q. Chen, Q. Yang, and A. C. To, "A modified method for estimating inherent strains from detailed process simulation for fast residual distortion prediction of single-walled structures fabricated by directed energy deposition," *Additive Manufacturing,* vol. 23, pp. 471-486, 2018/10/01/ 2018.

[89] A. Bensoussan, J. L. Lions, and G. C. Papanicolaou, "Boundary layers and homogenization of transport processes," *Publications of the Research Institute for Mathematical Sciences,* vol. 15, pp. 53-157, 1979.

[90] A. Bensoussan, J.-L. Lions, and G. Papanicolaou, *Asymptotic analysis for periodic structures* vol. 374: American Mathematical Soc., 2011.

[91] J. R. Willis, "Variational and related methods for the overall properties of composites," *Advances in applied mechanics,* vol. 21, pp. 1-78, 1981.

[92] N. S. Bakhvalov and G. Panasenko, *Homogenisation: averaging processes in periodic media: mathematical problems in the mechanics of composite materials* vol. 36: Springer Science & Business Media, 2012.

[93] S. Arabnejad and D. Pasini, "Mechanical properties of lattice materials via asymptotic homogenization and comparison with alternative homogenization methods," *International Journal of Mechanical Sciences,* vol. 77, pp. 249-262, 2013.

[94] S. J. Hollister and N. Kikuchi, "A comparison of homogenization and standard mechanics analyses for periodic porous composites," *Computational Mechanics,* vol. 10, pp. 73-95, 1992.

[95] E. Andreassen and C. S. Andreasen, "How to determine composite material properties using numerical homogenization," *Computational Materials Science,* vol. 83, pp. 488-495, 2014.

[96] G.-D. Cheng, Y.-W. Cai, and L. Xu, "Novel implementation of homogenization method to predict effective properties of periodic materials," *Acta Mechanica Sinica,* vol. 29, pp. 550-556, 2013.

[97] L. J. Gibson and M. F. Ashby, *Cellular solids: structure and properties*: Cambridge university press, 1997.

[98] L. J. Gibson, M. F. Ashby, and B. A. Harley, *Cellular materials in nature and medicine*: Cambridge University Press, 2010.

[99] A. Simone and L. Gibson, "The effects of cell face curvature and corrugations on the stiffness and strength of metallic foams," *Acta Materialia,* vol. 46, pp. 3929-3935, 1998.

[100] Z. Xia, Y. Zhang, and F. Ellyin, "A unified periodical boundary conditions for representative volume elements of composites and applications," *International Journal of Solids and Structures,* vol. 40, pp. 1907-1921, 2003.

[101] J. Aboudi, "Micromechanical prediction of initial and subsequent yield surfaces of metal matrix composites," *International Journal of Plasticity,* vol. 6, pp. 471-484, 1990.

[102] N. Bakhvalov and G. Panasenko, "Homogenization in periodic media, mathematical problems of the mechanics of composite materials," ed: Nauka, Moscow, 1984.

[103] C. Sun and R. Vaidya, "Prediction of composite properties from a representative volume element," *Composites Science and Technology,* vol. 56, pp. 171-179, 1996.

[104] P. Zhang, J. Toman, Y. Yu, E. Biyikli, M. Kirca, M. Chmielus, *et al.*, "Efficient design-optimization of variable-density hexagonal cellular structure by additive manufacturing: theory and validation," *Journal of Manufacturing Science and Engineering,* vol. 137, p. 021004, 2015.

[105] Y. Wang, H. Xu, and D. Pasini, "Multiscale isogeometric topology optimization for lattice materials," *Computer Methods in Applied Mechanics and Engineering,* 2016.

[106] L. Cheng, P. Zhang, E. Biyikli, J. X. Bai, J. Robbins, and A. To, "Efficient design optimization of variable-density cellular structures for additive manufacturing: theory and experimental validation," *Rapid Prototyping Journal,* vol. 23, pp. 660-677, 2017.

[107] K. Terada, M. Hori, T. Kyoya, and N. Kikuchi, "Simulation of the multi-scale convergence in computational homogenization approaches," *International Journal of Solids and Structures,* vol. 37, pp. 2285-2311, 2000.

[108] L. Cheng, J. Liu, and A. C. To, "Concurrent lattice infill with feature evolution optimization for additive manufactured heat conduction design," *Structural and Multidisciplinary Optimization,* January 30 2018.

[109] W. Zhang and S. Sun, "Scale-related topology optimization of cellular materials and structures," *International journal for numerical methods in engineering,* vol. 68, pp. 993-1011, 2006.

[110] K. Tantikom, T. Aizawa, and T. Mukai, "Symmetric and asymmetric deformation transition in the regularly cell-structured materials. Part I: experimental study," *International Journal of Solids and Structures,* vol. 42, pp. 2199-2210, 2005/04/01/ 2005.

[111] L. Cheng, J. Liu, X. Liang, and A. C. To, "Coupling lattice structure topology optimization with design-dependent feature evolution for additive manufactured heat conduction design," *Computer Methods in Applied Mechanics and Engineering,* vol. 332, pp. 408-439, 2018/04/15/ 2018.

[112] V. S. Deshpande, N. A. Fleck, and M. F. Ashby, "Effective properties of the octet-truss lattice material," *Journal of the Mechanics and Physics of Solids,* vol. 49, pp. 1747-1769, 2001.

[113] I. Gibson, D. W. Rosen, and B. Stucker, *Additive manufacturing technologies*: Springer, 2010.

[114] E. Biyikli and A. C. To, "Proportional Topology Optimization: A New Non-Sensitivity Method for Solving Stress Constrained and Minimum Compliance Problems and Its Implementation in MATLAB," *PloS one,* vol. 10, p. e0145041, 2015.

[115] I. Özdemir, W. Brekelmans, and M. Geers, "Computational homogenization for heat conduction in heterogeneous solids," *International journal for numerical methods in engineering,* vol. 73, pp. 185-204, 2008.

[116] F. J. Ramírez-Gil, M. d. S. G. Tsuzuki, and W. Montealegre-Rubio, "Global finite element matrix construction based on a CPU-GPU implementation," *arXiv preprint arXiv:1501.04784,* 2015.

[117] S. Zhang, A. L. Gain, and J. A. Norato, "Stress-based topology optimization with discrete geometric components," *Computer Methods in Applied Mechanics and Engineering,* vol. 325, pp. 1-21, 2017/10/01/ 2017.

[118] K. Svanberg, "The method of moving asymptotes—a new method for structural optimization," *International journal for numerical methods in engineering,* vol. 24, pp. 359-373, 1987.

[119] L. Shu, M. Y. Wang, Z. Fang, Z. Ma, and P. Wei, "Level set based structural topology optimization for minimizing frequency response," *Journal of Sound and Vibration,* vol. 330, pp. 5820-5834, 2011.

[120] N. H. Kim, J. Dong, K. K. Choi, N. Vlahopoulos, Z.-D. Ma, M. Castanier, *et al.*, "Design sensitivity analysis for sequential structural–acoustic problems," *Journal of Sound and Vibration,* vol. 263, pp. 569-591, 2003.

[121] D. Tcherniak, "Topology optimization of resonating structures using SIMP method," *International Journal for Numerical Methods in Engineering,* vol. 54, pp. 1605-1622, 2002.

[122] N. Olhoff, E. Lund, and A. Seyranian, "Sensitivity analysis and optimization of multiple eigenvalues in structural design problems," in *Proceedings of the AIAA/NASA/USAF/ISMO Symposium on Multidisciplinary Analysis and Optimization, Part,* 1994, pp. 625-640.

[123] K. Svanberg, "MMA and GCMMA, versions September 2007," *Optimization and Systems Theory,* 2007.

[124] K. Svanberg, "The method of moving a asymptotes--A new method for structural optimization," *International journal for numberical methods in engineering,* 1987.

[125] J. Chen, V. Shapiro, K. Suresh, and I. Tsukanov, "Shape optimization with topological changes and parametric control," *International journal for numerical methods in engineering,* vol. 71, pp. 313-346, 2007.

[126] V. Shapiro, "Theory of R-functions and applications: A primer," Cornell University1991.

[127] S. Cai, W. Zhang, J. Zhu, and T. Gao, "Stress constrained shape and topology optimization with fixed mesh: a B-spline finite cell method combined with level set

function," *Computer Methods in Applied Mechanics and Engineering,* vol. 278, pp. 361-387, 2014.

[128] R. Mittal and G. Iaccarino, "Immersed boundary methods," *Annu. Rev. Fluid Mech.,* vol. 37, pp. 239-261, 2005.

[129] C. S. Peskin, "The immersed boundary method," *Acta numerica,* vol. 11, pp. 479-517, 2002.

[130] J. A. Sethian and A. Wiegmann, "Structural boundary design via level set and immersed interface methods," *Journal of computational physics,* vol. 163, pp. 489-528, 2000.

[131] Z. Kang and Y. Wang, "Integrated topology optimization with embedded movable holes based on combined description by material density and level sets," *Computer methods in applied mechanics and engineering,* vol. 255, pp. 1-13, 2013.

[132] O. Sigmund, "A 99 line topology optimization code written in Matlab," *Structural and Multidisciplinary Optimization,* 2001.

[133] M. P. Bendsøe, *Optimization of structural topology, shape, and material* vol. 414: Springer, 1995.

[134] B. H. E. Hinton, "A review of homogenization and topology optimization II TOp using OC," *computer & Structures,* 1998.

[135] L. Cheng, P. Zhang, E. Biyikli, J. Bai, J. Robbins, and A. To, "Efficient design optimization of variable-density cellular structures for additive manufacturing: theory and experimental validation," *Rapid Prototyping Journal,* vol. 23, 2017.

[136] L. Cheng, X. Liang, E. Belski, X. Wang, J. M. Sietins, S. Ludwick, *et al.,* "Natural Frequency Optimization of Variable-Density Additively Manufactured Lattice Structure: Theory and Experimental Validation," *Journal of Manufacturing Science and Engineering,* vol. under review, 2017.

[137] E. Andreassen, A. Clausen, M. Schevenels, B. S. Lazarov, and O. Sigmund, "Efficient topology optimization in MATLAB using 88 lines of code," *Structural and Multidisciplinary Optimization,* vol. 43, pp. 1-16, 2010.

[138] X. Guo, W. Zhang, and W. Zhong, "Stress-related topology optimization of continuum structures involving multi-phase materials," *Computer Methods in Applied Mechanics and Engineering,* vol. 268, pp. 632-655, 2014.

[139] P. Mercelis and J.-P. Kruth, "Residual stresses in selective laser sintering and selective laser melting," *Rapid Prototyping Journal,* vol. 12, pp. 254-265, 2006.

[140] J.-P. Kruth, L. Froyen, J. Van Vaerenbergh, P. Mercelis, M. Rombouts, and B. Lauwers, "Selective laser melting of iron-based powder," *Journal of Materials Processing Technology,* vol. 149, pp. 616-622, 2004.

[141] L. Papadakis, A. Loizou, J. Risse, and J. Schrage, "Numerical computation of component shape distortion manufactured by selective laser melting," *Procedia CIRP,* vol. 18, pp. 90-95, 2014.

[142] A. E. Patterson, S. L. Messimer, and P. A. Farrington, "Overhanging Features and the SLM/DMLS Residual Stresses Problem: Review and Future Research Need," *Technologies,* vol. 5, p. 15, 2017.

[143] S. Leuders, M. Thöne, A. Riemer, T. Niendorf, T. Tröster, H. Richard, *et al.*, "On the mechanical behaviour of titanium alloy TiAl6V4 manufactured by selective laser melting: Fatigue resistance and crack growth performance," *International Journal of Fatigue,* vol. 48, pp. 300-307, 2013.

[144] E. O. t. Olakanmi, R. Cochrane, and K. Dalgarno, "A review on selective laser sintering/melting (SLS/SLM) of aluminium alloy powders: Processing, microstructure, and properties," *Progress in Materials Science,* vol. 74, pp. 401-477, 2015.

[145] B. Ahmad, S. O. van der Veen, M. E. Fitzpatrick, and H. Guo, "Residual stress evaluation in selective-laser-melting additively manufactured titanium (Ti-6Al-4V) and inconel 718 using the contour method and numerical simulation," *Additive Manufacturing,* vol. 22, pp. 571-582, 2018/08/01/ 2018.

[146] E. R. Denlinger, J. C. Heigel, P. Michaleris, and T. A. Palmer, "Effect of inter-layer dwell time on distortion and residual stress in additive manufacturing of titanium and nickel alloys," *Journal of Materials Processing Technology,* vol. 215, pp. 123-131, 2015/01/01/ 2015.

[147] T. Mukherjee, W. Zhang, and T. DebRoy, "An improved prediction of residual stresses and distortion in additive manufacturing," *Computational Materials Science,* vol. 126, pp. 360-372, 2017/01/01/ 2017.

[148] R. Paul and S. Anand, "Optimization of layered manufacturing process for reducing form errors with minimal support structures," *Journal of Manufacturing Systems,* vol. 36, pp. 231-243, 2015.

[149] P. Das, K. Mhapsekar, S. Chowdhury, R. Samant, and S. Anand, "Selection of build orientation for optimal support structures and minimum part errors in additive manufacturing," *Computer-Aided Design and Applications,* pp. 1-13, 2017.

[150] P. Das, R. Chandran, R. Samant, and S. Anand, "Optimum part build orientation in additive manufacturing for minimizing part errors and support structures," *Procedia Manufacturing,* vol. 1, pp. 343-354, 2015.

[151] X. Duan, F. Li, and X. Qin, "Topology optimization of incompressible Navier–Stokes problem by level set based adaptive mesh method," *Computers & Mathematics with Applications,* vol. 72, pp. 1131-1141, 2016/08/01/ 2016.

[152] Z. Yan, F. Zhang, J. Wang, F. Liu, X. Guo, K. Nan, *et al.*, "Controlled mechanical buckling for origami-inspired construction of 3D microstructures in advanced materials," *Advanced functional materials,* vol. 26, pp. 2629-2639, 2016.

[153] D. Schillinger, A. Düster, and E. Rank, "The hp-d-adaptive finite cell method for geometrically nonlinear problems of solid mechanics," *International Journal for Numerical Methods in Engineering,* vol. 89, pp. 1171-1202, 2012.

[154] O. Poyraz, E. Yasa, G. Akbulut, A. Orhangul, and S. Pilatin, "Investigation of support structures for direct metal laser sintering (DMLS) of IN625 parts," in *Proceedings of Solid Freeform Fabrication (SFF) Symposium, Austin, TX, USA*, 2015.

[155] J. Vanek, J. A. Galicia, and B. Benes, "Clever support: Efficient support structure generation for digital fabrication," in *Computer Graphics Forum*, 2014, pp. 117-125.

[156] R. Vaidya and S. Anand, "Optimum Support Structure Generation for Additive Manufacturing Using Unit Cell Structures and Support Removal Constraint," *Procedia Manufacturing,* vol. 5, pp. 1043-1059, 2016.

[157] A. Hussein, L. Hao, C. Yan, R. Everson, and P. Young, "Advanced lattice support structures for metal additive manufacturing," *Journal of Materials Processing Technology,* vol. 213, pp. 1019-1026, 2013.

[158] J. Parvizian, A. Düster, and E. Rank, "Finite cell method," *Computational Mechanics,* vol. 41, pp. 121-133, 2007.

[159] M. Schwarz and H.-P. Seidel, "Fast parallel surface and solid voxelization on GPUs," in *ACM Transactions on Graphics (TOG)*, 2010, p. 179.

[160] Z. Dong, W. Chen, H. Bao, H. Zhang, and Q. Peng, "Real-time voxelization for complex polygonal models," in *Computer Graphics and Applications, 2004. PG 2004. Proceedings. 12th Pacific Conference on*, 2004, pp. 43-50.

[161] B. Hassani and E. Hinton, "A review of homogenization and topology optimization I—homogenization theory for media with periodic structure," *Computers & Structures,* vol. 69, pp. 707-717, 1998.

[162] M. W. Jones, J. A. Baerentzen, and M. Sramek, "3D distance fields: A survey of techniques and applications," *IEEE Transactions on visualization and Computer Graphics,* vol. 12, pp. 581-599, 2006.

[163] L. Cheng, X. Liang, E. Belski, X. Wang, J. M. Sietins, S. Ludwick, *et al.*, "Natural Frequency Optimization of Variable-Density Additive Manufactured Lattice Structure: Theory and Experimental Validation," *Journal of Manufacturing Science and Engineering*, vol. 140, p. 105002, 2018.

[164] Q. Yang, P. Zhang, L. Cheng, Z. Min, M. Chyu, and A. C. To, "Finite element modeling and validation of thermomechanical behavior of Ti-6Al-4V in directed energy deposition additive manufacturing," *Additive Manufacturing,* vol. 12, pp. 169-177, 2016.

[165] W. Yan, S. Lin, O. L. Kafka, Y. Lian, C. Yu, Z. Liu, *et al.*, "Data-driven multi-scale multi-physics models to derive process–structure–property relationships for additive manufacturing," *Computational Mechanics,* pp. 1-21, 2018.

[166] B. Schoinochoritis, D. Chantzis, and K. Salonitis, "Simulation of metallic powder bed additive manufacturing processes with the finite element method: A critical review," *Proceedings of the Institution of Mechanical Engineers, Part B: Journal of Engineering Manufacture,* vol. 231, pp. 96-117, 2017.

[167] M. Masoomi, S. M. Thompson, and N. Shamsaei, "Laser powder bed fusion of Ti-6Al-4V parts: Thermal modeling and mechanical implications," *International Journal of Machine Tools and Manufacture,* vol. 118-119, pp. 73-90, 2017/08/01/ 2017.

[168] S. Shrestha and K. Chou, "A build surface study of Powder-Bed Electron Beam Additive Manufacturing by 3D thermo-fluid simulation and white-light interferometry," *International Journal of Machine Tools and Manufacture,* vol. 121, pp. 37-49, 2017/10/01/ 2017.

[169] N. Keller and V. Ploshikhin, "New method for fast predictions of residual stress and distortion of AM parts."

[170] C. Li, C. Fu, Y. Guo, and F. Fang, "Fast prediction and validation of part distortion in selective laser melting," *Procedia Manufacturing,* vol. 1, pp. 355-365, 2015.

[171] Y.-h. R. Tsai, "Rapid and accurate computation of the distance function using grids," *Journal of Computational Physics,* vol. 178, pp. 175-195, 2002.

[172] M. Siewert, F. Neugebauer, J. Epp, and V. Ploshikhin, "Validation of Mechanical Layer Equivalent Method for simulation of residual stresses in additive manufactured components," *Computers & Mathematics with Applications,* 2018/10/09/ 2018.

[173] R. Glowinski and Y. Kuznetsov, "Distributed Lagrange multipliers based on fictitious domain method for second order elliptic problems," *Computer Methods in Applied Mechanics and Engineering,* vol. 196, pp. 1498-1506, 2007.

[174] T. Yamada, K. Izui, S. Nishiwaki, and A. Takezawa, "A topology optimization method based on the level set method incorporating a fictitious interface energy," *Computer Methods in Applied Mechanics and Engineering,* vol. 199, pp. 2876-2891, 2010.

[175] I. Ramiere, P. Angot, and M. Belliard, "A fictitious domain approach with spread interface for elliptic problems with general boundary conditions," *Computer Methods in Applied Mechanics and Engineering,* vol. 196, pp. 766-781, 2007.

[176] Q. Cai, S. Kollmannsberger, R.-P. Mundani, and E. Rank, "The finite cell method for solute transport problems in porous media," in *Proceedings of the international conference on finite elements in flow problems*, 2011.

[177] M. Ruess, D. Tal, N. Trabelsi, Z. Yosibash, and E. Rank, "The finite cell method for bone simulations: verification and validation," *Biomechanics and modeling in mechanobiology*, vol. 11, pp. 425-437, 2012.

[178] Z. Yang, M. Ruess, S. Kollmannsberger, A. Düster, and E. Rank, "An efficient integration technique for the voxel‐based finite cell method," *International Journal for Numerical Methods in Engineering*, vol. 91, pp. 457-471, 2012.

[179] S. Ly, A. M. Rubenchik, S. A. Khairallah, G. Guss, and M. J. Matthews, "Metal vapor micro-jet controls material redistribution in laser powder bed fusion additive manufacturing," *Scientific reports*, vol. 7, p. 4085, 2017.

[180] J. Kennedy, "Particle swarm optimization," in *Encyclopedia of machine learning*, ed: Springer, 2011, pp. 760-766.

[181] I. Y. Kim and O. L. de Weck, "Adaptive weighted-sum method for bi-objective optimization: Pareto front generation," *Structural and multidisciplinary optimization*, vol. 29, pp. 149-158, 2005.

[182] M. Strantza, B. Vrancken, M. B. Prime, C. Truman, M. Rombouts, D. W. Brown, *et al.*, "Directional and oscillating residual stress on the mesoscale in additively manufactured Ti-6Al-4V," *Acta Materialia*, 2019/01/30/ 2019.

[183] R. Luciano and J. Willis, "Boundary-layer corrections for stress and strain fields in randomly heterogeneous materials," *Journal of the Mechanics and Physics of Solids*, vol. 51, pp. 1075-1088, 2003.

[184] A. Sharma and K. Maute, "Stress-based topology optimization using spatial gradient stabilized XFEM," *Structural and Multidisciplinary Optimization*, October 24 2017.

[185] P. Hansbo, M. G. Larson, and S. Zahedi, "A cut finite element method for a Stokes interface problem," *Applied Numerical Mathematics*, vol. 85, pp. 90-114, 2014.

[186] L. Cheng, P. Zhang, E. Biyikli, J. Bai, S. Pilz, and A. C. To, "Integration of Topology Optimization with Efficient Design of Additive Manufactured Cellular Structures," 2015.

[187] L. Cheng, J. Liu, X. Liang, and A. C. To, "Coupling Lattice Structure Topology Optimization with Design-Dependent Feature Evolution for Additive Manufactured Heat Conduction Design " *Computer Methods in Applied Mechanics and Engineering*, 2018.

[188] G. Barozzi and G. Pagliarini, "A method to solve conjugate heat transfer problems: the case of fully developed laminar flow in a pipe," *Journal of heat transfer*, vol. 107, pp. 77-83, 1985.

[189] A. Düster, J. Parvizian, Z. Yang, and E. Rank, "The finite cell method for three-dimensional problems of solid mechanics," *Computer methods in applied mechanics and engineering*, vol. 197, pp. 3768-3782, 2008.

[190] J. Luo, Z. Luo, L. Chen, L. Tong, and M. Y. Wang, "A semi-implicit level set method for structural shape and topology optimization," *Journal of Computational Physics*, vol. 227, pp. 5561-5581, 2008/05/10/ 2008.

[191] M. Langelaar, "Combined optimization of part topology, support structure layout and build orientation for additive manufacturing," *Structural and Multidisciplinary Optimization*, pp. 1-20, 2018.

[192] H. Zhao, "A fast sweeping method for eikonal equations," *Mathematics of computation*, vol. 74, pp. 603-627, 2005.